CONTROL OF MICROSTRUCTURE DURING SOLIDIFICATION & HOMOGENIZATION OF THIN-SLAB CAST DIRECT-ROLLING (TSCDR) MICROALLOYED STEELS

CONTROL OF MICROSTRUCTURE DURING SOLIDIFICATION & HOMOGENIZATION OF THIN-SLAB CAST DIRECT-ROLLING (TSCDR) MICROALLOYED STEELS

By

TIHE ZHOU, B. ENG, M. ENG.

A Thesis

Submitted to the School of Graduate Studies

in Partial Fulfillment of the Requirements

for the Degree

Doctor of Philosophy

DOCTOR OF PHILOSOPHY (2010) McMaster University

(Department of Materials Science and Engineering) Hamilton, Ontario

TITLE: **Control of Microstructure during Solidification & Homogenization of Thin-Slab Cast Direct-Rolling (TSCDR) Microalloyed Steels**

AUTHOR: **Tihe Zhou, B. Eng., M. Eng.**

SUPERVISOR: **Dr. Hatem S. Zurob**

NUMBER OF PAGES: xxvi, 232

ABSTRACT

The advantages of Thin-Slab Cast Direct-Rolling (TSCDR) process include reduced capital, energy, labour and inventory costs, as well as the ability to roll thinner strip compared to the conventional process of thick slab casting, reheating and hot rolling. There is great interest in utilizing this technology to produce microalloyed steels which can meet American Petroleum Institute (API) standards. However, whereas the conventional approach can produce APIX80, APIX100, and even APIX120 steels; the TSCDR process can only produce APIX70 and APIX80. The main obstacles in the way of achieving high API grades are the non-uniform initial as-cast microstructure and the large grains that result from grain growth at high temperature. The production of APIX80 and higher grade steels can only be achieved through a comprehensive research initiative that combines careful control of solidification, homogenization, thermomechanical-processing, cooling and coiling.

This contribution examines the solid state microstructure evolution of microalloyed steels under simulated TSCDR conditions. The grain growth kinetics in delta-ferrite and austenite were studied separately using two model alloys. At high temperatures and in the absence of precipitation, the growth kinetics in both delta-ferrite and austenite appeared to follow a simple parabolic growth law. The measured grain growth kinetics was then applied to the problem of grain-size control during the process of TSCDR. Several strategies of controlling and refining the grain size were examined. The kinetics of delta-ferrite to austenite

phase transformation was investigated using a quenching dilatometer; the results showed that the austenite phase formed along the original delta grain boundaries, and that the precipitation of austenite at the delta-ferrite grain boundaries effectively pins delta grain growth. The kinetics of the phase transformation was modeled using a local equilibrium model that captures the partitioning of the substitutional elements during the transformation.

A novel delta-ferrite/austenite duplex microstructure is proposed to achieve fine and uniform high-temperature microstructure. The grain growth of the matrix phase (delta-ferrite) is controlled by the coarsening mechanism of pinning phase (austenite). The effectiveness of this delta/austenite duplex microstructure was validated experimentally and analyzed in details using a physically-based model.

ACKNOWLEDGEMENTS

I would like to express my deep and sincere gratitude to my supervisor, Dr. Hatem S. Zurob for his constructive advice, knowledge, patience and understanding. He is not only a great counselor but also a great friend. I surely enjoyed every talk we have had, academic and non-academic. I am also deeply grateful my Ph. D supervisory committee members Dr. Nikolas Provatas and Dr. Sumanth Shankar for their valuable advice and supports throughout this work.

My sincere thanks are due to John Thomson, Jim Garret, Owen Kelly, Martin Vanooste and Connie Barry. Without their support, the melting and grain growth experiments would not have been so successful. I would like to acknowledge the aid given by Doug Culley, John Rodda and Ed McCaffery in the MSE Department. My thanks also go to the phase transformation research group of which I am honoured to be a part.

The financial support of the Steel Research Center, McMaster University and the RIEM Program are gratefully acknowledged. I also wish to acknowledge Dr. Ronald J. O`Malley from Nucor Steel Decatur, LLC and Dr. Sunday Abraham from Evraz Inc. NA for providing slab samples. Dr. Elachmi Essadiqi and Dr. Benoit Voyzelle from CANMET Materials Research Laboratory I gratefully acknowledge for their help in casting one of the model alloys and for performing the dilatometer experiments.

I owe my thanks to my wife Sujuan Ma for her never-ending encouragement and support, my two lovely sons Mike Mo Zhou and Mark Yu Zhou for the happiness brought to me. My profound love and appreciation also go to all members of my family in China. Above all, I thank GOD, if not by His grace and glory all this would have been for nothing.

TABLE OF CONTENTS

LIST OF FIGURES

Chapter 1

Chapter 2

Chapter 3

Chapter 4

Chapter 5

LIST OF TABLES

Chapter 3

Chapter 4

Chapter 5

LIST OF SYMBOLS

α	Geometric constant in grain growth equation
β	Geometric constant in limiting grain size equation
δ	Delta-ferrite
$\sigma_{\delta\gamma}$	Delta-ferrite and austenite interface energy
ε	Darken factor for non-ideality correction
γ	Austenite
γ_{gb}	Grain boundary energy
w	Grain boundary thickness
a	Lattice parameter
b	Magnitude of Burgers vector
C_{Al}^{o}	Initial aluminum concentration
C_{Al}^{γ}	Aluminum concentration in austenite
C_{Al}^{δ}	Aluminum concentration in delta-ferrite
C_{C}^{o}	Initial carbon concentration
C_{C}^{γ}	Carbon concentration in austenite
C_{C}^{δ}	Carbon concentration in delta-ferrite
C_{Mn}^{o}	Initial manganese concentration
C_{Mn}^{γ}	Manganese concentration in austenite

C_{Mn}^{δ} Manganese concentration in delta-ferrite

D Grain diameter

D_{Al} Aluminum diffusion coefficient in the delta-ferrite

D_{Bulk} Bulk diffusion coefficient

D_{C} Carbon diffusion coefficient in the delta-ferrite

D_{GB} Grain boundary diffusion coefficient

D_{L} Limiting grain size

D_{Mn} Manganese diffusion coefficient in the delta-ferrite

D_{Zener} Zener limiting grain size

D_{ZC} Limiting grain size regarding the effects of boundary-particle correlationship

$f(F_{V})$ A function of the particle volume fraction

F_{V} Particle volume fraction

k_{Al} Aluminum diffusion controlled particles coarsening constant

k_{C} Carbon diffusion controlled particles coarsening constant

k_{Mn} Manganese diffusion controlled particles coarsening constant

k_{Si} Silicon diffusion controlled particles coarsening constant

K Particles coarsening constant

M_{Pure} Grain boundary mobility of pure materials

$M_{\delta}(T)$ Delta Grain boundary mobility

$M_{\gamma}(T)$ Austenite Grain boundary mobility

n	Particle coarsening exponent
N_δ	Solute molar fraction in the delta-ferrite
P	Grain growth driving pressure
P_Z	Zener pinning pressure
P_{ZC}	Humphreys pinning pressure regarding the effects of boundary-particle correlationship
Q	Bulk diffusion activation energy
Q_{GB}	Grain boundary diffusion activation energy
r	Particle radius
r_o	Initial particle radius
r^*	Average particle radius
R	Grain radius
R_o	Initial grain radius
$\overline{R}$	Average grain radius
t	Time
t_o	Initial time for particle coarsening
t_1	Time reaches 900°C for austenite grain growth
T	Temperature
$T(t)$	Temperature as a function of time during reheating process
V_m	Molar volume
x	Distance from the interface

Preface

The Thin Slab Casting Direct Rolling (TSCDR) process has been labelled as the third revolution in the economics of steel production(Korchynsky 2005) thus being compared in significance to two previous revolutionary changes; the replacement of open hearth melting by the Basic Oxygen Furnace (BOF) converter and the change from ingot casting to continuous casting. The advantages of direct linking between casting and hot-rolling include reduced capital, energy, labour and inventory costs, as well as the ability to roll thinner strip compared with thick slab casting, reheating and hot rolling. Today variations on the direct linked theme have emerged from Danielli, Voest Alpine Industries and Arvedi. There are over 50 such installations operating worldwide producing about 55 million tons of hot-strip annually, or 14 percent of world output(Muller et al. 2005).

Along with the considerable engineering developments, advances in product metallurgy have expanded the range of steel grades produced via thin slab cast mills so that the range includes stainless steels, interstitial free steels, transformation induced plasticity steel (TRIP), high-strength low-alloy and dual-phase grades. In processing all steels by this route, the direct link between the caster and the rolling mill means that the cast microstructure is as never before the starting point for developing the as-rolled structure and properties. The direct link is particularly influential in the case of microalloyed high-strength low-alloy steels where

there are strong interactions between precipitation and recrystallization requiring careful control of the cast microstructure to achieve the intended result. An important market for microalloyed steels is that of line pipe steels for oil and gas transportation. The steels used for this application need to meet very stringent standard of the American Petroleum Institute (API) standards on strength, toughness and low ductile-to-brittle transition temperature (DBTT). Excellent control of the as-cast structure and subsequent grain coarsening in the solids state is essential for meeting the required specifications of the final product.

Experimental studies (Reip et al. 2005; Uranga et al. 2005; Wang et al. 2005; Zhang et al. 2005) clearly show that the austenite grain size in the as cast structure is large and non-uniform, and the large grains are believed to result from the casting, and subsequent grain growth in the solid state before entering the rolling mills. In order to meet the requirements of high strength and toughness, the final product must have small and very uniform grain size. To date, most efforts have been concentrated on using thermomechanical processing to transform the initial coarse and heterogeneous structure into a fine uniform structure; this approach has made it possible to produce APIX70 steels using the TSCDR process. Most companies, however, are still working on producing of the APIX80 grade (Korchynsky 2005). Reip et al (Reip et al. 2005) showed that while the required yield strength can be achieved using Nb-V and Nb-Mo steel grades, the required toughness and DBTT cannot be achieved. It is widely accepted that even a small volume fractions of large isolated grains is enough to impair the toughness and DBTT of the steel(Banks 2005; Reip et al. 2005).

Chapter 1 Introduction

1.1 Overview of TSCDR Microalloyed Steels

Because of its low capital and operating costs, thin slab casting and direct rolling (TSCDR) has become a major process for hot strip production in the world. Due to a high market demand for high strength grade steels, a significant effort has been made to develop microalloyed steels that can meet the American Petroleum Institute standards using TSCDR technology.

1.1.1 Thin Slab Cast Direct Rolling Technology

The first thin slab casting operation started in the late 1980`s. This technology was revolutionized in 1989 when Nucor linked a thin slab caster direct linked to a hot rolling mill to produce the first TSCDR line. As pioneered by SMS-Demag in Germany this technology is based on a novel funnel mould caster design that produces a "thin" 50 to 70 mm thick slab instead of the conventional slab thickness of 200 to 250 mm. Figure 1.1 shows the typical layout of the most common SMS-Demag-type "Compact Strip Production" mill(Klinkenberg and Hensger 2005). A "Soaking Furnace" is placed between the caster and the hot strip mill entry to keep the thin slab from cooling while it grows to the appropriate length for rolling.

The furnace usually also permits sideways transfer of the slab so that two casters can feed a single rolling mill, maximizing use of the rolling capacity. When the slab length is long enough, it is cut and enters into the rolling mills which consist of only five or six stands. The concept of direct linking makes the TSCDR production line of 300m long which is much shorter than conventional continuous casting and cold rolled (CCR) slab line which is 900m long(Cobo and Sellars 2001).

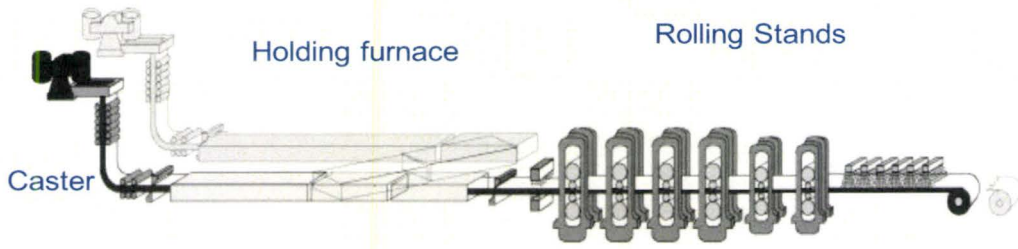

Figure 1-1 Layout of the most common SMS-Demag Compact Strip Production Mill (Klinkenberg and Hensger 2005)

Since then many new designs for TSCDR have been development. The most widely used production units include: In-line Strip Production (ISP), CONROLL Process, Quality Strip Production (QSP) and Flexible Thin Slab Rolling Process (fTSR). The cast-slab thickness in these new designs in which cast thickness ranges from 40 to 150 mm. Configurations also vary to include single and double strand casting, use of a coilbox instead of a soaking furnace, roughing mills before finishing, and direct feed to a plate or steckel mill

instead of a continuous strip mill (Imagumbai and Takechi 2003; Matlock et al. 2005; Watzinger et al. 2005).

1.1.2 Advantages of Thin Slab Cast Direct Rolling Technology

Compared to the CCR route, the striking advantage of the TSCDR technology is its speed and flexibility. Coiled products can be moved from the rolling mills within 20 minutes of the slab leaving the caster. The flexibility is based on the customers demand for smaller batches of different grades of steel at competitive price within a short time which is difficult for conventional integrated steelworks to achieve. The detail advantages of this technology are the following:

Low Capital Costs: The production line is compact, therefore less space are needed for casting and rolling equipment. No investment needed for a re-heating furnace and roughing mills as they are not required (Priestner 1998; Korchynsky 2005; Wang et al. 2005).

Energy Savings: No re-heating stage and production time is much shorter. Energy consumption is small(Priestner 1998; Muller et al. 2005).

Flexibility: TSCDR process can produce at low capacities, and products can easily be changed to meet customer's demands(Wang et al. 2005).

Environmental Advantages: TSCDR is usually supplied by electric arc furnace using scraps as raw materials which is friendly to the environment. In the CCR process, coal is often used in the re-heating stage and this leads to high emissions. The elimination of the re-heating stage in TSCDR process will also reduce energy consumption(Priestner 1998).

1.1.3 TSCDR Microalloyed Steels and API Standards

Based on these advantages of TSCDR technology, great efforts have been focused on using this technology to produce microalloyed steels that meet the American Petroleum Institute (API) standards (Priestner 1998; Cobo and Sellars 2001; Klinkenberg and Hensger 2005; Reip et al. 2005; Zhang et al. 2005). The API provides standards for pipe microalloyed steels that are suitable for conveying gas, water, and oil in both the oil and natural gas industries. Figure 1.2 shows the API specification 5L requirements with regard to chemical composition, strength and toughness. In addition to the requirements of the API 5L specification, the further requirements are often stipulated in the specifications and supply agreements made with the customer.

The main drawback of the TSCDR process is that so far it has only produced APIX70 grades (Figure 1.3) while the CCR Process can produce APIX80, APIX100 and even APIX120 grade. The new phenomena which stand in the way of producing higher strength grades using the TSCDR process are discussed next.

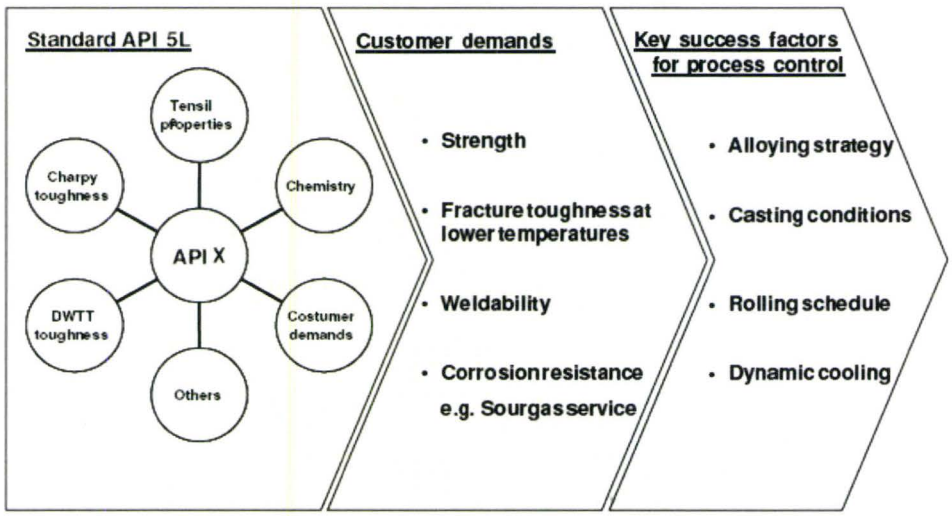

Figure 1-2 Demands on pipe steel according to API specification 5L, key success factors for processing via CSP technology(Klinkenberg and Hensger 2005)

Steel grade	Plant									
	Handan	Gallatin	Hylsa	TKS	NUCOR	ISG (Acme)	Megasteel	SDI	EZDK	Ispat
X52										
X60										
X70										
X80	Under development									

Figure 1-3 Examples of plants Developing Nb-(Ti)-API tube grades(Klinkenberg and Hensger 2005)

1.2 Peculiarities of Microstructure Evolution in TSCDR Microalloyed Steels

TSCDR microalloyed steel process introduces some new challenges compared to conventional casting and cold rolling process. Due to the reduced cross-sectional thickness and increased slab surface area per unit volume (4.5 times); the thin slabs solidify much more quickly than conventional thick slabs. This results in a reduction of the interdendritic spacing, which is beneficial in terms of less microsegregation and increasing composition homogeneity. A finer as cast austenite grain size is achieved in the structure, 550-600μm compared with 1000μm for a thick slab. However, after solidification the thin slab is placed in the tunnel furnace for 20 to 30 minutes at 1100 °C to 1150°C, and the initial austenite grains of ~500μm grow to about 2000μm(Pottore et al. 1991). The subsequent thermomechanical processing (5 to 6 passes only resulting in a thickness reduction ~80%) are insufficient to refine the austenite grain size. This point is highlighted in Figure 1.4 which compares TSCDR to the conventional rolling practice. In the conventional rolling process the austenite grain size is less than 50μm when the material enters the finishing mill. In contrast, the absence of the cooling and reheating cycle, as well as the elimination of roughing, result in some of the austenite grain being as large as 2000μm at the onset of rolling in TSCDR. The coarse grain as cast structure needs extensive refinement in the finish rolling process. As the slab thickness is much smaller than the conventional one; the total reduction for effective structural refinement is limited. The maximum available strain in TSCDR is only 2.0, whereas for conventional process is about 4.5(Cobo and Sellars 2001). These differences make it

necessary to control the as cast microstructure a key factor to produce high grade microalloyed steel used in the oil and gas industries.

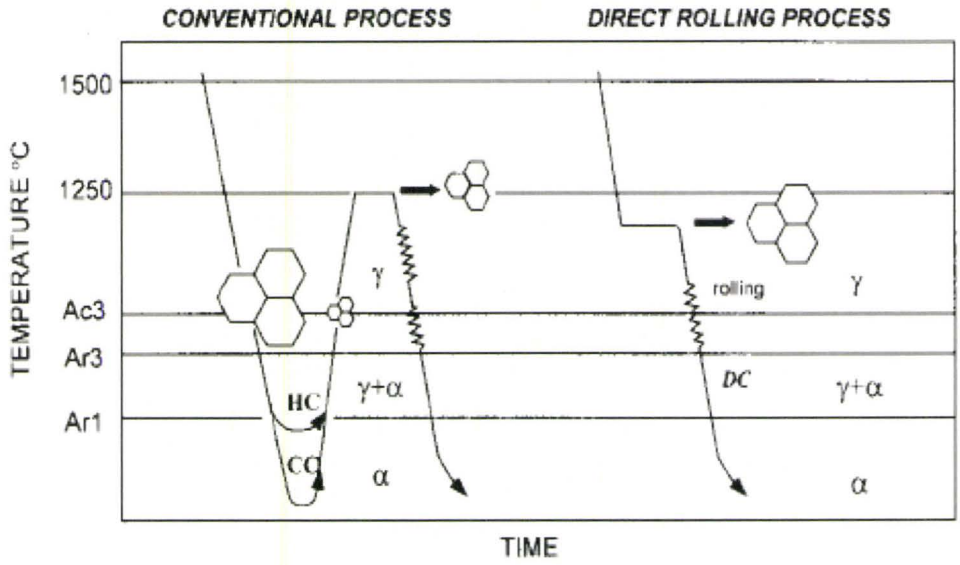

Figure 1-4 Temperature evolution during TSCDR in comparison with conventional cold rolling (Cobo and Sellars 2001)

Another new microstructural phenomenon is the modification of adding microalloy elements in the TSCDR process. For optimum dispersion strengthening, except for the case of Ti, the goal is to have the entire microalloying element content in solid solution before rolling. This is one of the most significant differences compared to the CCR process, where the use of long reheating times can produce a significant dissolution of microalloying elements. Figure 1.5 shows the main TSCDR stage and the corresponding microstructural changes that are involved in conjunction with microalloys(Rodriguez-lbabe 2005).

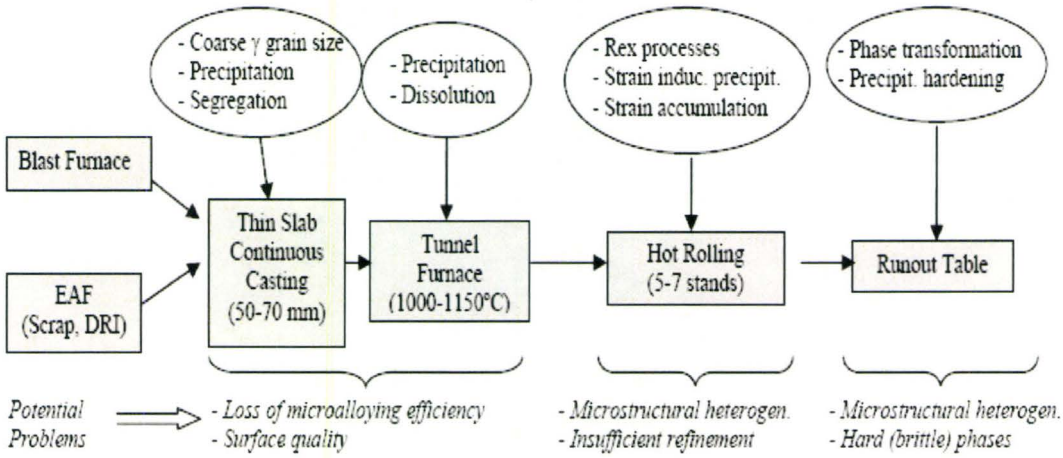

Figure 1-5 Scheme showing the metallurgical mechanisms that operate at the different stages of TSDR process as well as the potential problems related to microalloying(Rodriguez-lbabe 2005)

Due to the small number of deformation passes available during the processing of the TSCDR products, the non-uniformity of the as-cast microstructure will persist during the downstream processing. In what follows, the origin of the non-uniformity of the as-cast microstructure is reviewed in detail. In addition, the factors leading to the development of excessively large austenite grain size are also reviewed.

❖ Non-uniform as-cast microstructure

Figures 1.6 (a) and (b) show the dendrite morphology at the quarter point and second dendrite arm spacing (SDAS) in the as-cast slab of three typical microalloyed steels: 0.07Nb-0.016Ti, 0.035Nb-0.004Ti and 0.063Nb-0.039Ti. At the surface of the slab, the second

dendrite arm spacing (SDAS) is small, but it increases towards the center of the slab, with the maximum of the SDAS above 250μm(Wang et al. 2005). However on the surface the SDAS is only 50μm. These non-uniform as cast microstructure will affect the downstream operation and eventually affect the mechanical properties of the microalloyed steel.

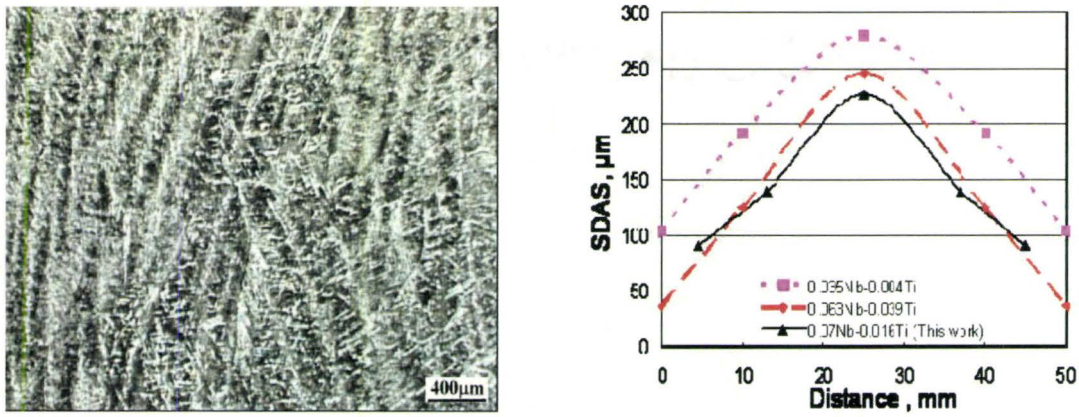

a) Dendrite morphology at quarter point b) The SDAS vs. the slab thickness position

Figure 1-6 Dendrite morphology and SDAS in the as cast slab(Wang et al. 2005)

Due to the large grain size and non-uniformity, some people try to use thermomechanical process to reduce grain size, but this method was not successful for the thick gauge (Bakkaloğlu 2002; Elwazri et al. 2005; Elwazri et al. 2005; Sellars and Palmiere 2005; Sim et al. 2005; Uranga et al. 2005; Zhu and Subramanian 2006). The slab thickness varies from 50 to 70mm; the final gauge thickness for some API grade microalloyed steel is 10mm or more. The deformation ratio is only 5 to 7; and the reduction must usually be achieved in 5 to 6 deformation passes. Figure 1.7 shows the results obtained for the schedules

corresponding to the final gauge thicknesses of 4 mm and 10 mm, respectively, at two rolling start temperatures of 1040°C and 1100°C. If the initial as-cast structure is not completely refined during the first interstand, some coarse unrecrystallized grains remain in the steel until the transformation. From Figure 1.7 (b), variations of austenite grain size exist for all start rolling temperatures.

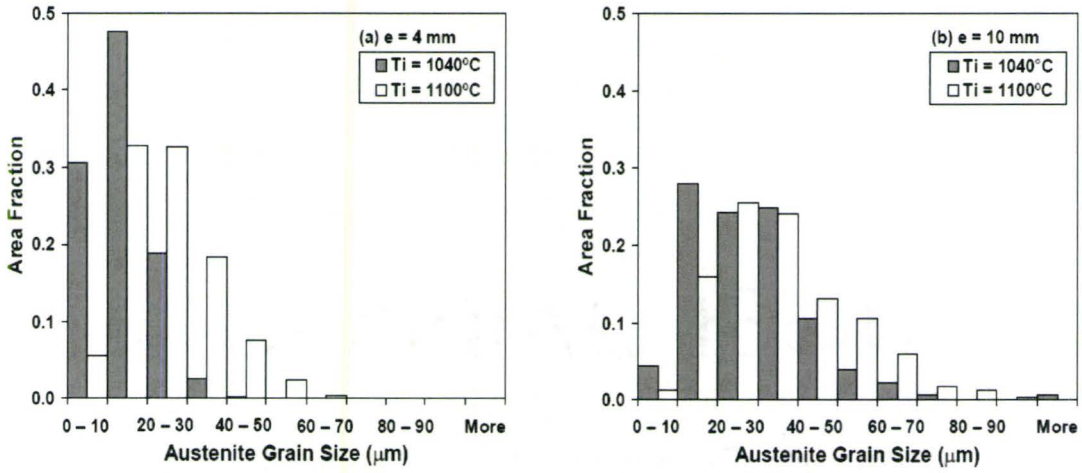

Figure 1-7 Austenite grain size distributions prior to transformation for final gauge of (a) 4 mm and(b) 10 mm and two rolling start temperatures of 1040°C and 1100°C(Uranga et al. 2005)

❖ Large austenite grain size

The large dendrite arm spacing at the centre along with subsequent grain growth in the solid state results in a large austenite grain in the centre. Figure 1.8(a) shows the austenite grains exhibited in the as-cast slab. The austenite grain is large and elongated. Figure 1.8(b) shows the grain size distribution of austenite. The average equivalent diameter of austenite

grains is 654±314 μm, with some grains as large as 1400 μm. The presence of a small number of large grains is important because even a small fraction of large austenite grains which is less than 3 percent will affect the recrystallization of the thermomechanical process(Wang et al. 2005).

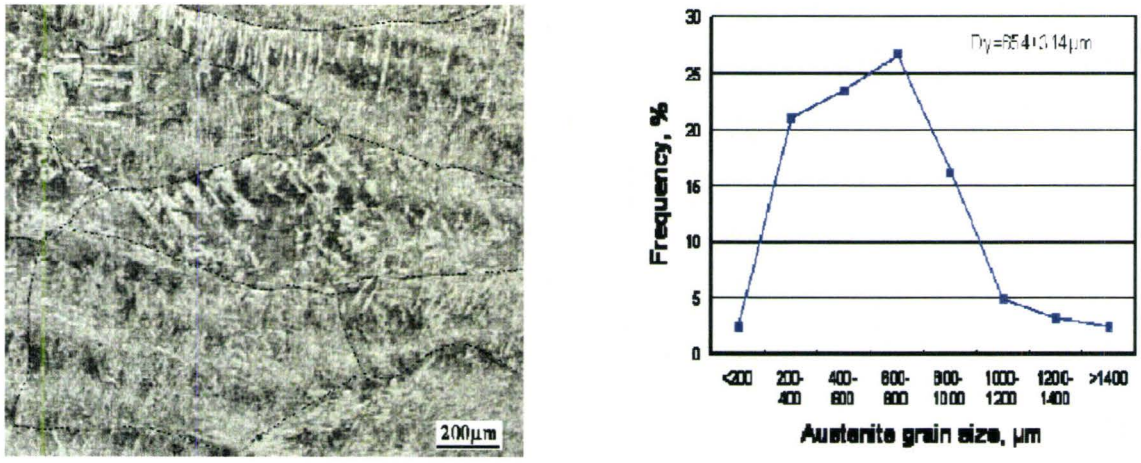

a) Austenite grains at the quarter position b) Austenite grain size distribution

Figure 1-8 Austenite grains in the as cast slab(Wang et al. 2005)

Figure 1.9 shows the evolution of the as-cast microstructure on subsequent cooling of a steel containing 0.08 pct carbon. At the beginning, austenite is nucleated at the delta-ferrite grain boundaries. The delta-ferrite to austenite phase transformation is completed at about 1460°C. During cooling from 1450 to 1380 °C, the austenite grains rapidly grow and the grain size increases from 500μm to 2000μm(Pottore et al. 1991). These large austenite grains will continue to grow in the soaking furnace.

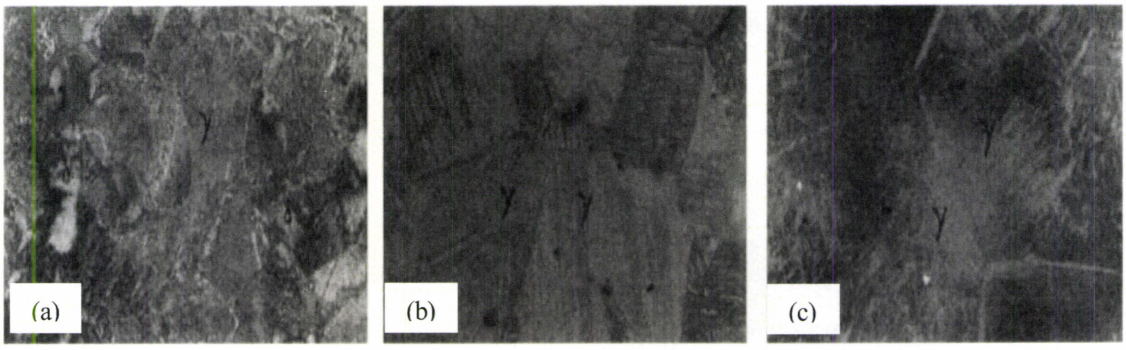

Figure 1-9 Microstructure evolution during subsequent cooling of a steel containing 0.08 pct carbon. The temperatures at the time of the quench were (a) 1460 °C, (b) 1430 °C and (c) 1380 °C

(Pottore et al. 1991)

❖ Persistence of Large Austenite Grains

Figure 1.10 summarizes the evolution of the microstructural at the end of each interstand time for two rolling sequences, corresponding to final thicknesses of (a) 4 mm and (b) 10 mm and a rolling temperature starting at 1040°C(Uranga et al. 2005). In this figure, D_{mean} is the mean grain size, $D_{\max}$ is the maximum grain size and D_C is the critical grain size which is defined such that grains with a diameter, D, greater than D_C would take up 10% of the volume fraction of the sample. The heterogeneity of the grain size distribution is characterized by the parameter ZD which is defined as $D_{\max} / D_{mean}$. From Figure 1.10 (a), ZD parameter decreased with the deformation pass, but for 10mm gauge thickness as shown in (b),

the ZD parameter is essentially unchanged meaning that material inherits the grain-size inhomogenity of the as-cast structure.

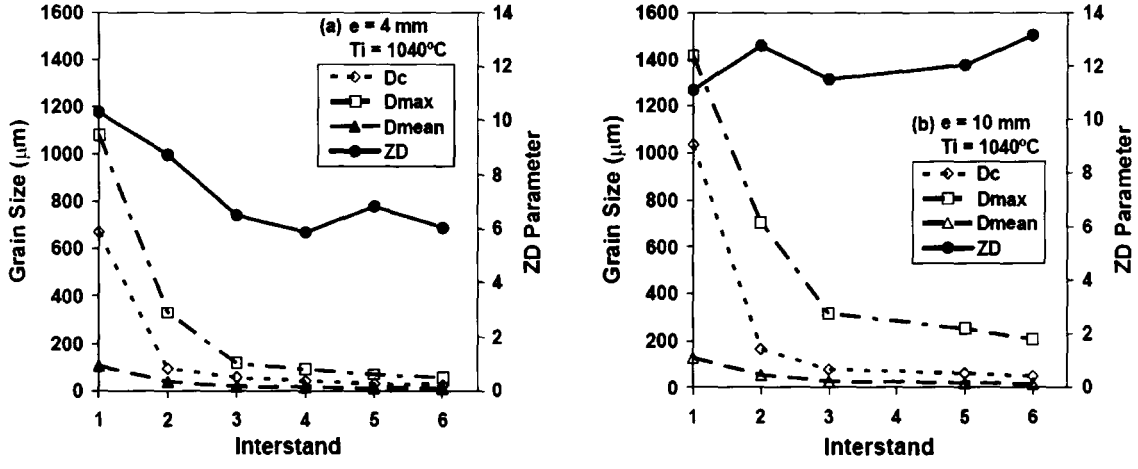

Figure 1-10 Microstructural evolution after each interstand corresponding to a final gauge of (a) 4 and (b) 10 mm and a rolling start temperature of 1040°C(Uranga et al. 2005)

From above, Thermomechanical process can reduce average grain size, but can not eliminate the non-uniformity; large grains still exist, and refinement is limited by the number of deformation passes. Therefore excellent control of the as-cast structure is an essential requirement for meeting the required specifications of the final product. In order to understand the non-uniformity of the as-cast microstructure, we need to understand the microstructural evolution during solidification, delta grain growth, delta-ferrite to austenite phase transformation and austenite grain growth prior and in the holding furnace.

1.3 Objective of This Study

The ultimate objective of this study is to develop the fundamental understanding needed to guide the development of high grades API standard microalloyed steels such as APIX80, APIX100 and APIX120 using the TSCDR technology. In order to achieve this goal, finer and more uniform as-cast microstructure must be obtained before entering the rolling mills in the TSCDR process. With this mind, this thesis has focused on solid state microstructure evolution prior to the beginning of the thermomechanical processing. Three specific microstructural changes were studied in detail:

1) Kinetics of delta grain growth: No information on delta grain growth of microalloyed steels at high temperature is available due to delta-ferrite transforms to austenite and subsequent transformation of austenite to alpha ferrite or martensite on quenching. A model alloy was used to study the kinetics of delta grain growth and a non-isothermal grain growth model was used to predict the delta grain growth at different positions within the slab (from the surface to centre). Microalloyed precipitates cannot pin delta grain growth at high temperature due to rapid Ostwald Ripening. A novel effective method of controlling the grain size using a duplex delta + austenite microstructure is introduced and its effectiveness is demonstrated.

2) Kinetics of delta to austenite phase transformation: The steels of interest are low carbon steels (<0.08wt %) which solidify as delta-ferrite. Upon cooling below approximately 1478°C, the delta phase starts to transform to austenite. Very little information is available

concerning the kinetics of this transformation and its effect on the grain size. The effects of temperature and different cooling rate on the transformation kinetics and final grain size were investigated with special emphasis on cooling rates that are similar to those at the surface and centre of the thin slab. In addition, the possibility of grain refinement through the nucleation of more than one austenite grain per delta-ferrite grain such as deformation was also studied.

3) Kinetics of austenite grain growth: Austenite grain growth is the main microstructural change following the delta-ferrite to austenite phase transformation and prior to the beginning of thermomechanical processing. A Ti-Nb free model alloy was used to study the kinetics of austenite grain growth at high temperature. The austenite grain growth model will be used to predict the austenite grain size with different slab positions both before entering the holding furnace and after leaving the holding furnace. Controlling austenite grain-growth through the use of a precipitate distribution and holding furnace temperature will be discussed.

The grain growth and phase transformation work described above is carried out on reheated specimens and as such it does not capture the effect of the as-cast/solidified microstructure on subsequently microstructure evolution. In order to validate the models that will be developed here under more realistic conditions, a simple laboratory-scale casting simulator was constructed to simulate the initial solidification stage of TSCDR process. The cooling rate was varied to re-produce industrial solidification rates and dendrite arm spacing. A novel etching technique was developed to reveal the dendrite morphology. The goal is to use

these realistic as-cast microstructures to simulate grain evolution during subsequent solid state processing.

Chapter 2 Literature Review

During continuous casting, the molten steel is fed via the ladle and tundish into a funnel-shaped mould which is cooled with an external water jacket. Solidification starts on the mould wall and the external solidified shell increases in thickness as the steel strand transits the mould. Leaving the mould, the thin slab runs through to the secondary cooling zone and continues its solidification. It is cut to length by a pendulum shear and following sent to the soaking furnace. After descaling, the slab is rolled in the CSP hot strip mill; the produced hot strip goes through the laminar cooling system and is fully coiled(Liu et al. 2003; Campbell et al. 2004; Muller et al. 2005).

According to API specification the carbon content is maintained below 0.08 wt%. As a result, the steel solidifies as delta-ferrite. In addition to solidification, the steel undergoes two additional phase transformation, namely, the delta-ferrite to austenite phase transformation and austenite to alpha-ferrite transformation. Solidification typically starts around 1525°C and is completed at about 1497°C. When temperature is decreased to 1477°C, austenite nucleates as secondary phase within delta-ferrite. The delta-ferrite to austenite phase transformation is completed at about 1448°C. The main microstructural event after the formation of austenite and prior to thermomechanical processing is austenite grain growth. After the completion of the thermomechanical process (above the Ar3) the steel is cooled and the austenite to alpha-

ferrite transformation takes place(Emi and Fredriksson 2005; Stefanscu 2006). Figure 2.1 is a sketch of microstructure evolution during the TSCDR process. The insert at the top left corner illustrates the relevant part of the phase diagram. This research project will focus on microstructural developments prior to the onset of thermomechanical processing. Solidification will be discussed in section 2.1. This will be followed by a discussion of grain growth in both delta and austenite (section 2.2 and 2.3); the delta to gamma transformation will be discussed in section 2.4.

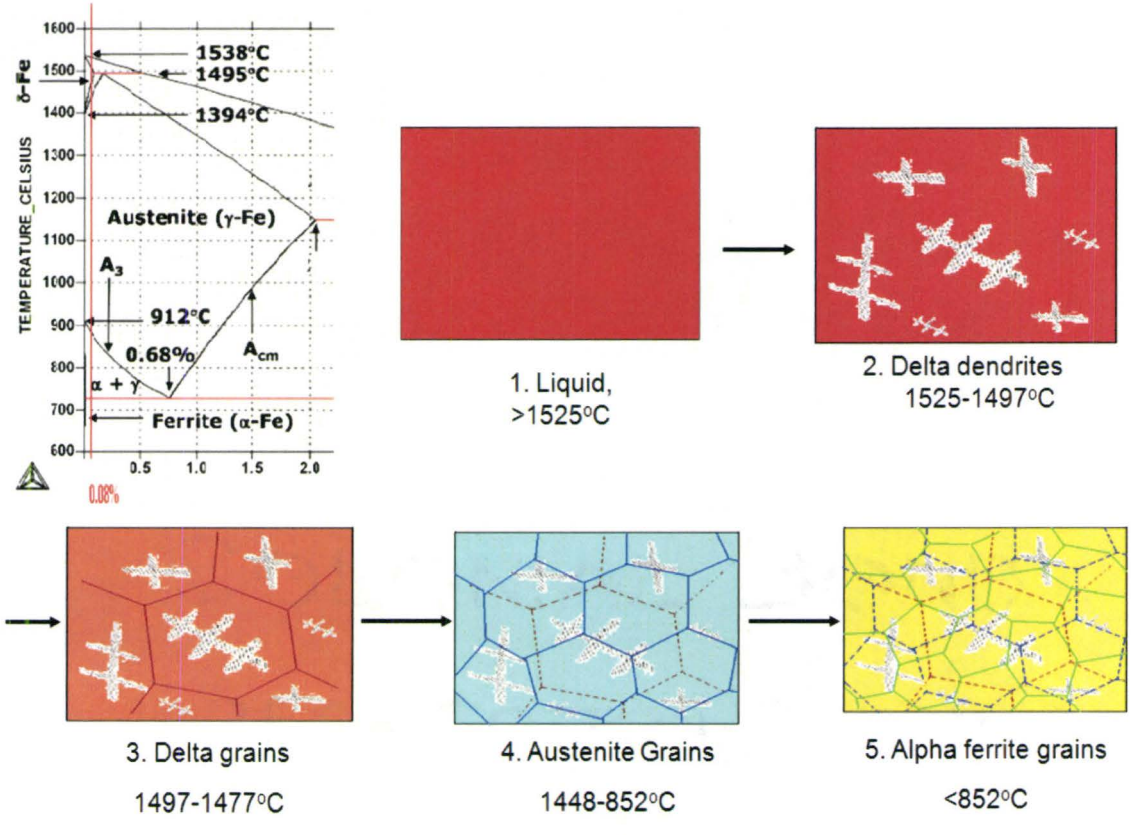

Figure 2-1 Sketch of microstructure evolution during TSCDR process

2.1 Solidification

Solidification science is a well established research area which mainly involves heat flow, mass flow, solute redistribution, solid-liquid interface kinetics and the relationship between processing parameters (temperature gradient, solidification rate and cooling rate) and microstructural parameters (primary dendrite arm spacing, second dendrite arm spacing and dendrite length)(Chalmers 1964; Winegard 1964; Flemings 1974; Kurz and Fisher 1998; Stefanscu 2006). There are a number of phenomena that must be reconsidered when we apply this science to TSCDR technology (Holzhauser et al. 1999; Holzhauser et al. 1999; Strezov et al. 2000; Yuan et al. 2004; Meng and Thomas 2006; Cramb 2007; Evans and Strezov 2000). In this brief survey of the literature the focus will be placed on thin-slab casting of low carbon steels and possible methods of controlling/refining the as-cast microstructure.

In order to refine and homogenize the as-cast microstructures, several methods can be used: (1) Increasing the cooling rate, (2) Stirring of the melt by mechanical means or by electromagnetic stirring (EMS) fields, (3) Addition of inoculants, and (4) core reduction to break the dendrite arms and homogenize the as cast microstructure. These methods are reviewed in section 2.1.1- 2.1.4.

2.1.1 Cooling Rate

Most fundamental solidification studies report that the microstructure evolution is a function of the temperature gradient (G) and growth rate (V) ahead of the microscopic solidification front. Experimental (McCarmey and Hunt. 1981; Mason et al. 1982; Somboonsuk and Trivedi 1984) and theoretical model (Kurz and Fisher 1981; Hunt and Lu 1996; Bouchard and Kirkaldy 1997) treatments of the effect of the temperature gradient and velocity on the primary dendrite arm spacing lead to an expression of the form:

$$\lambda_1 = A_1 G^{-m} V^{-n} \qquad \text{--- (2.1)}$$

where λ_1 is the primary arm spacing, G is the average temperature gradient in front of tip of dendrite in liquid side, V is average solidification velocity. A_1, m and n are constants. Regarding the second dendrite arm spacing, the most widely accepted expression for the relationship between λ_2 and cooling rate (GV) was proposed by Cahn and Haasen(Cahn and Haasen 1983):

$$\lambda_2 = B_1 (GV)^{-n} \qquad \text{--- (2.2)}$$

where B_1 and n are constants. Little is known about what controls the constant B_1, but is appears that it becomes smaller as the temperature interval between liquidus and solidus increases. In low carbon steels, M. A. Taha(Taha 1986) suggested the relationship is in the form:

$$\lambda_2 = B_1 (GV)^{-0.44} \quad \text{--- (2.3)}$$

From equations (2.1) to (2.3), it can be seen that increasing the cooling rate (GV) will decrease both the primary and second dendrite arm spacing. According to Wang et al ((Wang et al. 2005), the secondary dendrite arm spacing is about 50μm in the surface of the low carbon thin slab because of high cooling rate. The SDAS at the centre is typically 400μm for a 90mm slab. One approach of reducing the SDAS at the centre is increasing the cooling rate by reducing the slab thickness. The feasibility of this approach will be examined from scientific point of view in section 5.5.3. It should be kept in mind; however, the use of this approach is industrially more difficult as it would involve modification of the design of the casting line. If the results are promising, however, the proposed calculation could guide the design and development of future casting line.

2.1.2 Effects of Magnetic Field and Mechanical Stirring

The basic principle of EMS is to create an inhomogeneous Lorentz force, *F*, in the metal by an alternating magnetic field, *B*. In the works of Vives(Vives 1989), Campanella et al(Campanella et al. 2004), and Li et al(Li et al. 2007; Li et al. 2007a), the magnetic field caused the primary dendrite arm to deviate from the solidification direction, and this resulted in an increase in the growth of secondary and tertiary arms. Figure 2.2 shows the development of high order dendrite arms in the microstructure of Al-4.5 wt% Cu alloy under EMS stirring

during solidification process with different magnetic field. The microstructure of Figure 2.2 (a) without EMS is coarser than (b), (c) and (d) with different density *B*.

Mechanical stirring was studied by Li et al (Li et al. 2007) who observed the rotation of primary microstructure in a shear flow induces a stabilizing effect on the morphological instability at the solid–liquid interface and promotes the globular growth of solidification microstructure after it is nucleated in the melt. The main drawback of both stirring methods is the special set-up is needed.

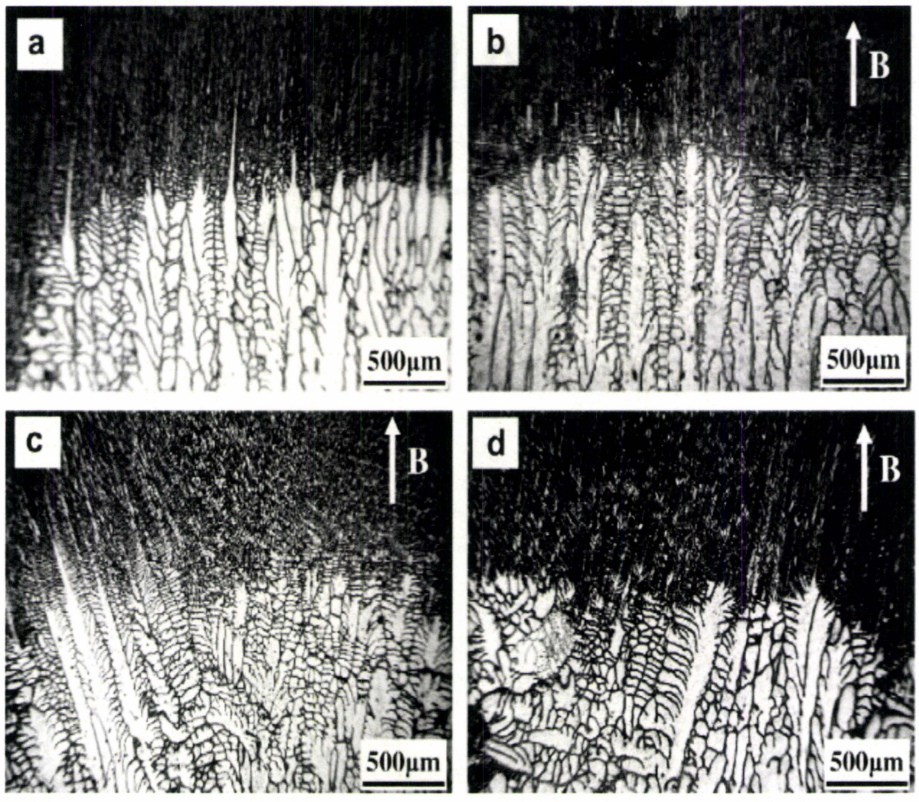

Figure 2-2 Effect of the magnetic field intensity on the dendritic microstructure of Al–4.5 wt.% Cu alloy (a) 0 T; (b) 0.2 T;(c) 0.5 T; (d) 2 T; (e) 6 T; and (f) 10 T(Li, Fautrelle et al. 2007a)

2.1.3 Effects of Dispersoids

The addition of inoculants such as TiB_2 and TiC in aluminum alloys is well established(Dahle and Arnberg 1997; Hu and Li 1998). In steel production, the effect of dispersoids as inoculants for initiation of both solidification and promoting nucleation during subsequent solid state transformation has gained increased attention in recent years (Andersson et al. 2006; Grong et al. 2006; Suito et al. 2006). In stainless steel, titanium oxide and titanium nitride are excellent nucleants for solidification(Cramb 2007).

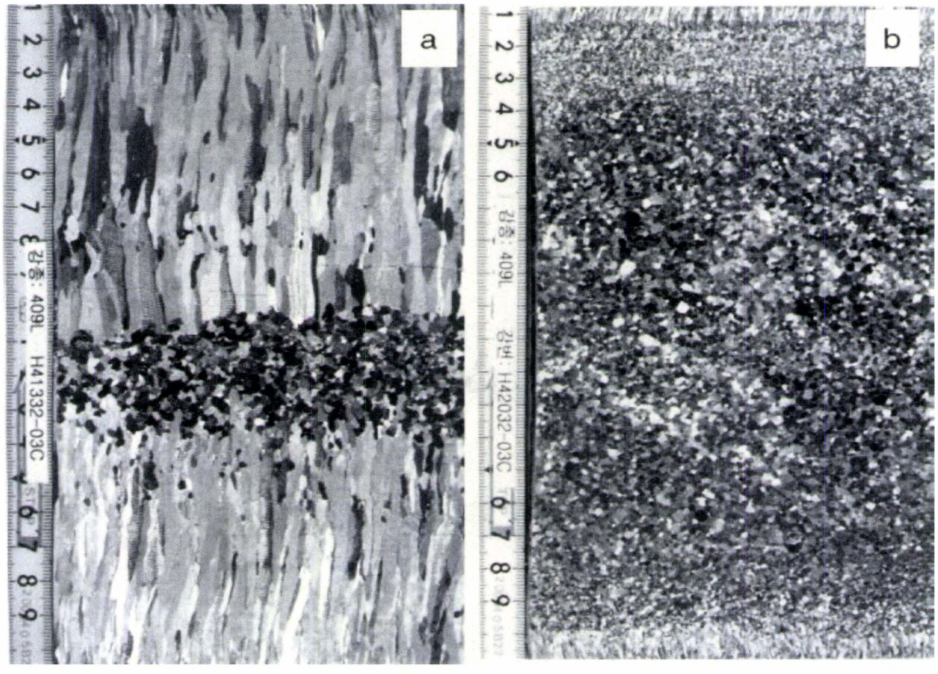

Figure 2-3 Structural changes of a STS 409L steel due to inclusion chemistry change during casting (Hu and Li 1998)

An example of the effect of chemically induced solidification is shown in Figure 2.3, where 100% equiaxed solidification structures are possible if the correct inclusion chemistry, size distribution and quantity are produced in the liquid steel before solidification. In Figure 2.3 (a), the normal microstructure is observed, where there is a combination of the equiaxed and columnar microstructures. If, however, there are inoculants present, a complete equiaxed structure is possible. Oxides and nitrides in steels can be used as inoculants for steel solidification, but at high temperature, these oxide particles tend to accumulate and become harmful to the matrix(Cramb 2007).

2.1.4 Effects of Liquid Core Reduction

Some variations of the TSCDR process allow for dynamic strand guiding during casting. As shown in Figure 2.4, stand thickness is reduced just below the mold by means of the tapered roll guide configuration of the segment "0." Further strand reduction with liquid core to approximately 40 mm is to be achieved within the multiple roller segments by means of many hydraulically adjustable roller pairs(Zhou et al. 2001). Megahed et al(Megahed et al. 2005) stated that in the production of APIX60 and X70, liquid core reduction (LCR) was used to reduce the slab thickness from 90 to 70 mm and to minimize the center line segregation and porosity. The mechanical properties are all above the specification standards. The microstructures with and without core reduction are shown in Figure 2.5. The samples are taken from the same position in the slab, Figure 2.5 (a) without core reduction and (b) is with

core reduction. The microstructure with core reduction is much finer and segregation analysis shows that the sample which underwent core reduction is better homogenized(Sobral et al. 2003). However, core reduction requires special set-up and many TSCDR production lines have no such facilities.

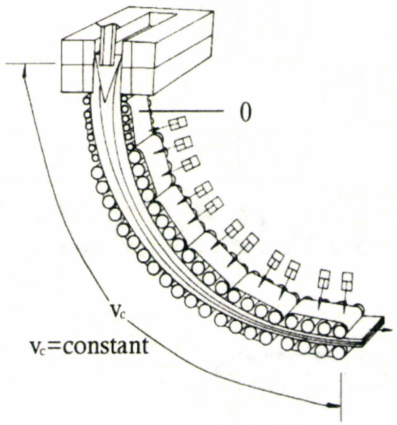

Figure 2-4 TSCDR process with liquid core reduction(Zhou et al. 2001)

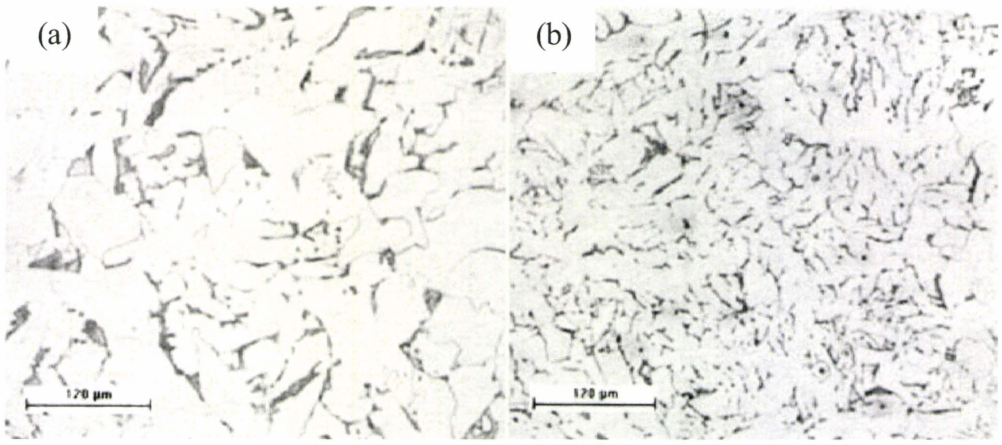

Figure 2-5 Comparison of microstructure of (a) without core reduction, (b) with core reduction(Sobral et al. 2003)

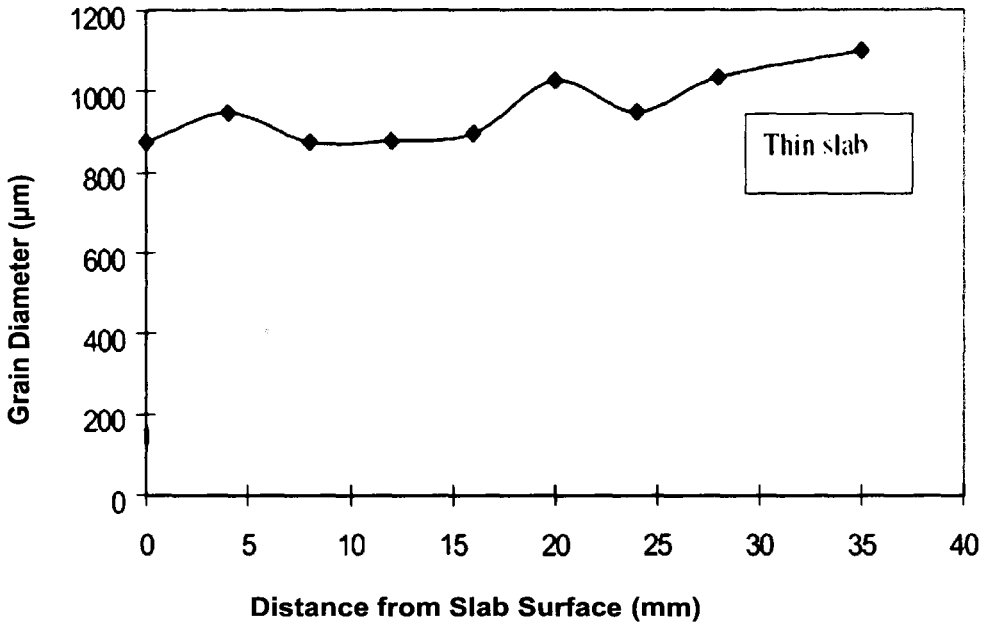

Figure 2-6 Dependence of austenite grain size on distance from the surface for 70 mm thin slab (Zhang, Pang et al. 2005)

Based on the literature review, there is no simple universal method that can lead to a homogenous and uniform microstructure under thin slab casting conditions. Even when the facilities are available for refining the microstructure (stirring or soft core reduction) one still needs to examine the influence of grain growth in the solid state. For example, Zhang et al (Zhang et al. 2005) showed that even though the initial dendrite arm spacing at the surface was 50μm as shown in Figure 1.6 (b), grain growth in the delta-ferrite and austenite resulted in a

final grain size of 900μm as shown in Figure 2.6. At the centre of the slab, the dendrite arm spacing was about 250μm. Grain growth increased this value to about 1050μm at the exit of the homogenization furnace. Immediately after solidification, the ratio of dendrite arm spacing in the center to that at the surface is 5 (250μm/50μm=5). After exiting the homogenization furnace, the ratio of austenite grain size in the center to that on the surface is about 1 (1050μm/900μm=1.2). From the comparison, we can conclude that controlling grain growth in the solid state is essential for maintaining a fine grain size, interestingly however, if the grain is pinned in the solid, the variation of gain size between the slab surface and centre will be inherited. As such, it is essential to control both solidification step and the grain growth in the solid state microstructure evolution in order to achieve a uniform and fine grain size. Grain growth is reviewed next.

2.2 Grain Growth in Delta-ferrite

For API standard microalloyed steels with <0.08% C, delta dendritic microstructure will form when temperature drops below 1525°C. Once solidification is complete, delta grain will be formed as shown in Figure 2.1. Since delta-ferrite transforms to austenite and austenite transforms to alpha ferrite during cooling, no information about the kinetics of delta grain growth is available. As a result, the review below will focus on grain growth in general and the general theories should be applicable to grain growth in delta-ferrite as well as in austenite (to be discussed in section 2.3).

2.2.1 Grain Growth in Single Phase

Grain growth in single-phase alloys has been studied extensively through theoretical and experimental approaches and grain growth models are well established (Burke and Turnbull 1952; Hillert 1965; Gladman 1966; Yoshinaga et al. 1995; Bacroix 2004; Kang 2007). The main obstacle for using these models in the present case is the lack of kinetic data on delta grain growth at the temperatures of interest.

According to reaction rate theory(Turnbull 1951; Burke and Turnbull 1952), and in the absence of solute interaction with grain boundary, the grain growth rate V is directly proportional to the net pressure P on the boundary:

$$V = MP \qquad \text{--- (2.4)}$$

The constant of the proportionality, M, is the mobility of the boundary and is assumed to be independent of the driving force and the details of the mechanism of the boundary migration. In pure material, Turnbull(Turnbull 1951) derived the following expression for the mobility of grain boundaries in pure materials which is also known as intrinsic mobility:

$$M_{pure} = \frac{wD_{GB}V_m}{b^2 \Re T} \qquad \text{--- (2.5)}$$

In this equation, w is the grain boundary thickness, D_{GB} is the grain boundary self-diffusion coefficient, V_m is the molar volume, b is the magnitude of the Burgers vector, T is absolute temperature, and $\Re$ is the gas constant. Based on experimental results, the temperature dependence of the pre-exponential is weak and the data is often expressed as an Arrhenius type relationship:

$$M = M_o \exp\left(\frac{-Q}{KT}\right) \qquad \text{--- (2.6)}$$

where M_o is a constant, Q is the activation energy. The global driving force for grain growth, P, can be expressed in term of the curvature, $1/\bar{R}$, where $\bar{R}$ is the average grain radius. This leads to an expression in the following form(Burke and Turnbull 1952; Humphreys and Hatherly 2004):

$$P = \frac{\alpha\gamma_{gb}}{\bar{R}} \qquad \text{--- (2.7)}$$

where α is a geometric constant, and γ_{gb} is the grain boundary energy, Equation (2.4) can be expressed as:

$$\frac{dR}{dt} = M\left(\frac{\alpha\gamma_{gb}}{R}\right) \qquad \text{--- (2.8)}$$

and therefore

$$\bar{R}^2 - \bar{R}_o^2 = 2\alpha M r_{gb} t \qquad \text{--- (2.9)}$$

$\bar{R}$ is the average grain size at time t, $\bar{R}_o$ is the initial average grain size. Equation (2.9) may be written in the more general form:

$$\bar{R}^n - \bar{R}_o^n = ct \qquad \text{--- (2.10)}$$

n and c are constants, n is often termed ad the grain growth exponent. Only in the case of ultra high purity metals annealed at temperatures very close to the melting point does n approach 2.

In 1965, Hillert developed a statistical grain growth model based on the assumption that the grain boundary velocity is inversely proportional to its radius curvature in single phase materials. He used analysis of the Ostwald ripening of a distribution of second phase particles to obtain the grain growth rate(Hillert 1965):

$$\frac{dR}{dt} = \alpha M \gamma_{gb} \left(\frac{1}{R_{crit}} - \frac{1}{R} \right) \qquad \text{--- (2.11)}$$

where $\alpha = 1/2$ for a 2-D array and 1 for 3-D array. R_{crit} is a critical grain size which varies with time according to the following equation:

$$\frac{d(R_{crit})}{dt} = \frac{\alpha M \gamma_{gb}}{4 R_{crit}} \qquad \text{--- (2.12)}$$

A grain with $R < R_{crit}$ will shrink and with $R > R_{crit}$ will grow. When the grain topology is taken into account, the average grain radius $\bar{R}$ is equal to R_{crit} and equation (2.12) predicts parabolic grain growth kinetics of the form of equation (2.9). Hillert also obtained the grain size distribution f(R,t) form equation (2.11) and he argued that if the initial grain size distribution contained no grain larger than $1.8\bar{R}$ then normal grain growth would result and the grain size distribution will be self-similar. On the contrary, if grain larger than $1.8\bar{R}$ were present, abnormal grain growth would result.

2.2.2 Effect of Solutes on Grain Growth

Microalloyed steels which contain niobium, vanadium, and titanium microalloying addition. These are present (at least partly) in solid solution at high temperature. As a result it is necessary to review the effects of solutes on grain growth in order to assess the importance of this effect in microalloyed steels at high temperature. Most theories of solute effects on boundary motions are based on that proposed by Lücke and Detert(Lücke and Detert 1957) for dilute solid solutions. The theory was further developed by Cahn(Cahn 1962) and Lücke and Stüwe(Lücke and Stüwe 1963), later extended to include higher solute contents by Lücke and Stüwe (Lücke and Stüwe 1971) and by Hillert and Sundman(Hillert and Sundman 1976). The Cahn-Lücke-Stüwe's (CLS) model is widely accepted as giving a good semi-quantitative account of the effects of solute on boundary migration.

According to CLS model, solute atoms within the grain boundary have a different energy (E) compared to those in the grain interior because of the different local atomic environment. As a result there is an interaction force between the boundary and solute atoms. For a stationary grain boundary, the solute distribution around the boundary is symmetric and has a maximum value of:

$$c = c_o \exp(-\frac{E}{kT}) \qquad \text{--- (2.13)}$$

When the boundary moves, the solute profile becomes asymmetric, such that the center of gravity of the distribution lags behind the boundary and consequently there is a net force due to the solute, dragging the boundary in the direction opposite to the direction of boundary motion. In the case of low boundary velocity, the relationship between the driving pressure P and boundary velocity V was approximately as(Cahn 1962):

$$P = V(\lambda + \alpha C_o) \qquad \text{--- (2.14)}$$

where

$$\alpha = \frac{N_v (kT)^2}{\delta E_o D}\left(\sin\left[\frac{E_o}{kT}\right] - \frac{E_o}{kT}\right) \qquad \text{--- (2.15)}$$

The relationship between boundary velocity and driving force at intermediate velocities is very difficult to calculate. However, when the grain boundary velocity is large, the

solute atoms can no longer keep up with the boundary and the grain boundary breaks away from its atmosphere, the pressure-velocity relationship is given by:

$$P = V\lambda + \frac{\alpha C_o}{\beta^2 V} \qquad \text{--- (2.16)}$$

where

$$\beta^2 = \frac{\alpha kT\omega}{2N_v E^2{}_o D} \qquad \text{--- (2.17)}$$

In the above equations, λ is the inverse of the intrinsic mobility, C_o is bulk solute concentration, N_v the number of atoms per unit volume, ω is the boundary width, E_o is the binding energy of solute to the boundary, and D is the solute diffusion coefficient across the interface. The key prediction of the CLS model is that the solute drag effect varies with boundary velocity, reaching a maximum value as shown in Figure 2.7. This figure also shows that the solute drag becomes less effective at high temperatures, because under these conditions the solute segregation to the grain boundary decreases according to equation (2.14), so that the solute atmosphere effectively evaporates. The relationship between velocity and solute concentration is shown is Figure 2.8. For low concentration, the curve is continuous, and there is only a small deviation from the straight line corresponding to an ideally pure metal. This implies that the foreign atoms cannot follow the migrating interface after it has broken away from its impurity atmosphere. For high solute concentrations the curve has two

branches and velocity will change discontinuously from one branch of the curve to the other at the some critical driving force as indicated by the dashed line in Figure 2.8.

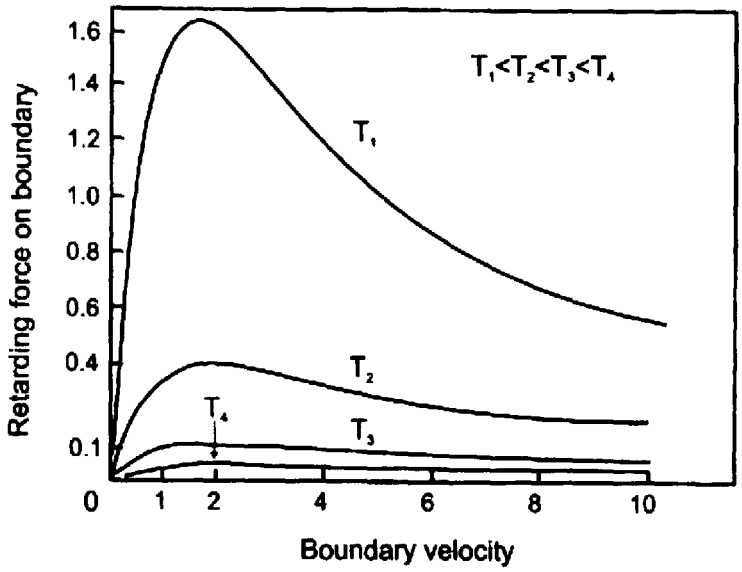

Figure 2-7 The variation of solute drag force with boundary velocity and temperature(Lücke and Stüwe 1963)

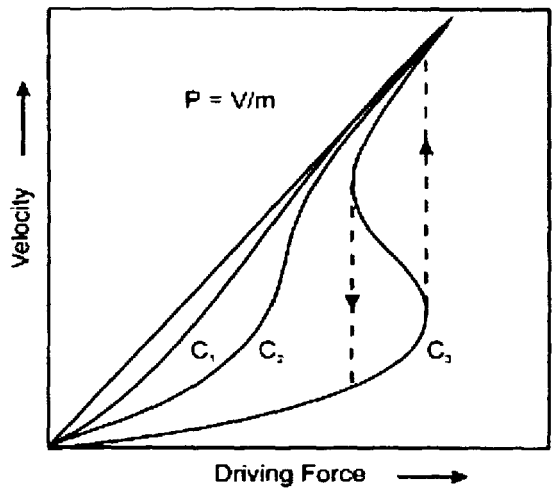

Figure 2-8 Predicted grain boundary velocity as a function of the driving force for different solute concentrations c3>c2>c1(Lücke and Stüwe 1963)

Zurob et al (Zurob et al. 2002) and Hutchinson et al(Hutchinson et al. 2007) successfully used this model to predict the solute drag effect on the austenite grain boundary mobility, but no information was available on the delta grain boundary mobility.

2.3 Grain Growth in Austenite

Pottore et al(Pottore et al. 1991) argued that grain growth in austenite is the greatest contributor to large grain size in the as-cast microstructure. In order to maintain a fine austenite grain size, dispersoids that can be present in the liquid or precipitates that formed in the austenite are needed to inhibit the austenite grain boundary motion. For a given microalloyed steel composition, the amount of undissolved carbonitrides is often discussed in terms of the solubility products of the various carbides and nitrides. The literature on carbides, nitrides, and carbonitrides solubility in microalloyed steels is reviewed next.

2.3.1 Solubility of Microalloyed Carbides, Nitrides and Carbonitrides

The reaction between a microalloying element, M, and an interstitial, X, to form a compound of type MX at temperature T can be represented symbolically as:

$$[M] + [X] \leftrightarrow (MX) \qquad \text{--- (2.18)}$$

where [M], and [X] are the concentration of M and X dissolved in austenite, (MX) is the constituent phase. The temperature dependence of the solubility product is expressed by an Arrhenius relationship:

$$\log k_s = A - \frac{B}{T} \qquad \text{--- (2.19)}$$

where A and B are constants for a given microalloyed steel, k_s is the equilibrium constant of reaction (2.18). Let M_T and X_T are total wt% of M, X in the alloy, and M_{MX} and X_{MX} be the wt% of M, X in the second phase MX at a given temperature. Then, if $M_T \bullet X_T > k_s$, there will be undissovled second phase particles, i.e. MX which are then available for grain growth inhibition. The remaining (dissolved) [M] and [X] will be available for the formation of fine interphase precipitation during cooling.

The solubility products of the microalloy carbides and nitrides are summarized in Figure 2.9(Gladman 1997). For each of the microalloying elements the nitrides are more stable than the carbides in austenite. TiN is by far the most stable of the microalloy carbides and nitrides. In fact, the solubility of TiN in the liquid at temperature up to 1600°C is very similar to those of most other microalloy carbides and nitrides in austenite at temperature of around 1200°C. Therefore TiN can be used to inhibit grain growth at higher temperature(Nagata et al. 2002). On the contrary, vanadium carbide is by far the most soluble compounds. Vanadium carbide is used to strengthen higher carbon steels while vanadium nitride has a powerful effect in increasing strength in steels with enhanced nitrogen contents. More complex mutually

soluble carbonitrides arise from the simultaneous additions of two or more of the microalloying elements. The solubility data can be obtained from the solubility data for the individual microalloy carbides and nitrides using different models which was summarized by Gladman(Gladman 1997). The solubility of the microalloyed carbides, nitrides and carbonitrides offer clear direction for the selection of specific microalloying additions to inhibit grain growth in austenite at different temperature range.

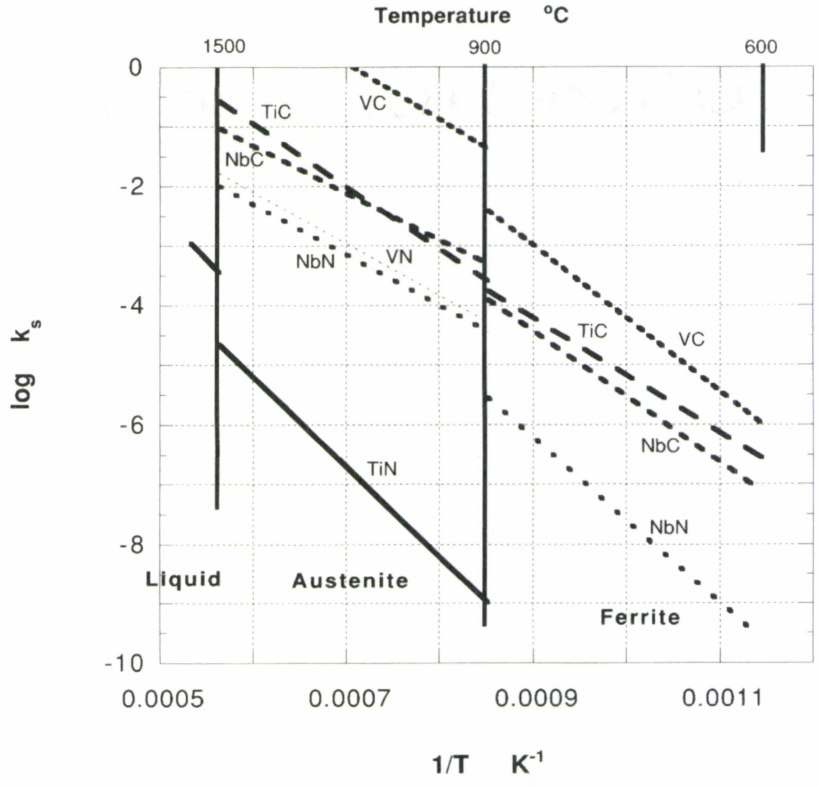

Figure 2-9 The solubility products of the microalloy carbides and nitrides(Gladman 1997)

The kinetics of carbides, nitrides and carbonitrides precipitation in austenite is extremely slow in absence of deformation which provides the heterogeneous nucleation sites needed for precipitation(Woodhead and Morrison 1963). As a result it is difficult to obtain a fine distribution of these precipitates prior to thermomechanical processing. Even if precipitation took place within reasonable times at high temperatures, the strong pinning by the microalloying carbonitrides may interfere with recrystallization during subsequent thermomechanical processing(Chakrabartia et al. 2005). This is a serious complication due to the fact that thermomechanical process relies on repeated recrystallization in order to achieve fine grain size.

2.3.2 The Effects of Second Phase Particles on Austenite Grain Growth

During austenite grain growth, the motion of grain boundaries will be inhibited by second phase particles such as Ti(C, N), oxide particles(Grong et al. 2006; Suito et al. 2006) and other precipitates (carbides, nitrides and carbonitrides). The retardation force will mainly depend on the particle size and particle volume fraction. Other factors such as particle morphology, degree of coherency between the particles and the matrix, grain boundary-particle correlation and the particle distribution will change the magnitude of the drag force. If the second phase particles coarsen because of Oswald ripening, then the grain growth rate will be controlled by the particles coarsening process. Details of particles pinning on grain growth are reviewed next.

2.3.2.1 Particle Pinning Pressure

The particle pinning was first modeled by Smith on the suggestion of Zener(Smith 1948). The effect is commonly referred to as Zener drag. The original treatment was applied to the case of a boundary of specific energy γ_{gb} which is contacted with an incoherent spherical particle of radius r. If the boundary meets the particle at an angle θ as shown in Figure 2.10 then the restraining force on the boundary is:

$$F = 2\pi\gamma_{gb} r \cos\theta \sin\theta \qquad \text{--- (2.20)}$$

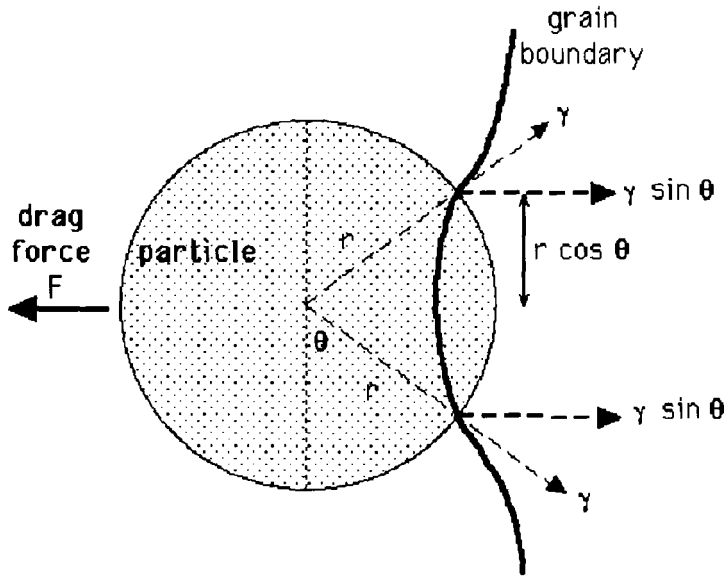

Figure 2-10 The interaction between a grain boundary and a spherical particle(Smith 1948).

When $\theta = 45^{\circ}$, the maximum restraining effect (F_m) is obtained:

$$F_m = \pi r \gamma_{gb} \qquad \text{--- (2.21)}$$

where F is pinning force per particle. For a volume fraction F_v of randomly distributed spherical particles of radius r, the pinning pressure exerted by the particles on unit area of the boundary is given by:

$$P_Z = \frac{3F_v \gamma_{gb}}{2r} \qquad \text{--- (2.22)}$$

If the particle shape is not spherical, the shape factor will modify the drag force but will not change the general form of the equation. Nes et al(Nes et al. 1985) and Li and Easterling(Li and Easterling 1990) considered the interaction of a boundary with an ellipsoidal particle and stated that the pinning force is only significantly larger than that of a spherical particle for the case of thin plates meeting the boundary flat on and long needles meeting the boundary edges on. Ringer et al(Ringer et al. 1989) have analysed the interaction of a boundary with cubic particles. Dragging force depends upon the orientation of the cube relative to the boundary and in the extreme case, when the cube side is parallel to the boundary; the drag force is almost twice that of a sphere of the same volume. Nes et al and Randle et al(Nes et al. 1985; Randle and Ralph 1986; Li and Easterling 1990) studied the effects of coherent particles on the grain boundary and concluded that the drag force of coherent particles is twice bigger that of incoherent

$$D_z = \frac{4\alpha r}{3F_v} \qquad \text{--- (2.25)}$$

setting $\alpha = 1$, the well know Zener limiting grain size is obtained(Smith 1948; Humphreys and Hatherly 2004):

$$D_{zener} = \frac{4r}{3F_v} \qquad \text{--- (2.26)}$$

In order to investigate the effects of particle pinning on the kinetics of grain growth and on the grain size distribution, Hillert(Hillert 1965) modified his growth rate model for single-phase materials (equation 2.11) as following:

$$\frac{dR}{dt} = \alpha M \gamma_{gb} \left(\frac{1}{R_{crit}} - \frac{1}{R} \pm \frac{z}{\alpha} \right) \qquad \text{--- (2.27)}$$

where $\alpha = ½$ for a 2-D array and 1 for 3-D array, $z = 3F_V / 4r$.

For grains in the size range of $1/R \pm z/\alpha$, no growth or shrinkage will occur. Grains larger or smaller than this size will shrink or grow at a reduced rate. The mean grain growth rate is:

$$\frac{d\bar{R}}{dt} = \frac{\alpha}{2} M \gamma_{gb} \left(1 - \frac{z\bar{R}}{\alpha} \right)^2 \qquad \text{--- (2.28)}$$

Hillert(Hillert 1965) points out that the grain size distribution will be also be affected by particle pinning, the width of the grain size distribution during normal grain growth should

be reduced by particle pinning. When R is large, let $1/R_{crit} = z/\alpha$, Hillert(Hillert 1965) also derived a limiting grain size from equation 2.26:

$$D_{Hillert} = \frac{8r}{3F_v} \qquad \text{--- (2.29)}$$

for the 3-D array analysis, Hillert's limiting grain size is twice as big as that of Zener.

In the case of randomly distributed second-phase particles, numerous modification to the Zener relationship have been comprehensively reviewed by Manohar and Ferry et al(Manohar et al. 1998), and these refinement generally predict a limiting grain size which is of a similar form to equation 2.26.

2.3.2.3 Effects of Particle-Boundary Correlations on Grain Growth

The Zener pinning pressure of equation 4.24 is based the assumption of macroscopically planar boundary. However, if the grain size is similar to the interparticle spacing, the non-random correlation of particles and boundaries must be taken into account. This will be particularly important in materials with large volume fractions of particles. Humphreys and Hatherly(Humphreys and Hatherly 2004) summarized the works of Hellman and Hillert(Hellman and Hillert 1975), Hutchinson and Duggan(Hutchinson and Duggan 1978), Hillert(Hillert 1988), and Hunder and Ryum(Hunderi and Ryum 1992) and identified four important cases as shown in Figure 2.11.

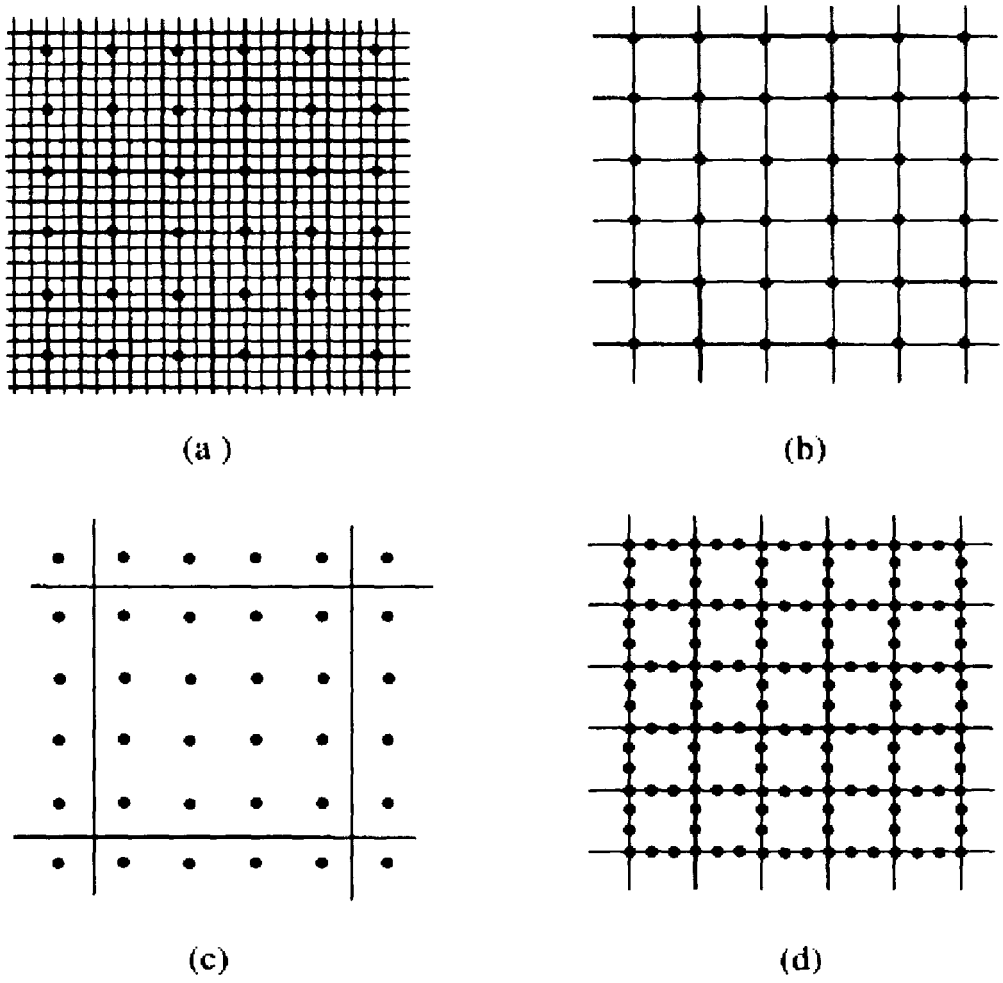

Figure 2-11 Schematic diagram of the correlation between particles and boundaries as function of grain size(Humphreys and Hatherly 2004).

In Figure 2.11(a) the grains are much smaller than the particle spacing, in Figure 2.11(b) the particle spacing and grain size are similar, in Figure 2.11(c) the grain size is much larger than the particle spacing and in Figure 2.11 (d), and the particles are inhomogeneously

distributed so as to lie only on the boundaries. In all these cases there is a strong correlation between the particles and the boundaries.

For case (a) and (b), it is reasonable to assume that all the particles lie not only on boundaries, but at vertices in the grain structure. If the grain edge length is D, for incoherent spherical particles the pinning pressure on the boundary (P_{zc}) is:

$$P_{zc} = \frac{3DF_v\gamma_{gb}}{4r^2} \qquad \text{--- (2.30)}$$

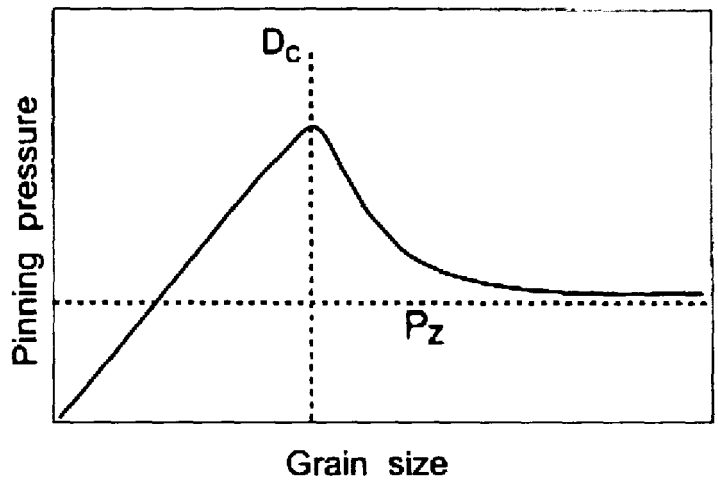

Figure 2-12 The effect of grain size on the Zener pinning force for a given particle dispersion(Humphreys and Hatherly 2004)

This relationship will be valid for grain size (D_c) is equal to particle spacing as shown in Figure 2.11(b) at which point the pinning force reaches a maximum. As the grain size increases beyond the particles spacing, the number of particles per unit area of boundary will decrease and the Zener pinning pressure is reached as given by equation (2.22). The

effect of grain size on the Zener pinning force for a given particle dispersion is shown in Figure 2.12.

Using equation (2.7) for grain growth equal to the particle pinning pressure equation (2.30), the limiting grain size in case of particle-boundary correlation effects is:

$$D_{z1} = r\left(\frac{8\alpha}{3F_v}\right)^{1/2} \approx \frac{1.6\alpha^{1/2}r}{F_v^{1/2}} \qquad \text{--- (2.31)}$$

The limiting grain size, D_{Z1}, which represents the situation when all particles are on boundary corners but not all boundary corners are occupied by particles (Figure2.11a), represents a lower bound for the limiting grain size and grain growth will actually continue to occur until all grain corners are pinned, i.e. the grain size is equal to the particle spacing:

$$D_{zc} = D_c \approx \frac{\beta r}{F_v^{1/3}} \qquad \text{--- (2.32)}$$

where β is a geometric constant, Hillert(Hillert 1988) suggested that $\beta = 3.6$.

2.3.2.4 Effects of Particle Coarsening on Grain Growth

Grain growth can completely be pinned by second phase particles. However, second phase particles will coarsen at elevated temperature, a process known as particle

coarsening or Ostwald ripening process(Greenwood 1956; Gladman 1997). As the average particle size increases, the Zener pinning force will decrease with time according to equation 2.22. In the case in which the grain size is equal to the limiting grain size and the grain growth rate is controlled by the particle coarsening rate:

$$\frac{dR}{dt} = k\frac{dr}{dt} \qquad \text{--- (2.33)}$$

where the constant k is $2\alpha / 3F_v$ for low volume fractions and $\beta / 2F_v^{1/3}$ for large volume fractions of particles. The rate of particle coarsening will depend on the rate controlling mechanism which will be discussed in the following:

Bulk Diffusion control: The particle coarsening in the matrix under bulk diffusion of solute was first treated by Greenwood based on the Gibbs-Thomson equation for the concentration of solute in equilibrium with a particle of given radius, r, and Fick's law for the diffusion(Greenwood 1956). The coarsening theory was further developed by Lifshitz and Slyozov(Lifshitz and Slyozov 1961) and independently by Wagner(Wagner 1961) and usually is referred to as the LSW theory. It predicts that the average particles size will vary with time as:

$$r^3 - r_o^3 = \frac{8D\sigma N_\alpha V_m t}{9\Re T} \qquad \text{--- (2.34)}$$

where r is the average particle radius at time t, r_o is the initial particle radius ($t=0$), D is the bulk diffusion coefficient of the rate limiting solute, σ is the interfacial energy, N_α is the solute

molar fraction and V_m is the molar volume. The LSW theory corresponds to a zero volume fraction approximation which breaks down for large volume fractions of second phase. In order to take the second phase volume fraction into the frame work of the LSW theory, Ardell (Ardell 1972) assumed that the diffusion of the solute to a growing particle will depend on a distance characteristics of the spatial distribution of particles in the matrix. This leads to an expression of the form:

$$r^3 - r_o^3 = \frac{8k(f_v)D\sigma N_\alpha V_m t}{9\Re T} \qquad \text{--- (2.35)}$$

where $k(f_v)$ is a function of the particle volume fraction. Other models have been proposed by Brailsford and Wynblatt(Brailsford and Wynblatt 1979), Davies et al(Davies et al. 1980), Voorhees and Glicksman(Voorhees and Glicksman 1984a; Voorhees and Glicksman 1984b), Marqusee and Ross(Marqusee and Ross 1984), and Tokuyama and Kawaski (Tokuyama and Kawaski 1984; Tokuyama and Kawaski 1984). All of the above models lead to an equation similar to equation (2.35) with different expressions for $k(f_v)$. Overall, Ardell's model appears to predict the highest coarsening rate and is therefore viewed as an upper limit.

Interface Reaction Control: In the particle coarsening process, the slowest step may be the transfer of atoms across the precipitate matrix/interface. The local rate of precipitate growth will then be determined by the rate at which solute atoms can join or leave the precipitate across the interface, a process driven by the local departure from equilibrium. Wagner(Wagner

1961) derived the following expression for the particles coarsening rate controlled by the interface:

$$r^2 - r_o^2 = \frac{64K\sigma N_\alpha V_m t}{81\Re T} \qquad \text{--- (2.36)}$$

where K is the proportional constant that should include the unknown interfacial mobility.

Diffusion along Grain Boundaries: When particles are predominantly distributed on grain boundaries due to the large particle volume fraction, the coarsening of particles may be controlled by the diffusion flux along the grain boundaries, rather than by bulk diffusion. Under these circumstances the appropriate diffusion coefficient is that for grain boundary diffusion which results in a much faster coarsening rate. This type of particle coarsening process has been considered theoretically by Speight(Speight 1968) and Kirchner(Kirchner 1971). The equation for the coarsening of particles situated on grain boundaries where the grain boundary paths dominate the diffusion process is(Kirchner 1971):

$$r^4 - r_o^4 = \frac{9wD_{gb}\sigma N_{\alpha(gb)} V_m t}{32AB\Re T} \qquad \text{--- (2.37)}$$

where $N_{\alpha(gb)}$ is the solute molar fraction at a grain boundary in equilibrium with an infinitely large particle, w is the grain boundary thickness, A and B are define as: $A = 2/3 + (\sigma_b / 2\sigma) + (1/3)(\sigma_b / 2\sigma)^3$ and $B = (1/2)\ln(1/f_b)$, where σ_b is the grain boundary energy and f_b is the fraction of the grain boundary covered by the precipitates.

Diffusion along Low Angle Boundaries (Dislocation): Kreye(Kreye 1970) has considered the coarsening of particles on low angle grain boundaries where the pipe diffusion down the dislocations is the rate controlling process. In this situation, the particles coarsening following the following equation:

$$r^5 - r_o^5 = kt \qquad \text{--- (2.38)}$$

where k is a constant that should include the dislocation spacing and the boundary misorientation.

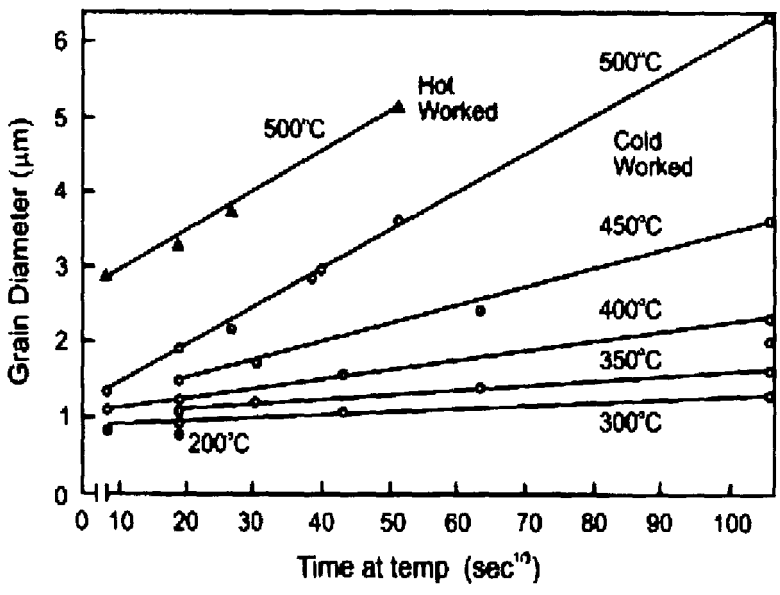

Figure 2-13 The kinetics of grain growth when controlled by particle coarsening for an Al–6wt%Ni alloy containing a volume fraction of 0.10 of NiAl3 particles(Humphreys and Hatherly 2004)

Figure 2.13 shows the kinetics of grain growth in an Al–6wt%Ni alloy which contains a volume fraction of 0.1 of $NiAl_3$ particles of initial diameter 0.3 μm. The grain growth kinetics is controlled by the particle coarsening of bulk diffusion over a wide temperature range. Figure 2.14 shows the relationship between the size of the grains and the second-phase particles in the same alloy system. The grain size is found to be proportional to the particle size as would be predicted by equation (2.33). From the slope of the line, the constant β in the equation is found to be 3.4(Humphreys and Hatherly 2004).

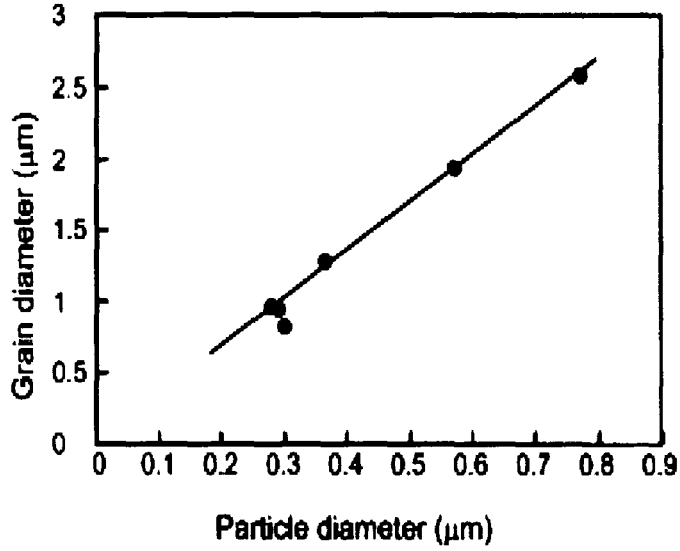

Figure 2-14 The relationship between grain size and particle diameter for an Al– 6wt%Ni alloy containing a volume fraction of 0.10 of NiAl3 particles(Humphreys and Hatherly 2004)

2.4 Delta-Ferrite to Austenite Phase Transformation

As discussed in section 2.2, the steels of interest are low carbon steels (<0.08wt %) which solidify as delta-ferrite. This has the advantage of allowing substantial homogenization in the solid due to the fast diffusion of alloying elements in delta-ferrite to austenite. Upon cooling below about 1477°C, the delta-ferrite phase begins to transform to austenite. Very little information is available concerning the kinetics of this transformation and its effect on the grain size. Some information available is reviewed next.

2.4.1 Experimental Observation of Delta-Ferrite to Austenite Transformation

Yin et al(Yin et al. 1999) used a confocal scanning laser microscope combined with an infrared image furnace to study the δ-ferrite to γ austenite phase transformation. At the very beginning of phase transformation, austenite nucleated at the delta-grain boundaries and triple points. Figure 2.15 shows austenite phase nucleation sites. In Figure 2.15(a) where a low carbon steel sample was cooled at 2 K/min, an austenite-cell forms at the delta grain boundaries at 1706 K. On further cooling, the cell grows along the delta grain boundaries, and the number of austenite cells in delta grain boundaries increases as shown in Figure 2.15(b). These cells merge at the delta grain boundaries in Figure 2.15 (c) and finally form a layer of austenite phase along the original delta-grain boundaries. When the delta to austenite transformation occurs at a high degree of supercooling (>7 K), a clear finger pattern of the delta/austenite interphase boundary is observed to form on the free surface of the sample

which is shown in Figure 2.16. Yin et al(Yin et al. 1999) argued that this morphology could be described by Mullins-Sekerka type stability theory.

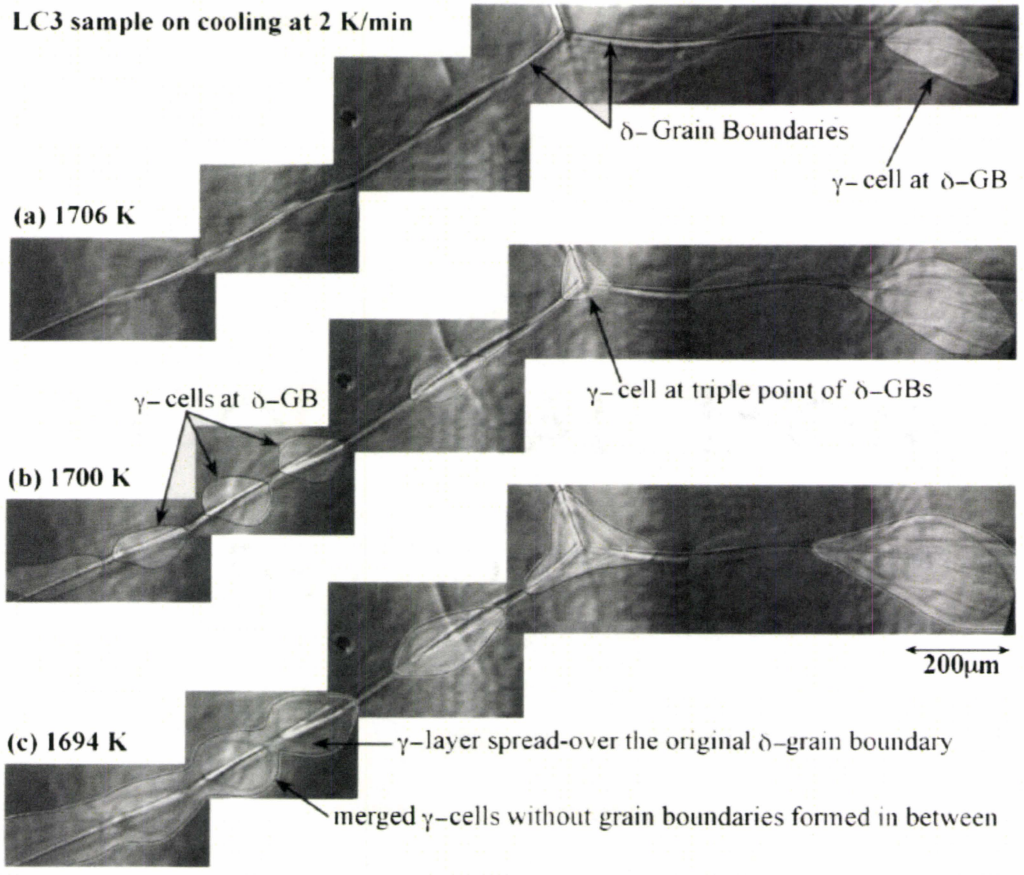

Figure 2-15 Austenite phase merge during cooling(Yin et al. 1999)

D. Phelan and R. Dippenaar (Phelan and Dippenaar 2004) stated that the newly formed austenite phase proceeds along sub-boundaries in the delta-ferrite phase and the morphology was not developed by an unstable growth mechanism of the Mullins-Sekerka type(Liu et al.

2006). Sub-boundaries in the δ ferrite phase have a great influence on the kinetics of the delta to austenite phase transformation. Preferred growth along sub-boundaries in the delta-ferrite phase leads to finger-like morphology.

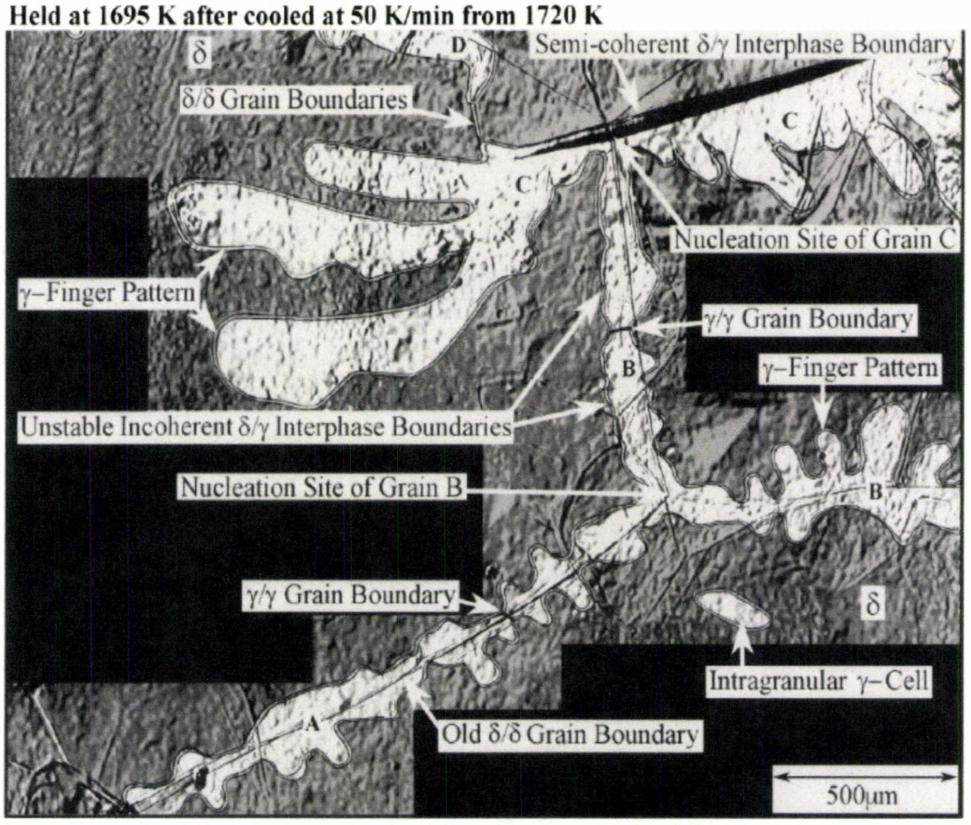

Figure 2-16 Unstable growth morphology of the delta to austenite phase transformation(Yin et al. 1999)

From reviewing the mechanism of delta-ferrite to austenite phase transformation, the great chance to refine and homogenise the microstructure in the solid state is to increase the austenite nucleation sites inside the delta-ferrite grains. Thermomechanical treatment during

delta to austenite phase transformation, and oxide particles could provide heterogeneous nucleation sites for austenite inside the delta-ferrite. This possibility is reviewed next.

2.4.2 Thermomechanical Treatment during Delta-Ferrite to Austenite Phase Transformation

Thermomechanical treatment can be applied during solidification, in the delta region or during the delta-ferrite to austenite phase transformation. According to Zarandi and Yue(Zarandi and Yue 2005), and Elwazri et al(Elwazri et al. 2005) deformation was effective at refining the grain size only when the deformation was applied during the transformation. Figure 2.17 shows that the application of ε=0.1 compression during the delta-ferrite to austenite phase transformation, has resulted in a refined microstructure. Figure 2.17(a) is the microstructure without compression, while Figure 2.17(b) shows the microstructure of the sample that was compressed to a strain of 0.1. As can be seen, ferrite grains are decorated with relatively fine austenite grains. The resulting refinement is evident by comparing Figure 2.17(a) and 2.17(b).

The observed grain refinement could have occurred either by static/dynamic recrystallization of austenite after the initial nucleation of the gamma grains. Another possibility is that provided the additional nucleation sites for the gamma grains and resulted in more austenite grains per delta grain. Zarandi and Yue(Zarandi and Yue 2005) suggested that

deformation during δ to γ transformation can result in grain refinement through enhanced nucleation at grain boundaries and inside grains sub grain boundaries.

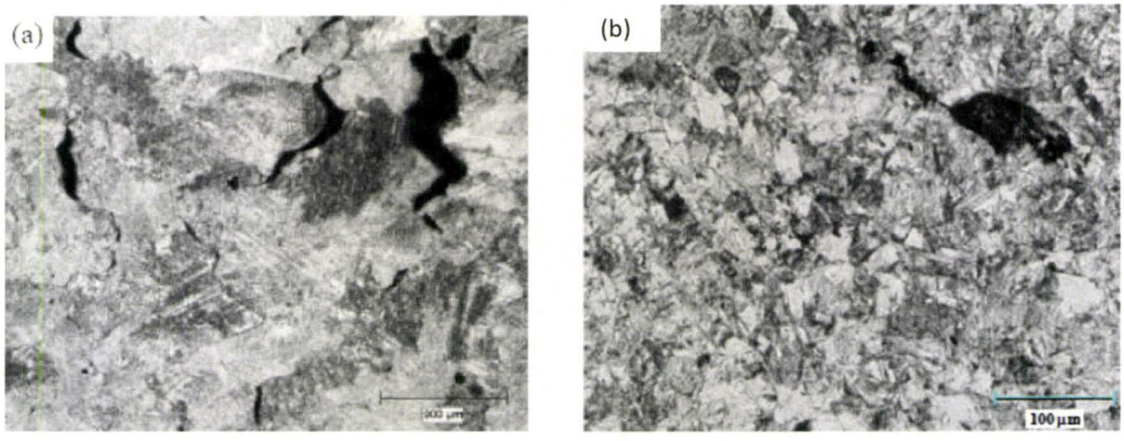

Figure 2-17(a) microstructure of specimen quenched without deformation, (b) microstructure of a specimen subjected to a compression (Zarandi and Yue 2005)

2.4.3 Oxide Particles as Heterogeneous Nucleation Sites for Austenite during Delta-Ferrite to Austenite Phase Transformation

Oxide Inclusions can act as nucleation sites for austenite in the delta-ferrite during delta to austenite phase transformation. Suito et al(Suito et al. 2006) suggests that various oxide particles can act as heterogeneous nucleation sites for austenite. This is a very attractive possibility given that most steelmaking processes could be modified to allow the formation of fine dispersions of such oxides (Andersson et al. 2006; Grong et al. 2006; Karasev and Suito 2006).

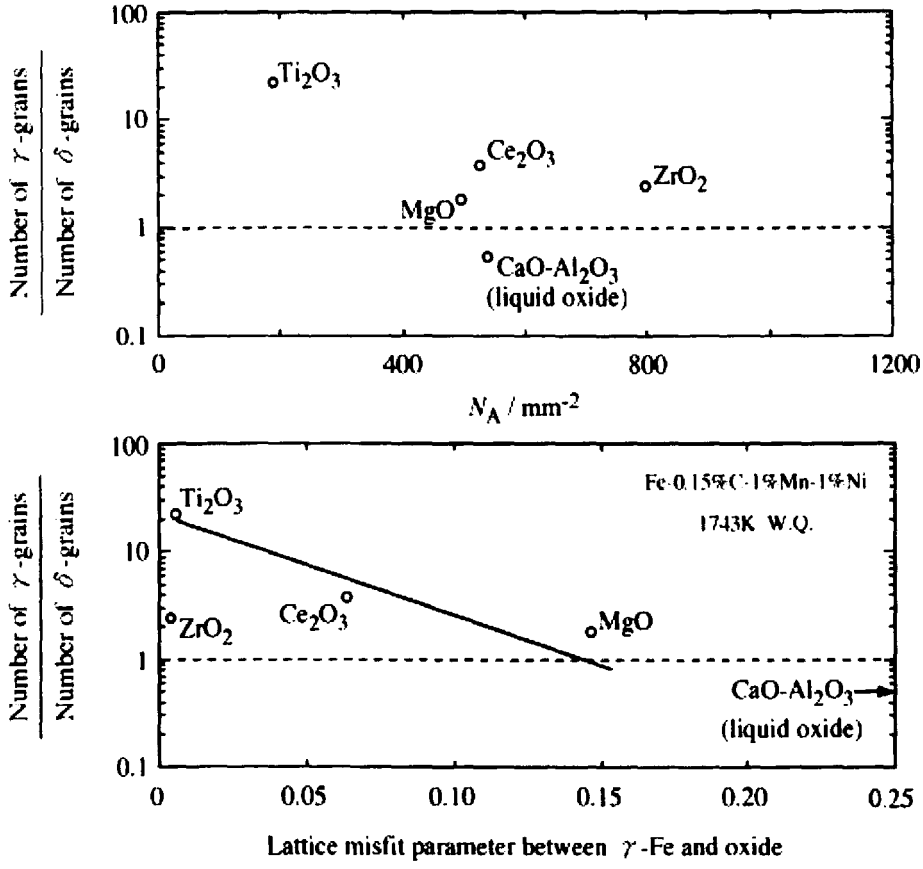

Figure 2-18 Number of δ-grains to number of γ-grains per unit are plotted against N_A (upper diagram) and lattice misfit parameter between γ-Fe and oxide (lower diagram)(Suito et al. 2006)

Figure 2.18 shows the relationship between the ratio of the number of austenite grains to that of delta-grains per unit area and the lattice misfit parameter between γ-Fe and oxide particles. From the diagram it can be seen that this ratio increases with a decrease in the misfit parameter indicating that the inclusions become more potent nucleation sites. In other words, more than one nucleation event per δ-grain occurs. In addition to acting as a heterogeneous

nucleation site for austenite, the oxide particles can pin the grain boundaries and reduce the grain growth. The grain-growth-inhibiting effect by oxide particles has been studied by a number of investigators on theoretical grounds and on the basis of experimental studies(Karasev and Suito 2006). This aspect has been reviewed in the section on grain growth in two-phase materials (Section 2.3.2).

Based on the literature review, the non-uniformity of microstructure comes from the solidification process due to the variation of cooling rate from the slab surface to centre. The large grain-sizes come from the post solidification stage including the delta-ferrite and austenite grain growth. Even though a fine as cast microstructure can be obtained in the solidification stage, the microstructure will be coarsening quickly in the solid state. Particle pinning is an effective method for preventing grain growth. The application of particle pinning at very high temperatures (T> 1360°C) is, however, very challenging especially because this has to be done in such away as not to interfere with recrystallization during downstream thermomechanical processing. Moreover, it should be realized that pinning grain growth at high temperatures will not eliminate the problem of the non-uniformity of the microstructure since this non-uniformity is inherited from the as-cast microstructure. In order to find ways of achieving a uniform and fine grain size, extensive experiments have been carried out to investigate the initial solidification stage (Section 3.1) and microstructure evolution in the solid state which includes kinetic of delta grain growth (Section 3.2), austenite grain growth (Section 3.3) and the delta-ferrite to austenite phase transformation (Section 3.5). In addition, the literature review on the effects of particle coarsening on grain growth have led the present

author to data on duplex microstructure in which grain growth is extremely slow. As result, it was decided to investigate this phenomenon and try to use this idea to develop a novel steel chemistry in which grain growth is effectively pinned at high temperature (Section 3.4).

Chapter 3 Experimental Work

In this chapter, the details of the experimental work will be introduced. A wide range of experiments was performed. Section 3.1 will cover experimental work in solidification, section 3.2 and 3.3 will discuss grain growth in the delta-ferrite and austenite, section 3.4 will introduce the experimental work on delta-ferrite/austenite duplex microstructure, and section 3.5 will deal with the delta to austenite phase transformation. In each case, the preparation of the experimental materials will be described first, followed by a description of experimental set-up and procedure used.

3.1 Solidification Simulation

The purpose of the solidification simulation experiments is to re-produce industrial solidification rates and microstructure at the surface and centre of the slab. These realistic as cast microstructures will be used to simulate grain evolution during subsequent solid state processing. A simple laboratory-scale casting simulator was used to simulate the initial solidification stage of TSCDR process as described below.

3.1.1 Materials

The material used to study microstructure evolution during the solidification process was a 90 mm thick industrial thin slab APIX60 provided by Nucor Steel. The chemical composition is shown in Table3-1.

Table 3-1 Sample steel chemical compositions (wt %)

Wt %	C	Mn	Si	Al	Ti	Nb	N
Thin slab APIX60	0.0531	1.0954	0.205	0.021	0.0085	0.032	0.0093
Fe-2.5Al% model alloy	0.053	1.10	0.4	2.5	0	0	0
Fe-1.5Al% model alloy	0.051	1.00	0.36	1.5	0	0	0
Nb/Ti-free model alloy	0.0527	1.12	0.205	0	0	0	0

3.1.2 Experimental Set-up

A simple laboratory-scale set-up was developed to simulate the early stages of solidification during thin-slab casting. The experiments consisted of melting 300g of steel in an induction furnace under a controlled atmosphere (commercial purity Ar). A copper or a steel rod was then lowered into the molten metal to initiate solidification as shown in Figure 3.1. The material and diameter of the dipping bar were varied in order to access a wide range of cooling rates. The most important feature of the present design is the possibility of interrupting solidification at a specific time by lifting the dipping bar out of the liquid. In this way, the microstructure that has developed up to a given time can be investigated in detail and

the evolution of shell thickness, segregation and dispersoids distribution can be monitored for the first time.

The dipping bars were 3 inches long and with the end polished after cutting. The thermocouples were spot welded to the surface at the top, bottom, and in the centre of the rod in order to record temperatures during the simulation process.

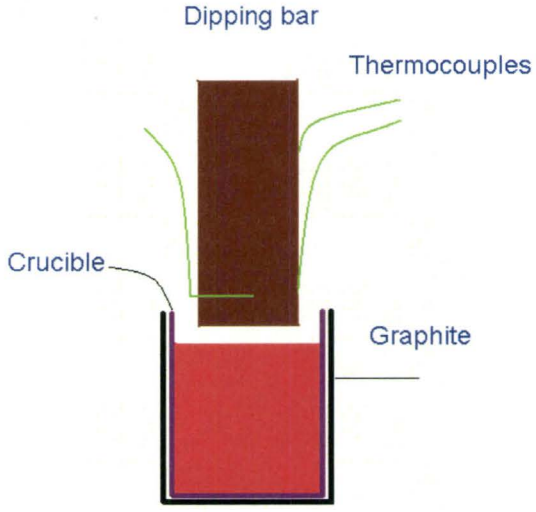

Figure 3-1 Illustration of the setup to simulate the thin slab casting

The experiment was carried in an ADL-MP Crystal Growth Furnace. Figure 3.2 shows a picture of the experimental setup and its key components. ADL-MP Crystal Growth Furnace is essentially a vacuum chamber that can be connected to a RF source. Primary and secondary vacuum systems make it possible to rapidly evacuate air from the furnace and to

back fill with Ar. Several parts were designed to allow the insertion and removal of the bars without opening the furnace.

ADL Model-MP Crystal Growing Furnace

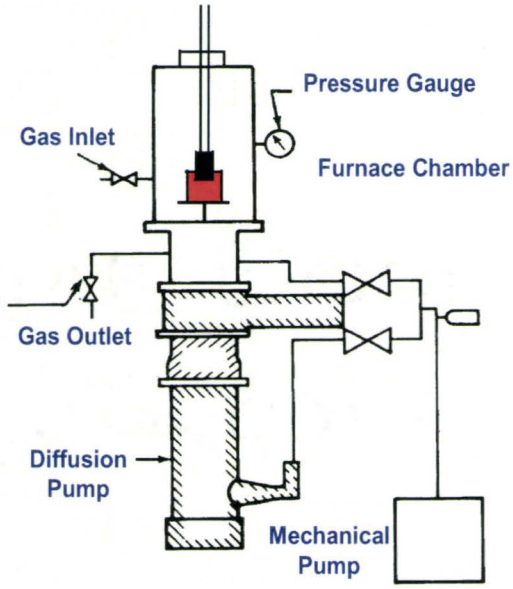

Sketch of ADL Model-MP Furnace

Figure 3-2 ADL-MP Crystal Growing Furnace

3.1.3 Experimental Procedure

The basic procedure for studying initial solidification shell is following:

The furnace is evacuated and backfilled with Ar at least three times.

A charge of approximately 300g of steel is melted under Ar.

Power is turned off and the dipping bar is inserted into the liquid for a given time.

The bar is pulled out of the melt and then allowed to cool in air or quenched into water.

When the sample is cut from different directions, the dendrite morphology is different. Figure 3.3 shows how the samples are cut in this study. Longitudinal and transverse sections are both parallel to the heat extraction direction.

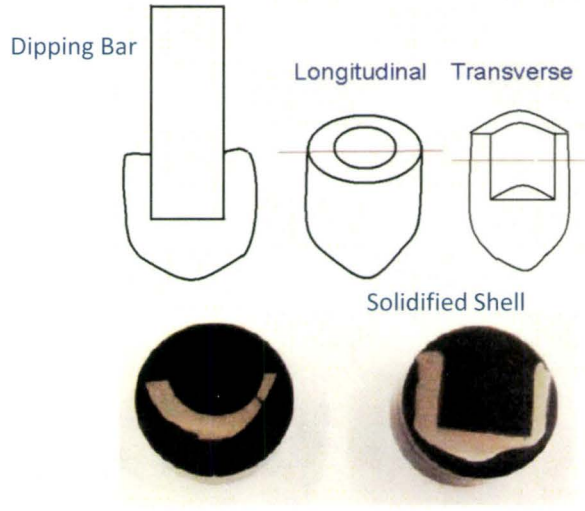

Figure 3-3 Sample cut from different direction

3.2 Delta-Ferrite Grain Growth Kinetics

The purpose of grain growth experiments is to understand the kinetics of delta-ferrite grain growth, kinetics of austenite grain growth, and use the developed grain growth model to

predict the grain evolution in the TSCDR process prior thermomechanical processing. Based on these investigation, effective solutions to refine and homogenize the as cast microstructure in the TSCDR process will be proposed. The materials and procedure for delta grain growth are following:

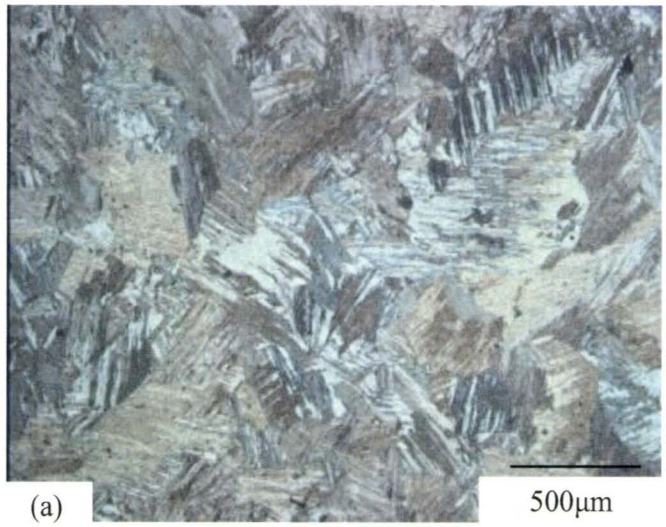

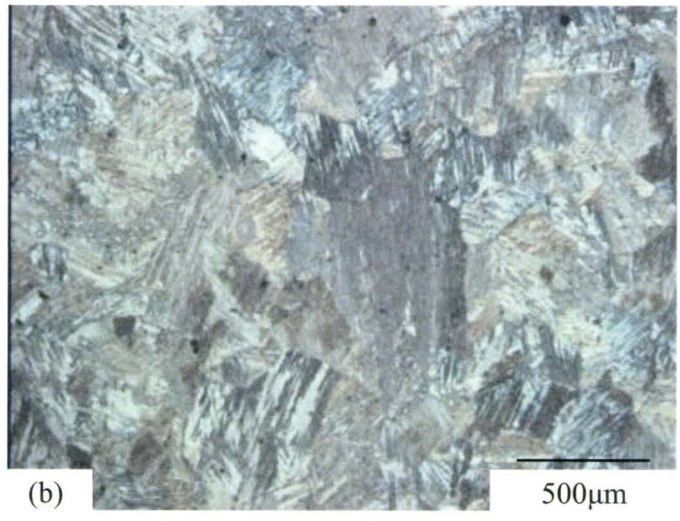

Figure 3-4 APIX60 heated up to delta region1480°C for (a) 100 seconds and (b) 200 seconds, then icy water quenching

3.2.1 Materials

Direct observation of the grain growth in delta-ferrite is extremely difficult because delta-ferrite transforms to austenite and subsequently martensite on quenching. Figure 3.4 shows the microstructures of APIX60 heated up to the delta region (1480°C) holding for 100 seconds and 200 seconds before being quenched into icy water. It is difficult to distinguish the former delta grain boundaries from the alpha ferrite, martensite and former austenite grain boundaries using standard metallographic techniques. This renders the investigation of grain growth in delta-ferrite extremely difficult.

In order to study the kinetics of grain growth in delta-ferrite, a model alloy with 2.5 wt% Al was used. The addition of Al is based on the fact that Al is the most efficient delta-ferrite stabilizer. An addition of as little as 2.5 wt% Al is sufficient to avoid austenite formation and retain delta-ferrite down to room temperature as shown in Figure 3.5. The composition of the alloy used to study grain-growth in delta-ferrite is shown in Table 3-1. This alloy will be referred to as the "Fe-2.5Al% model" alloy and it is simply used to allow direct measurement of delta-ferrite grain-growth kinetics in a system which is comparable to industrial alloys.

The model alloy was prepared by arc melting small finger-ingots of 20-30g in an argon atmosphere. The as-cast delta grain size was as large as 2000μm as shown in Figure 3.6(a) and as such unsuitable for studying the kinetics of grain-growth. In order to refine the grain size, the as-cast specimen was annealed at 650°C for 2hours then cold-deformed and recrystalized three times. The cold reduction steps were 30%, 55% and 55% and the recrystallization

temperature was 750°C. The annealing times were 4 hours after the first and second reductions and 8 hours after the third reduction. This heat treatment resulted in a uniform grain-size of 27μm as shown in Figure 3.6(b). In one batch of samples, the grain size achieved was higher, 183μm. This higher initial grain size was taken into account during subsequent modeling.

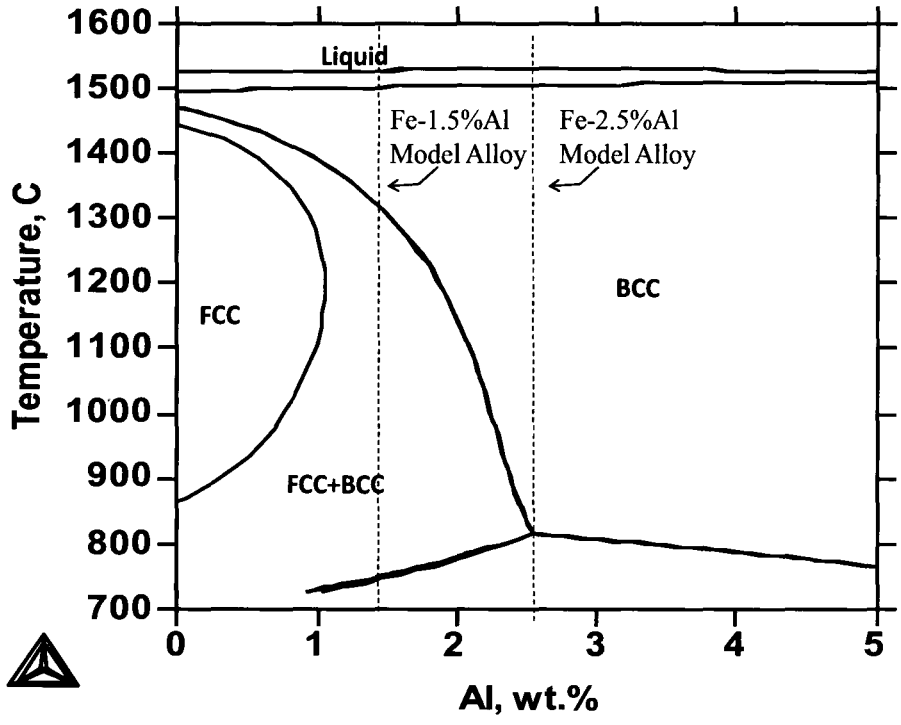

Figure 3-5 Phase diagram of Fe-Al model alloy

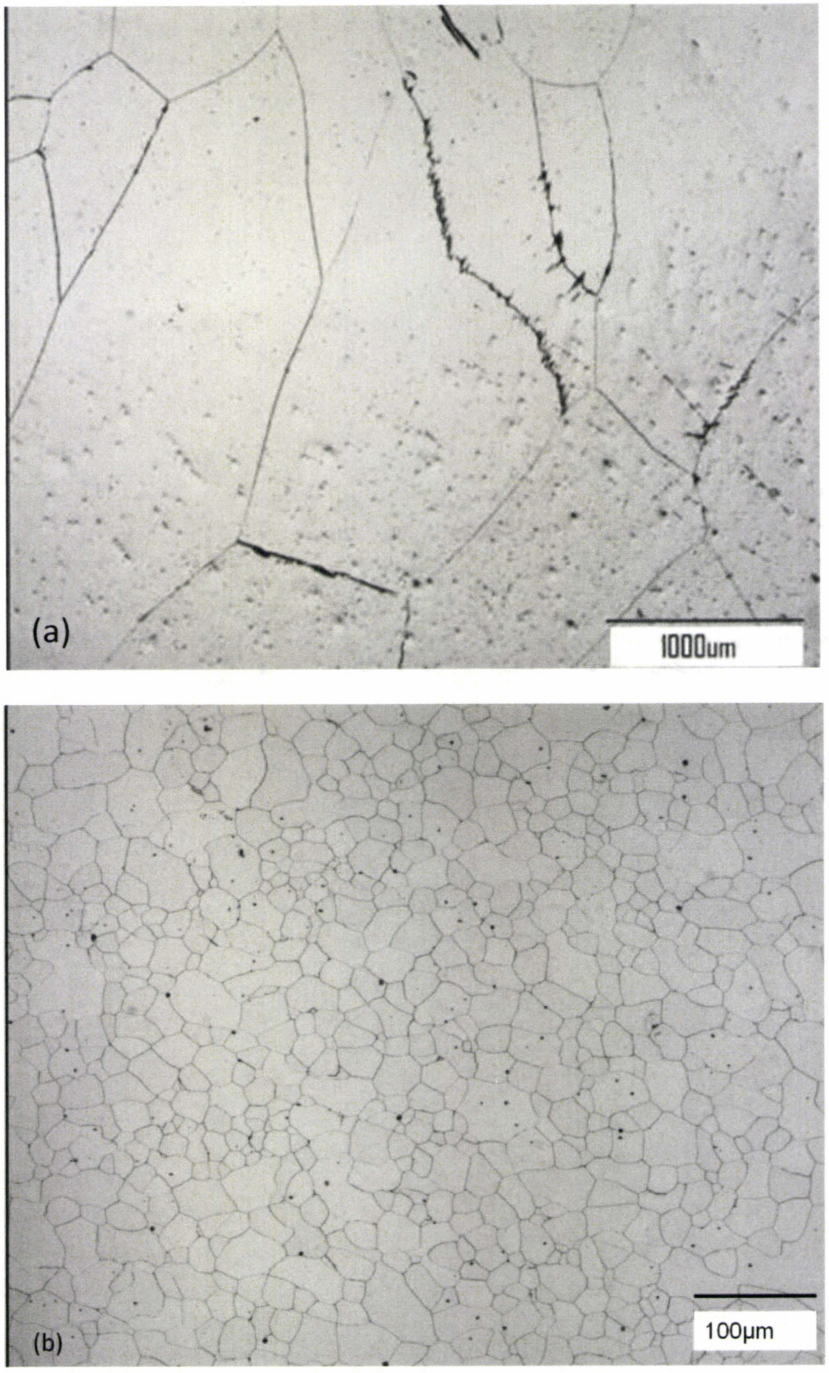

Figure 3-6 Fe-2.5%Al model alloy for delta grain growth (a) as cast microstructure, (b) recrystallization microstructure

3.2.2 Experimental Procedure

The delta grain growth experiments were carried out using a high temperature furnace as shown in Figure 3.7(a) which can be operated using vacuum or different atmosphere. The sample was direct connected to the thermocouple as shown in Figure 3.7(b) during heating process.

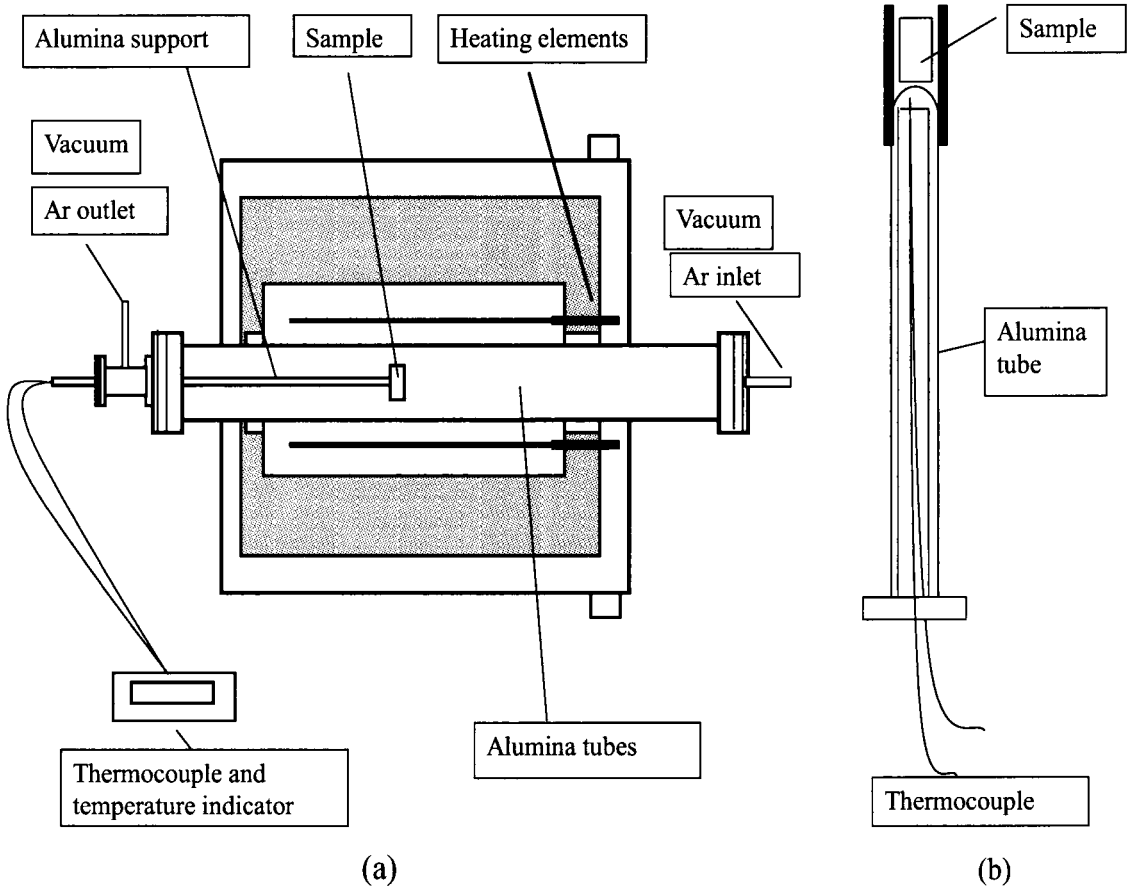

Figure 3-7 Experimental equipment (a) and experimental set-up (b) for delta grain growth

The grain-refined model alloy was heated to temperatures of 1000°C, 1100°C, 1200°C, 1300°C and 1470°C and held for different times before being quenched into ice water. The complete thermal history of each sample was recorded using a B-type thermocouple and an acquisition frequency of 7.5 Hz. The annealing treatments were carried out under an atmosphere of CO-CO_2 whose carbon activity corresponds to that of the alloy at the isothermal holding temperature. This was essential in order to avoid decarburization of the specimen during the annealing treatments. The delta-ferrite grain structure in the model alloy was revealed using an etching solution of supersaturated picric acid with sodium dodecylbenzene sulfonate wetting agent.

3.3 Austenite Grain Growth Kinetics

The materials and experimental procedure for austenite grain growth are introduced in the following section.

3.3.1 Materials

Observation of austenite-grain growth was carried out on two materials: the first one is APIX60 steel from Nucor and the second is an Nb- and Ti- free version of APIX60 steel. The Nb-Ti free alloy was used because abnormal grain growth took place in the standard APIX60 alloy due to the dissolution of the precipitates on reheating. The use of a "precipitate-free"

alloy avoids this complication. The Nb-Ti free alloy was prepared by arc melting and its composition is shown in Table 3-1. The as-cast material was homogenized for 3 days at 1100°C to break down the as cast microstructure. Two cycles of austenitization at 875°C for 15 minutes followed by quenching in ice water were used to refine the grain-size. In order to estimate the initial austenite grain size for subsequent grain-growth experiments, one of the grain-refined specimens was heated to 900°C and quenched. The austenite grain size of this specimen was found to be 40μm as shown in Figure 3.8. This was used as the initial grain size in the subsequent austenite grain growth studies.

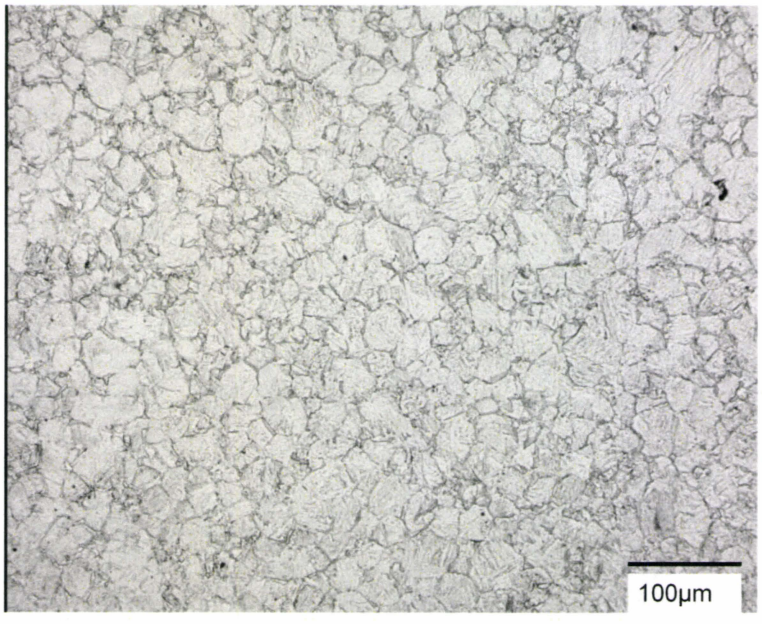

Figure 3-8 Nb/Ti-free alloy used for investigating grain-growth in austenite. The austenite grain size at the beginning of the grain growth experiments (i.e. at 900°C) was 40μm

3.3.2 Experimental Procedure

For each experiment the sample was cut in the form of 10mm×10mm×10mm and was placed inside an alumina crucible which connected to a thermocouple as shown in Figure 3.7(b). The samples were heated to 1200°C, 1300°C and 1400°C (all in austenite range) using the same set up described earlier. The complete thermal history was recorded for each specimen and an appropriate CO-CO_2 atmosphere was used to prevent decarburization. The former austenite grain boundaries were revealed using an aqueous solution of picric acid with sodium dodecylbenzene sulfonate and different additions of hydrochloric acid for the different annealing temperatures (Speer and Hansen 1989; Pottore et al. 1991; Zhang et al. 2005).

3.4 Coarsening Behaviour of Delta-Ferrite/Austenite Duplex Microstructure

This experiment was to investigate the austenite particles coarsening mechanism and delta grain growth behaviour in delta-ferrite/austenite duplex microstructure at high temperature.

3.4.1 Materials

In order to investigate the pinning of delta grain growth at high temperatures, a new model alloy was introduced in which a small volume fraction of austenite was used to pin delta

grain growth. This idea was inspired by the use of Fe-2.5%Al to study the delta grain growth. If the aluminum content is reduced to 1.5%, a two phase mixture of delta-ferrite and austenite will exist at temperatures between 1310°C and the eutectoid. This duplex microstructure is expected to be very resistant to coarsening as discussed in the literature review. The composition of new Fe-Al alloy was presented in Table 3-1 and the critical temperature for this alloy are shown in Figure 3.5. The volume fraction of austenite phase particles can be obtained as a function of temperature by using the TCFE2 database of ThermoCalc. This model alloy will be referred as "Fe-1.5%Al model alloy".

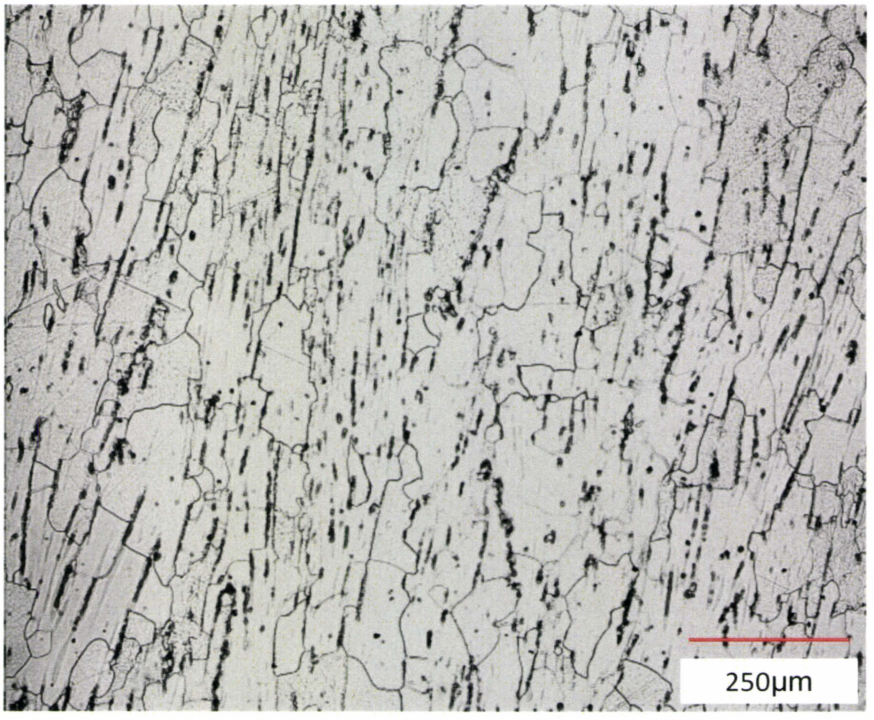

Figure 3-9 The as-received microstructure of Fe-1.5%Al model alloy

The Fe-1.5Al% alloy was prepared by induction melting at CANMET Materials Technology Lab (Ottawa, Canada); a heat of 40kg was cast and hot rolled to a plate of 10mm thickness. The as-received microstructure is delta-ferrite with grain size of approximately 85 μm which is shown in Figure 3.9. In Figure 3.9, the darker microstructure is cementite carbide which will dissolve when reheating is above 750°C according to the TCFE2 database.

3.4.2 Experimental Procedure

The coarsening of austenite particles (minor phase) and the grain growth of the delta-ferrite (major phase) were studied using the high temperature tube furnace as described in section 3.2.2. Samples were cut to size of 10mm×10mm×15mmand sealed individually in vitreous silica under a back pressure of helium which varied so as to produce a pressure of 1 atm at the holding temperature.

In order to establish the coarsening kinetics at various temperatures and in the presence of various particles volume fractions, the samples were heated to different temperatures within the delta + austenite two phase region for different holding times. The complete list of temperature and times investigated is shown in Table 3-2. After each heat treatment, the samples were quenched into icy water and the capsules were broken in order to accelerate the cooling rate. The samples were then sectioned and prepared using standard metallographic techniques. The delta grain boundaries were revealed by using supersaturated picric acid with sodium dodecylbenzene sulfonate wetting agent and/or 2% Nital in enthal as necessary. The

microstructure was studied using the optical microscope, SEM and Clemex PE5.0 software. In order to obtain reliable statistics, six micrographs were analyzed for each sample, thus ensuring that at least 2000 particles were automatically analyzed using different magnifications according the particle size. The average austenite phase particle size was measured based on the equivalent circular diameter. The austenite particle size distribution and the area fraction were also measured.

Table 3-2 Heating temperature and holding time

Holding Temperature (°C)	850	1060	1200	1260	1280	1295	1299	1305
Predicted γ Fraction (vol. %)	8	30	30	15	8	1.2	0.2	0
Holding Time	16hrs	1hr	5mins		5mins	5mins		5mins
	48hrs	4hrs	15mins	15mins	15mins	15mins	15mins	15mins
	144hrs	24hrs	60mins		30mins	30mins		30mins
	216hrs	48hrs	90mins		60mins	60mins		
	288hrs	144hrs	180mins		90mins			

3.5 Delta-Ferrite to Austenite Phase Transformation

This experiment was trying to understand the kinetics of the delta-ferrite to austenite phase transformation and its effects on the subsequently grain growth using different cooling rates which is similar to the industrial TSCDR process from the slab surface to centre. The

effects of holding temperature, method to increase austenite nucleation sites using deformation during the phase transformation are also investigated.

3.5.1 Materials

The delta-ferrite to austenite phase transformation was studied using a quenching dilatometer at CANMET Materials Technology Lab. Once again, the Fe-1.5%Al model alloy was used. In this alloy the reheating temperature required to obtain a completely ferritic microstructure is 1310°C compared to 1477°C for APIX60 thin slab provided by Nucor steel as shown in Figure 2.1. The low temperature made it possible to achieve more accurate heating and cooling rates using the dilatometer and avoid problem related to the interdiffusion between the samples and the thermocouples. Most importantly, the model alloy retained delta-ferrite on quenching which made it easy to distinguish delta-ferrite and austenite. The dilatometer samples were in the form of 6mm diameter rod with a length of 10mm. In order to avoid the decarburization of the samples during the experiments a 50nm layer of carbon was deposited on the surface using electron-beam deposition and reheating was carried out under high purity Ar atmosphere. The experiment setup is shown in Figure 3.10.

3.5.2 Experimental Procedure

Three type experiments were carried out. The first examined the effects of cooling rate on the transformation. The samples were heated into the delta region at approximately 1310 °C and held for 60 seconds to ensure that the microstructure is 100% delta-ferrite. The samples were then cooled at different rates to 1125 °C which is the maximum volume fraction of austenite in delta-ferrite expected. The cooling rates used for this experiment were 50, 2 and 0.5 °C/sec. These were chosen to present the cooling rate at the surface, quarter point and center of a 90mm industrial thin slab.

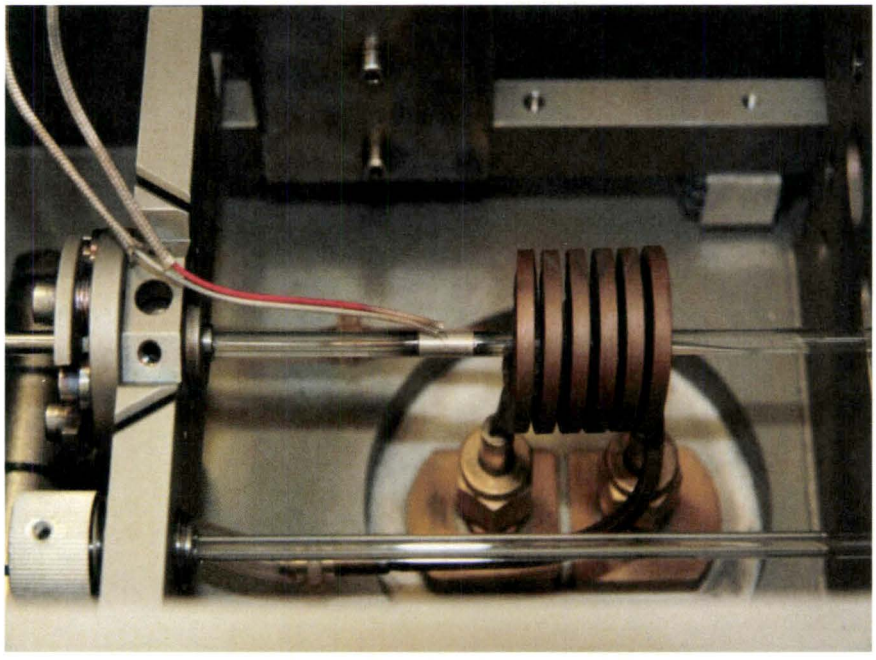

Figure 3-10 The experiment setup for delta-ferrite to austenite phase transformation

The second type of experiments investigated the effect of temperature. The samples were heated into the delta region as before, then quenched into the two phase (delta + gamma) region at different temperature for different holding time and the kinetics of the phase transformation were followed by means of dilatometer and measurement of austenite volume fraction. The list of temperature and times investigated is shown in Table 3.3.

Table 3-3 Effects of temperature

Holding Temperature, °C	Holding time, s			
1125	15	45	120	300
850	60	200	600	1800

The third studied the possibility to increase the austenite nucleation sites just on set this transformation to refine grain size. The samples are heated into the delta region, deformed (ε = 20%) just on set the phase transformation, and then cooled at constant rates (50°C/s, 0.5°C/s) to different temperature (850°C/s, 1125°C/s). Once the transformation was complete, the samples were quenched to room temperature. All the microstructures were studied using standard metallography techniques as discussed section 3.1-3.4. The alloy element concentrations in different phases were determined by Energy dispersive X-ray analysis attached to SEM.

Chapter 4 Results

In this chapter, experimental results on delta-ferrite grain growth and austenite grain growth will be summarized in section 4.2 - 4.3. Results on the novel approach of using austenite phase particles to pin delta grain growth at high temperature is presented in section 4.4. The delta-ferrite to austenite phase transformation will be described in section 4.5.

4.1 Solidification

Based on the literature review the solidification step is responsible for the inhomogenity of the microstructure while the solid state evolution is responsible for the large grain size. This thesis will focus on controlling the grain size and homogeneity through the solid state processing. Some work on solidification was performed to reproduce the as-cast microstructure are summarized in Appendix I. These will be used as starting microstructure for validating our model for grain size evolution in the solid.

4.2 Grain Growth Kinetics in Delta-Ferrite

The use of the Fe-2.5Al% model alloy permitted accurate determination of the delta grain size evolution in the temperature range 1470°C down to 1000°C. The results are summarized below is section 4.2.1 and section 4.2.2.

4.2.1 Microstructure Evolution of Delta Grain Growth

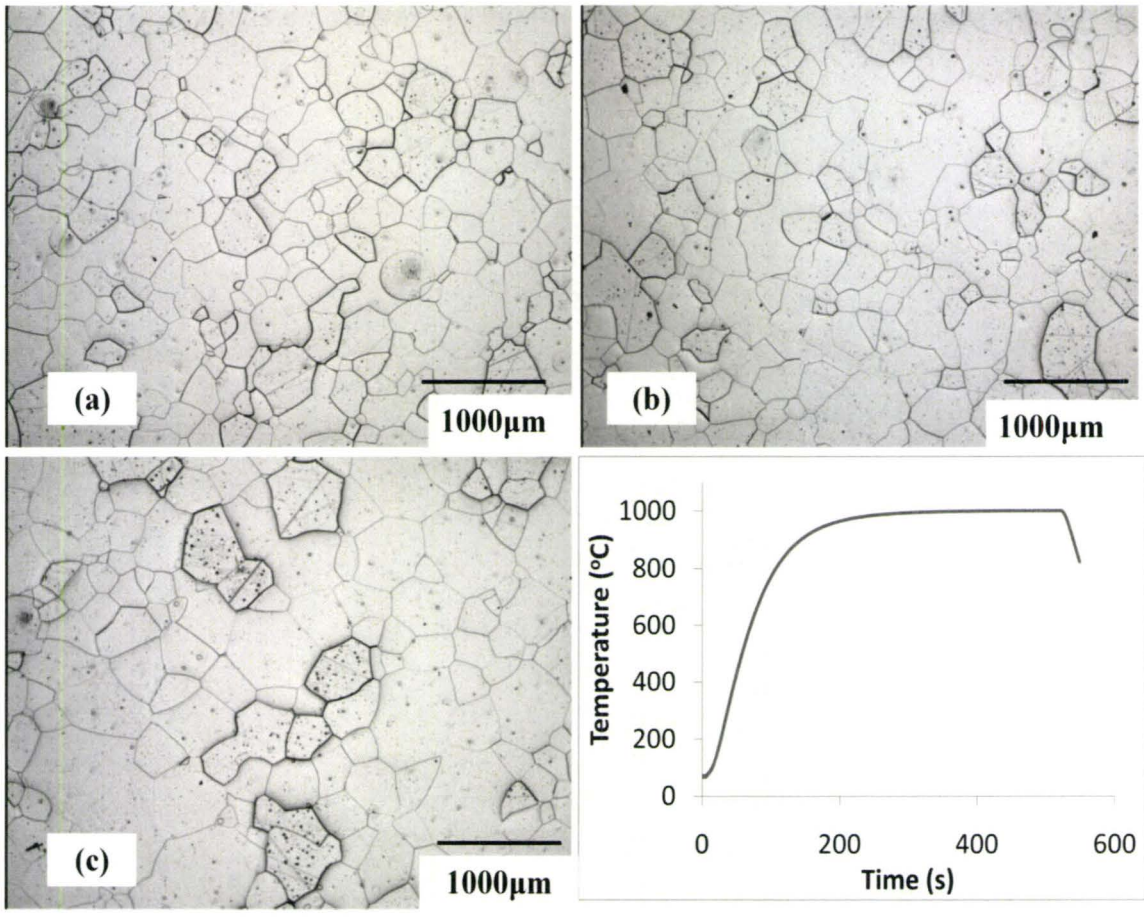

Figure 4-1 Microstructure of Fe-2.5Al% model alloy after heating to 1000°C for (a) 360s, (b) 480s, (c) 1180s. (d) illustration of the heating profile was recorded for each sample

Figure 4.1 shows the delta grain size evolution of specimens held at 1000°C for times of 360s, 480s and 1180s. From the microstructure evolution, it can be seen that delta grains grow with holding time. The times given represent the total time, including heating time, which can be a significant fraction of the total time as shown by the thermal profile in Figure 4.1(d). As such, the measured grain growth kinetics is not strictly isothermal and the complete thermal profile needs to be analyzed in order to quantitatively interpret the grain-growth data. A detailed analysis which takes into account the effect of the heating rate is presented in the discussion section.

For comparison, Figure 4.2 shows the delta grain size evolution after reheating to 1100°C for times of 360s, 480s and 1180s. The delta grain size holding at 1100°C is coarser than that of holding at 1000°C for the same time.

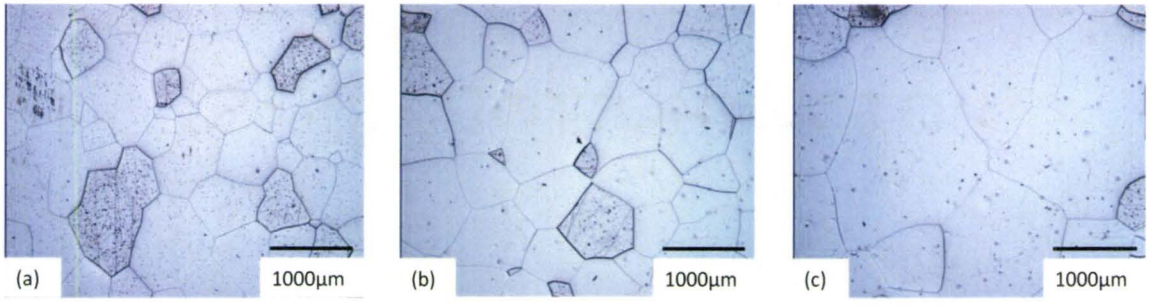

Figure 4-2 Microstructure evolution of Fe-2.5Al% model alloy after heating to 1100°C for (a) 360s, (b) 480s, (c) 1180s.

The delta grain microstructure evolution at 1200 °C holding for different time is shown in Figure 4.3. Figure 4.3 (a) shows the delta grain at 1200°C for 30 seconds, (b) shows for

120seconds and (c) is for 180 seconds. When reheating temperature increased to 1470°C, it took only 120s for the grain size larger enough to across the sample thickness.

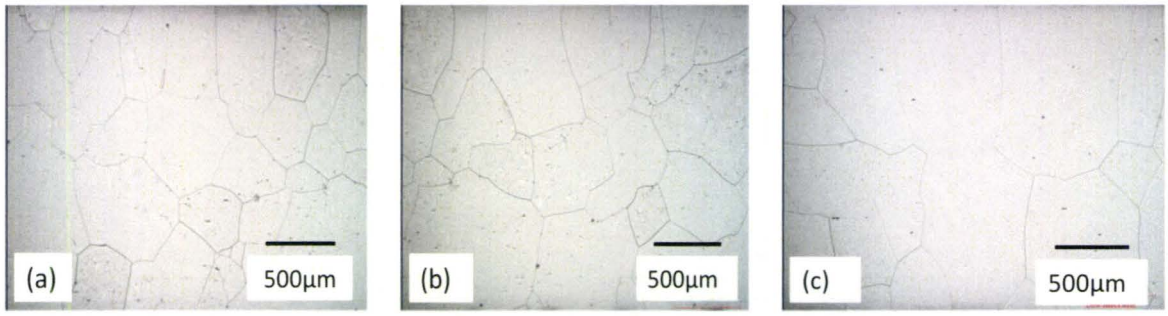

Figure 4-3 Microstructure evolution of Fe-2.5Al% model alloy after heating to 1200°C (a)60s, (b)120s and (c)180s

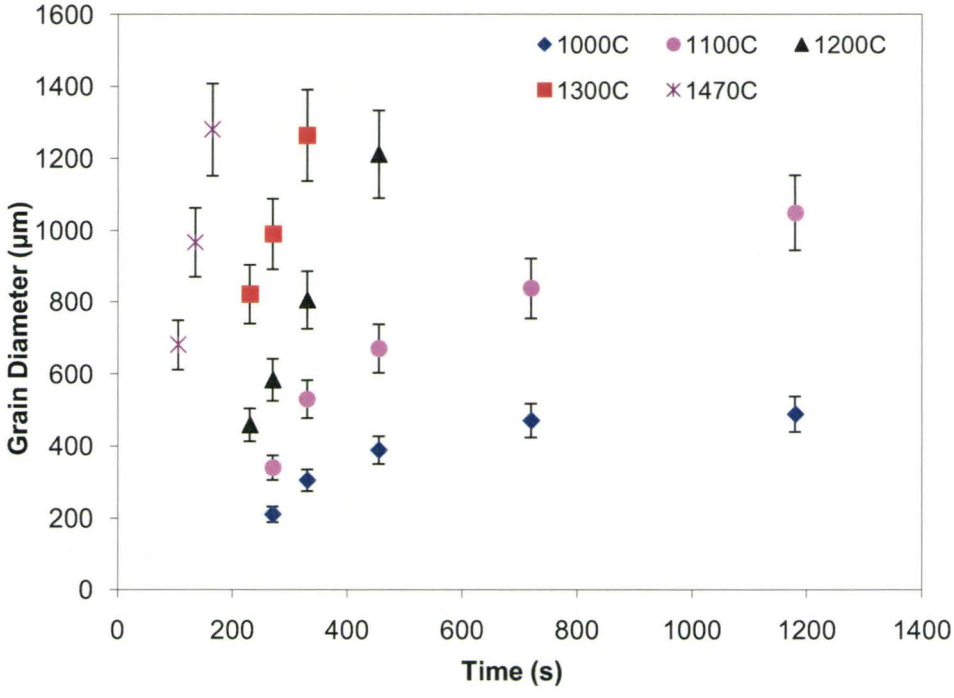

Figure 4-4 Delta-ferrite grain kinetics of the Fe-Al model alloy.

Note: Measurement errors consist of statistical constitutions and system contributions. The error bars for particles and grains represent standard deviation through this thesis due to the system errors can be neglected.

4.2.2 Kinetics of Delta Grain Growth

The measured grain size as a function of reheating temperature and holding time are summarized in Figure 4.4. Once again, the times shown are the total time spent in the furnace, including heating time. The delta grain size was measured using the linear intercept method and the true three-dimensional grain diameter was calculated as 1.61 times the linear intercept diameter(Gladman 1997).

4.3 Grain Growth Kinetics in Austenite

The austenite grain growth kinetics was measured by etching the former austenite grain boundaries in both APIX60 and Nb-Ti free model alloy. The APIX60 steel contained Nb and Ti additions which lead to the formation of complex Nb, Ti carbonitrides. During the reheating experiment, the dissolution of some of the precipitates Nb(C,N) will result in some grains unpinning and these unpinned grains consume other grains by an abnormal grain growth process between 1100 to 1200°C. In the TSCDR process, the slab is not reheated and as such this process is not encountered. In order to bypass this complication, only kinetics of gain growth in Nb-Ti free model alloy will be discussed here. The kinetics of abnormal grain growth in APIX60 will be summarized and discussed in Appendix II.

4.3.1 Microstructure Evolution of Austenite Grain Growth

Figure 4.5 shows the austenite microstructure evolution of Nb-Ti free model alloy for a reheating temperature of 1200°C for times of 5mins, 15mins and 30mins. The thermocouple recorded the temperature profile during heating process as shown in Figure 4.5(d). As seeing from the heating curve, the measured austenite grain growth kinetics is also non-isothermal and the complete thermal profile needs to be used to analyze the grain-growth data.

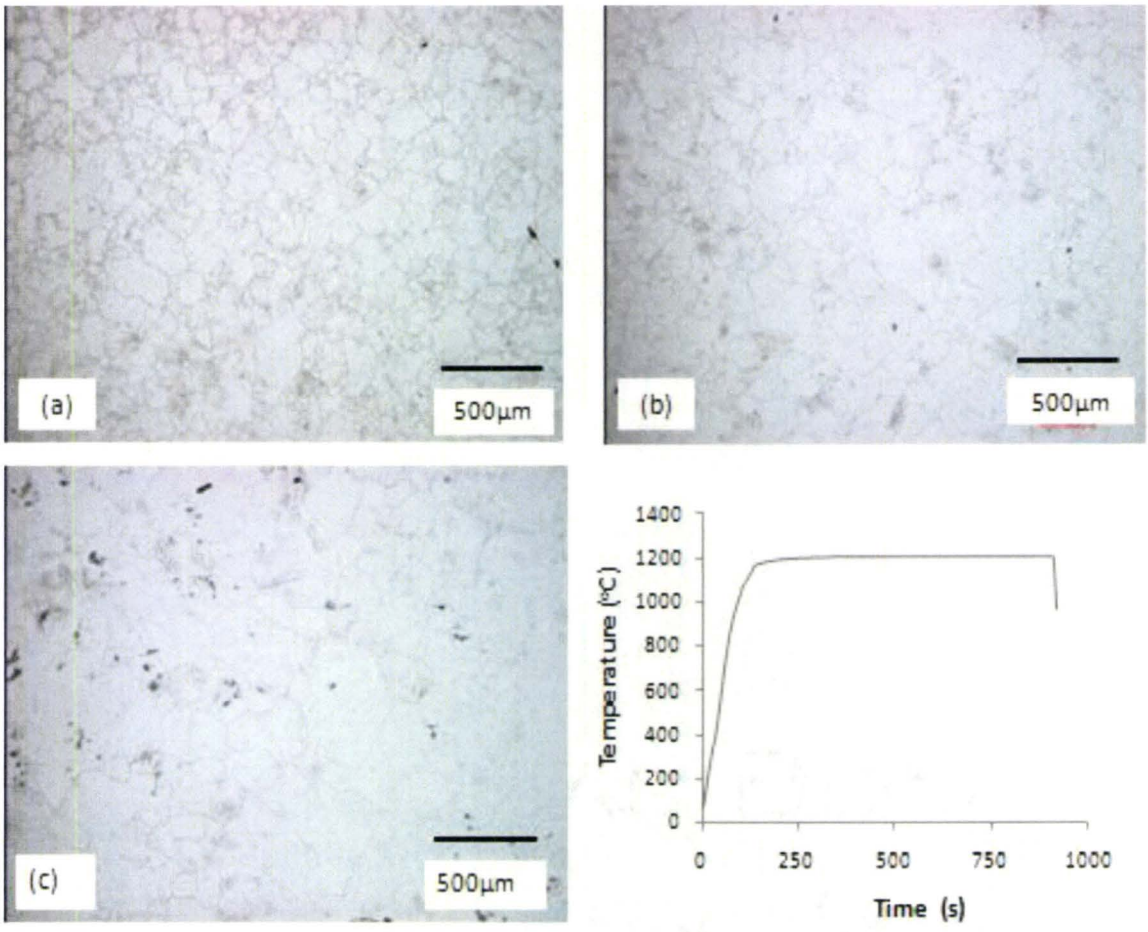

Figure 4-5 Microstructure Ti-Nb free model alloy after heating to 1200°C for (a)5mis, (b) 15mins, (c) 30mins. (d) illustration of the heating profile was recorded for each sample

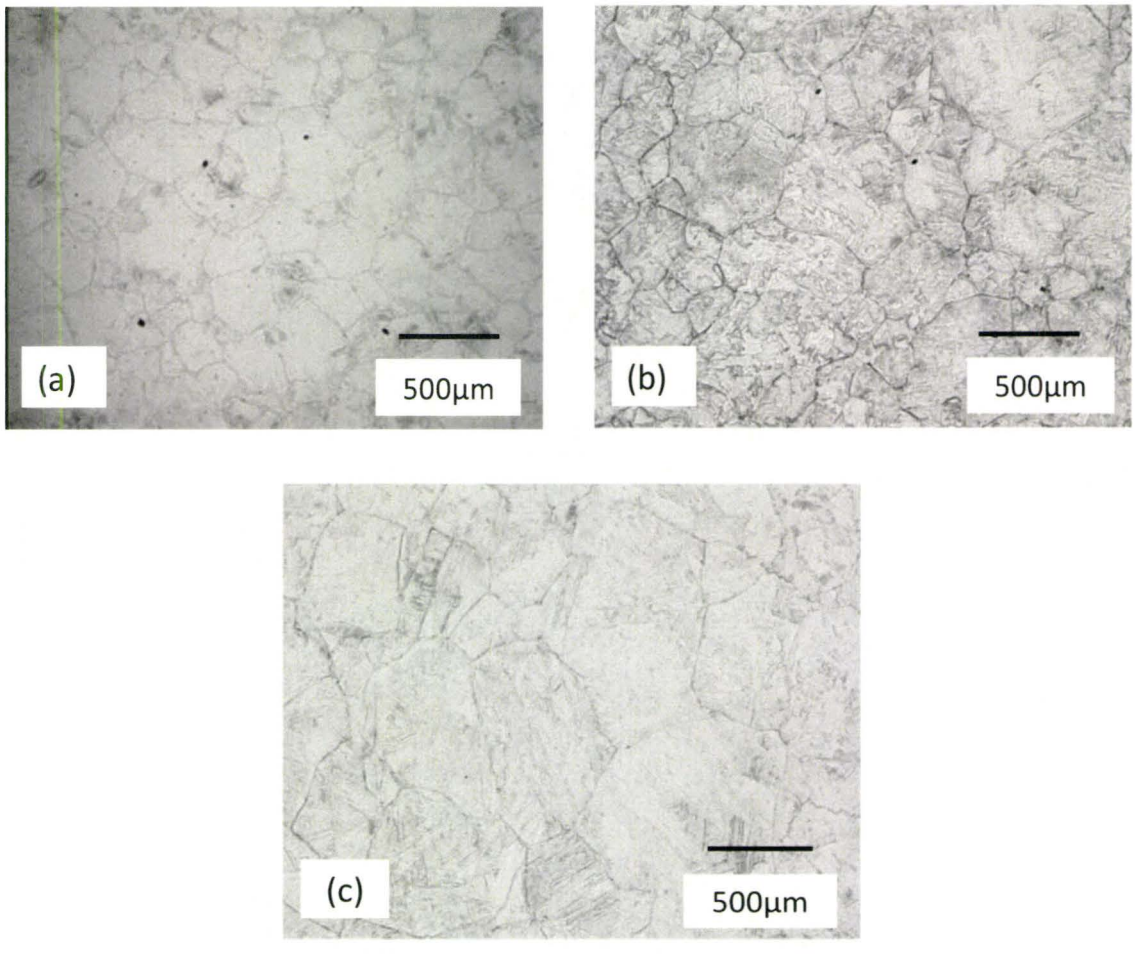

Figure 4-6 Microstructure Ti-Nb free model alloy after heating to 1300°C for (a)5mis, (b) 15mins, (c) 45mins.

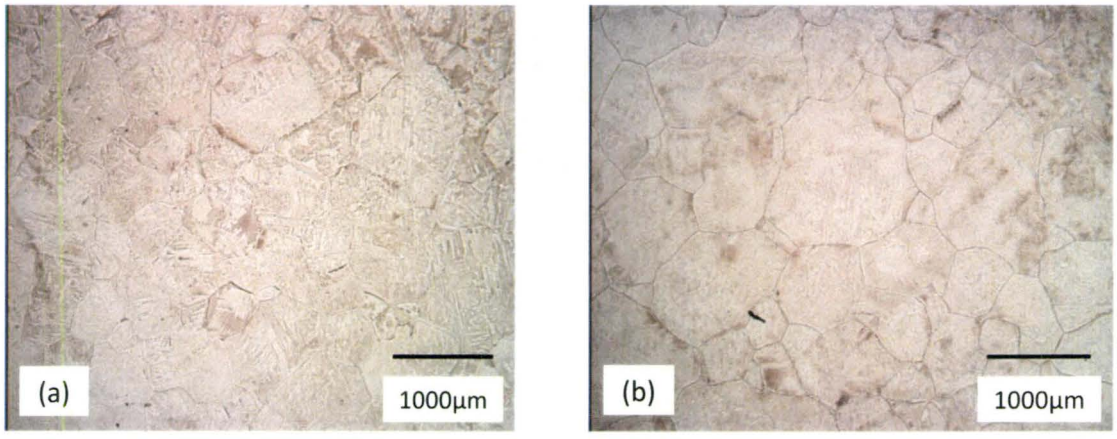

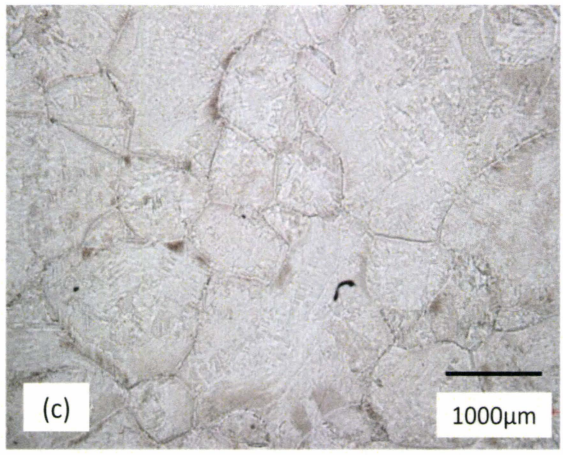

Figure 4-7 Microstructure Ti-Nb free model alloy after heating to 1400°C for (a)5mis, (b) 10mins, (c) 15mins

The austenite grain microstructure evolution at 1300 °C is shown in Figure 4.6, while that at 1400°C is shown in Figure 4.7. In the experimental range from 1200°C to 1400°C, there is no precipitation dissolution for Ti-Nb free model alloy and the austenite grain shows "normal grain growth" behavior.

4.3.2 Kinetics of Austenite Grain Growth

The kinetics of austenite grain-growth is summarized in Figure 4.8. Once again, the time refers to the total time in the furnace, including the heating time. The austenite grain size was also measured using the linear intercept method and the true three-dimensional grain diameter was calculated as 1.61 times the linear intercept diameter as delta grain growth.

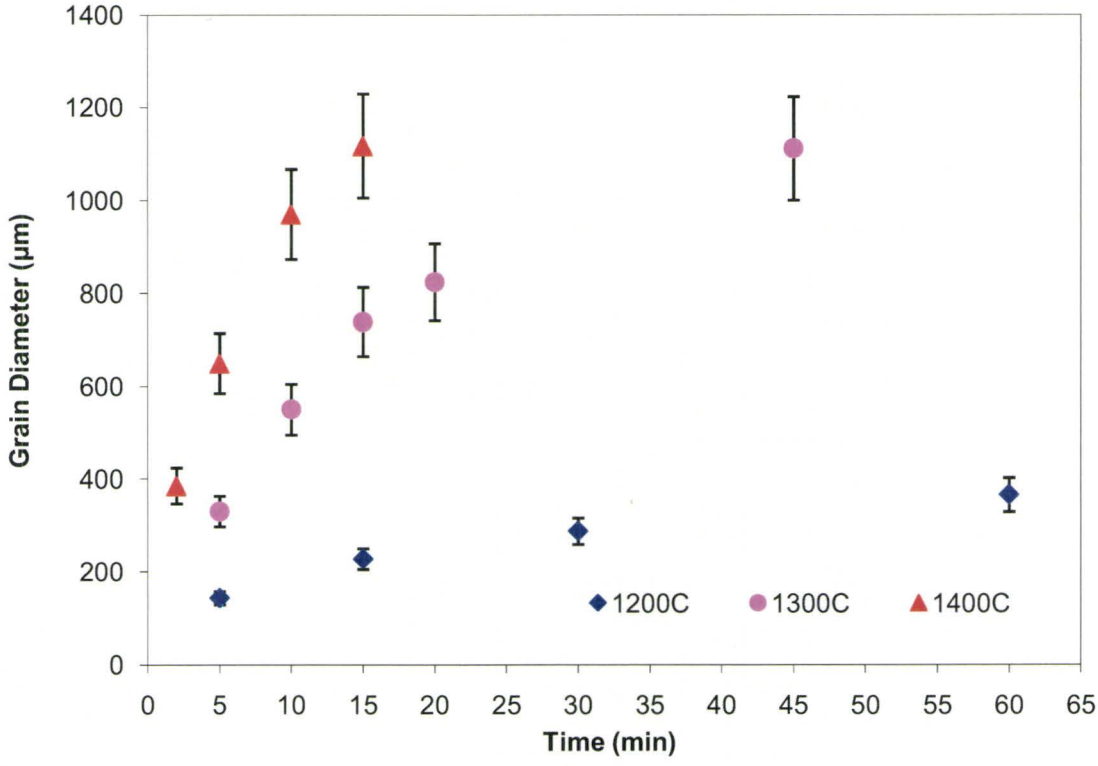

Figure 4-8 Austenite grain kinetics of the Ti-Nb free model alloy

4.4 Coarsening Behaviour of Delta-Ferrite/Austenite Duplex Microstructure

The austenite phase fraction as a function of temperature was calculated using the ThermoCalc TCFE2 database for an alloy of Fe-1.5%Al. The result is shown in Figure 4.11 along with experimental conditions selected for this study. The volume fraction of the austenite phase varies from 0% at 1310°C to a maximum of 34% at 1130°C. The volume fraction then decreases to 5% at 780°C. Below this temperature, eutectoid reaction takes place. Using the Fe-1.5Al% model alloy permitted accurate investigation into the particle coarsening

behavior and their relationship with kinetics of delta grain growth under different volume fractions at different temperatures. The microstructure evolution of this model alloy is presented in section 4.4.1, and kinetics of austenite particles coarsening and delta-ferrite grain growth are summarized in section 4.4.2.

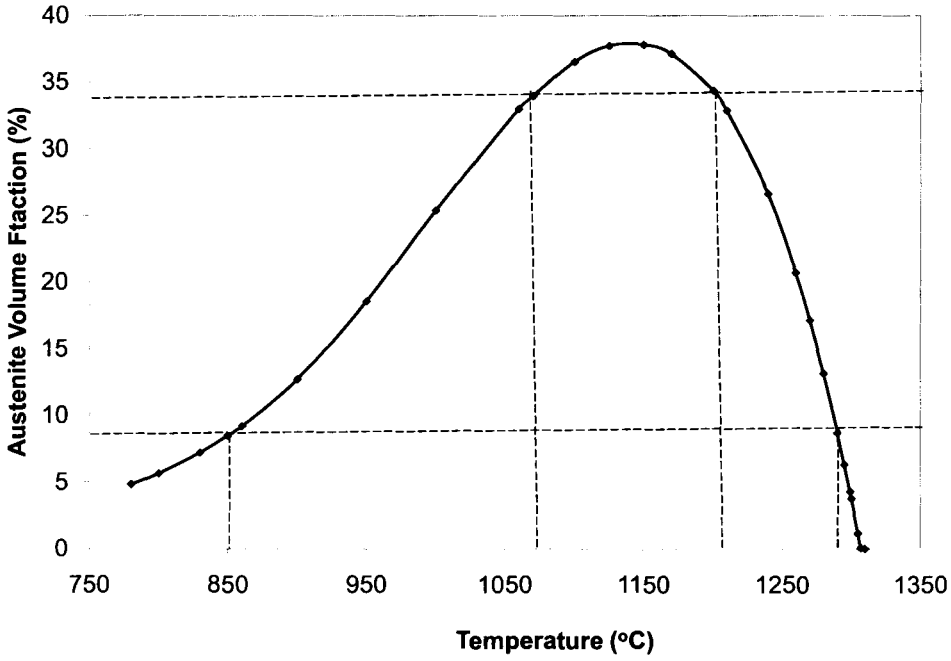

Figure 4-9 ThermoCalc prediction of austenite particle volume fraction with temperature in Fe-1.5%Al model alloy

4.4.1 Delta-Ferrite/Austenite Duplex Microstructure Evolution

When the samples were reheated to different temperatures, the average particle area fractions at different holding times, as calculated using Clemex PE5.0 software are

summarized in Table 4.1. As mentioned in Chapter 3, six microstructures were analyzed to obtain the average particle area fraction and particle size distribution for each holding time at specific temperatures. From Table 4-1, the austenite phase volume fractions keep constant at specific temperatures for different holing times.

Table 4-1 Average particle area fraction at different reheating temperature

Temperature(°C)	Austenite Area Fraction with Different Holding Time					
850	Time (hour)	16	48	144	216	288
	Fv (%)	8.3	8.6	8.3	8.7	8.3
1060	Time (hour)	1	4	24	48	144
	Fv (%)	17	18.6	19.3	18.5	18.1
1200	Time (min)	5	15	60	90	180
	Fv (%)	20.3	19.3	21.6	21.0	20.8
1260	Time (min)	15				
	Fv (%)	12.1				
1280	Time (min)	5	15	30	60	90
	Fv (%)	9.6	9.3	9.4	10.6	8.5
1295	Time (min)	5	15	30	60	
	Fv (%)	6.8	6.6	6.8	6.5	
1299	Time (min)	15				
	Fv (%)	2.6				
1302	Time (min)	15				
	Fv (%)	2.0				
1305	Time (min)	5	15	30		
	Fv (%)	1.3	1.1	1.0		
1310	Time (min)	15				
	Fv (%)	0				

When the reheating temperature is 850°C, ThermoCalc predicted an austenite volume fraction of about 8% which is the same as the actually measured austenite phase volume fraction as shown in Table 4.1. The austenite phase particle and delta-ferrite grain microstructure evolution at 850°C are shown in Figure 4.10. The dark color particles are the austenite phase which transformed to martensite when quenched to room temperature and the matrix is delta-ferrite. The austenite phase particles are distributed along the delta-ferrite grain boundaries. At low temperatures, the austenite particles coarsen very slowly and the delta grain size is almost constant over the times investigated.

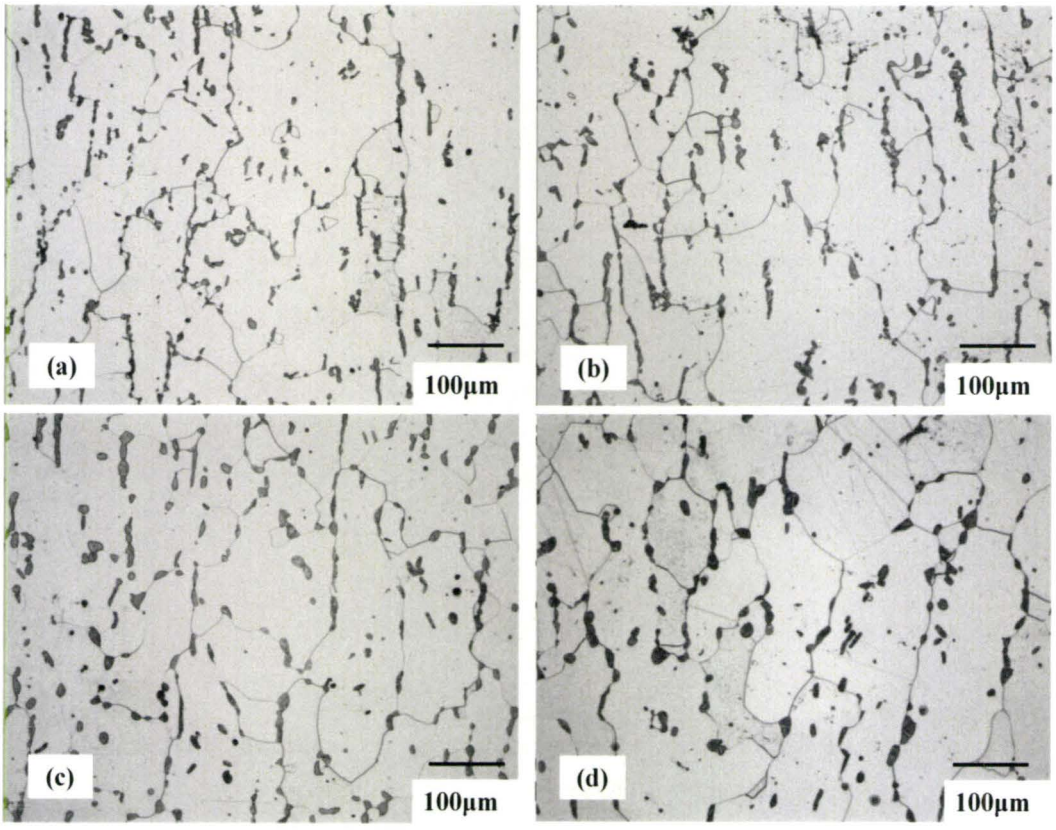

Figure 4-10 Fe-1.5%Al model alloy microstructure evolution after heating to 850°C for (a)16 hrs, (b)48hrs, (c)144hrs and (d)288hrs

Figure 4.11 shows the microstructure evolution at different holding times for a reheating temperature of 1060°C. The measured austenite particle area fraction is constantly at about 19%. With such high volume fraction, the austenite particles are connected along the delta grain boundaries. At short holding times, there is no significant change in the delta grain size, however, when the holding time is longer than 30 minutes, the delta grains grow with increasing holding time.

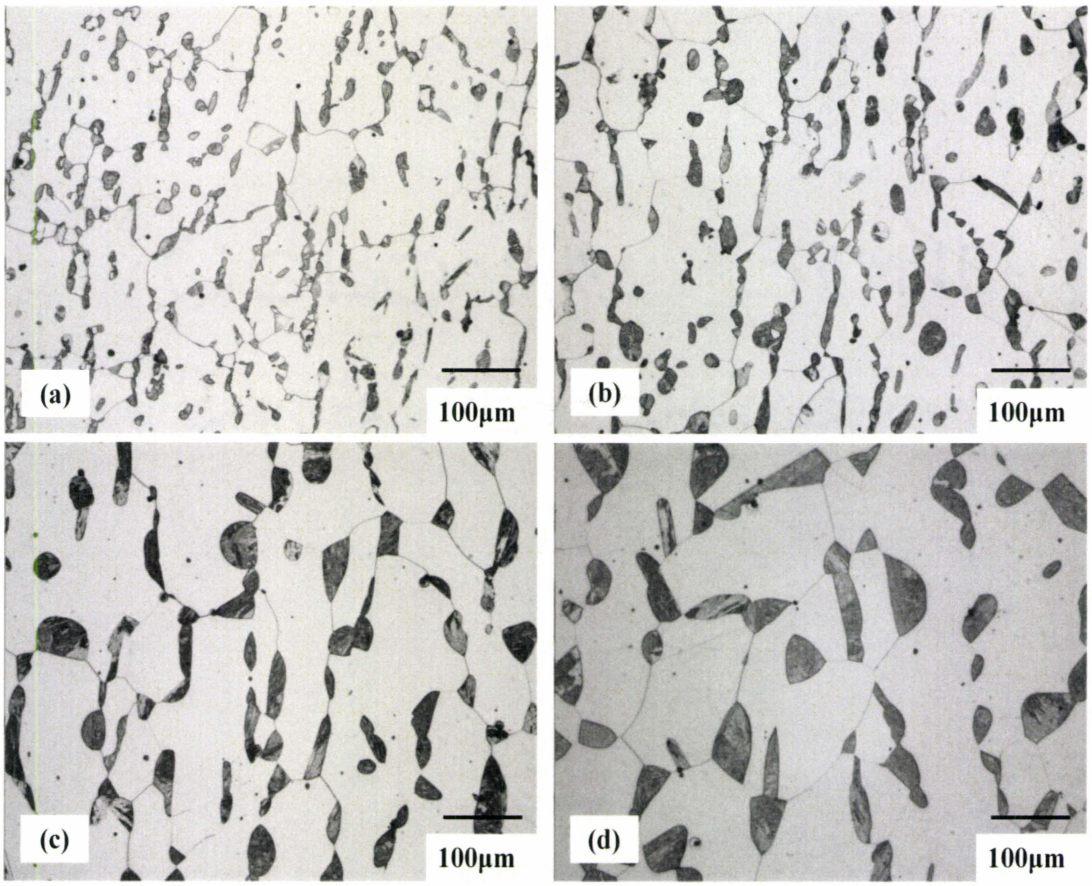

Figure 4-11 Fe-1.5%Al model alloy microstructure evolution after heating to 1060°C (a)1hr, (b)4hrs, (c)48hrs and (d)144hrs

Figure 4.12 captures the microstructure evolution when the heating temperature is increased to 1200°C. The measured austenite particle area fraction is constantly 19%, which is the same value obtained at 1060°C. This made it possible to investigate the effect of temperature on the particle coarsening behavior while keeping the volume fraction of particles constant. At this reheating temperature, the austenite particle and the delta grain size are seen to increase with time due to particle coarsening and grain growth respectively.

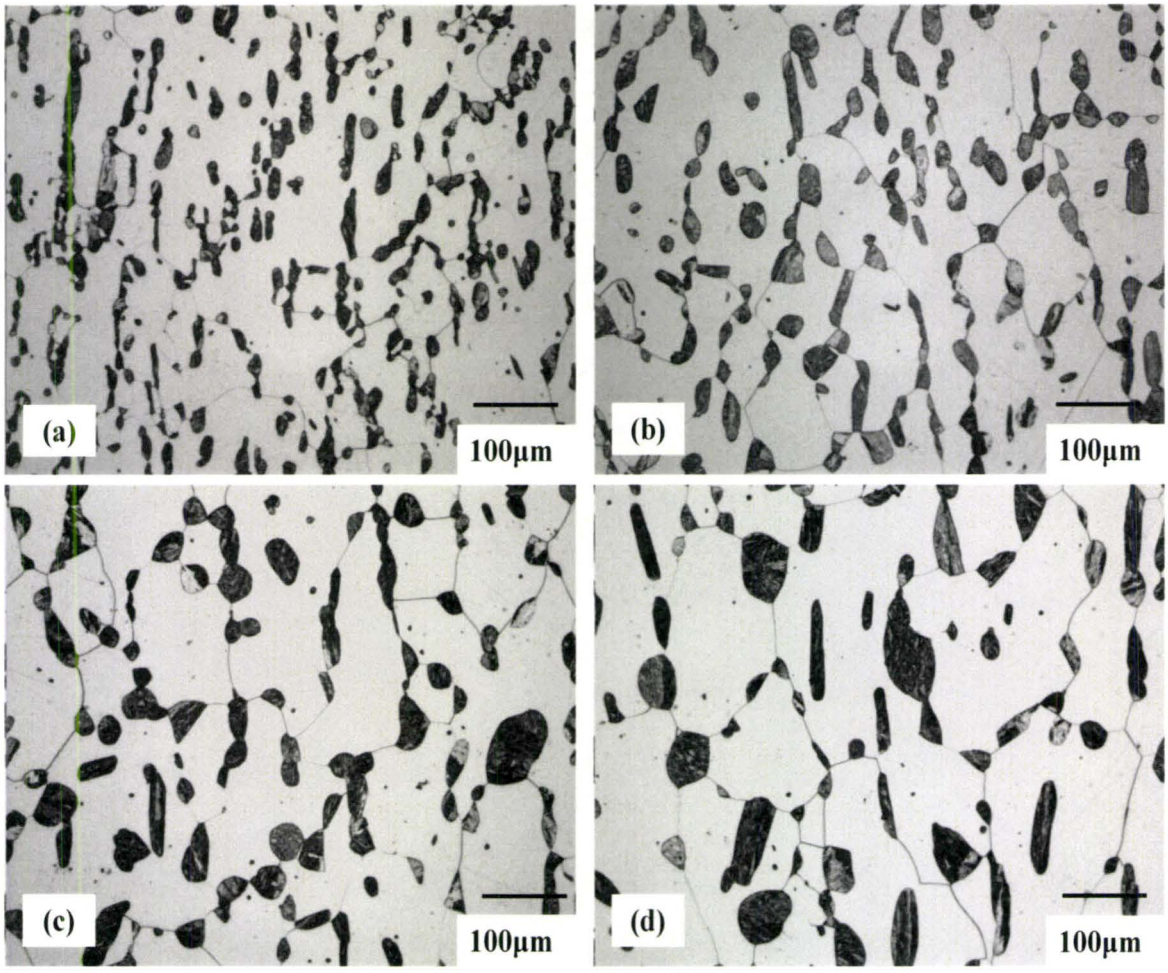

Figure 4-12 Fe-1.5%Al model alloy microstructure evolution after heating to 1200°C (a)5mins, (b)60mins, (c)90mins and (d)180mins

When the reheat temperature is increased to 1280°C, the austenite particle area fraction is 9%. The microstructure evolution for this treatment is shown in Figure 4.13. The austenite particle size and the delta grain size increased with holding time. It should be noted that particle area fraction at 1280°C has the same value as that of at 850°C. Once again this makes it possible to study the effect of temperature on coarsening and grain growth for a constant volume of particles.

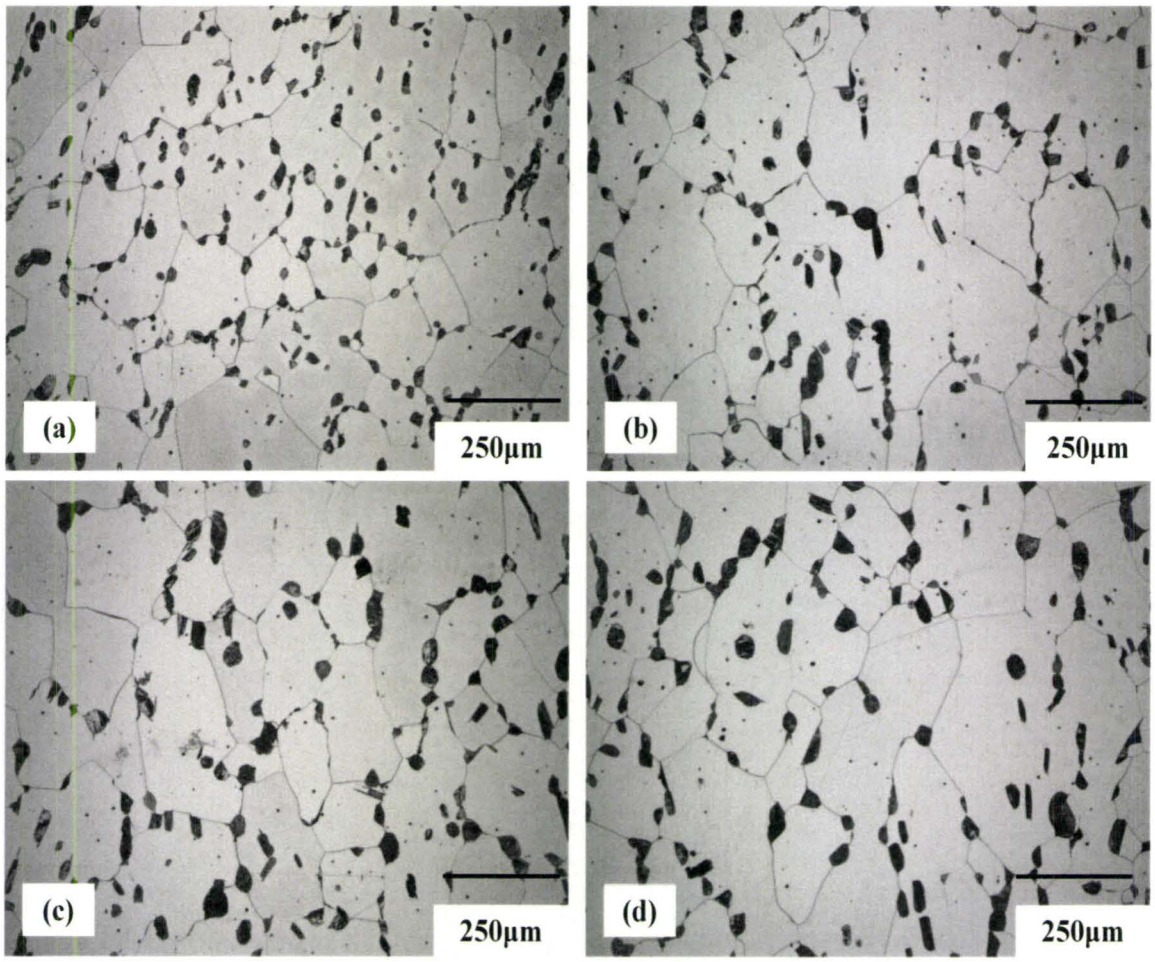

Figure 4-13 Fe-1.5%Al model alloy microstructure evolution after heating to 1280°C, (a)5mins, (b)15mins, (c)30mins and (d)90mins

Figure 4.14 shows the microstructure evolution when the reheating temperature is increased to 1295°C. The measured austenite particle area fraction is constantly 6% for all holding times. It can be seen that particle size and delta grain size changed faster as function of time compared to previous heat treatment. With the volume fraction decreasing, the austenite particles on the delta grain boundaries are no longer in direct contact.

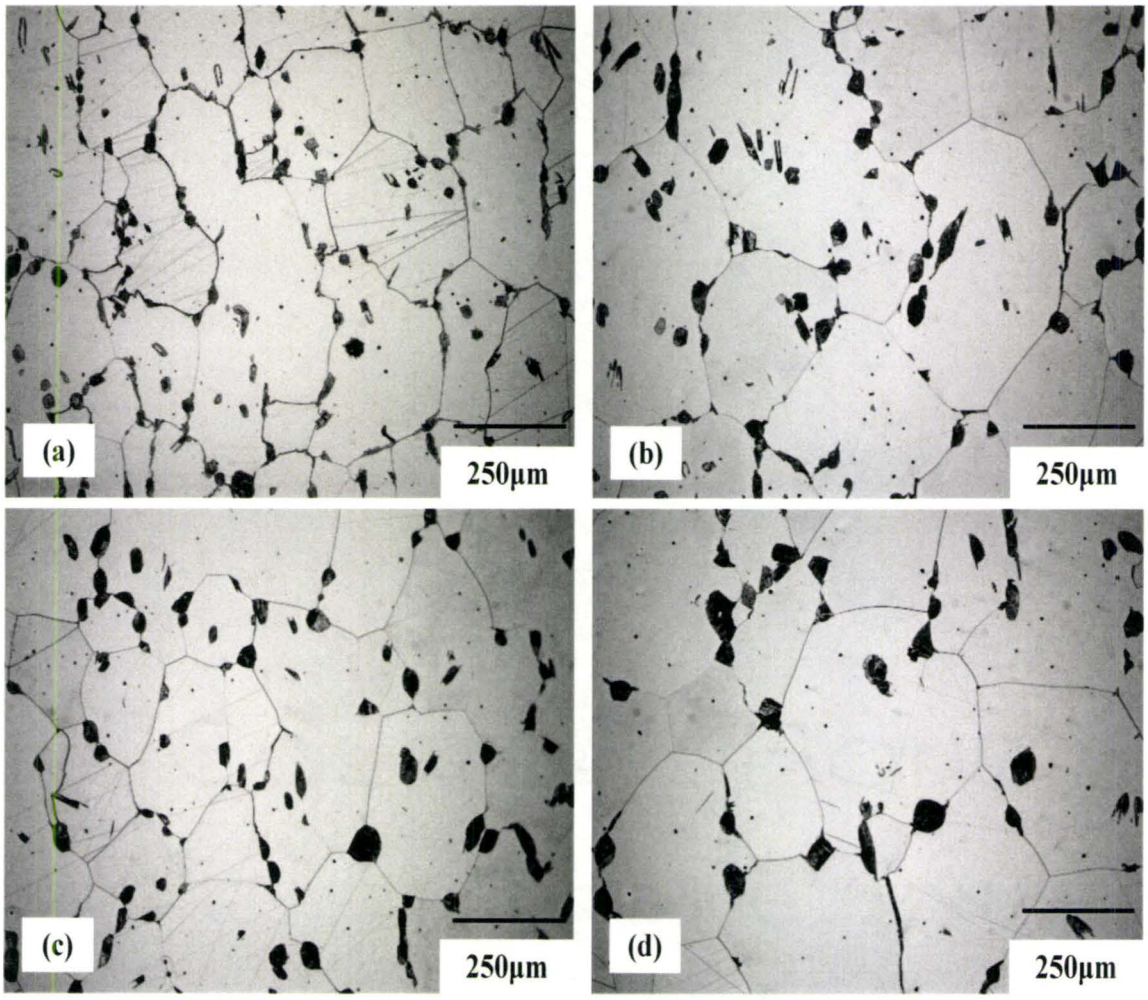

Figure 4-14 Fe-1.5%Al model alloy microstructure evolution after heating to 1295°C, (a)5mins, (b)15mins, (c)30mins and (d)60mins

Higher reheating temperatures 1299°C, 1302°C, 1305°C and 1310°C were also investigated. An example of microstructure evolution at 1299°C and 1305°C for 15 minutes is shown in Figure 4.15 respectively. For holding temperature 1299°C, the measured particle volume fraction F_v is 2.6%; for temperature 1305°C, the austenite particle volume fraction F_v is only 1%. The austenite phase particle can inhibit delta grain growth up to 1305°C.

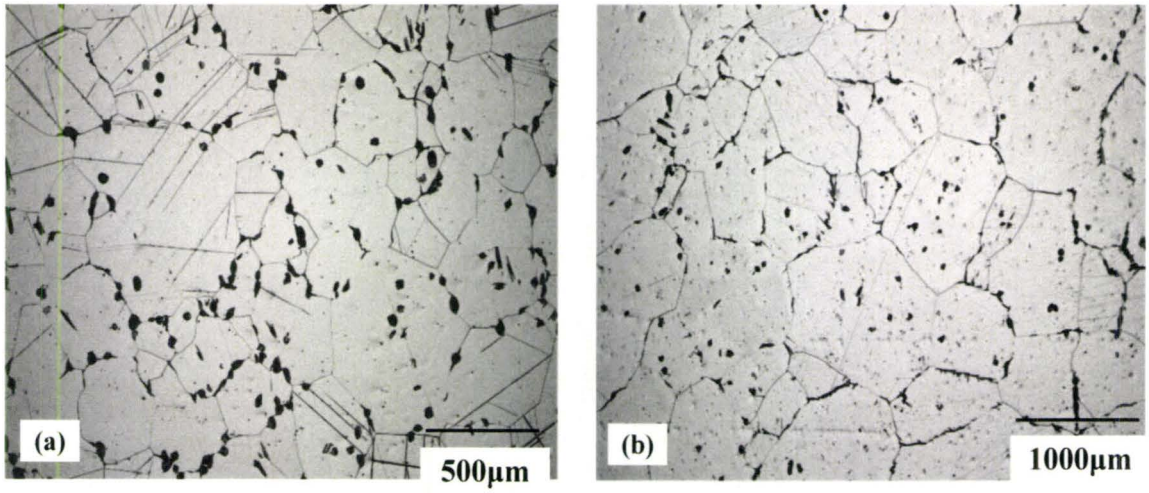

Figure 4-15 Fe-1.5%Al model alloy microstructure evolution at holding (a) 1299°C and (b)1305°C for 15minutes

4.4.2 Kinetics of Austenite Particles Coarsening and Delta Grain Growth

The measured austenite particles as a function of reheating temperature and holding time are summarized in Figure 4.16. At low temperature (850°C), the austenite particles coarsen very slowly, however, the particles coarsening rate increases with increasing reheating temperature. The austenite particles coarsening rate depends on the coarsening mechanism,

particles volume fraction, temperature, and chemical composition. The detail discussion will be presented in section 5.4.

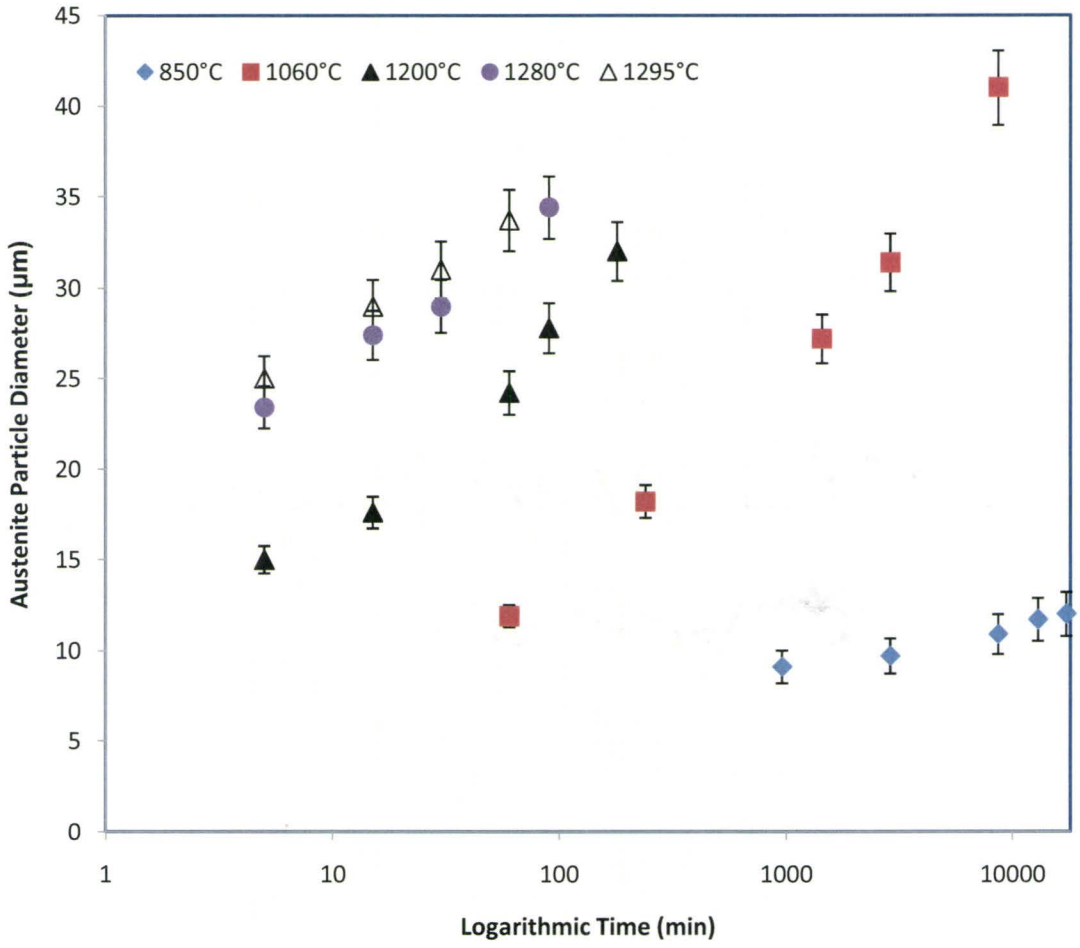

Figure 4-16 The measured austenite particles as a function of reheating temperature and holding time

The measured delta grain size as a function of reheating temperature and holding time are summarized in Figure 4.17. There is no obvious delta grain size changing when the

reheating temperature is 850°C. Increasing reheating temperature to 1060°C and 1200°C, the grain growths as function of time has two regions: at shorter holding time, the grain size is almost constant, after longer time, grains grow with increasing holding time. When reheating temperature increased to 1280°C and 1295°C, the delta grains growth size increased with time over the times investigated.

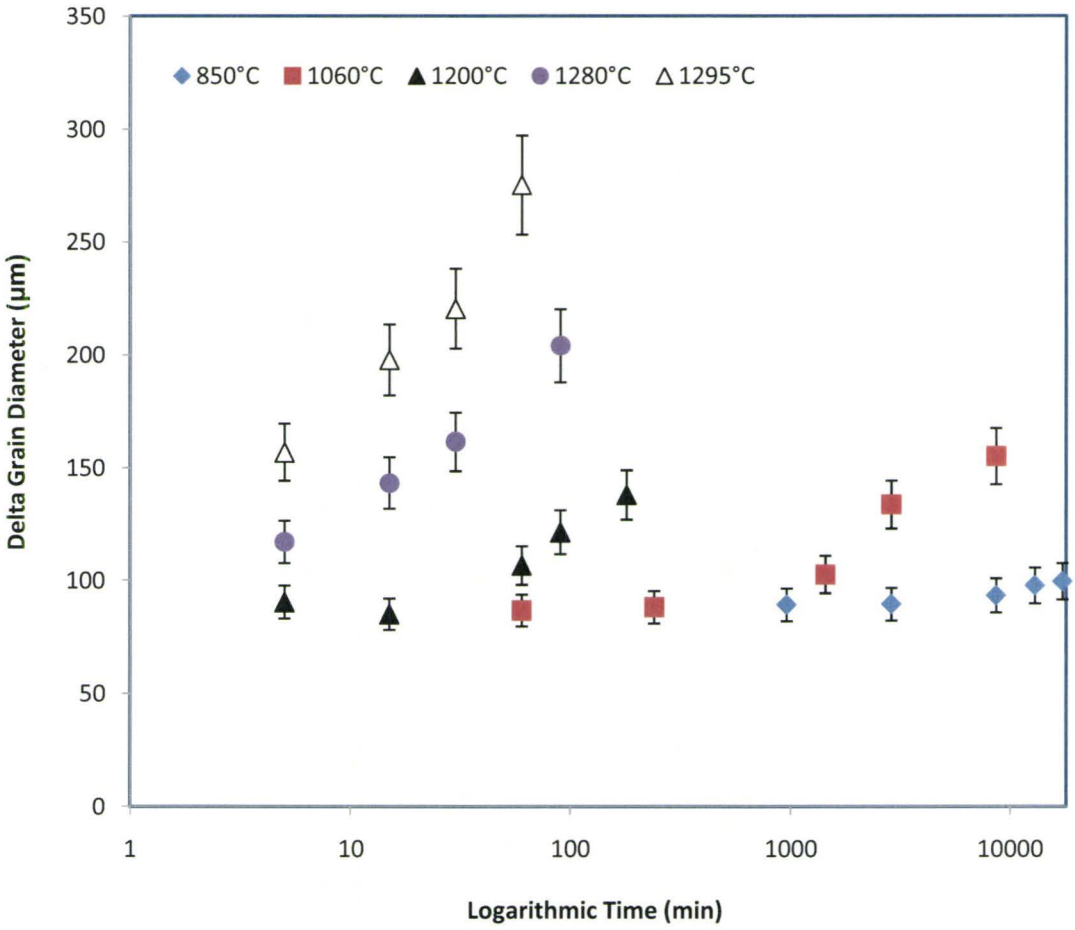

Figure 4-17 The measured delta grain as a function of reheating temperature and holding time

4.5 Delta-Ferrite to Austenite Phase Transformation

The use of Fe-1.5%Al model alloy (section 3.4) made it possible to directly observe the microstructure during the delta-ferrite to austenite phase transformation and to investigate the effects of cooling rates, temperature and deformation on the transformation and on subsequent grain growth. The results of the phase transformation study are summarized in the following sections.

4.5.1 Effects of Temperature

The microstructure evolution of the specimens that were heated in the delta region (1310°C) for 60 seconds, then isothermally transformed at 1125°C for 15s, 45s, 120s and 300s is shown in Figure 4.18. The light phase is the delta-ferrite and the dark one is the austenite that transformed to martensite during quenching. The austenite volume fraction as a function of holding time is shown in Figure 4.19. It appears that the delta-ferrite to austenite phase transformation was completely finished after 120s of holding; a constant austenite volume fraction of 21% was reached. Energy dispersive X-ray analysis was used to determine the aluminium, manganese and silicon concentrations in the delta-ferrite and austenite is shown in Figure 4.20. While the absolute values of the concentrations are not accurate, the results seem to indicate that Al (and possibly Mn) is partitioning between austenite and the delta-ferrite.

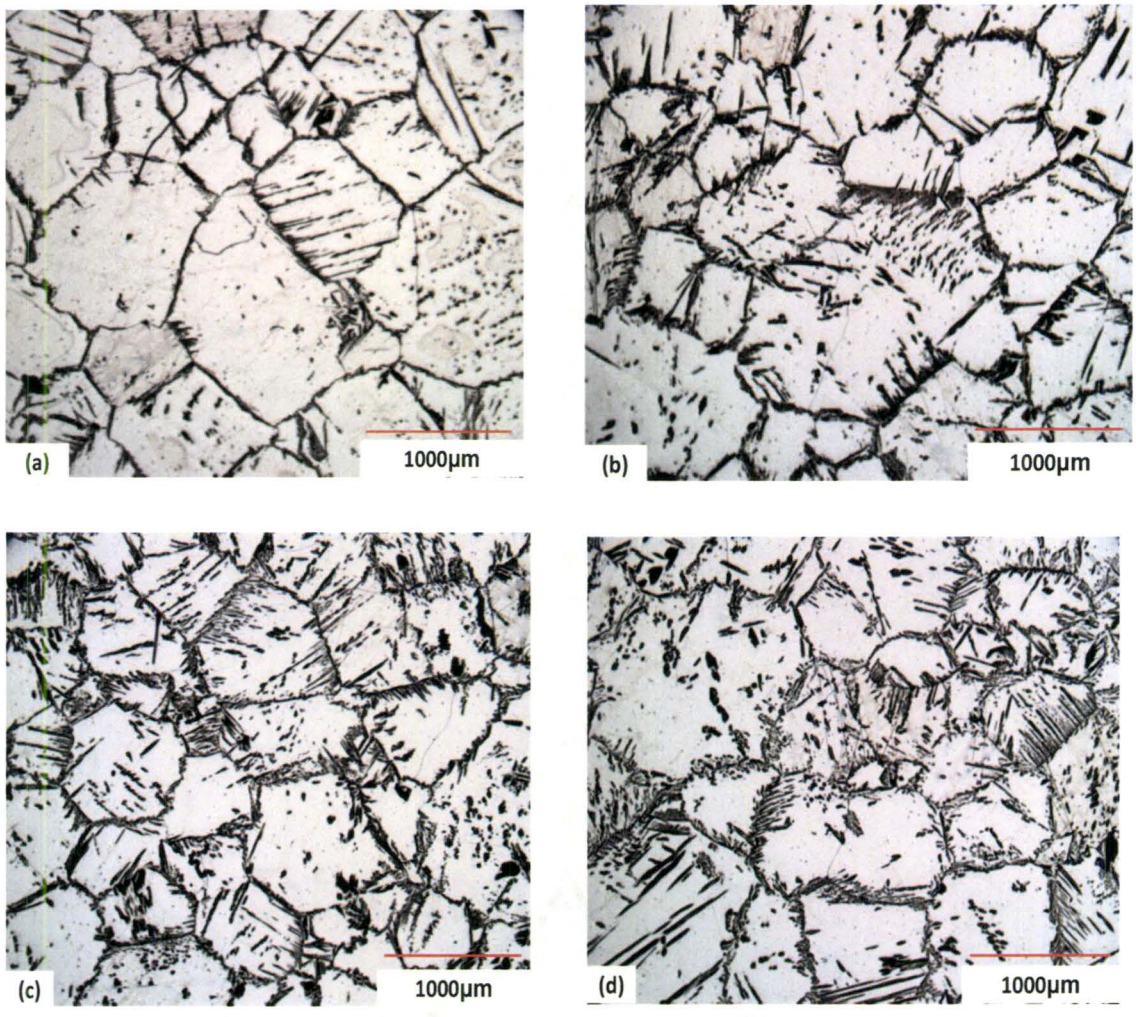

Figure 4-18 Microstructure evolution of 1125°C for different holding time (a)15s, (b) 45s, (c) 120s, and (d)300s

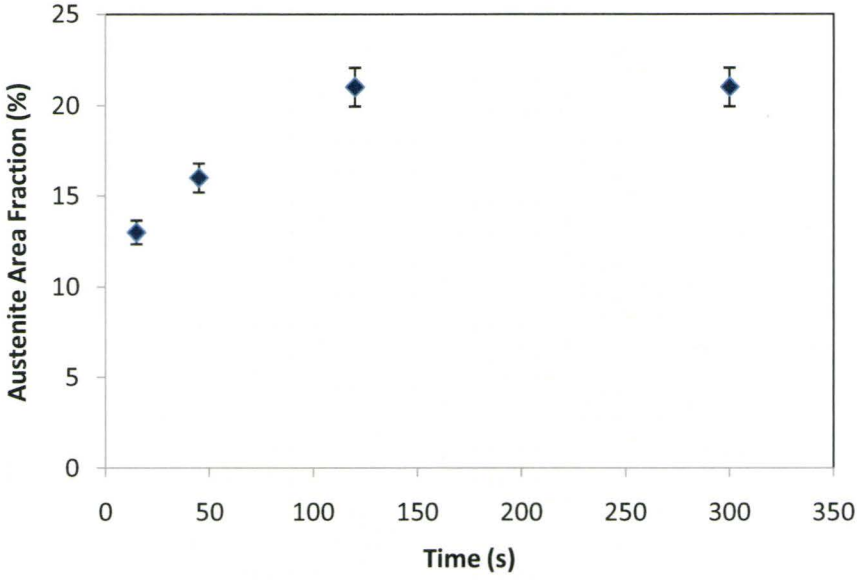

Figure 4-19 Austenite volume fraction as function of time at 1125°C

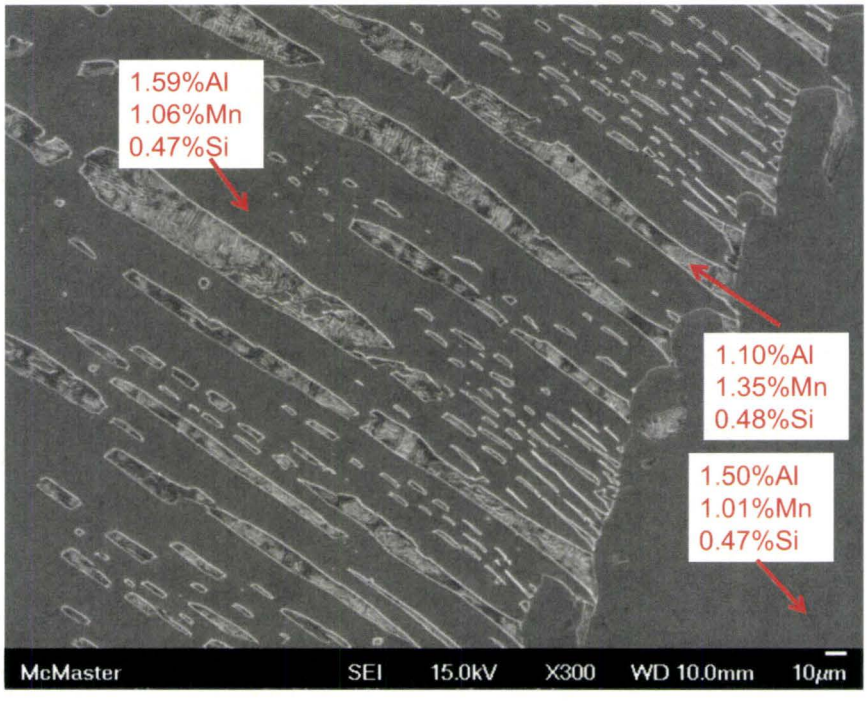

Figure 4-20 EDS determined Al, Mn, and Si concentration in the delta-ferrite and austenite of specimen reheated to delta region for 60 seconds, then cooling down with of 50°C/s to 1125°C for 300s

When the specimen was cooled down and isothermally held at 850°C, the transformation appeared to proceed at a much slower rate as shown in Figure 4.21. The evolution of austenite volume fraction with holding time at 850°C is shown in Figure 4.22. After a holding time of 1800s, the delta-ferrite to austenite phase transformation appears to stop and the volume fraction of austenite was 9% which is very close to the equilibrium value predicted by the TCFE2 database. Once again, EDX analysis indicates that the transformation requires the partition of the substitutional alloying elements as shown in Figure 4-23.

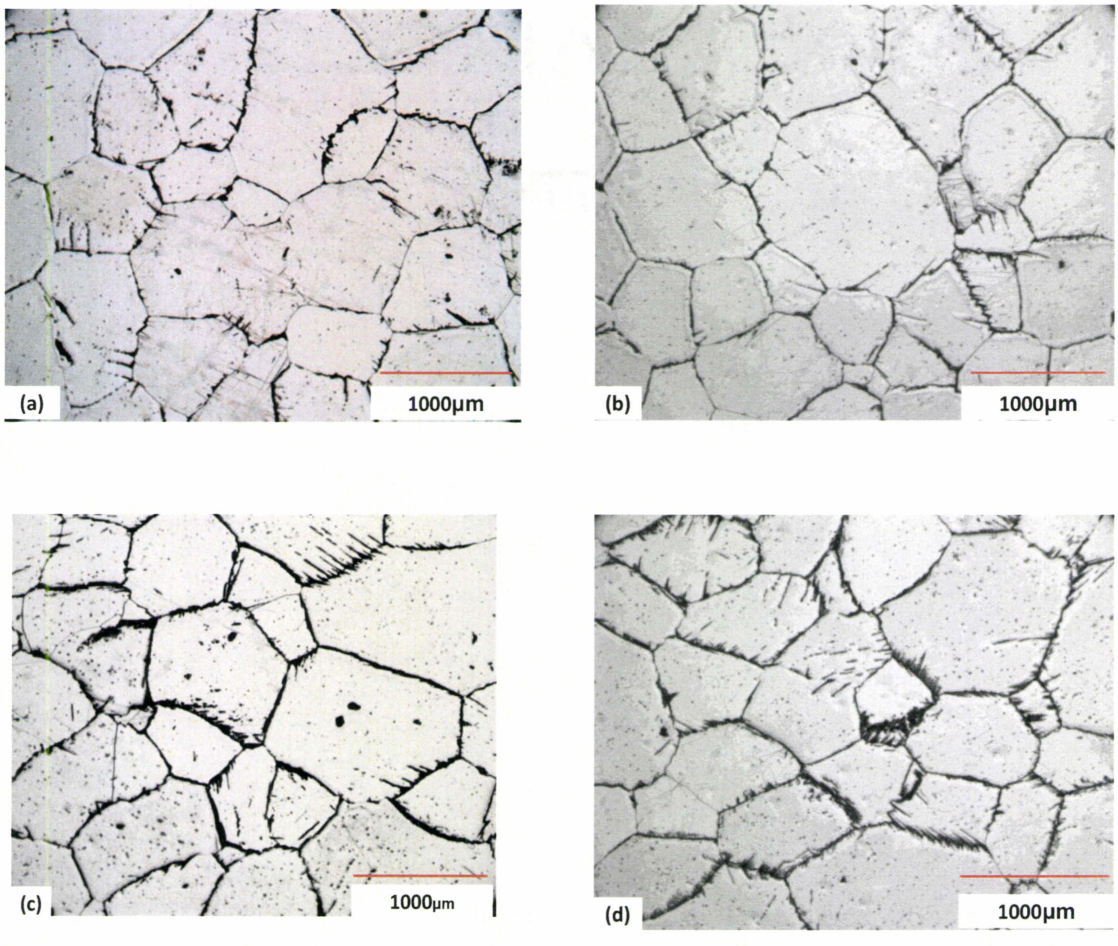

Figure 4-21 Microstructure evolution of 850°C for (a) 60s, (b) 200s, (c) 600s, and (d)1800s

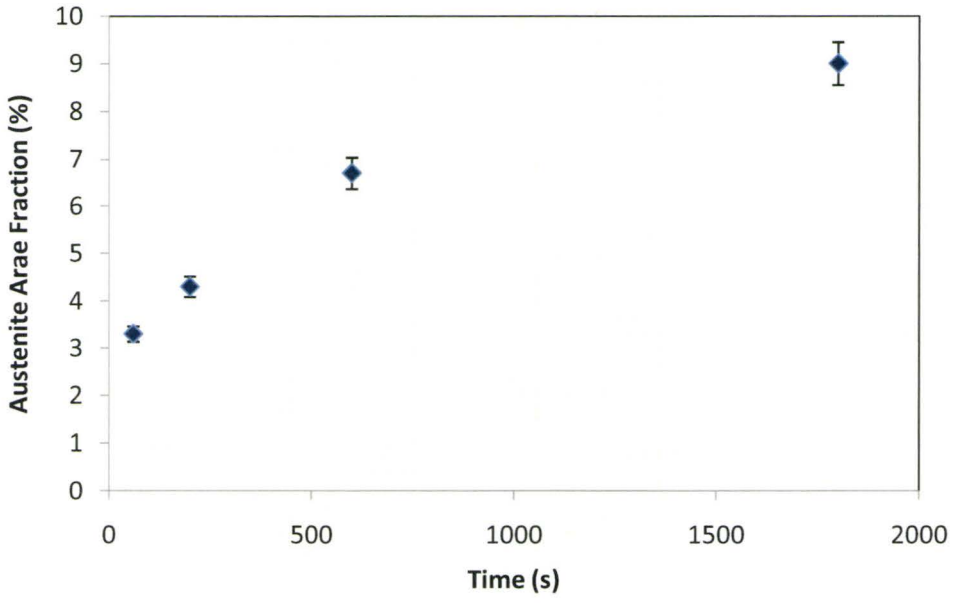

Figure 4-22 Austenite volume fraction as function of time at 1125°C

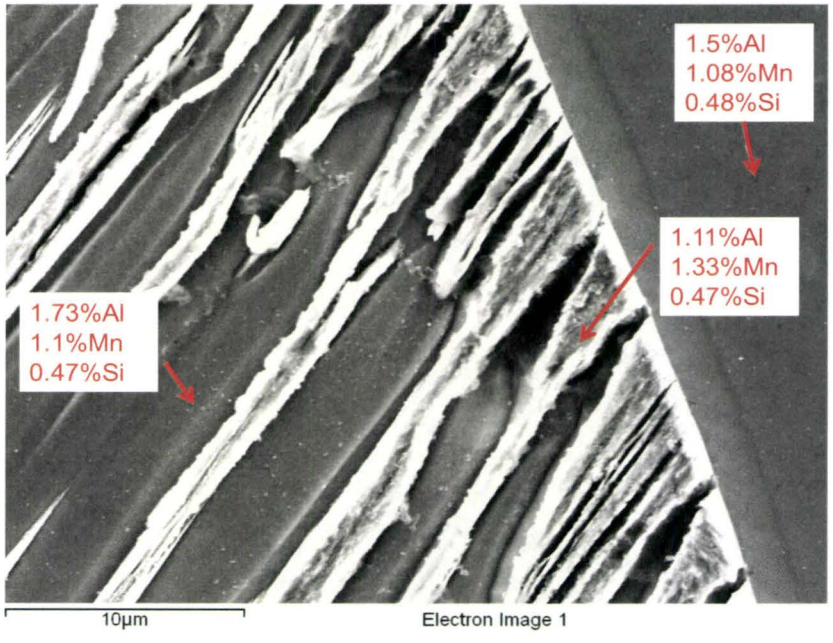

Figure 4-23 EDS determined Al, Mn, and Si concentration in delta-ferrite and austenite of specimen reheated to delta region for 60 seconds, then cooling down with of 50°C/s to 850°C for 1800s

4.5.2 Effects of Cooling Rate

In order to investigate the phase transformation kinetics under non-isothermal cooling conditions, several specimens were heated into the delta region 1310°C for 60 seconds, then cooled down to 1125°C at different cooling rate of 50°C/, 2°C/s, and 0.5°C/s. After reaching 1125°C, the specimens were quenched to room temperature using a He jet (estimated cooling rate 30K/sec). The resulting microstructures are shown in Figure 4.26(a) 50°C/, (b) 2°C/s, and (c) 0.5°C/s respectively.

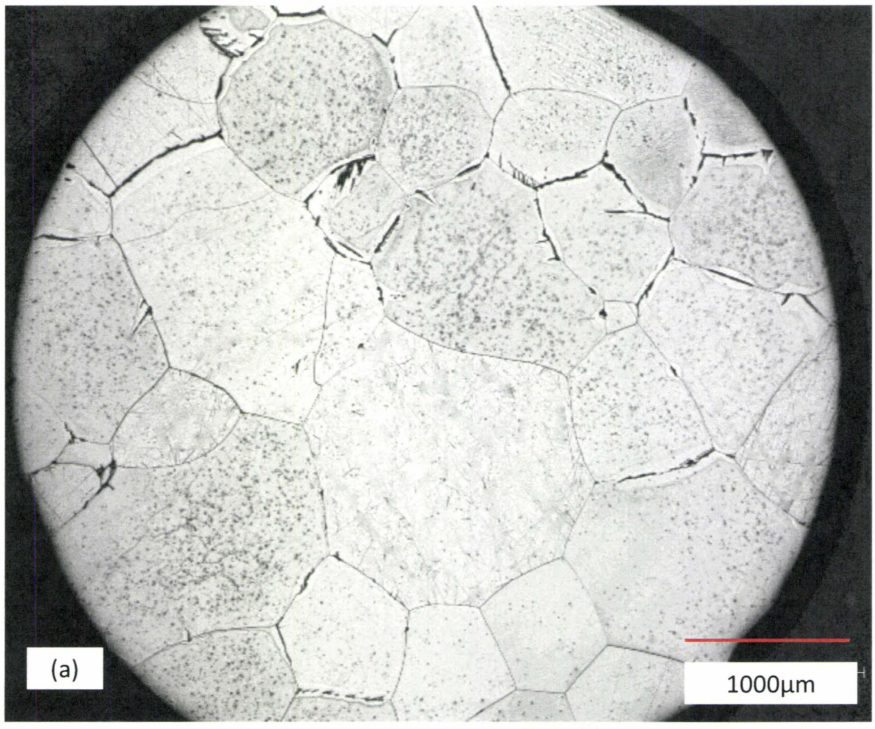

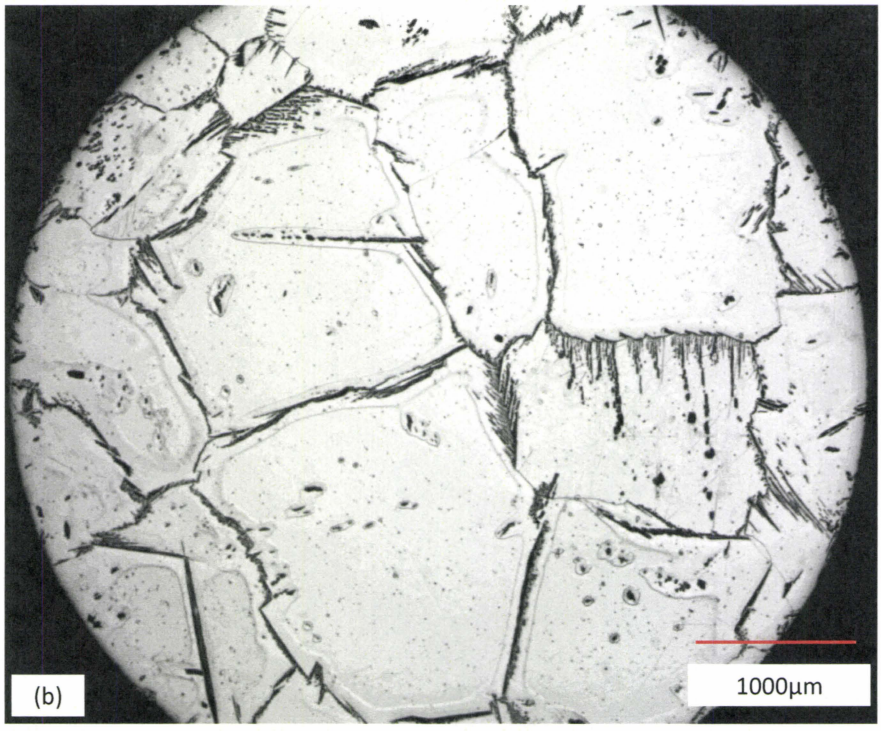

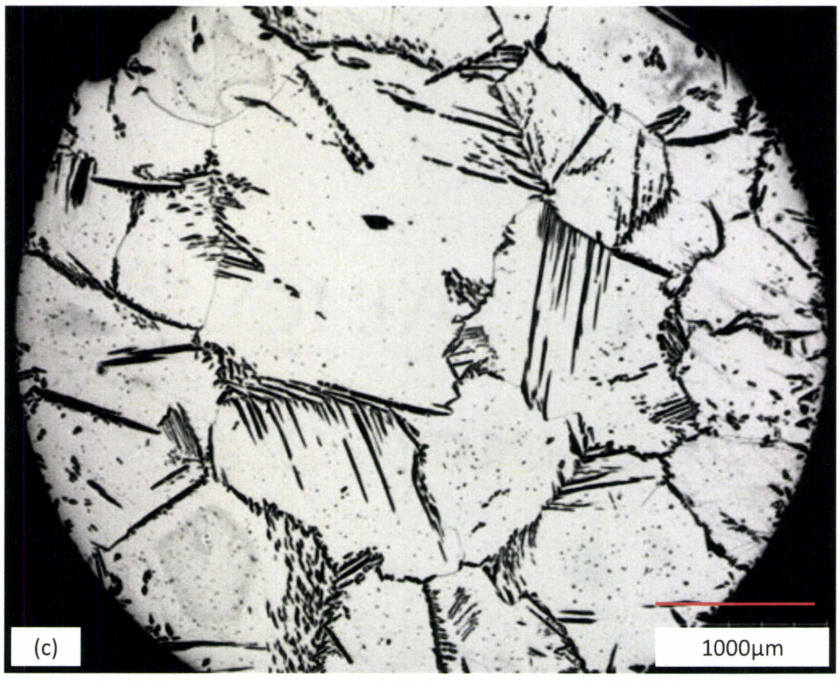

Figure 4-24 Microstructure evolution of different cooling rate (a) 50°C/s, (b) 2°C/s, and (c) 0.5°C/s

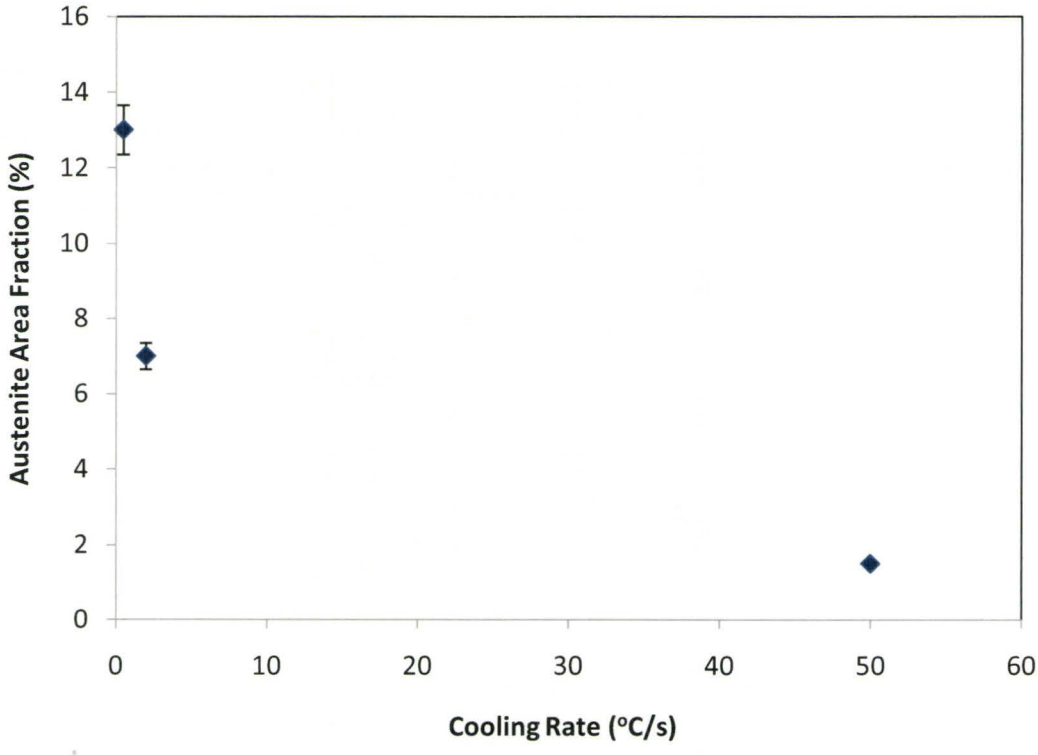

Figure 4-25 The relationship between austenite volume fraction and cooling rate

When the cooing rate is 50°C/s, the austenite volume fraction is about 1% which confirms that this cooling rate was a good choice for the isothermal experiments described in section 4.5.1 because minimal transformation is expected during the cooling step prior to isothermal holding. When the cooling rate was reduced to 2°C/s, the austenite volume fraction increased to 7%. Reducing the cooling rate to 0.5°C/s, resulted in an austenite volume fraction is 13%. The relation between austenite volume fraction and cooling rate is shown in Figure 4.25. It is clear that even for the slowest cooling rate (0.5°C/s) the volume fraction of austenite formed is well below the "equilibrium" value obtained after extended holding at 1125°C.

4.5.3 Effects of Deformation

Previous work in the literature indirectly showed that deformation can increase the austenite nucleation sites during the delta-ferrite to austenite phase transformation. This conclusion is confirmed by the microstructures shown in Figure 4-26. The specimens were reheated to 1310°C for 60 seconds, and cooled down to 1125°C at cooling rates of 50 and 0.5°C/sec. A compressive strain of 20% was applied at the onset of the transformation. In Figure 4.26 (a) and (d) the specimens were held at 1125°C for 15 seconds before quenching to room temperature (RT), while in Figures 4.26 (b) and (c) the specimen was quenched to room temperature as soon as it reached a temperature of 1125°C. The presence of fine ferrite grains within the original grains is clearly observed. Higher magnification SEM images (Figure 4.27) indicate that the boundaries of these grains are decorated by fine austenite precipitates.

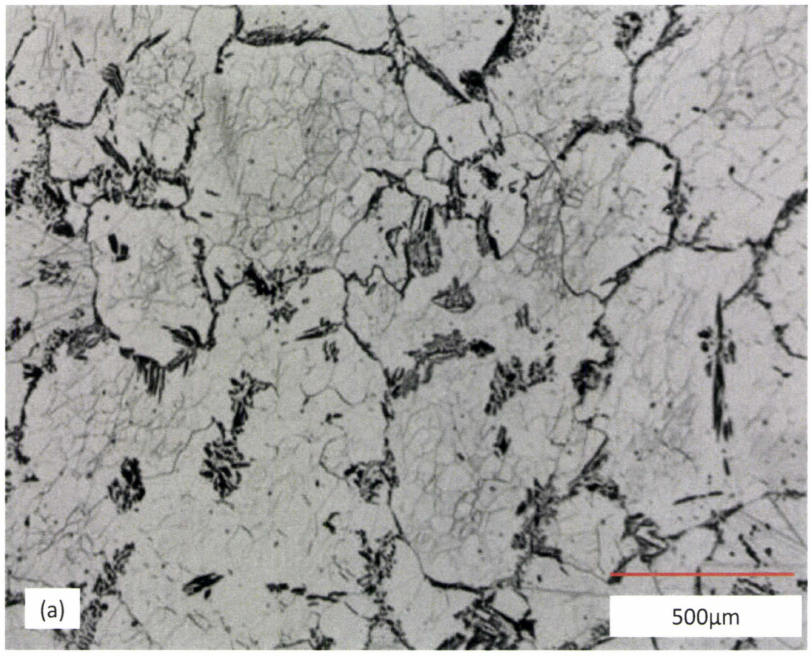

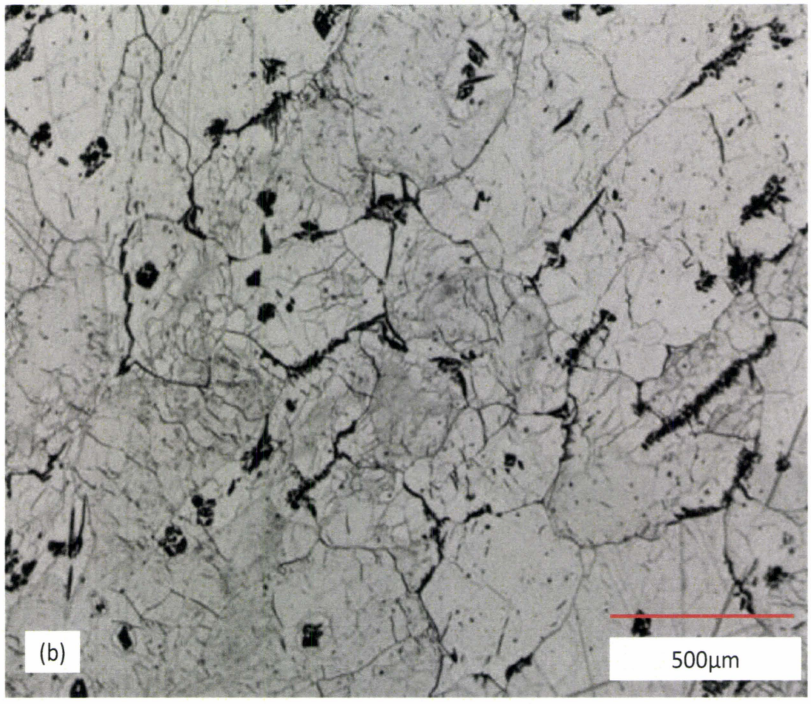
(b)
500µm

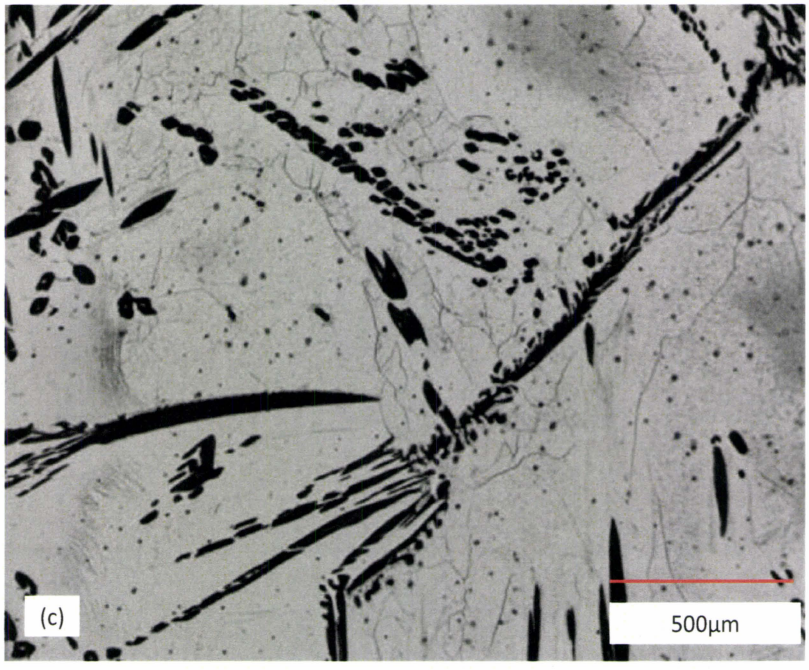
(c)
500µm

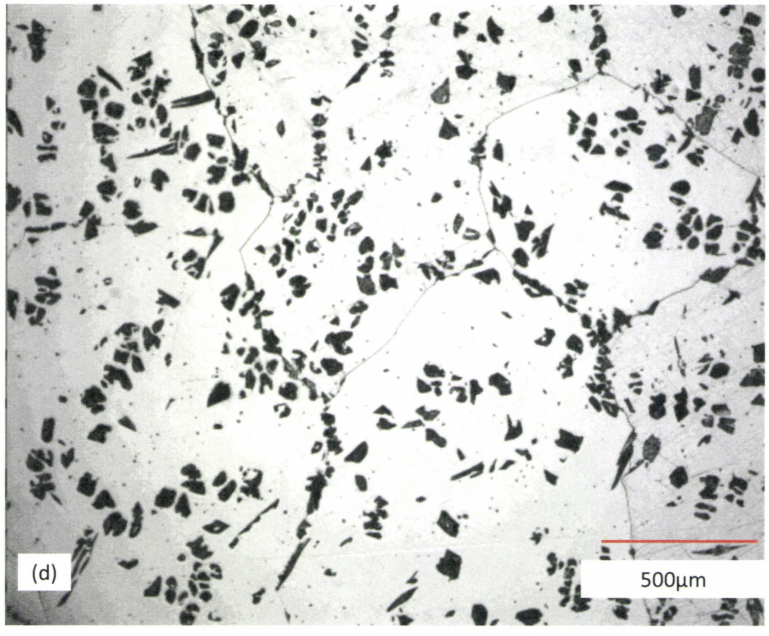

Figure 4-26 microstructures evolution of 20% deformation rate with different cooling rate and holding time at 11250°C: (a) 50°C/s to 1125°C holding for 15 seconds, then quenched to RT, (b) 50°C/s to 1125°C, directly quenched to RT, (c) 0.5°C/s to 1125°C, then directly quenched to RT, and (d) 0.5°C/s to 1125°C, holding for 15seconds then directly quenched to RT.

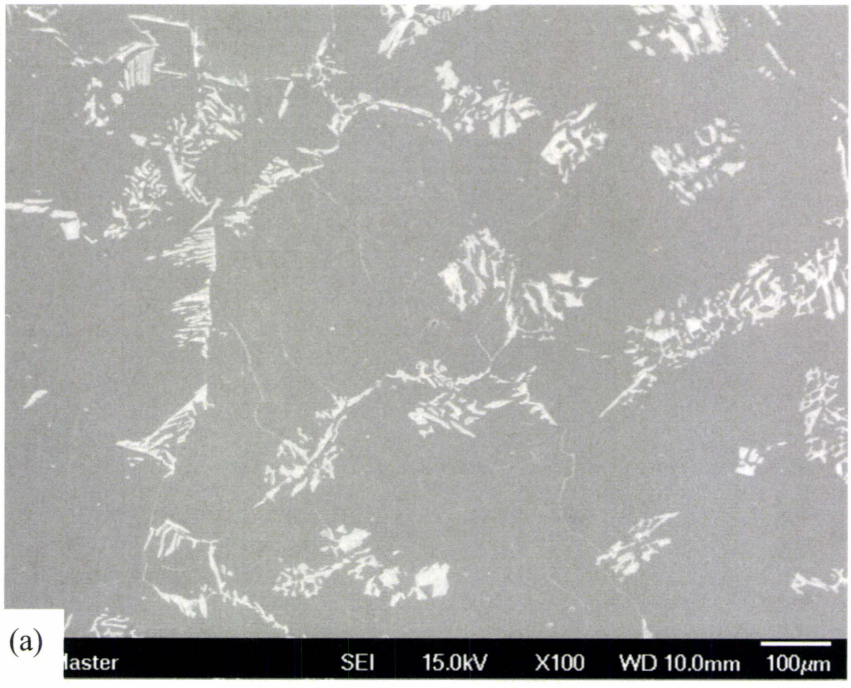

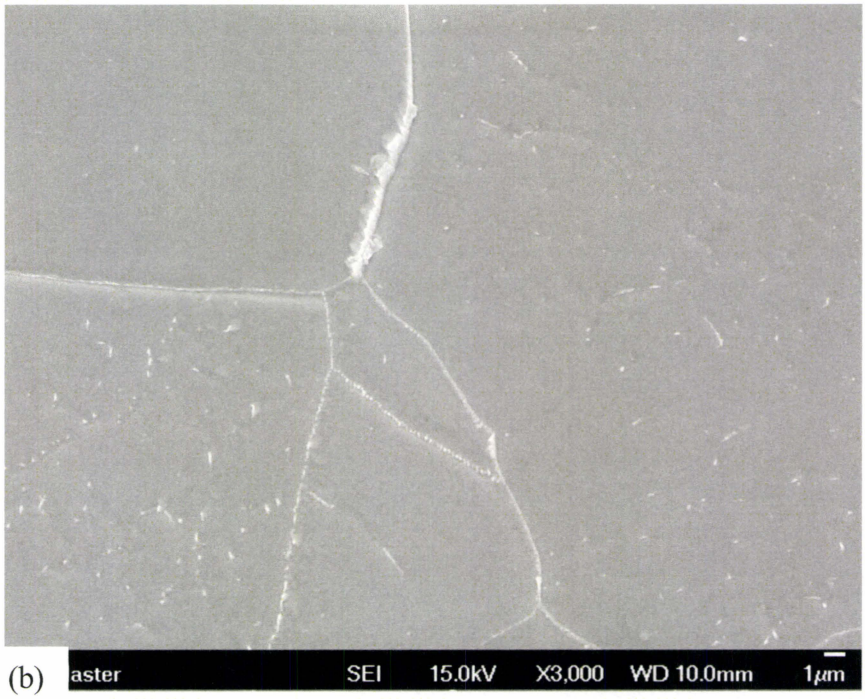

Figure 4-27 Austenite nucleates (a) along the original and (b) new recrystalized delta grain boundaries

Chapter 5 Discussion

In this chapter, discussions on delta-ferrite grain growth and austenite grain growth will be presented in section 5.1-5.2. Austenite particle coarsening mechanism and delta grain growth in the delta-ferrite/austenite duplex microstructure will be discussed in section 5.3. Discussion on the delta-ferrite to austenite phase transformation will be described in section 5.4. Application to the design of improved TSCDR process will be presented in section 5.5.

5.1 Grain Growth in Delta-Ferrite

As discussed in section 3.2, directly observation of delta grain growth in microalloyed steel is impossible. In order to facilitate the study of grain growth in delta-ferrite, a model alloy with 2.5 wt% Al was prepared in order to stabilize delta-ferrite down to room temperature. Thermodynamic calculations using the TCFe2 database of ThermoCalc indicate that at the temperature of interest Al is in solid solution and as such it would not contribute any additional precipitate pinning compared to the Al-free alloy(Smith 1948). At the same time it is unlikely that Al would exert strong solute drag at the migrating grain boundaries at the very high temperatures being investigated in this work(Cahn 1962). For these reasons, it is argued that the addition of Al should not significantly modify the grain growth kinetics of the model alloy compared to Al-free steel. It should also be pointed out that, unlike conventional APIX60

steels, the model alloy does not contain Nb or Ti additions. Once again it is argued that this difference is not significant, because the solute-drag effect of these elements was shown to be negligible(Zurob et al. 2002) at temperatures above 1200°C. Furthermore, the Zener pinning effect is small, since the volume fraction of microalloyed precipitates in the delta region in conventional steels is very small and any undissolved particles would rapidly coarsen to a size (and number density) that would render them ineffective at pinning the boundary.

According to Turnbull (Turnbull 1951; Burke and Turnbull 1952) reaction rate theory, which neglected the interaction of solute with grain boundary and the particle pinning effects, the grain growth rate can be assumed to be proportional to the driving force due to the curvature of the grains:

$$\frac{d\bar{R}}{dt} = M\frac{2\gamma_{gb}}{\bar{R}} \qquad \text{--- (5.1)}$$

However, in order to model the grain growth kinetics including the effect of heating time, a non-isothermal grain growth model should be used:

$$\frac{d\bar{R}}{dt} = M(T)\frac{2\gamma_{gb}}{R} \qquad \text{--- (5.2)}$$

In this equation, $\bar{R}$ is the average radius of the grain, *M (T)* is the grain boundary mobility and γ_{gb} is the grain boundary energy which is assumed to be constant, 0.375J/m^2(Humphreys and Hatherly 2004). The grain boundary mobility is a function of time, *t*, in order to capture the change in temperature during heating. Integration of Eq. (5.2) leads to:

$$\bar{R}^2 = \bar{R}_o^2 + 4\gamma_{gb}\int_o^t M(T)dt \qquad \text{--- (5.3)}$$

where, $\bar{R}_o$, is the initial grain radius. In the present experiment, the initial grain size was 13.5μm as shown in Figure 3.6 (b). As mentioned in section 3.2.1, one batch of samples had an initial grain size of $\bar{R}_o$ =91.5μm. This batch was used for grain growth experiments at 1000 and 1100°C and as such $\bar{R}_o$ is 91.5 μm in these two cases.

The Turnbull mobility(Turnbull 1951) was used as an initial estimate of the grain-boundary mobility:

$$M_{pure} = \frac{wD_{GB}V_m}{b^2\Re T} \qquad \text{--- (5.4)}$$

In this equation, D_{GB} is the grain boundary self-diffusion coefficient, V_m is the molar volume, b is the magnitude of the Burgers vector, T is the absolute temperature, w is the grain boundary thickness, and $\Re$ is the gas constant. In the delta-ferrite the burgers vector is of **b**=1/2[111] and b= $\sqrt{3}$ **a**/2, where **a** is the lattice parameter of delta-ferrite, 0.286nm. The molar volume, V_m=7.11cm^3. The activation energy for diffusion along the grain boundary was taken to be $Q_{GB} = 0.68Q$, where Q=256kJ/mole is the activation energy for bulk diffusion. Finally, w=*1nm*, D_{GBo} =$1.67\times10^{-4}m^3/s$ (Gladman 1997; Wilkinson 2000). The grain boundary mobility in this way overestimates the experimental grain growth kinetics. The best fit of the experimental data was obtained using a mobility which is 1/3 of the Turnbull estimate. This is

not surprising giving the fact that the Turnbull mobility does not take into account attachment kinetics and is therefore an overestimate of the actual mobility. Therefore, the delta grain mobility used in this work is:

$$M_\delta(T) = \frac{0.7075}{T(t)} \times \exp\left(\frac{-20995.43}{T(t)}\right) \qquad \text{--- (5.5)}$$

In order to evaluate the integral in equation (5.3), an expression for the temperature as a function of time is needed. This was obtained experimentally from the data recorded by the thermocouple attached to each specimen.

The results of this model are compared to the experimental data on delta grain growth at 1000°C, 1100°C, 1200°C, 1300°C and 1470°C shown in Figure 5.1 (a), (b), (c), (d) and (e) respectively. The dash line is the temperature profile during the heating process (secondary axis), the solid line is the model predicted grain diameter. The points represent experimental data. In general, excellent agreement is obtained between the experimental data and the model predictions. It is noted that the model overestimates the grain size at the longest times. This is believed to be due to the fact that at long times the grain size becomes comparable to the sample thickness (2.5mm) and the measured grain-growth kinetics no longer represents grain growth in the bulk. The fact that the data could be fitted with the present model, which does not include Zener pinning or solute drag, adds further support to the argument that the addition of the Al does not significantly change the rate of grain growth in delta-ferrite; the role of Al is simply to stabilize delta-ferrite down to room temperature. The results obtained here, are therefore believed to be applicable to delta grain growth in APIX60 steels.

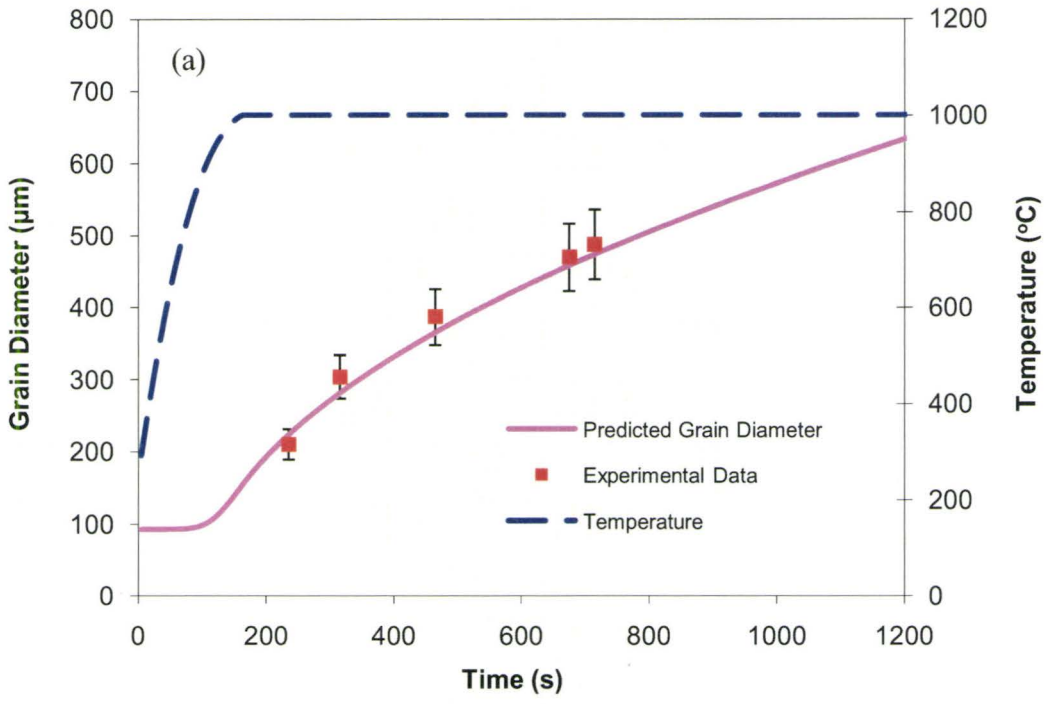
(a)
Grain Diameter (µm)
Temperature (°C)
Time (s)
Predicted Grain Diameter
Experimental Data
Temperature
0
100
200
300
400
500
600
700
800
0
200
400
600
800
1000
1200

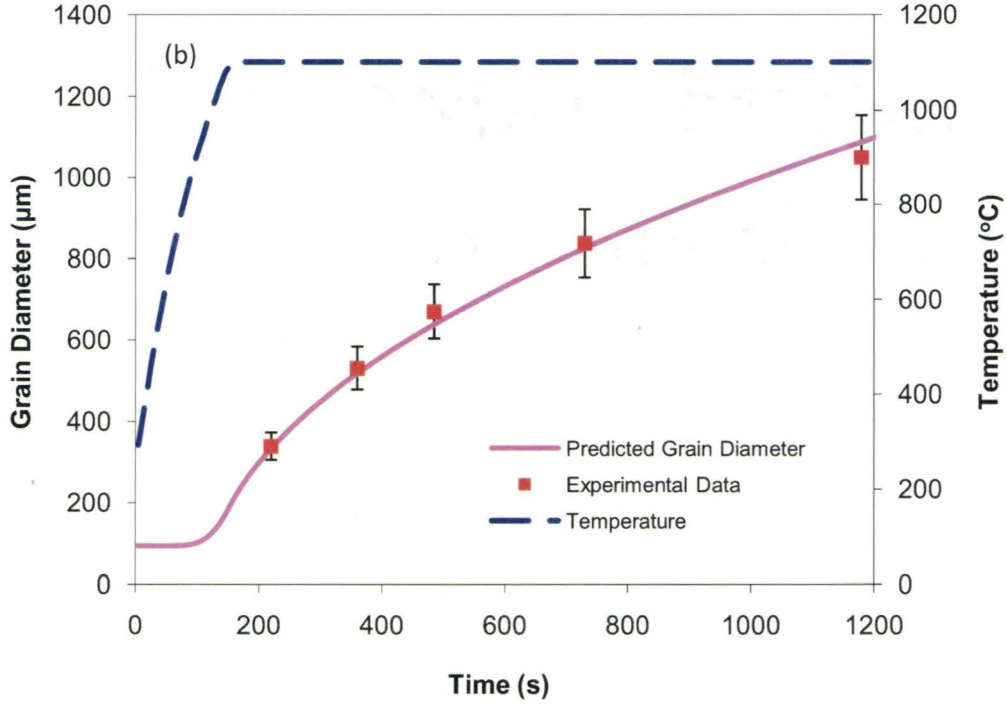
(b)
Grain Diameter (µm)
Temperature (°C)
Time (s)
Predicted Grain Diameter
Experimental Data
Temperature
0
200
400
600
800
1000
1200
1400
0
200
400
600
800
1000
1200

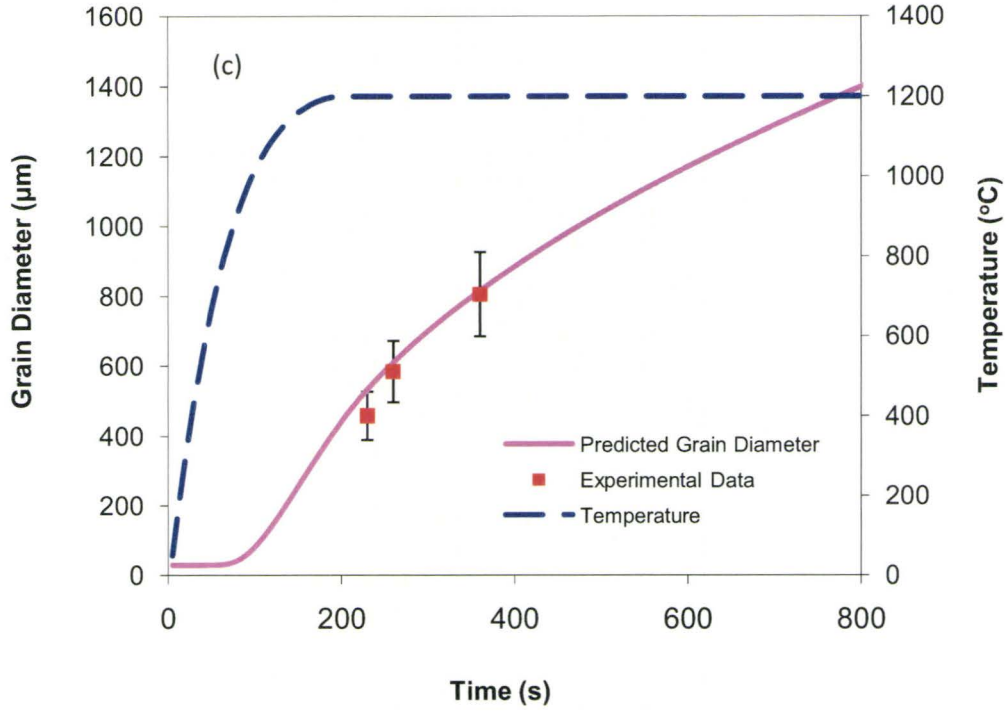
(c)
Grain Diameter (µm)
Temperature (°C)
Time (s)
Predicted Grain Diameter
Experimental Data
Temperature
0
200
400
600
800
1000
1200
1400
1600

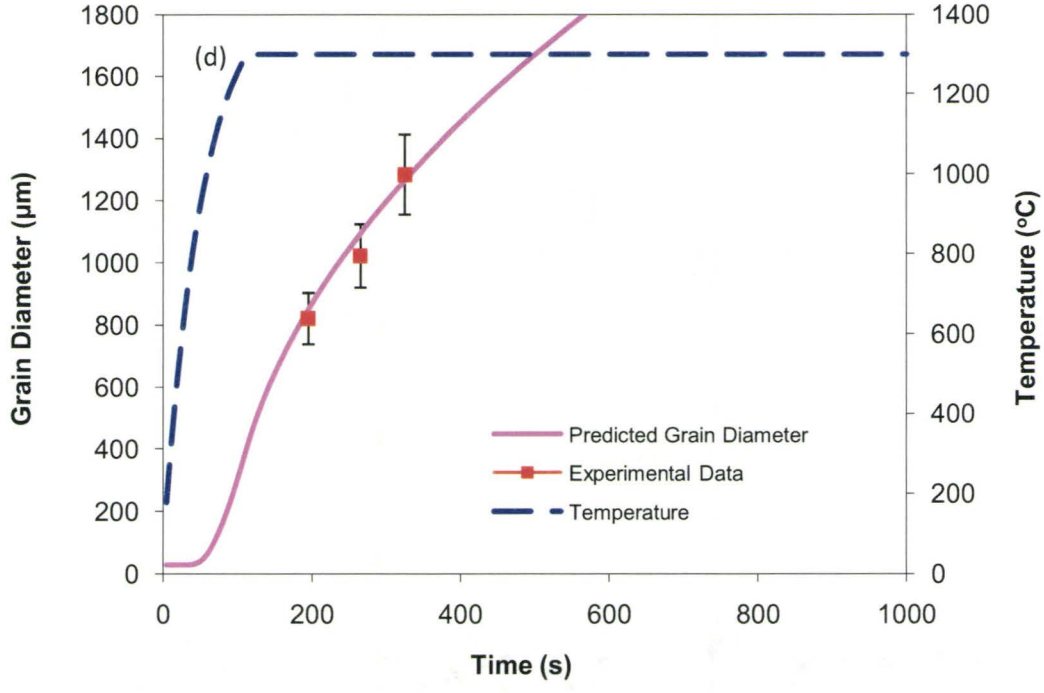
(d)
Grain Diameter (µm)
Temperature (°C)
Time (s)
Predicted Grain Diameter
Experimental Data
Temperature
0
200
400
600
800
1000
1200
1400
1600
1800

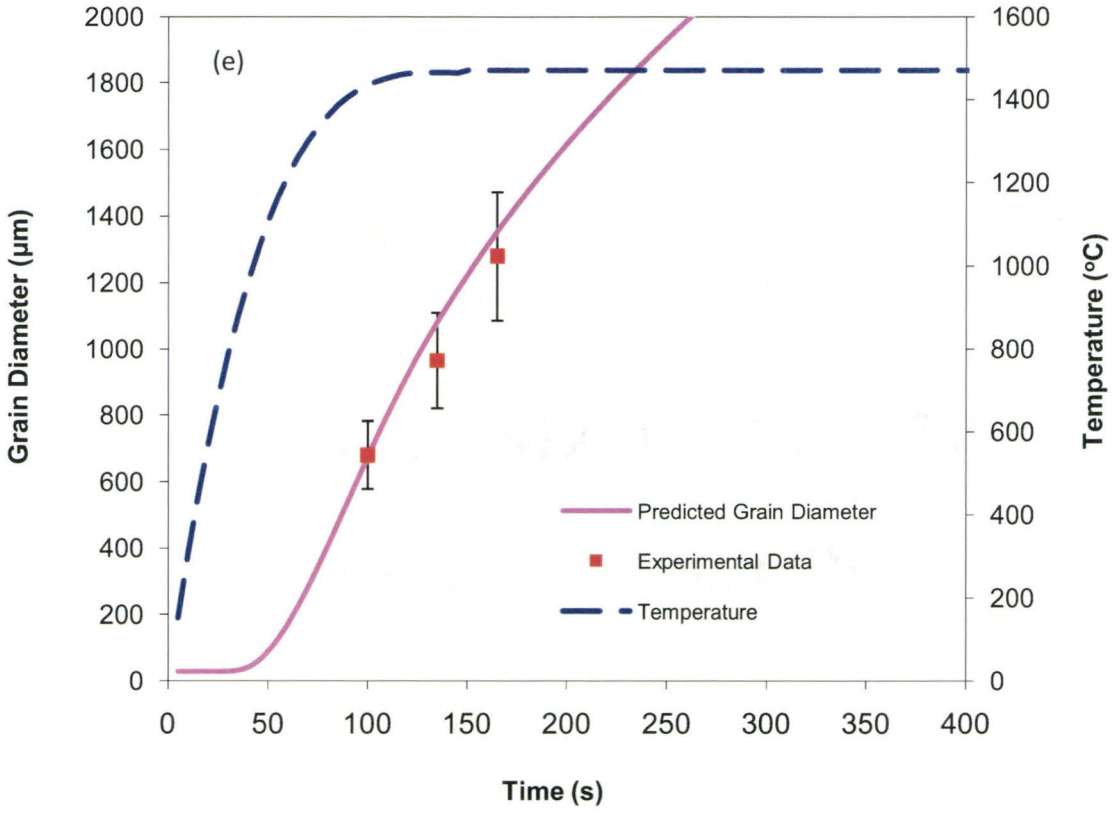

Figure 5-1 Modeling prediction of delta grain growth and experimental data at (a) 1000°C, (b) 1100°C, (c) 1200°C, (d) 1300°C, and (e) 1470°C

5.2 Grain Growth in Austenite

In the investigated temperature range, the Ti-Nb free model alloy shows normal grain growth behavior as shown in Figure 4.5, 4.6 and 4.7. In the absence of precipitates pinning and neglecting the solute drag effects; austenite grain growth at 1300 and 1400°C could be modeled using the non-isothermal grain growth model described in section 5.1.1, provided that the initial austenite grain size is known. The challenge here is that the alloy consists of a

mixture of ferrite and pearlite at room temperature. Austenite will be formed during the heating process. In order to bypass this complication, the integral in equation (5.3) was evaluated from t_1 to t, where t_1 is the time at which the temperature has reached 900°C. Consequently, the initial radius, r_0, should now be the radius when the temperature is 900°C, which was taken to be 40 μm as shown in Figure 3.8. Finally, it was necessary to estimate the mobility of the austenite grain boundaries. For austenite **b**=1/2<110>, and therefore, b=$\sqrt{2}$ a/2, where a is 0.357nm. The molar volume, V_m is 6.85cm^3, the bulk diffusion activation energy in FCC Q=284kJ/mole, and that of grain boundary diffusion is: $Q_{GB} = 0.61Q$. $w=1nm$, *and* $D_{GBo} = 0.49\times10^{-4}m^3/s$ (Gladman 1997; Wilkinson 2000). Once again, the Turnbull mobility (Turnbull 1951) will lead to an overestimation of the grain growth kinetics. The best fit of the experimental data was obtained with a mobility which is 0.6 times the Turnbull estimate:

$$M_\gamma(T) = \frac{0.1920}{T(t)} \times \exp\left(\frac{-20837.14}{T(t)}\right) \qquad \text{--- (5.6)}$$

The modeling results at 1300°C and 1400°C are shown in Figure 5.2 (a) and (b), and appear to be in good agreement with the experimental data. This confirms, once again, that the grain growth model based on curvature can capture grain growth kinetics at high temperature when solute drag and Zener pinning are insignificant.

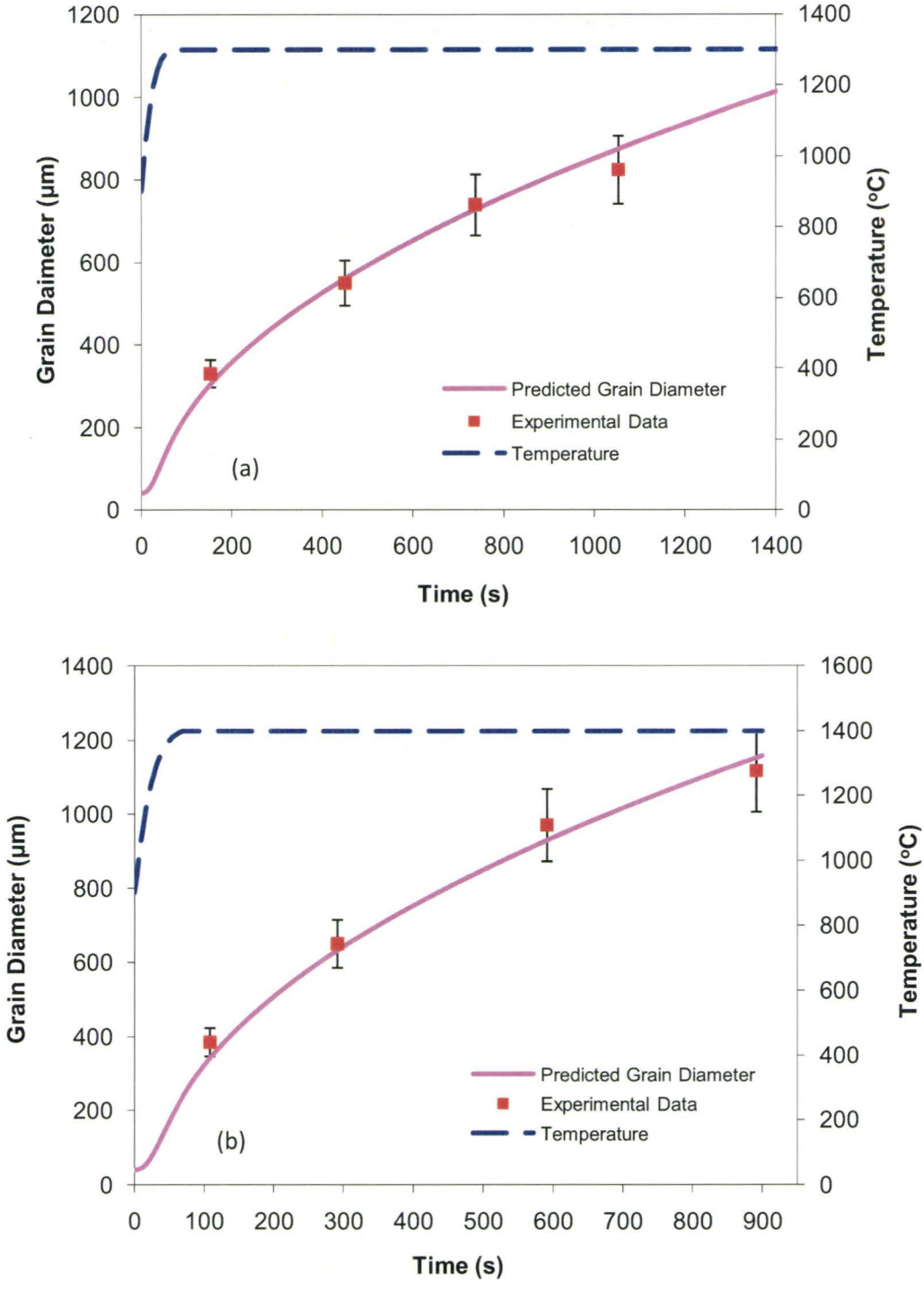

Figure 5-2 Modeling prediction of austenite grain growth and experimental data at (a) 1300 °C and (b) at 1400°C

5.3 Coarsening Behavior of Delta-ferrite/Austenite Duplex Microstructure

In the Fe-1.5%Al model alloy, austenite phase particles can be used to pin the grain growth of delta-ferrite over a wide temperature range. Experimental results suggest that delta grain growth is suppressed up to 1305°C. This delta-ferrite/austenite duplex microstructure could provide a novel method to pin grain growth at higher temperature in the TSCDR process. This section consists of two parts, the first deals with the austenite particle coarsening kinetics, while the second deals with delta grain growth behavior.

5.3.1 Austenite particle Coarsening Mechanism

The microstructure evolution in section 4.4 shows marked changes in the austenite phase particle size during high temperature holding. The increase of the average austenite phase particles size by dissolution of the smaller particles and growth of the larger ones is often referred as Ostwald ripening. The theory of Ostwald ripening has been developed by Greenwood(Greenwood 1956), Lifshitz and Slyozov(Lifshitz and Slyozov 1961), and Wagner(Wagner 1961), and is often referred to as LSW theory. These approaches relied on a diffusion analysis in which the rate of change of the diameter of each particle is independent of the position of other particles. The LSW theory corresponds to a zero volume fraction approximation which obviously is not valid for large volume fractions of second phase particles. Asimov(Asimow 1963) and Ardell (Ardell 1972) were the first to incorporate the

second phase volume fraction into the frame work of the LSW theory leading to the so-called MLSW theory. The Ardell(Ardell 1972) assumed that the diffusion of the solute to a growing particle will depend on a distance characteristic of the spatial distribution of particles in the matrix; Asimov(Asimow 1963) model modified the coarsening theory by modifying the diffusion geometry, but he failed to perform the statistical averaging of the diffusion interactions between particles that is necessary for a satisfactory solution to this problem. Brailsford-Wynblatt Model(Brailsford and Wynblatt 1979) overcame this problem by using chemical rate theory to perform the statistical averaging. Voorhees and Glicksman model(Voorhees and Glicksman 1984a; Voorhees and Glicksman 1984b) approached the problem of multi-particle diffusion by using computer simulation techniques. Marquese and Ross model(Marqusee and Ross 1984) used a statistical method to model coarsening. These models all underestimate the effect of the particle volume fraction. Davies, Nash et al model(Davies et al. 1980) investigated the effect of coalescence or encounters between particles and also shows less effects of volume fraction. The principal predictions of LSW models were the linear increase of the cube of average particle size with time, and the self-similarity of the particle size distribution.

The variation of average austenite phase particle radius with time was plotted in Figure 5.3(a) 850°C, (b) 1060°C, (c) 1200°C, (d) 1280°C and (e) 1295°C. In these plots the x-axis is $(r^n - r_o^n)$, where r_o is the initial average austenite particle radius at time t_o, r is the average particle size at time t. At 850°C, the relationship between $(r^n - r_o^n)$ and $(t - t_o)$ is close to linearity for n=4. Similar analysis revealed that a fit based on n=4 are best fit for 1060°C. On

the other hand, both n=3 and n=4 give equally good fits at 1200°C. However, when the reheating temperature is above 1200°C, the best fit is obtained with n=3. These results can be interpreted in terms of volume diffusion control (n=3) at high temperature and grin boundary control (n=4) at lower temperature.

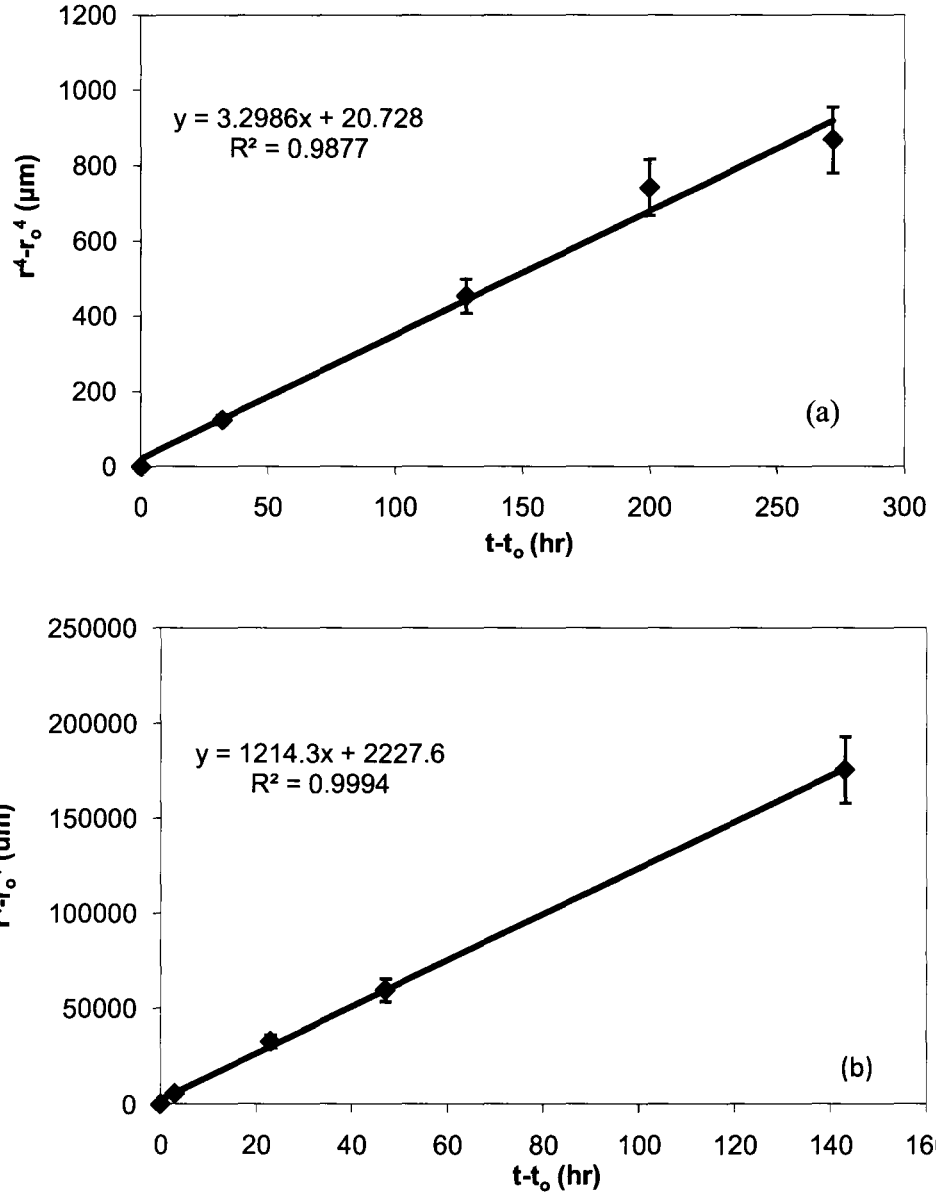

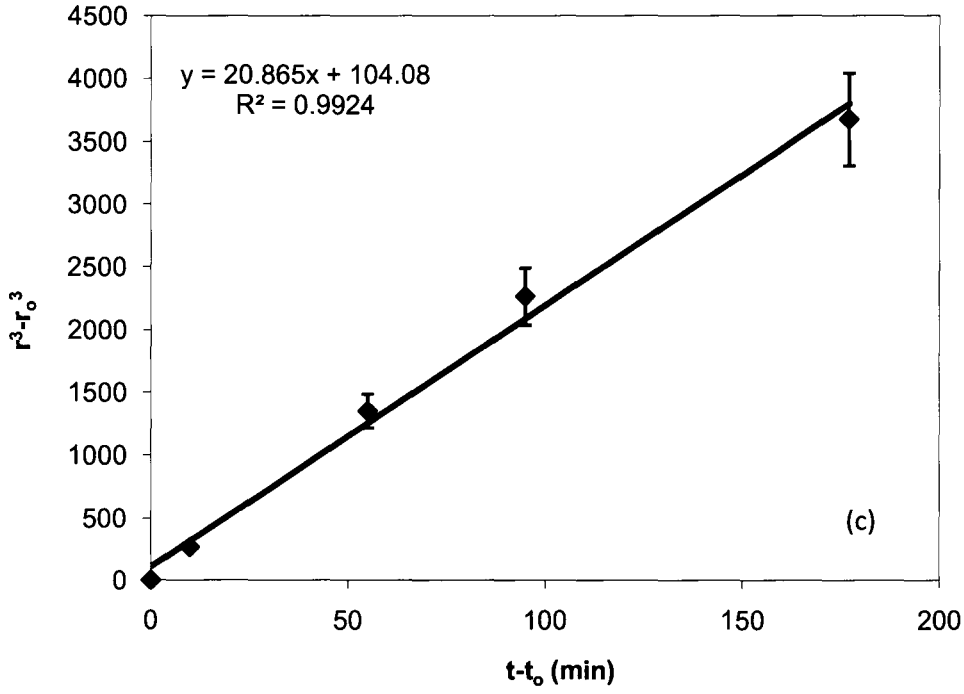
y = 20.865x + 104.08
R² = 0.9924
(c)
r³-r₀³
t-t₀ (min)
4500
4000
3500
3000
2500
2000
1500
1000
500
0
0
50
100
150
200

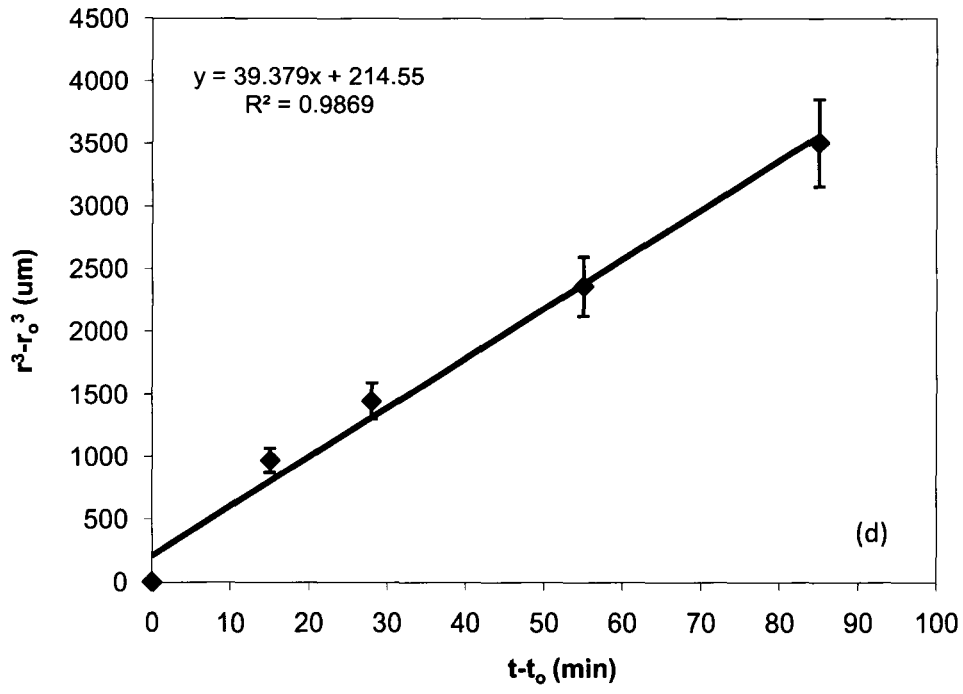
y = 39.379x + 214.55
R² = 0.9869
(d)
r³-r₀³ (um)
t-t₀ (min)
4500
4000
3500
3000
2500
2000
1500
1000
500
0
0
10
20
30
40
50
60
70
80
90
100

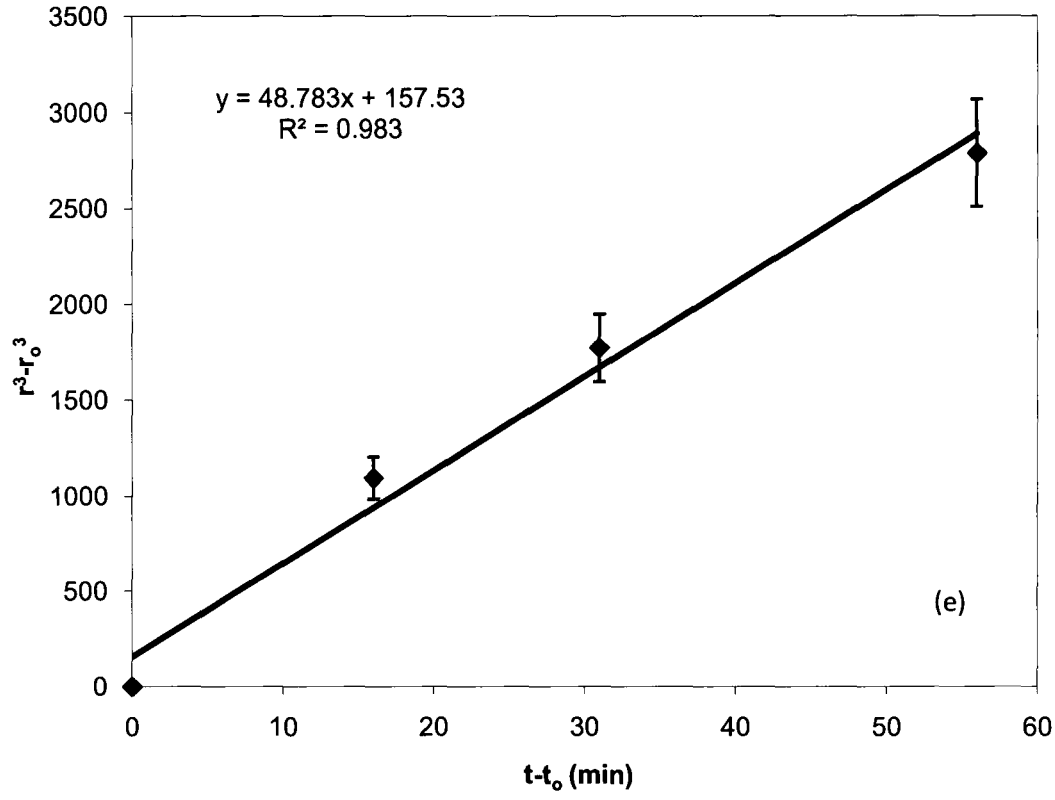

Figure 5-3 Plots of (r^n-r_o^n) vs.(t-t_o) for different heat treatment (a) 850°C, (b) 1060°C, (c) 1200°C, (d) 1280°C, and (e) at 12950°C

5.3.1.1 Bulk Diffusion- Rate Controlling Step:

As shown in Figure 4.12, 4.13, 4.14 and 4.15, the austenite particles are mostly distributed at the delta-ferrite grain boundaries. In order to understand the mechanism controlling the coarsening process a sketch of the key steps in the austenite particle coarsening process is shown in Figure 5.4. Thermodynamic calculations using the TCFe2 database of ThermoCalc indicate that Mn and C partition to the austenite phase, Al partitions to the delta-ferrite matrix, and Si has essentially the same concentration in both austenite and delta-ferrite.

If the growth of larger austenite phase particles at the expanse of the smaller austenite particles does not create a vacancy concentration higher than the equilibrium vacancy concentration, then the austenite particles growth process will involve the following steps: atoms of Mn and C in the shrinking particles jump across the austenite-delta boundary and diffuse to the delta-ferrite matrix near the growing austenite particle. Atoms of Al in the delta matrix near the growing austenite particles diffuse toward the shrinking particle and jump across the delta-austenite boundary of shrinking particle. The delta-ferrite matrix adjacent to the growing austenite particle is converted to austenite phase and the part of the shrinking austenite particle near delta-austenite interface is converted to delta phase, resulting in the movement of interfaces as shown in Figure 5.4

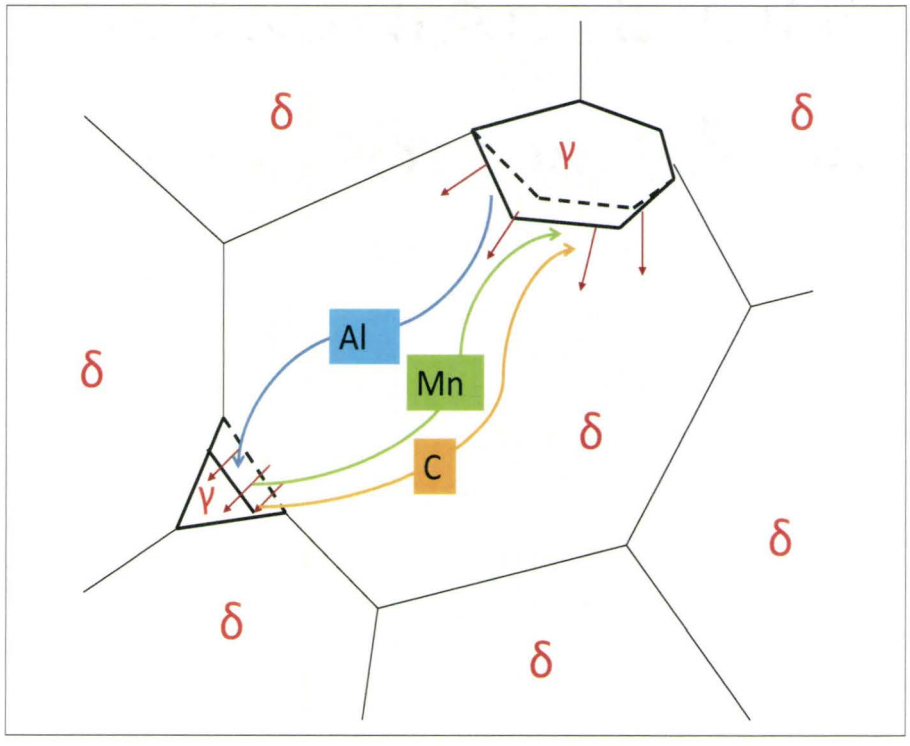

Figure 5-4 Schematic of austenite phase particle growth process

When heat treatment temperature is above 1200°C, the exponent n=3, which suggested that austenite phase particle coarsening was controlled by bulk diffusion through the delta-ferrite matrix. According to LSW theory(Greenwood 1956; Lifshitz and Slyozov 1961; Wagner 1961):

$$r_\gamma^3 - r_{\gamma o}^3 = \frac{8D\sigma_{\delta\gamma}N_\delta V_m t}{9RT} \qquad \text{--- (5.7)}$$

where r_γ is the austenite particle radius at time t, $r_{\gamma o}$ is the initial austenite particle radius ($t=0$), D is the rate limiting solute bulk diffusivity in the delta-ferrite matrix, $\sigma_{\delta\gamma}$ is the austenite/delta-ferrite interfacial energy, N_δ is the solute molar fraction in the delta-ferrite and V_m is the molar volume.

Taking the effect of second phase volume fraction into the frame work of the LSW theory, and considering the effect of non-limiting solid solution the particle coarsening rate in a two-phase concentrated alloy is given by Martin et al(Martin et al. 1997):

$$r_\gamma^3 - r_{\gamma o}^3 = Kt \qquad \text{--- (5.8a)}$$

where

$$K = \frac{8f(F_v)D\sigma_{\delta\gamma}N_\delta(1-N_\delta)V_m}{9RT(N_\gamma - N_\delta)^2\left[1+\partial \ln r / \partial \ln N_\delta\right]} \qquad \text{--- (5.8b)}$$

In this equation, $f(F_v)$ is a function of the particle volume fraction, N_γ is the solute molar fraction in austenite, $\varepsilon = 1 + (\partial \ln r / \partial \ln N_\alpha)$ is referred to as Darken correction factor for non-ideality. The delta-ferrite/austenite interface is incoherent, and a reasonable value for $\sigma_{\delta\gamma}$ is 0.56 Jm^{-2}(Martin et al. 1997). The molar volume, V_m, is 7.11cm^3. The values of the equilibrium compositions of the austenite and delta phases were determined by Thermo-Calc using TCFE2 database and double checked by using the Energy Dispersive X-ray analysis. The measured concentrations were in agreement with the equilibrium values suggesting that full partitioning of the substitutional elements is taking place. The equilibrium composition of austenite and delta phase at different temperature calculated by Thermo-Calc is shown in Table 5-1.

Table 5-1 Equilibrium composition of austenite and delta-ferrite at different temperature

Temperature	C_{Al}^{Delta}	C_{Mn}^{Delta}	$C_{Al}^{Austenite}$	$C_{Mn}^{Austenite}$
1305°C	0.02955	0.00967	0.02212	0.01248
1295°C	0.02995	0.00980	0.02235	0.01238
1280°C	0.030519	0.00961	0.02264	0.01225
1200°C	0.032732	0.00890	0.02340	0.01195

The diffusion coefficients of aluminum and manganese in the delta-ferrite matrix as obtained by MOB2 database of DICTRA are shown in Table 5.2. The Darken factor was also

calculated ($\partial G_\delta / \partial \ln N_\delta = RT(1+(\partial \ln r / \partial \ln N_\delta))$)(Cahn and Haasen 1983; Martin et al. 1997) using ThermoCalc TCFE2 database; the value of ε at different temperature is shown in Table 5.3.

Table 5-2 DICTRA calculated Al and Mn diffusion coefficient

Temperature (°C)	1305	1295	1280	1200
D_{Al} (m^2/s)	4.60465×10^{-12}	4.13138×10^{-12}	3.49821×10^{-12}	1.34269×10^{-12}
D_{Mn} (m^2/s)	3.49216×10^{-12}	3.15942×10^{-12}	2.71072×10^{-12}	1.12628×10^{-12}

Table 5-3 ThermoCalc calculated Darken Factor ε

Temperature (°C)	1305	1295	1280	1200
ε_{Al}	1.250	1.380	1.369	1.424
ε_{Mn}	0.764	0.976	1.119	1.092

In multicomponent systems with infinitely particle volume fractions, Morral and Purdy(Morral and Purdy 1994) derived the following expression for particle coarsening, taking into account the effect of cross-diffusion:

$$K = \frac{8\sigma_{\delta\gamma}V_m}{9\left(N_\gamma - N_\delta\right]\left[M\right]^{-1}\left[N_\gamma - N_\delta\right)} \qquad \text{--- (5.9)}$$

In this equation square brackets refer to a square (n-1) × (n-1) matrix, e.g. [A], while the round bracket followed by a square one, e.g. (A], represents a 1 × (n-1) row matrix. Using the same notation, an (n-1) ×1 column matrix is represented by a square bracket followed by a round one, e.g. [A). Thus $[M]^{-1}$ represents the inverse of the diffusion mobility matrix, $\left(N_\gamma - N_\delta\right]$ is a 1× (n-1) row concentration matrix, and $\left[N_\gamma - N_\delta\right)$ is a (n-1) × 1 column concentration matrix. It can be shown that when the cross-diffusion effects are negligible, the coarsening kinetics predicted by Equation (5.9) simplifies to:

$$\frac{1}{K_{Total}} = \frac{1}{K_{Al}} + \frac{1}{K_{Mn}} + \frac{1}{K_{Si}} + \frac{1}{K_C} \qquad \text{--- (5.10)}$$

where K_{Al}, K_{Mn} , K_{si}, and K_C capture the effect of individual solute elements:

$$K_C = \frac{8\sigma_{\delta\gamma} D_C N_C^{Delta}(1 - N_C^{Delta})}{9\Re T(N_C^{Austenite} - N_C^{Delta})^2 \left[1 + \partial \ln r \Big/ \partial \ln N_C^{Delta}\right]} \qquad \text{--- (5.11)}$$

$$K_{Si} = \frac{8\sigma_{\delta\gamma} D_{Si} N_{Si}^{Delta}(1 - N_{Si}^{Delta})}{9\Re T(N_{Si}^{Austenite} - N_{Si}^{Delta})^2 \left[1 + \partial \ln r \Big/ \partial \ln N_{Si}^{Delta}\right]} \qquad \text{--- (5.12)}$$

$$K_{Al} = \frac{8\sigma_{\delta\gamma} D_{Al} N_{Al}^{Delta}(1 - N_{Al}^{Delta})}{9\Re T(N_{Al}^{Austenite} - N_{Al}^{Delta})^2 \left[1 + \partial \ln r \Big/ \partial \ln N_{Al}^{Delta}\right]} \qquad \text{--- (5.13)}$$

$$K_{Mn} = \frac{8\sigma_{\delta\lambda} D_{Mn} N_{Mn}^{Delta}(1 - N_{Mn}^{Delta})}{9\Re T(N_{Mn}^{Austenite} - N_{Mn}^{Delta})^2 \left[1 + \partial \ln r / \partial \ln N_{Mn}^{Delta}\right]} \quad \text{--- (5.14)}$$

The same expression has applied by (Lee 1990; Lee et al. 1991a; Martin et al. 1997), In order to assess the applicability of this simplification to the present alloy system, the coarsening constant K, was evaluated from equation (5.9) using the full diffusion matrix and using equation (5.10), which only includes the diagonal diffusion coefficient. The results were found to be within 1.2% of each other. As a result, the simplified equation is used below as they offer a more transparent picture of what is controlling the coarsening kinetics.

Further simplifications are possible since carbon diffuses by interstitial mechanism $K_c \gg K_{Al}, K_{Mn}$, as a result, its contribution to K could be ignored. In addition, the concentration of Si in austenite and delta-ferrite are almost same, as a result, $K_{Si} \gg K_{Al}, K_{Mn}$. Therefore equation (5.14) can be simplified as:

$$\frac{1}{K_{Total}} = \frac{1}{K_{Al}} + \frac{1}{K_{Mn}} \quad \text{--- (5.15)}$$

Then, Equation (5.8b) can be written as

$$K = f(F_v) K_{Total} \quad \text{--- (5.16)}$$

To start, the volume correction fraction $f(F_v)$ is assumed to be 1 which is strictly true only for infinitely small particle volume fractions. The predicted austenite particle coarsening

rate constant based on Equation (5.16) and that measured experimentally are compared in Table 5.4. The ratio of the measured to the model predicted coarsening rate shows a strong dependence on the austenite particles fraction. This ratio varies from 2.03 at low volume fraction of 1.16% to a value of 4.72 at a volume fraction of 34.36%. These measured ratios could be used to back-calculate the volume correction factor $f(F_v)$. The results of this calculation are compared with the prediction of the models summarized by Jayanth and Nash(Jayanth and Nash 1989), and Martin et al(Martin et al. 1997) as shown in Figure 5.5. The measured ratio is between Ardell model and the Asimow and Brailsford-Wynblatt Model. From above calculation and discussion, it can be concluded that the discrepancy between the calculations (Equations 5.16) and the experiments are solely due to the volume fraction correction factor.

Table 5-4 Comparison of model predicted austenite particle coarsening rate constant and measured data

Temperature (°C)	Austenite Vol.%	Model Predicted $K(F_v=0)$ ($\mu m^3/min$)	Experimental Data $K(F_v)$($\mu m^3/min$)	$f(F_v)=K(F_v)/K(F_v=0)$
1305	1.16	24.442	49.804	2.03
1295	6.31	20.836	48.783	2.34
1280	13.17	14.838	39.379	2.65
1200	34.36	4.423	20.865	4.72

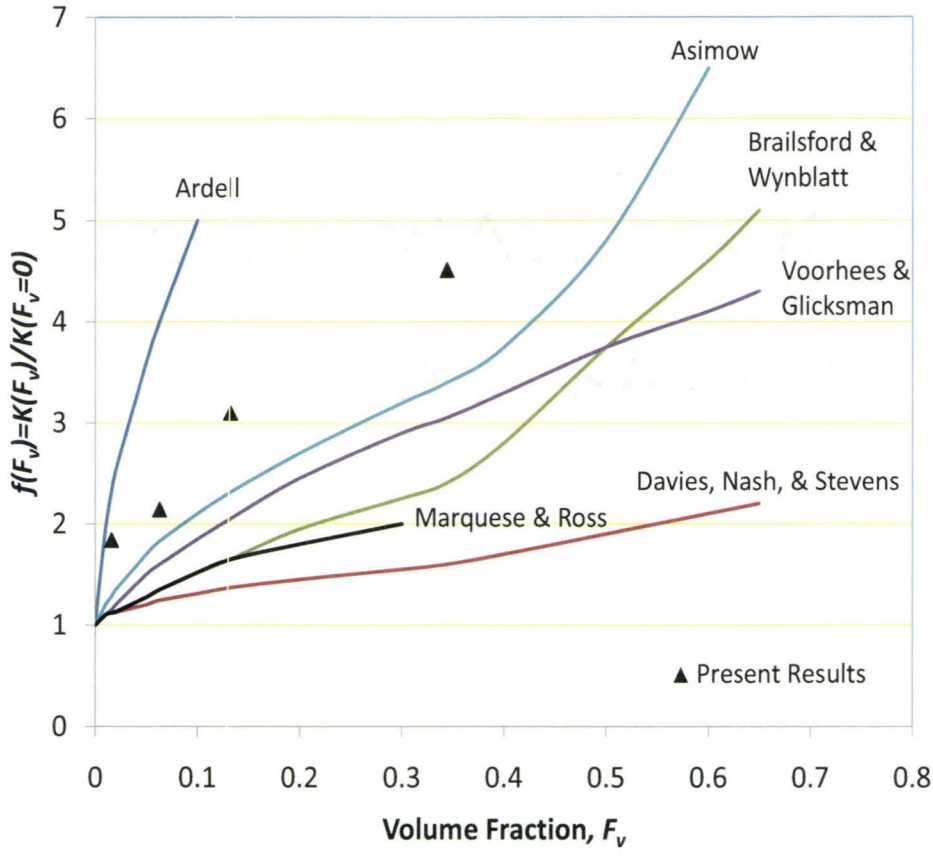

Figure 5-5 Comparison of model prediction of $f(F_v)$ and the present results

A particularly interesting trend in Figure 5.5 is that the general tendency for the various volume fraction effect models to either greatly underestimates or overestimate observed behavior and this provide a simpler method of testing different volume fraction effects models. The Ardell(Ardell 1972) assumed that the diffusion of the solute to a growing particle will depend on a distance characteristic of the spatial distribution of particles in the matrix; this localized interaction of the diffusion fields around particles will exaggerate the effect of volume fraction on coarsening rate. However, Brailsford-Wynblatt Model (terms as BWEM model)(Brailsford and Wynblatt 1979) and Voorhees and Glicksman model(Voorhees and

Glicksman 1984a; Voorhees and Glicksman 1984b) approached the problem by accounting for the short and long range influence on diffusion field of the source and sink behavior of a collection of particles. From Figure 5.5, it can be seen that the different models all agree that the particle coarsening rate increases with volume fraction but at a slower rate than suggested by Ardell.

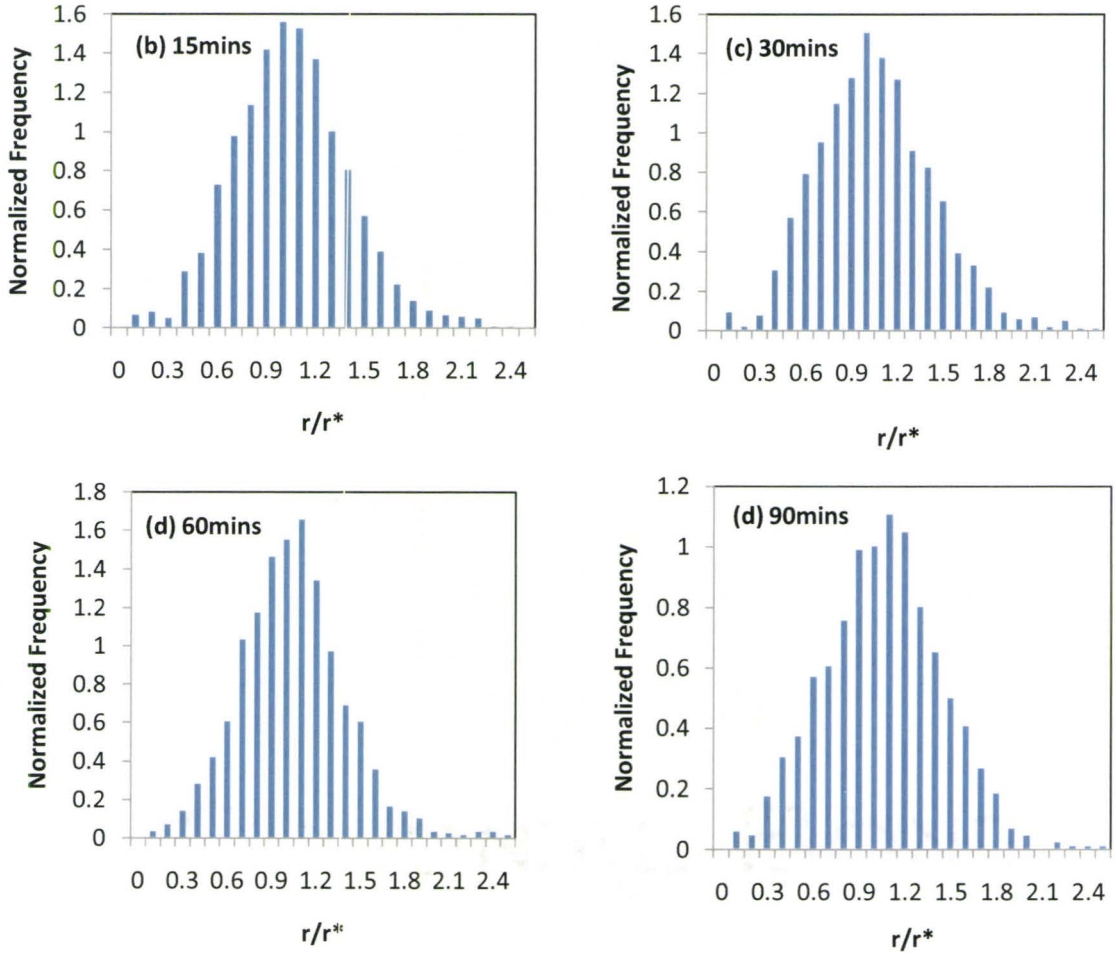

Figure 5-6 Austenite particle size distribution heat treated at 1280°C for (a)15min, (b) 30mins, (c) 60 mins and (d) 90mins

Quantitative optical metallography clearly showed that austenite particle volume fraction was constant during holding at a given reheating (Table 4.1). For example, when the materials is reheated to 1280°C, for a holding time of 5minutes, austenite particles area fraction is 9.6%±1.5%, after 15minutes, 9.3%±1.5%,, after 30 minutes, 9.4%±1.5%,, after 60 minutes, 10.6%±1.5%,, and 8.5%±1.5%, after 90 minutes. In addition, the normalized austenite particles size distribution was invariant with time (self-similar) as expected under coarsening conditions. An example of austenite particles size distribution at 1280°C for different time is shown in Figure 5.6. The plots revealed that the maximum value of r/r^* was about 2 and the peak in the distribution was approximately 1.4.

The measured and predicted particle size distribution is compared in Figure 5.7. When the particle volume faction is less than 6.5%, the measured size distributions are in good agreement with the LSW model (Figure 5.7 (b)): a maximum frequency of 1.93 is observed at r/r^* =1.1 when the particle volume fraction is 1.3%, a maximum frequency of 1.8 is seen at r/r^* =1.1 when the volume fraction is 2.6%, and when the volume fraction is 6.5%, a maximum frequency of 1.6 at r/r^* =1.1. Once the volume fraction is above 6.5%, the experimental data appears to be in better agreement with the Brailsford Wynblatt (BWEM) distribution (Figure 5.7 (c)). A maximum frequency 1.5 is observed at r/r^* =1.1 with volume fraction of 9%. With increasing volume fraction, the determination of the particle-size distribution became more difficult due to the increasing aspect ratio of the particles. However, the general trend is that the distribution is broader and more symmetrical as the volume fraction increases.

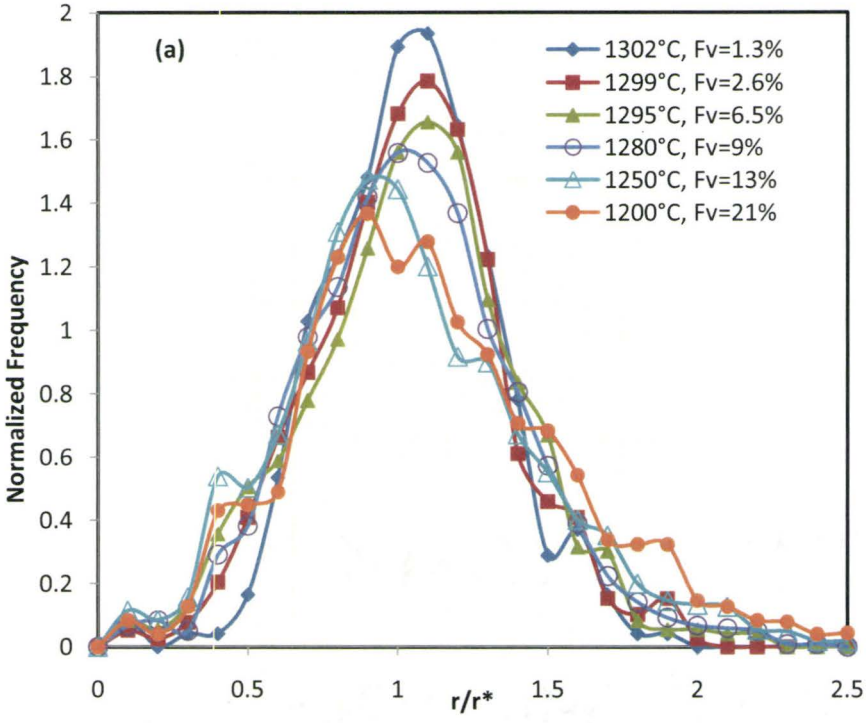
(a)
1302°C, Fv=1.3%
1299°C, Fv=2.6%
1295°C, Fv=6.5%
1280°C, Fv=9%
1250°C, Fv=13%
1200°C, Fv=21%
Normalized Frequency
r/r*
0
0.2
0.4
0.6
0.8
1
1.2
1.4
1.6
1.8
2
0.5
1.5
2.5

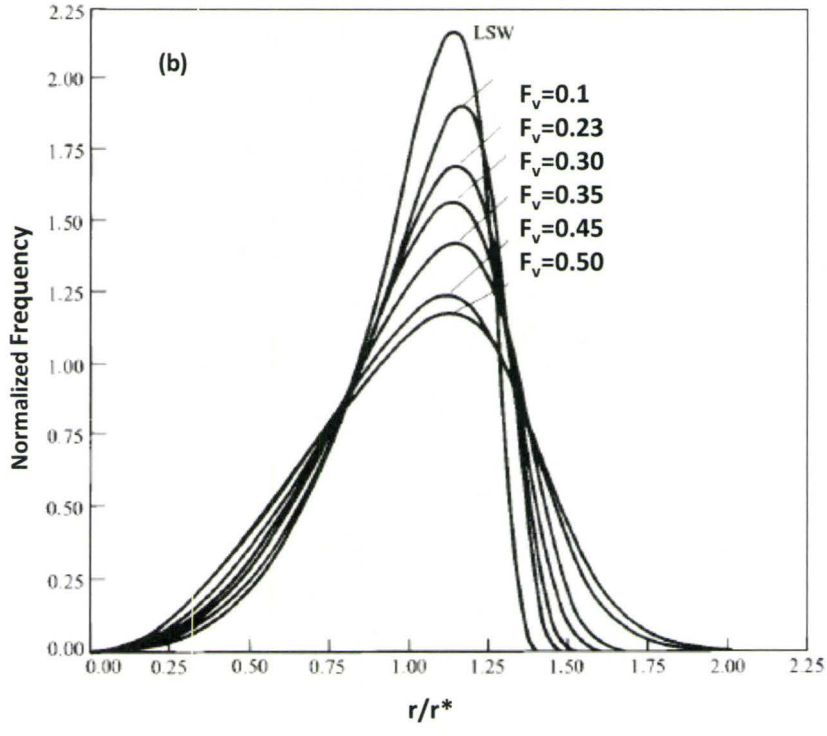
(b)
LSW
F_v=0.1
F_v=0.23
F_v=0.30
F_v=0.35
F_v=0.45
F_v=0.50
Normalized Frequency
r/r*
0.00
0.25
0.50
0.75
1.00
1.25
1.50
1.75
2.00
2.25

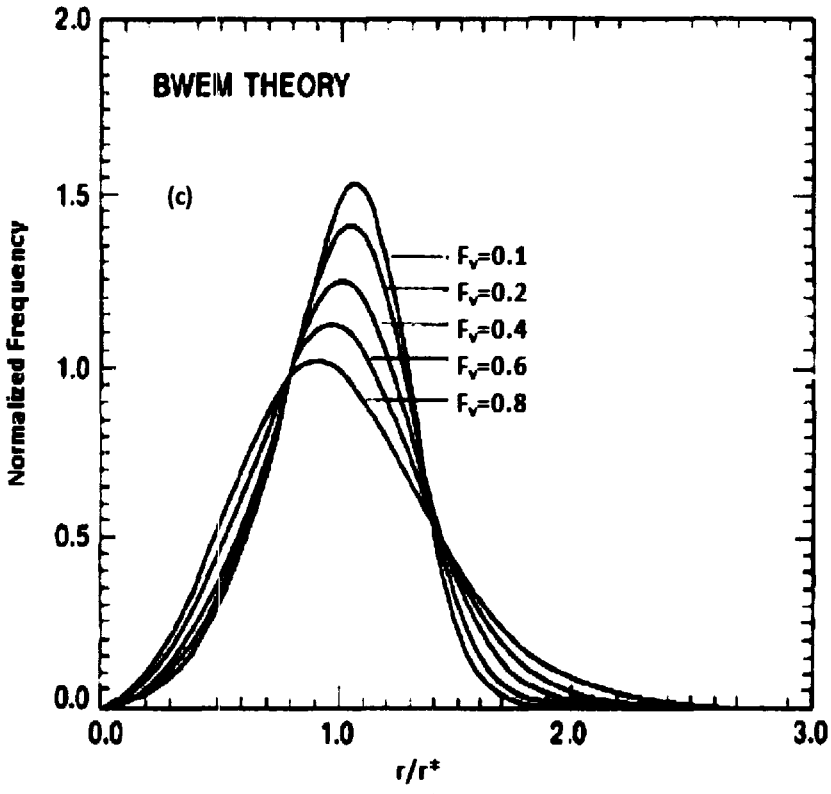

Figure 5-7 The comparison of measured and model predicted particle size distribution

(a) Experimental measurement, (b) LSW model predicted size distribution(Voorhees and Glicksman 1984b), and (c) Brailsford Wynblatt (BWEM) model distribution(Brailsford and Wynblatt 1979)

5.3.1.2 Grain Boundary Diffusion- Rate Controlling Step:

It is well know that grain boundary diffusion becomes dominant when the reheating temperature is below 0.75 to $0.8T_m$ (Porter and Easterling 1992). The apparent diffusion coefficient, D is related to the grain boundary and bulk diffusivities by the following equation:

$$D = \left(1 + \frac{D_{gb} \times \delta}{D_{Bulk} \times r}\right) \times D_{Bulk} \qquad \text{--- (5.17)}$$

where D_{Bulk} is the bulk diffusion coefficient, D_{gb} is the grain boundary diffusion coefficient, and r is the mean grain size. When $D_{gb} \times \delta > D_{Bulk} \times r$, grain boundary diffusion becomes dominant diffusion mechanism. A typical microstructure of a sample that was held at 1060°C for 4 hours is shown in Figure 5.8. The austenite particles are situated along the delta-ferrite grain boundaries. It is therefore possible for the austenite particle coarsening to occur by diffusion along delta grain boundaries. In addition, when the reheating temperature is lower than 1200°C, the particle coarsening exponent n=4, that is ($r^4 - r_o^4 = k(t - t_o)$). An exponent of 4 is typically associated with grain boundary controlled coarsening mechanism (Fischmeister and Grimvall 1973).

The equation for the coarsening particles situated on grain boundaries where the grain boundary paths dominate the diffusion process was derived by Kirchner (Kirchner 1971):

$$r_\gamma^4 - r_{\gamma o}^4 = \frac{9wD_{gb}\sigma N_{\alpha(gb)} V_m t}{32ABRT} \qquad \text{--- (2.37)}$$

where $N_{\alpha(gb)}$ is the solute molar fraction at a grain boundary in equilibrium with an infinitely large particle, w is the grain boundary thickness, and A and B are define as: $A = 2/3 + (\sigma_b / 2\sigma) + (1/3)(\sigma_b / 2\sigma)^3$ and $B = (1/2)\ln(1/f_b)$, where σ_b is the grain boundary energy and f_b is the fraction of the grain boundary covered by the precipitates. It is very difficult to determine the values of the grain boundary diffusivities and f_b, therefore, equation (2.37) was not directly used to model grain boundary control of the coarsening kinetics.

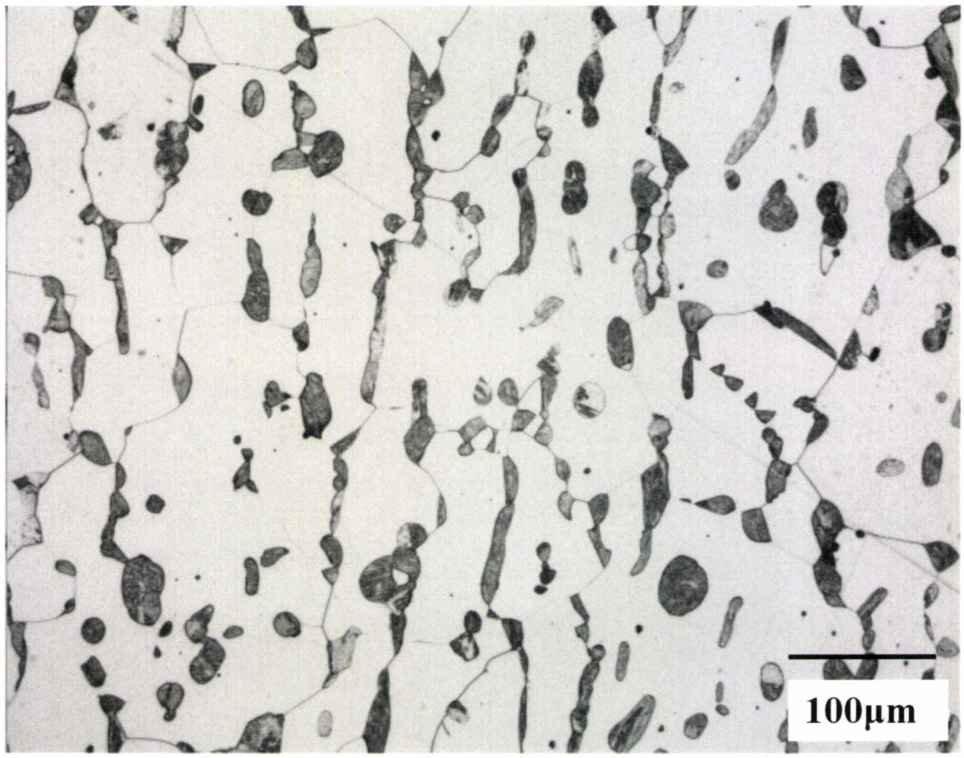

Figure 5-8 Grain boundary structure of Fe-1.5%Al model alloy after reheating to 1060°C for 4 hours

5.3.2 Delta Grain Growth in Delta-Ferrite/Austenite Duplex Microstructure

In single phase materials, the grain growth rate is proportional to the driving force as shown in equation (5.1). According to Turnbull`s rate theory(Turnbull 1951):

$$\frac{d\bar{R}}{dt} = M\frac{\alpha\gamma_{gb}}{\bar{R}} \qquad \text{--- (5.1)}$$

where the driving pressure is:

$$P = \frac{\alpha \gamma_{gb}}{\overline{R}} \qquad \text{--- (5.18)}$$

In this equation, α is a small geometric constant, $\overline{R}$ is the mean radius of an individual and γ_{gb} denotes the grain boundary interfacial energy. In this delta-ferrite/austenite duplex microstructure, the delta grain growth will be inhabited by the austenite phase particles. This pinning pressure can also be termed as Zener drag(Smith 1948) P_z. The magnitude of Zener drag pressure mainly depends on the austenite phase particle volume fraction F_v and the mean particle radius r. Other factors which influence P_z include the particle morphology, degree of coherence between particle and the matrix, the nature of particle distribution such as random or nonrandom. If the spherical particles randomly distribute in the matrix and the grain size is much larger than the interparticle spacing, the Zener pressure is:

$$P_Z = \frac{3F_v \gamma_{gb}}{2r} \qquad \text{--- (5.19)}$$

In case of large volume fraction of second phase particles, the interparticle spacing may have the same value or smaller value than the grain size and equation (5.19) is no longer available. Humphreys and Hatherly(Humphreys and Hatherly 2004) summarized the works of Hellman and Hillert(Hellman and Hillert 1975), Hutchinson and Duggan(Hutchinson and Duggan 1978), Hillert(Hillert 1988) and Hunder and Ryum(Hunderi and Ryum 1992) regarding the effects of boundary-particle correlation and arrived at the conclusion that the maximum pinning pressure P_{ZC} is obtained when all of the particles are located at the grain corner. This pressure is given by:

$$P_{ZC} \simeq \frac{1.2F_v^{2/3}\gamma_{gb}}{r} \qquad \text{--- (5.20)}$$

A generalized equation for Zener drag could be used to describe all boundary-particle correlations:

$$P_{ZG} = \frac{\beta F^n{}_v \gamma_{gb}}{r} \qquad \text{--- (5.21)}$$

where β is constant, r is the austenite particles radius. The delta grain growth rate is related to the effective driving pressure $\Delta P = P - P_Z$ (Gladman 1966; Hillert 1988; Humphreys and Hatherly 2004):

$$\frac{dR_\delta}{dt} = M\Delta P = M\left(\frac{\alpha\gamma_{gb}}{R} - \frac{\beta F_v^n \gamma_{gb}}{r}\right) \qquad \text{-- (5.22)}$$

When the driving force P shown in equation (5.18) is equal to the particle drag pressure P_{ZG} shown in equation (5.21), delta grain growth will stagnate due to the complete pinning of grain growth by the austenite particle. However, the austenite particles will be coarsening at high temperature and this may permit some ferrite growth to occur at a rate which is controlled by the rate of change of particle size (Hillert 1965; Gladman 1966; Martin et al. 1997; Humphreys and Hatherly 2004).

$$\frac{dR_\delta}{dt} = k\frac{dr_\gamma}{dt} \qquad \text{--- (2.33)}$$

The rate of particles coarsening will depend on the rate controlling mechanism (bulk vs. boundary diffusion) as discussed in section 5.3.1. The relationship between delta grain size and austenite particle radius at different temperature are shown in Figure 5.9. Not surprisingly, the slope k of these plots increased as the temperature increased from 1060°C to 1295°C, as the results of the increase in $^{dr}/_{dt}$ with temperature.

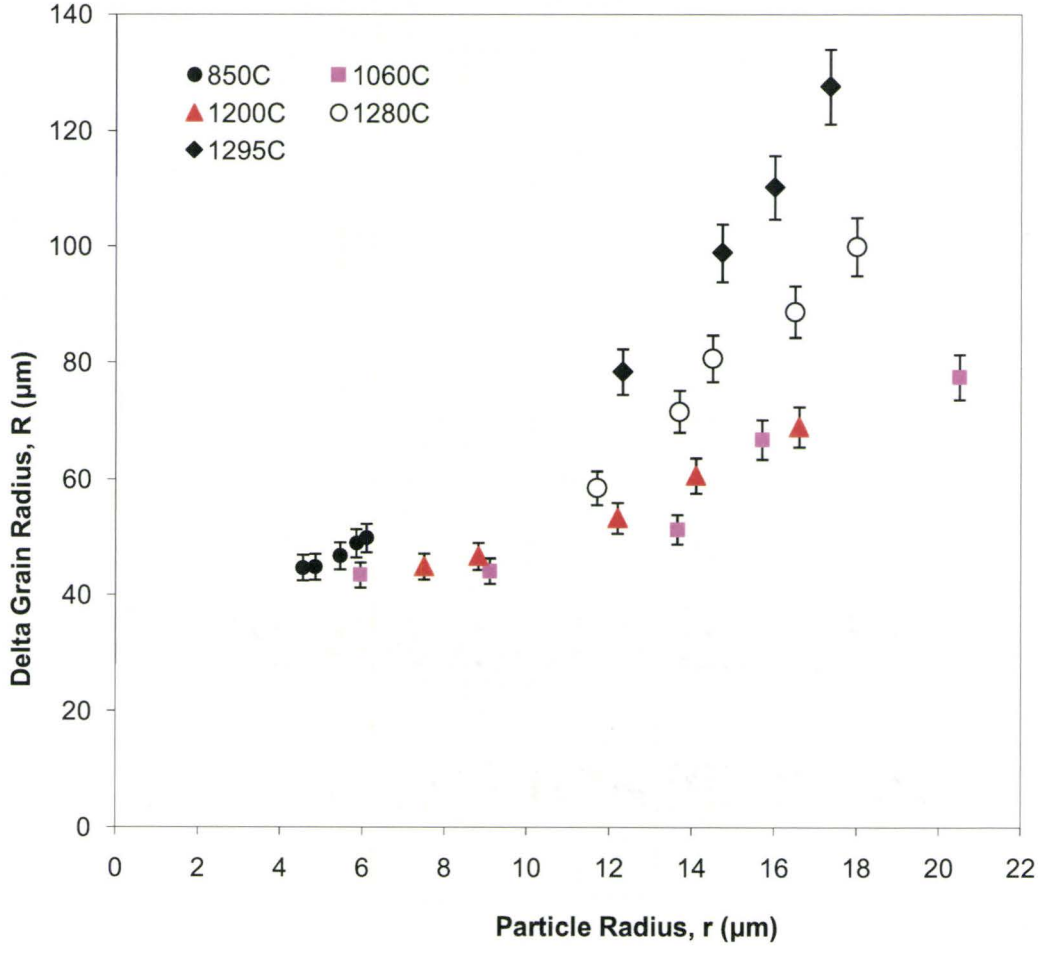

Figure 5-9 The relationship between delta grain radius and austenite particle radius at different temperature

According to equation (5.22) and Figure 5.9, the delta grain growth can be divided into three categories in austenite/delta duplex microstructure:

(1) $P_Z >> P$, that is the austenite particles pinning pressure is much larger than the driving force for grain growth, the grain growth is completely arrested.

(2) $P_Z \geq P$, meaning the austenite particles pinning pressure has the same value as the driving force, and the grain growth proceeds at a rate controlled by the coarsening kinetics of the particles.

(3) $P_Z < P$, the pinning pressure is smaller than the driving force and grain growth occurs with a net driving force of $P - P_z$.

These three cases are discussed in detail in the following section.

5.3.2.1 Delta Grain Growth is Over Pinned in Case of $P_Z >> P$

When the particles pinning pressure is much larger than the driving force, the delta grain boundaries will be totally pinned and no obvious grain growth can be observed. An example of this is observed when the model alloy is reheated to 850°C. As shown Figure 4.10, no grain growth can be observed over the experimental time range. The austenite particle volume fraction was constant about 8.4%. The driving pressure due to grain boundary curvature and the particle pinning pressure were calculated for different holding time at 850°C

as shown in Table 5.5. Zener refers to the classical Zener estimate (equation 5.19) and Humphreys refers to equation 5.20.

Table 5-5 Effective driving pressure for delta grain growth at 850°C

Holding Time	Vol.%	Grain Radium	Particle radium	Driving Pressure	Zener	Humphreys	Effective $P(N/m^2)$	Effective $P1(N/m^2)$
t (h)	Fv	R(um)	r(um)	$P(N/m^2)$	$P_z(N/m^2)$	$P_{zc}(N/m^2)$	$\Delta P=P-P_z$	$\Delta P1=P-P_{zc}$
16	8.3	44.7	4.6	21276.6	13681.3	24884.1	7595.3	-3607.5
48	8.6	44.8	4.8	21202.4	13299.0	23906.9	7906.4	-2701.6
144	8.3	46.7	5.4	20342.6	11422.0	20774.8	8920.6	-432.2
216	8.7	48.9	5.8	19427.4	11153.9	19974.4	8273.6	-545.0
288	8.5	49.8	6.0	19076.3	10375.0	19173.9	8701.3	-97.6

In this calculation, the surface energy was $0.5J/m^2$, and α= 1.9 in equation (5.18) for driving pressure. Zener drag pressure assuming a random distribution of particles, P_z is much smaller than Humphrey's P_{zc} which assumes that all of the particles are located at the corner of the delta grains and Equation (5.20) is a reasonable estimation of the particle pinning pressure. The effective driving pressure for delta grain growth is negative until the holding time is longer than 288 hours. This means that the system is "over pinned" and as a result even though the austenite particles are coarsening with time, the particle pinning pressure (equation (5.20)) is still larger than the driving pressure for delta grain growth, therefore there is no delta grain growth under this condition. The results are convenient summarized in Figure 5.10 which

shows the delta grain radius and austenite particle radius evolution with time. The delta grain radius is constant while the austenite particle radius coarsening with time as $t^{1/4}$.

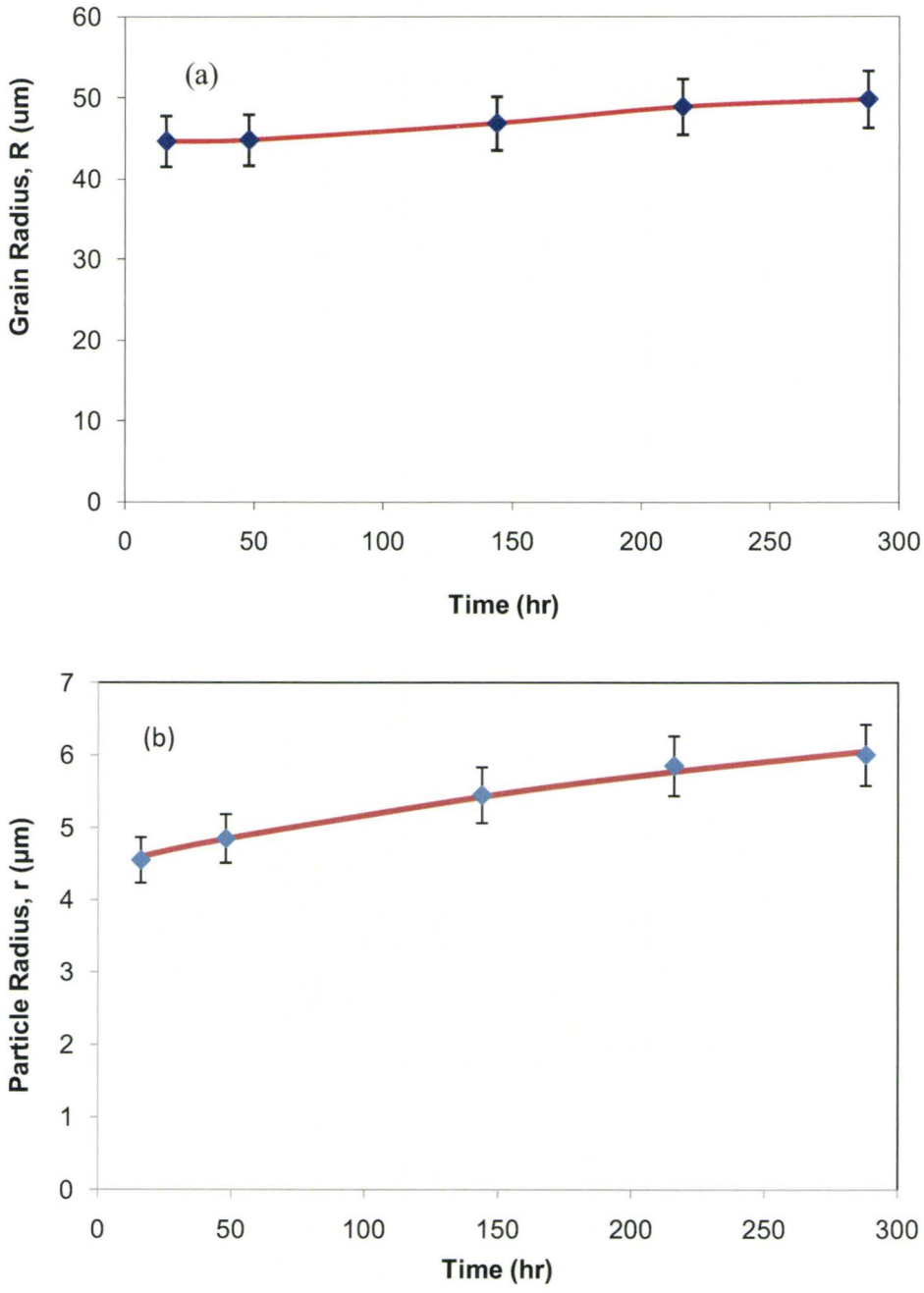

Figure 5-10 Delta grain radius (a) and particle radius (b) with time at 850°C

5.3.2.2 Delta Grain Growth Unpinned in Case of $P_Z \geq P$

When the austenite particle pinning pressure has the same value as the driving force, delta grain growth is pinned at the initially stage, but it can start to occur due to the coarsening of the austenite particles. When the reheating temperature was 1060°C, the delta grain size remained constant at about 90μm for holding time of less than 4 hours. A holding for time longer than 4 hours, delta grain growth started to take place as shown in Figure 4.11 and 5.9. The calculation of the effective driving pressure for delta grain growth is shown in Table 5.6. The effective driving pressure for delta grain growth becomes positive when the holding time is longer than 4 hours, and this appears to be in good agreement with the experimental observations. According to Figure 5.9 and as discussed section 5.4.1, the austenite particle will coarsen with time by grain boundary diffusion which according to the equation: $\bar{r} = kt^{1/4} + b$. The coarsening process will decrease the particle pinning pressure according to equation (5.20). When the particle pinning pressure is smaller than the driving pressure for delta grain growth, the delta grain will be unpinned and grain growth would occur again. Two cases are distinguished in this case. The growth could occur at "zero" net driving force, meaning that at anytime the structure is globally pinned and growth is only possible at some local grain corners that get unpinned due to the dissolution of particles during coarsening. If this is the case, growth rate will be directly proportional to the particle coarsening rate. The other possibility is that the drop in the pinning force is very rapid and grain growth occurs under a positive net driving force. It is not clear which of these two cases is applicable here. On the

other hand, Table 5.6 supports the second possibility (positive driving force for t > 4 hrs), while Figure 5.9 which shows a linear dependence of R on r, would support the first possibility.

Table 5-6 Effective driving pressure for delta grain growth at 1060°C

Holding Time	Vol.%	Grain Radium	Particle radium	Driving Pressure	Zener	Humphreys	Effective $P(N/m^2)$	Effective $P1(N/m^2)$
t (h)	Fv	R(um)	r(um)	$P(N/m^2)$	$P_z(N/m^2)$	$P_{zc}(N/m^2)$	$\Delta P=P-P_z$	$\Delta P1=P-P_{zc}$
1	17.0	43.4	6.0	2428.6	21889.4	30763.5	460.8	-8874.1
4	18.6	44.1	9.1	15329.7	21542.0	21364.1	6212.3	177.9
24	19.3	51.3	13.6	10643.4	18518.5	14653.3	7875.1	3865.2
48	18.5	66.8	15.7	8837.6	14221.6	12338.3	5384.0	1883.2
144	18.1	77.5	20.5	6622.0	12258.1	9312.0	5636.1	2946.1

Table 5-7 Effective driving pressure for delta grain growth at 1200°C

Holding Time	Vol.%	Grain Radium	Particle radium	Driving Pressure	Zener	Humphreys	Effective $P(N/m^2)$	Effective $P1(N/m^2)$
t (min)	Fv	R(um)	r(um)	$P(N/m^2)$	$P_z(N/m^2)$	$P_{zc}(N/m^2)$	$\Delta P=P-P_z$	$\Delta P1=P-P_{zc}$
5	19.6	44.9	7.5	21181.72	20000	26847.36	1181.717	-5665.64
15	18.7	48.15	8.82	19730.01	17005.84	22096.56	2724.172	-2366.55
60	19.4	53.3	12.1	17823.64	12396.69	16526.96	5426.946	1296.677
100	21.0	60.7	13.9	15663.64	10791.37	15163.57	4872.277	500.0691
182	20.9	69.0	16	13778.1	9375	13129.58	4403.1	648.5241

Similar results are seen at 1200°C. Figure 4.12 and Figure 5.9 show that when the heat treatment temperature increased to 1200°C, delta grain growth was pinned for the first 15minutes. The particle coarsening kinetics was in Figure 4.16. Using these results, the effective driving pressure for delta grain growth at 1200°C is calculated and shown in Table 5.7. Once again, a good agreement is observed for the onset of grain growth which is predicted to happen between 15 and 60 minutes in agreement with the experiments. In this case, the net driving force is relatively small and the calculations are not inconsistent with the grain growth rate being linearly proportional to the particle coarsening rate.

From Figure 5.9, it is interesting to know that the slope of R vs. r is the same at 1060°C and 1200°C. This would not be the case if there was a positive driving force for grain growth because then the mobility would make a contribution to the rate of change of R ($dR/dt = M(T)\, dr/dt$). However if the grain growth occurring under "zero" driving force, then R would be a function of r only and the two temperatures should give the same grain R vs. r. It is therefore concluded that grain growth at 1060 and 1200°C is most likely occurring under "zero" global driving force.

The delta grain radius and particle radius evolution with time at 1200°C in Figure 5.11 is a good presentation of this case: delta grain growth is first pinned, then starts unpinned and the grain grows at low rate which is controlled by the austenite particle coarsening process. The particle coarsening is controlled by $r = kt^{1/4} + b$ or $r = kt^{1/3} + b$.

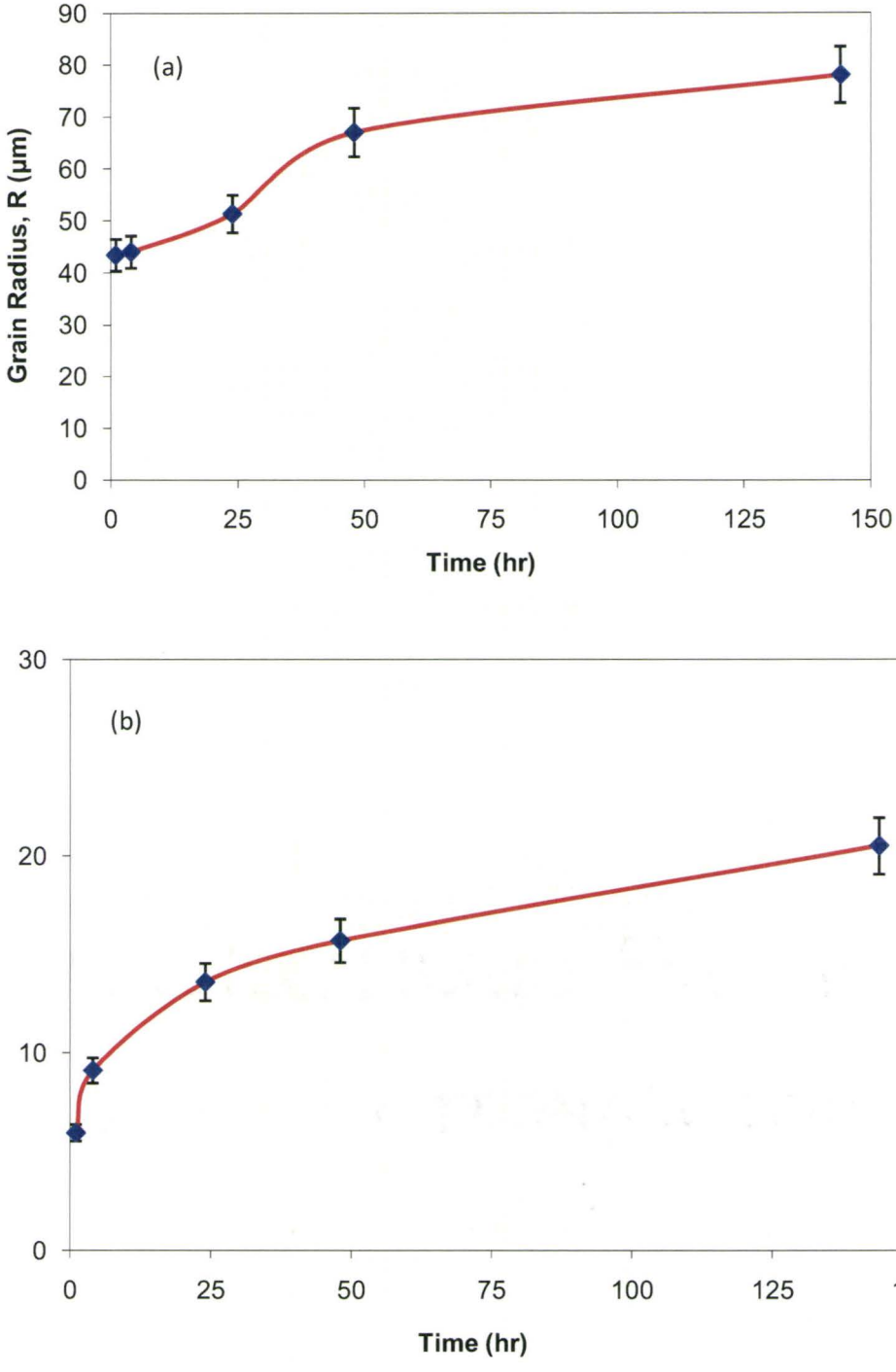

Figure 5-11 Delta grain radius (a) and particle radius (b) with time at 1060°C

5.3.2.3 Delta Grain Growth at Slowdown Rate in Case of $P_Z < P$

In the case when the austenite particles pinning pressure is smaller than the driving pressure; delta grain growth would not stop. In fact, grain growth would occur under a net driving force of $P - P_z$. The calculations of the effective particle pinning pressure at 1280°C and 1295°C are shown in Table 5.8 and 5.9. In this case, the effective driving force is positive at all times. In contrast to the previous two cases, the net driving force decreases with time. This is due to the increase in grain size which lowers the curvature of the grains. For comparison to case one and case two, the typical grain growth and particle coarsening with time in this case is shown in Figure 5.12.

Table 5-8 Effective driving pressure for delta grain growth at 1280°C

Holding Time	Vol.%	Grain radius	Particle radius	Driving Pressure	Zener	Humphreys	Effective $P(N/m^2)$	Effective $P1(N/m^2)$
t (min)	Fv	R(um)	r(um)	$P(N/m^2)$	$P_z(N/m^2)$	$P_{zc}(N/m^2)$	$\Delta P=P-P_z$	$\Delta P1=P-P_{zc}$
5	9.6	58.5	11.7	16239.32	6076.923	10668.1	10162.39	5571.215
20	9.3	71.6	13.7	13268.16	5189.781	8918.961	8078.375	4349.196
33	9.4	80.7	14.5	11772	4903.448	8487.483	6868.547	3284.512
60	10.6	88.8	15.82	10698.2	4311.704	8088.827	6386.494	2609.372
90	8.5	102.0	17.22	9313.725	4133.721	6688.573	5180.005	2625.152

Table 5-9 Effective driving pressure for delta grain growth at 1295°C

Holding Time	Vol.%	Grain Radium	Particle radium	Driving Pressure	Zener	Humphreys	Effective $P(N/m^2)$	Effective $P1(N/m^2)$
t (min)	Fv	R(um)	r(um)	$P(N/m^2)$	$P_z(N/m^2)$	$P_{zc}(N/m^2)$	$\Delta P=P-P_z$	$\Delta P1=P-P_{zc}$
4	6.8	78.4	12.5	12117.35	4080	7925.419	8037.347	4191.928
20	6.6	98.9	14.5	9608.091	3413.793	6696.96	6194.298	2911.131
35	6.8	110.3	15.5	8616.78	3290.323	6391.467	5326.457	2225.313
60	6.5	137.6	16.8	6904.07	2893.175	5704.312	4010.895	1199.757

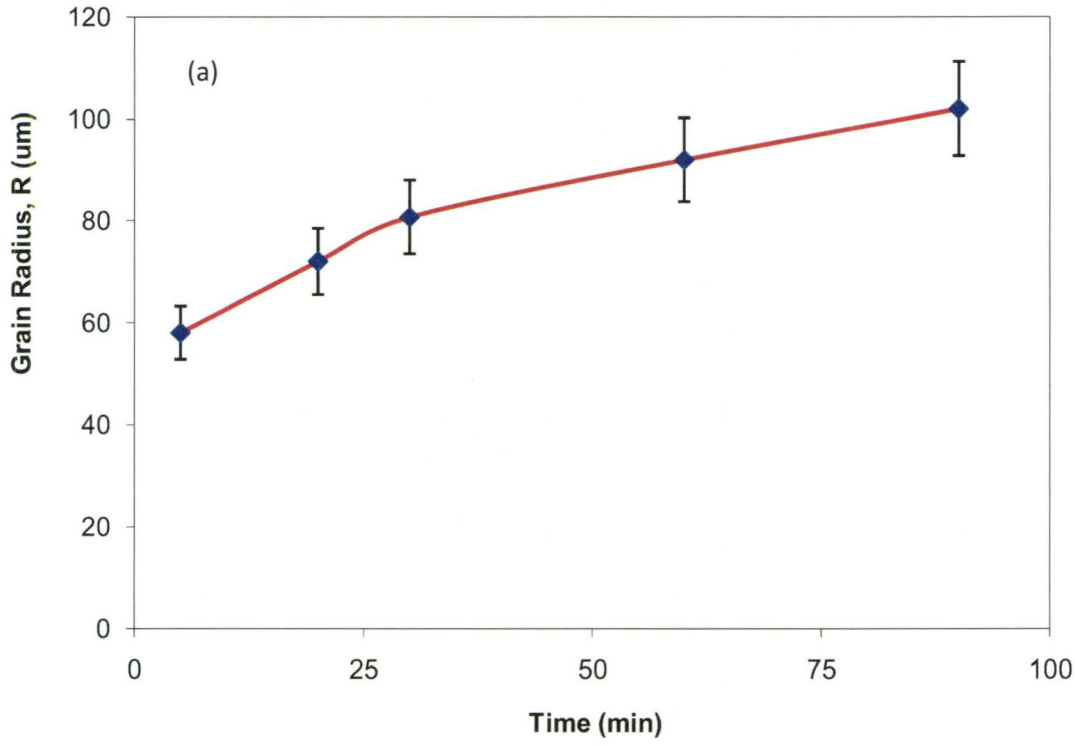

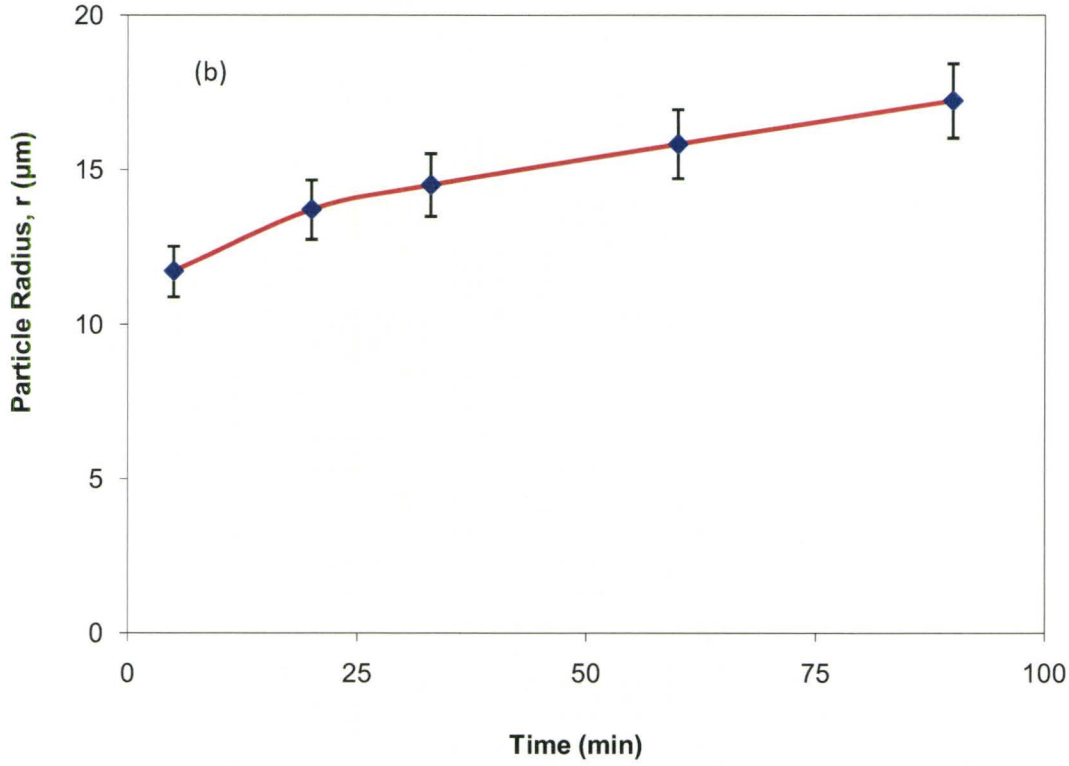

Figure 5-12 Delta grain radius (a) and particle radius (b) with time at 1280°C

As shown in Figure 5.9, the slope of R vs. r curve at 1295°C is bigger than that at 1280°C. The slope of the grain size vs. particle size line depends on the magnitude of the pinning force as well as the mobility of the grain boundaries. Both effects would favor a larger slope at the higher temperature, the pinning force decreases as the volume fraction of austenite drops from 9.5% at 1280°C to 6.5% at 1295° and the mobility increases exponentially with temperature.

5.3.2.4 Limiting Delta Grain Size

In a two phase mixture a limiting grain size can be found using Equation (5.22) such that $dR_\delta/dt = 0$. This occurs when the austenite particles pinning pressure becomes equal to the driving pressure for delta grain growth:

$$\frac{\alpha\gamma_{gb}}{R} = \frac{\beta F_v^n \gamma_{gb}}{r} \qquad \text{--- (5.23)}$$

The limiting grain size is:

$$D_L = \frac{2\alpha r}{\beta F_V^n} \qquad \text{--- (5.24)}$$

The limiting grain size, D_L depends on both the particle radius, r, and particle volume fraction, F_V . If the particles coarsen, the limiting grain size will change with time as discussed earlier. According to Zener's model, the limiting grain size is: $D_{Zener} = 4r/3F_V$. Even though numerous efforts have been put into refining of Zener's treatment (Gladman 1966; Ashby and Centamore 1968; Hellman and Hillert 1975; Louat 1982; Nes et al. 1985; Hillert 1988; Hunderi and Ryum 1992) all approaches generally predict a linear dependence of D_L on r/F_V , in agreement with the classical Zener treatment. As mentioned earlier, the preceding models for particle pinning are based on the assumption of a macroscopically planar boundary and a random distribution of finely spaced particles. However, when the interparticle spacing is of the same or smaller that of the grain size and the volume fraction of the particles is high,

this assumption breaks down, and non-random correlation of particles and boundaries must be taken into account(Humphreys and Hatherly 2004). In this situation, the limiting grain size:

$$D_{ZC} \simeq \frac{\beta r}{F_V^{1/3}} \qquad \text{--- (5.25)}$$

where β is a small geometric constant. Hellman and Hillert(Hellman and Hillert 1975) have shown that $D_L = 3.6r / F_V^{1/3}$. According to these authors, the non-correlated limiting delta grain size D_{ZC} obtainable at high volume fractions can be estimated from the following equation:

$$D_{ZC} \simeq 4.8 \frac{r}{F_V^{1/3}} \qquad \text{--- (5.26)}$$

Figure 5.13 is a comparison of the limiting grain size values D_{ZC} predicted by the models of Zener(Smith 1948), Hellman and Hillert(Hellman and Hillert 1975), and the present model equation (5.26). Experimental data obtained from the current work are also superimposed in this figure. It can be seen that the experimental data is in good agreement with the predictions of equation (5.26) when the particle volume fraction is greater than 5%. The Hellman and Hillert(Hellman and Hillert 1975) model underestimates the limiting grain size at all volume fractions, but displays the correct functional dependence on F_V at all particle volume fractions. On the contrary, Zener's model underestimates the values of D / r when particle volume fraction F_V larger than 5%. It is in good agreement when the particle volume fraction is smaller than 5%. Humphreys and Hatherly(Humphreys and Hatherly 2004)

summarized the previous works of Hillert(Hillert 1988), Hunderi and Ryum, and Manohar et al (Hunderi and Ryum 1992; Manohar et al. 1998) and concluded that a transition from a particle-boundary correlated limiting grain size to a non-correlated limiting grain size occurs at a volume fraction of about 5% in agreement with the current results.

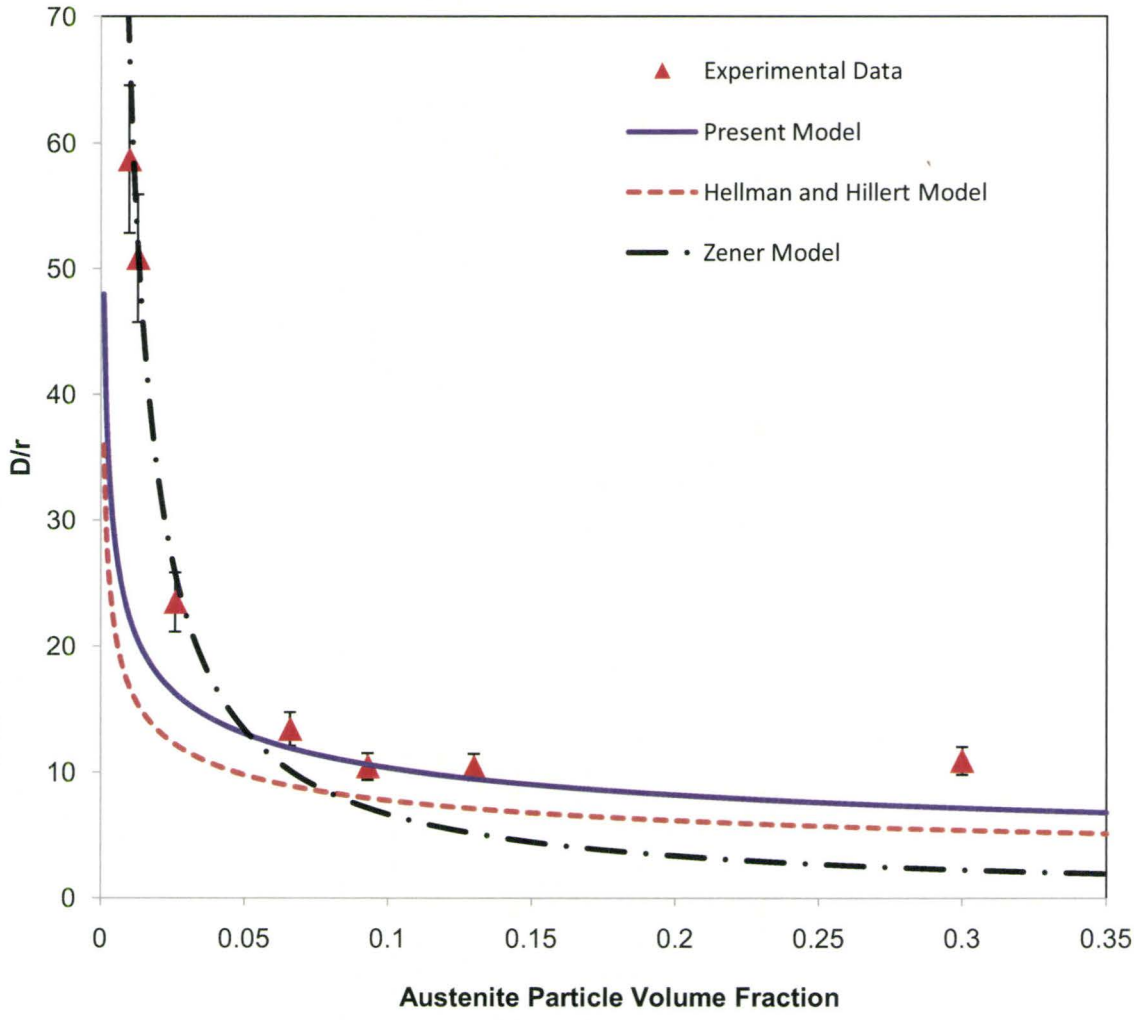

Figure 5-13 Effects of austenite particle volume fraction on the limited grain size

5.4 Delta-Ferrite to Austenite Phase Transformation

The kinetics of the delta-ferrite to austenite phase transformation was investigated using the Fe-1.5% model alloy. The effects of holding temperature and cooling rate as well as the effect of deformation are discussed below. A model for austenite growth with alloying elements partitioning was implemented in order to rationalize the experimental data. Details are described next.

5.4.1 Effects of Holding Temperature and Cooling Rate

It can be seen from the isopleths that the Fe-1.5%Al model alloy is completely transformed to delta-ferrite when it is reheated to1310°C. When the sample is cooled from 1310 to 1125°C at a cooling rate of 50°C/s, the transformed austenite morphology suggested a mixture of cellular precipitation mode (Figure 5.14(a)) and Widmanstätten precipitation. The cellar structure becomes coarser with decreasing cooing rate (Figure 4.7). However, when the sample was cooled down to 850°C with the same cooling rate (50°C/s), the austenite morphology clearly resembled that of Widmanstätten pattern (Figure 5.14(b)(Porter and Easterling 1992). EDX analysis indicates that for both morphologies aluminum and manganese partitioned during the delta-ferrite to austenite phase transformation. This is not surprising given the high transformation temperatures employed here. In fact, the alternative, that is non-partitioning local equilibrium (NP-LE) (Gilmour et al. 1972; Ågren et al. 2006), does not provide a solution for the diffusion problem for the present alloy at the above

temperatures. This means that the growth of the alloy phase is controlled by the diffusion of the substitutional elements, which in turn explains the sluggish transformation kinetics.

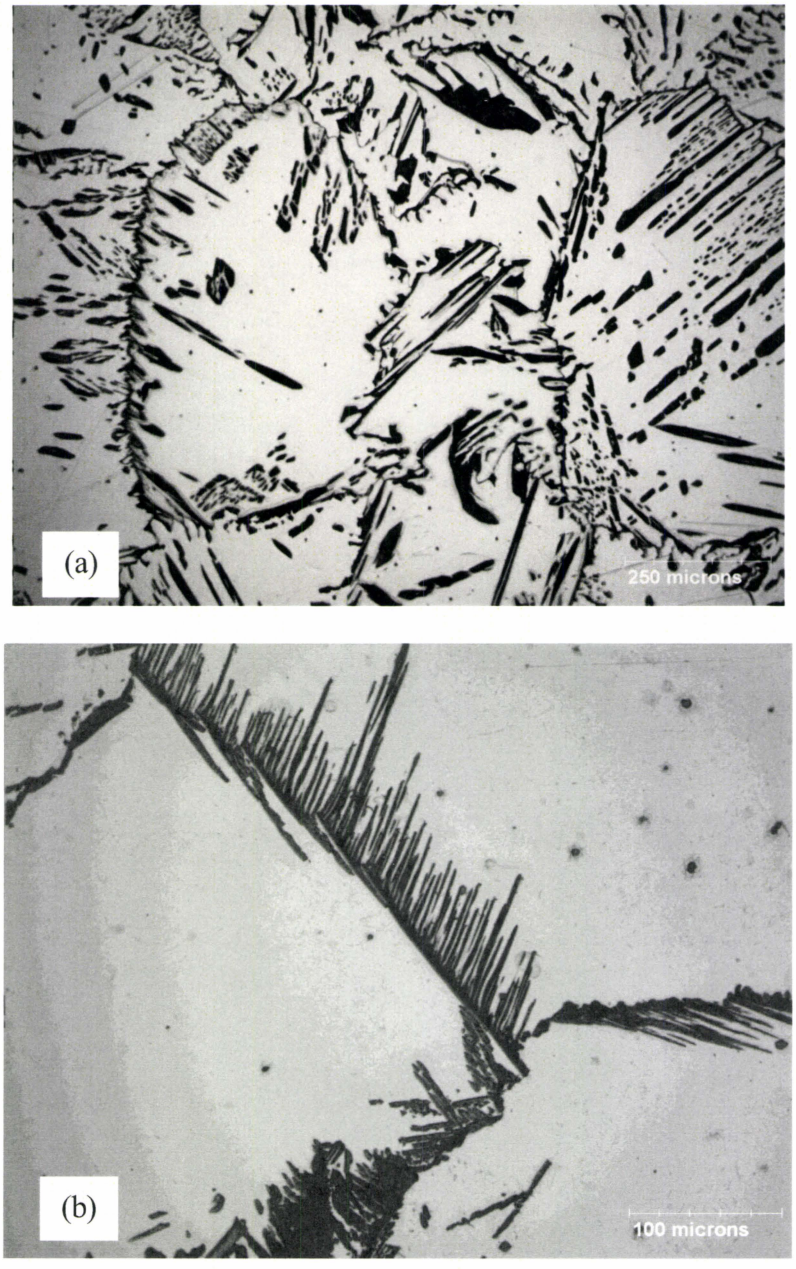

Figure 5-14 Different transformed austenite morphology: (a) cell pattern, 1120°C, 300s (b) Widmanstätten pattern, 850°C, 1800s

5.4.2 Austenite Growth with Alloying Elements Partitioning

In order to model a diffusional phase transformation in a multi-component system it is necessary to develop: (a) a global mass balance for each of alloying elements as well as (b) a local mass balance, at the interface, for each of the alloying elements. The interfacial mass balance is a function of the interface velocity and it is necessary to select a tie-line for which all of the interfacial mass balances lead to the same velocity. Purdy, Weichert et al (Purdy et al. 1964) examined this problem in ternary Fe-C-X systems in which X is a substitutional element and determined two sets of solutions. In one case, the growth occurs without the partitioning of the substitutional element (Non-partitioning local equilibrium) and in the other growth requires the partitioning of the substitutional element (Partitioning Local Equilibrium). The alloy composition and temperatures used here fall within the regime of partitioning local equilibrium, meaning that the diffusion of the substitutional elements is necessary for growth to occur. The initial tie-line is that which would simultaneously satisfy all of the local (interfacial) mass balances. This tie-line would continue to operate until the overlap of the diffusion profiles of one (or more) of the alloying elements. When this happens, the operating tie-line will begin to shift in such a way as to satisfy the global and local mass balances.

Assuming the transformation is controlled by volume diffusion, interface compositions are determined by equilibrium tie line on the phase diagram.

$$C_C^{\delta} = k_1 C_C^{\gamma} \qquad \text{--- (5.27)}$$

$$C_{Mn}^{\delta} = k_2 C_{Mn}^{\gamma} \quad \text{--- (5.28)}$$

$$C_{Al}^{\delta} = k_3 C_{Al}^{\gamma} \quad \text{--- (5.29)}$$

where k_1, k_2, k_3 are distribution coefficient for carbon, manganese and aluminum respectively. C_C^{δ}, C_{Mn}^{δ}, C_{Al}^{δ} , C_C^{γ}, C_{Mn}^{γ}, C_{Al}^{γ} are carbon, manganese and aluminum concentration in the delta-ferrite and austenite accordingly. In order to arrive at the same interface velocity, it is necessary (Wycliffe et al. 1981):

$$\left|\frac{J_{Mn}}{\Delta C_{Mn}}\right| = \left|\frac{J_{Al}}{\Delta C_{Al}}\right| = \left|\frac{J_c}{\Delta C_c}\right| \quad \text{--- (5.30)}$$

where the flux J is given by the Fick`s first law:

$$J_i = -D\frac{dC_i}{dx} \quad \text{--- (5.31)}$$

Combining equations (5.30) and (5.31), and using a linear diffusion profile in the delta-ferrite, the following equation obtained:

$$\sqrt{\frac{D_{Mn}}{t}}\frac{C_{Mn}^{o} - C_{Mn}^{\delta}}{C_{Mn}^{\gamma} - C_{Mn}^{\delta}} = \sqrt{\frac{D_{Al}}{t}}\frac{C_{Al}^{o} - C_{Al}^{\delta}}{C_{Al}^{\gamma} - C_{Al}^{\delta}} \quad \text{--- (5.32)}$$

$$\sqrt{\frac{D_C}{t}}\frac{C_C^{o} - C_C^{\delta}}{C_C^{\gamma} - C_C^{\delta}} = \sqrt{\frac{D_{Al}}{t}}\frac{C_{Al}^{o} - C_{Al}^{\delta}}{C_{Al}^{\gamma} - C_{Al}^{\delta}} \quad \text{--- (5.33)}$$

where C_C^o, C_{Mn}^o, C_{Al}^o are the bulk carbon, manganese and aluminum concentration in Fe-1.5%Al model alloy. The distribution coefficient and diffusion constants in Equations (5.32) and (5.33) were obtained, respectively, from TCFE2 and MOB2data base of ThermoCalc. These values are summarizes in Table 5.10. The initial tie-line for precipitation in then calculated at 850°C and 1125°C (Table 5.11).

Table 5-10 Calculated distribution coefficient and diffusion coefficient

Temperature	Distribution Coefficient			Diffusion Coefficient in BCC		
	k_1	k_2	k_3	D_C	D_{Mn}	D_{Al}
850°C	0.0719	0.491	1.994	3.71389E-10	3.73438E-15	2.34111E-15
1125°C	0.281	0.704	1.473	1.9559E-09	4.59459E-13	4.93761E-13

Table 5-11 Calculated alloy elements concentration in the delta-ferrite and austenite

Temperature	$C_{Mn}^{\delta}(\%)$	$C_{Mn}^{\gamma}(\%)$	$C_{Al}^{\delta}(\%)$	$C_{Al}^{\gamma}(\%)$	$C_C^{\delta}(\%)$	$C_C^{r}(\%)$
850°C	0.736	1.498	1.919	0.963	0.493	0.686
1125°C	1.233	0.868	1.689	1.147	0.493	1.754

EDS was used to determine manganese, and aluminum concentration profiles at 850°C and 11250°C are shown in Figure 5.15 (a) and (b) respectively. The solid points are measured data and the dash lines show the approximate position of the phase boundary. The manganese

concentration increases in austenite and decreases in the delta-ferrite, while the aluminum concentration increases in the delta-ferrite and decreases in austenite. It should be note that interaction volume of electron beam (15.0Kv) is approximately 0.8μm in this alloy. As a result, EDX analysis in the vicinity of the interface will include contribution from both phases. These results confirm that the growth of austenite occurs with partitioning of the substitutional elements.

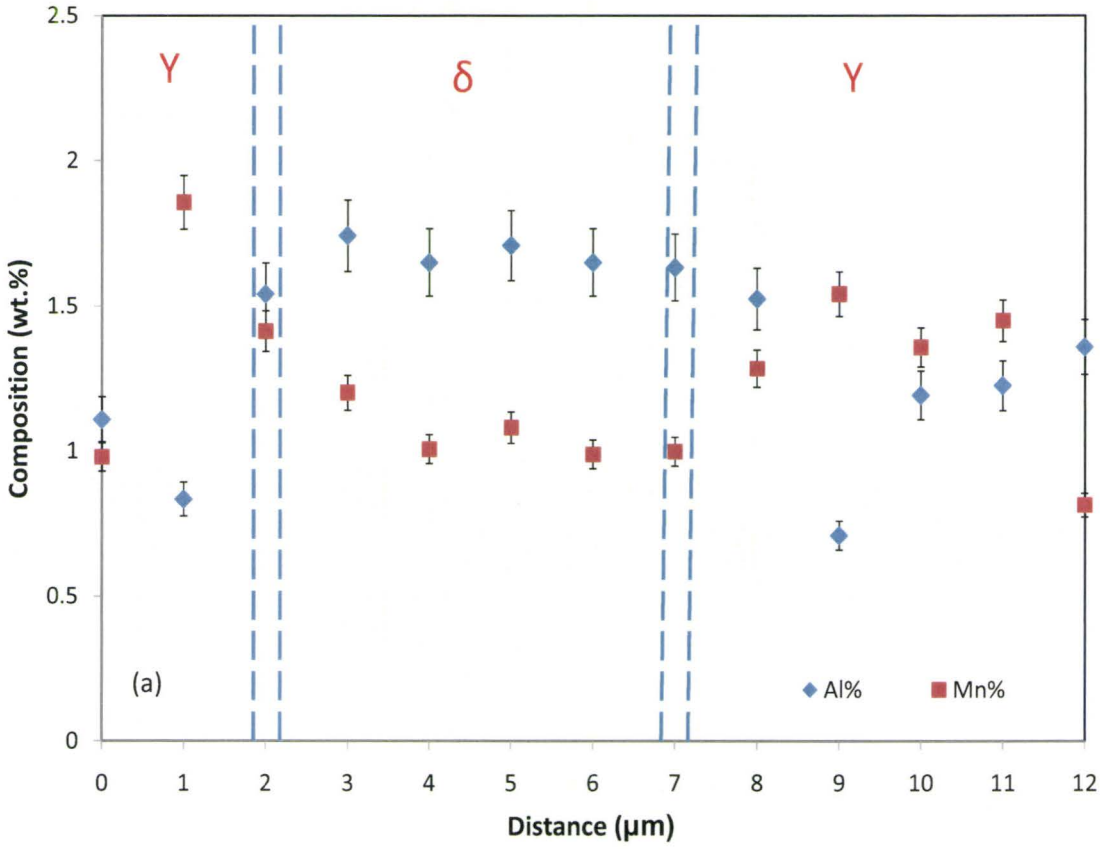

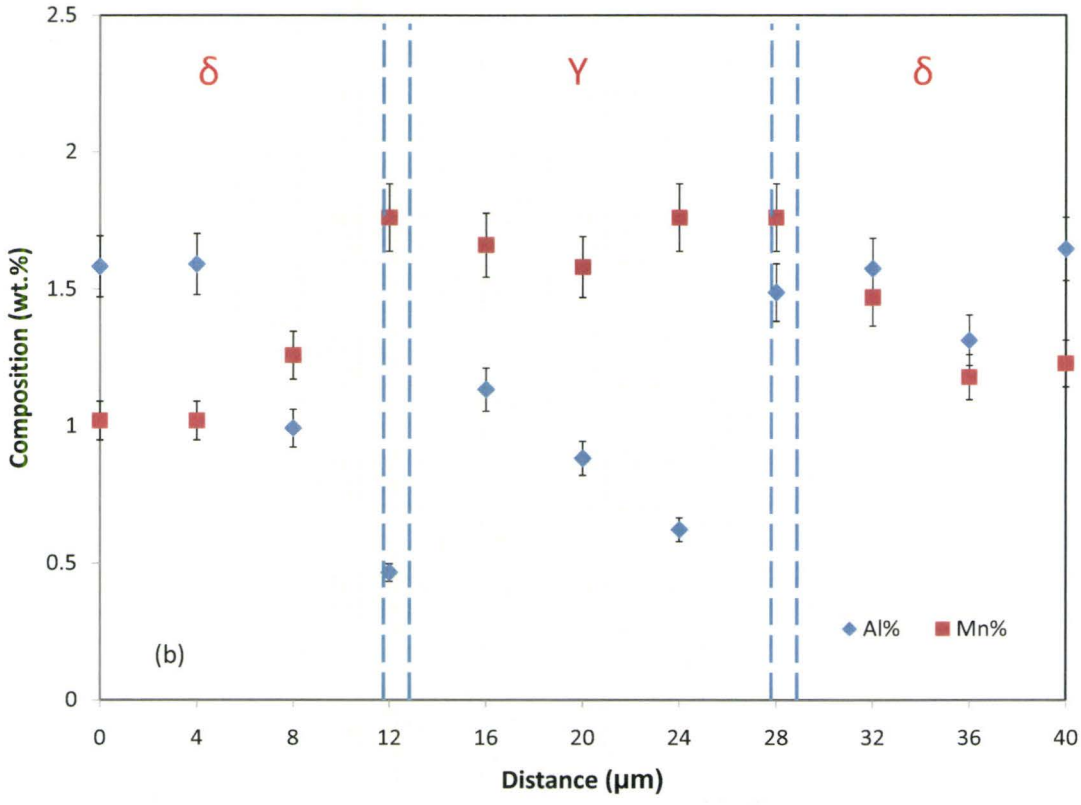

Figure 5-15 Comparison of calculated manganese, aluminum concentration profile with experimental data at holding (a) 850°C, 1800s and (b)1125°C, 300s

Note: Concentration error bars represent errors from the EDS system

Figure 5.16 is a sequence of images illustrating the growth of austenite at 850°C. Initially, a thin layer of austenite nucleates along the delta grain boundary (Figure 5.15(a), 60s); then, the plane front breaks down (Figure 5.15(a), 200s). It appears, however, that the austenite plates grow as a front which is similar to cellular precipitation. Kikuchi et al (Kikuchi et al. 1990) and Kikuchi et al (Kikuchi et al. 1991)suggested that the front advances at a rate which is controlled by carbon diffusion (Figure 5.15(a), 600s and 1800s), while the spacing of the phase is controlled by the diffusion of the substitutional elements (Figure 5.15(b)).

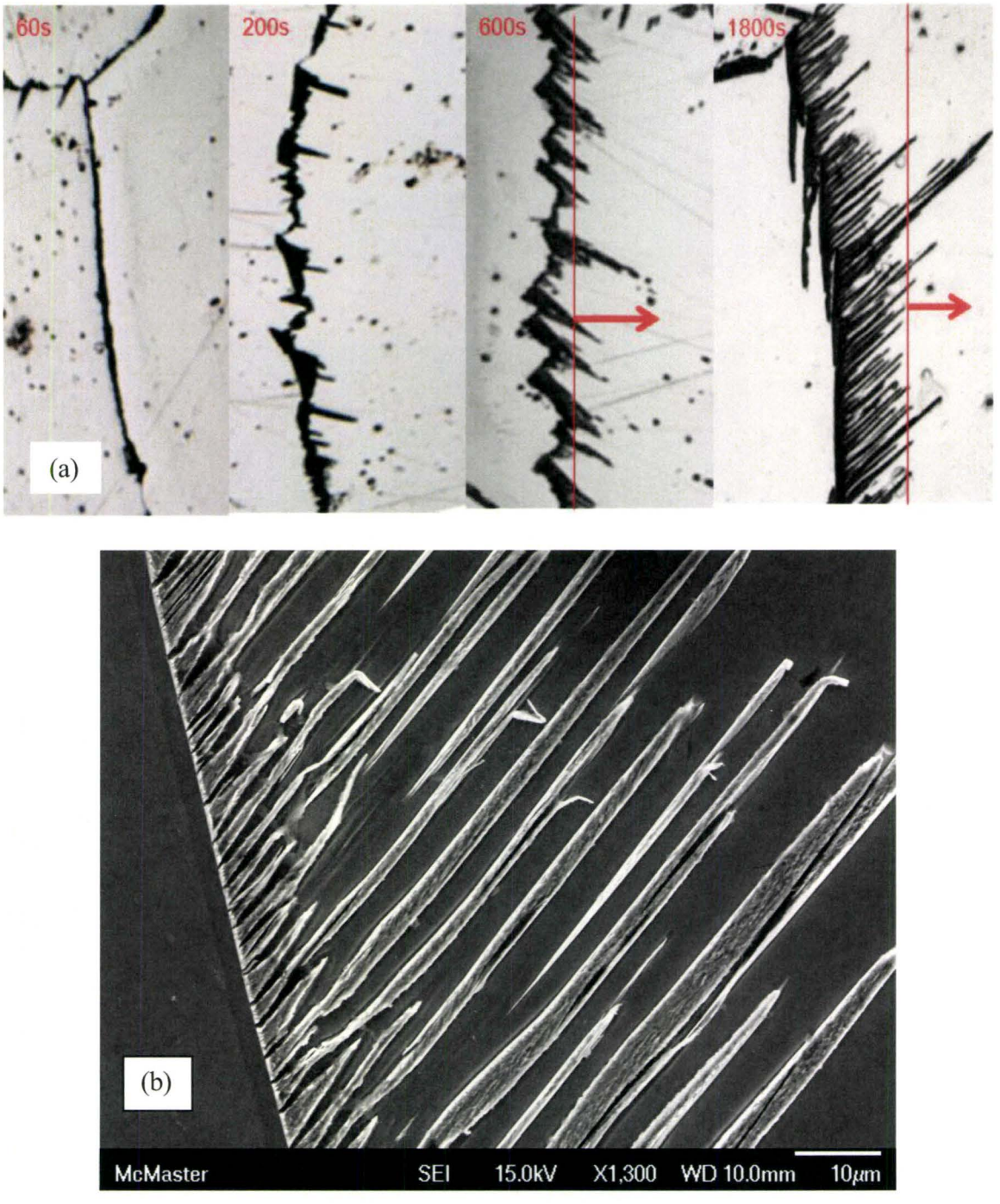

Figure 5-16 Austenite phase growth (a) the plate front grow into the fresh delta grain by carbon diffusion controlling and (b) inter-plate coarsening by aluminum and manganese diffusion controlling

Figure 5.17 shows the proposed carbon diffusion profile. The velocity of the austenite front can be estimated as:

$$v = \frac{dx}{dt} = \frac{J_C^{\delta} - J_C^{\gamma}}{\Delta C_c} \qquad \text{--- (5.34)}$$

It is reasonable to take the flux in austenite to zero, $J_C^{\gamma} = 0$. Assuming the carbon diffusion profile in the delta-ferrite is linear, equation (5.34) leads to the following expression for the width of the austenite layer (x):

$$\chi = 2\sqrt{D_C t}\,\frac{C_C^{o} - C_C^{\delta}}{C_C^{\gamma} - C_C^{\delta}} \qquad \text{--- (5.35)}$$

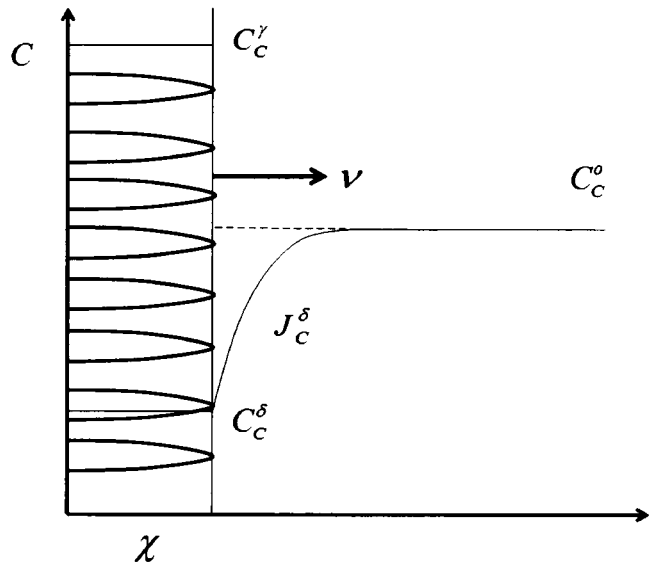

Figure 5-17 Carbon concentration profile during the austenite front grows into the fresh delta-ferrite

The measured austenite front thickness compared to $\sqrt{D_C t}$ at 850°C and 1125°C are shown in Figure 5.18(a) and (b) respectively. The austenite front was measured visually as shown is Figure 5.16(a). Diffusion data came from Table 5-10, the bulk carbon concentration is 0.05%, carbon concentration in the delta-ferrite and austenite were obtained by ThermoCalc using TCFE2 data base at corresponding temperature. In general, excellent agreement is obtained between the experimental data and the model prediction. This is confirmed that the advance of the austenite front is controlled by the long-range diffusion of the interstitial element as observed by in Fe-Cr-N alloys(Kikuchi et al. 1990; Kikuchi et al. 1991). It should be noted that the austenite front thickness increases, the difference between the model prediction and the experimental date becomes larger. This difference is most likely due to the sectioning effects when cutting these samples.

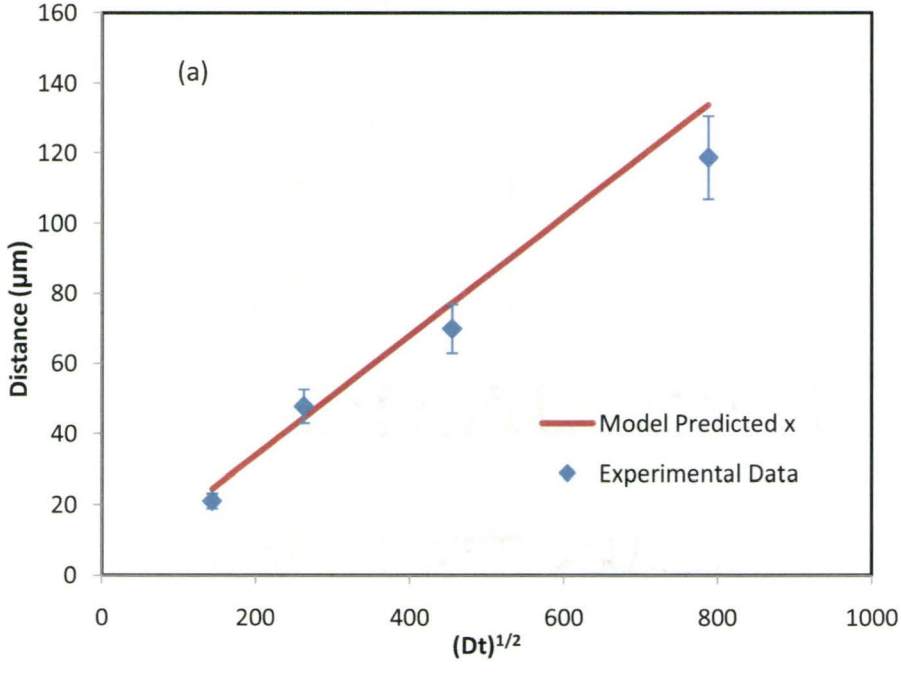

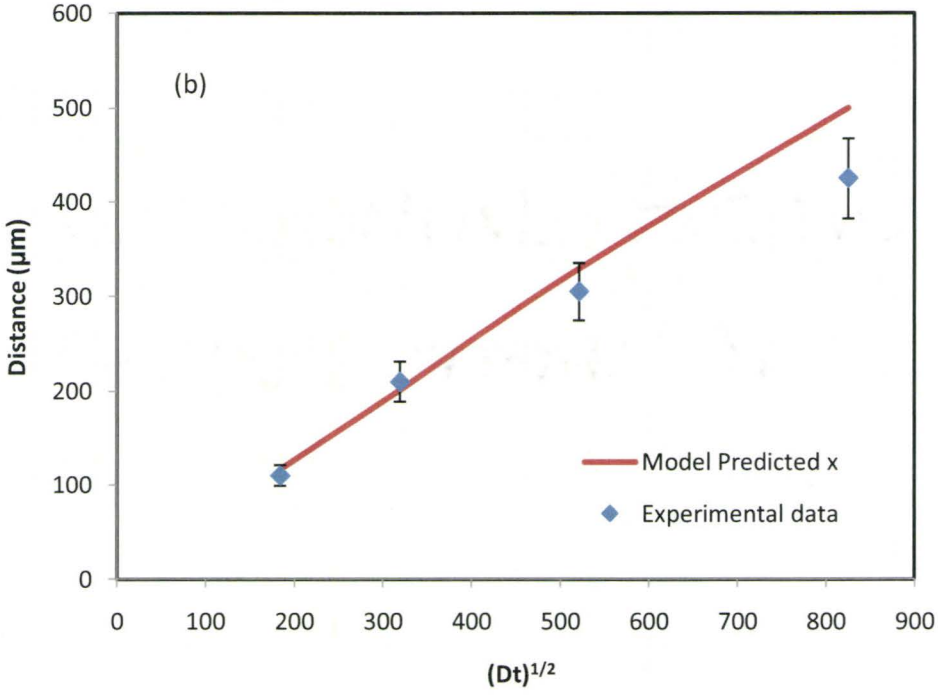

Figure 5-18 The calculated austenite front distance with $\sqrt{D_C t}$ compared to the experimental data at (a) 850°C and (b) 1125°C

In addition, the inter-plate spacing was compared to $\sqrt{D_{Al} t}$ at 850°C and 1125°C as shown in Figure 5.19 (a) and (b) respectively. Overall, the plate spacing is proportional to $t^{0.5}$. If manganese diffusion coefficient is used, the same trend is obtained. This trend seems to support the argument that the inter-plate spacing is controlled by Al and Mn diffusion during the delta-ferrite to austenite phase transformation. From Figure 5.16(b), it also can be seen that some plates disappeared which is analogous to the dendritic arm spacing coarsening process with the delta-ferrite replacing the liquid. Further discussion is beyond this thesis; the details model can refer to Flemings Chapter 5(Flemings 1974).

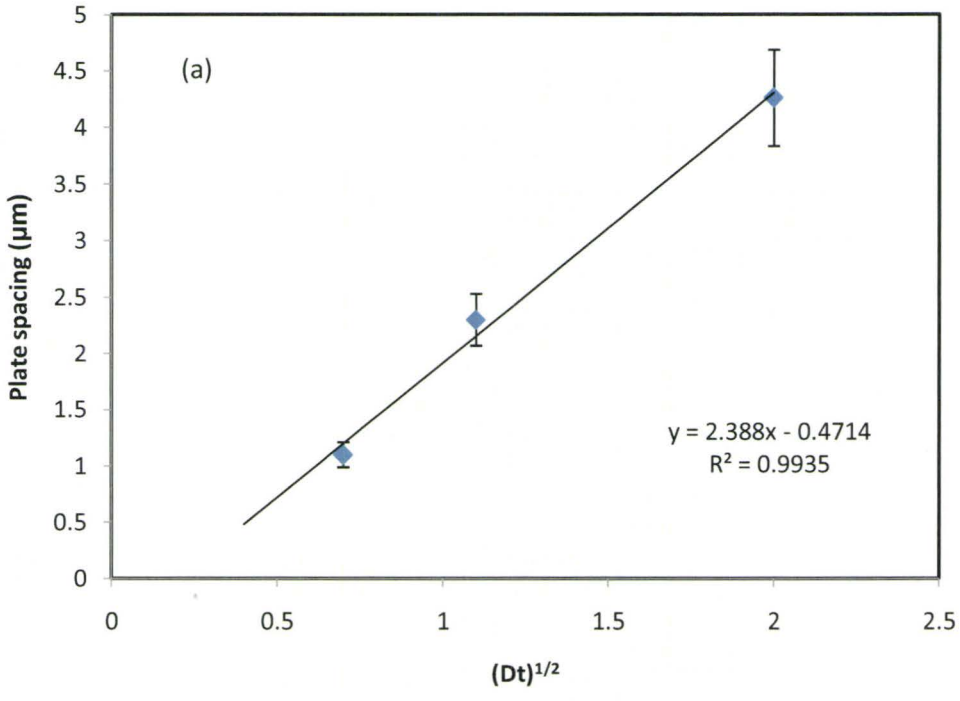

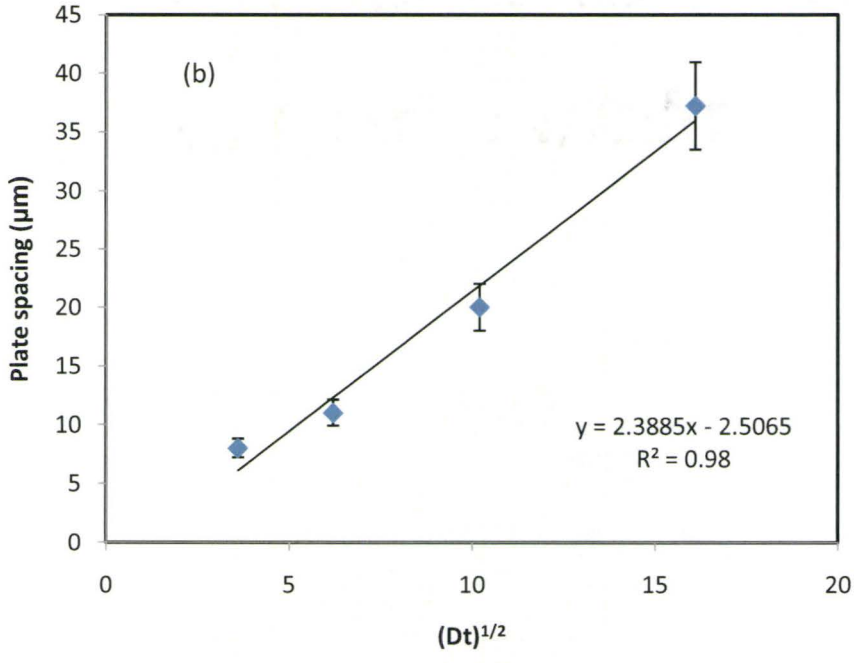

Figure 5-19 The relationship between inter-plate spacing and $\sqrt{D_{Al}t}$ at (a) 850°C and (b) 1125°C

5.4.3 Effects of Deformation

Figure 4.26 suggests that the deformed delta-ferrite recrystallized before the onset of the delta-ferrite to austenite phase transformation. During the phase transformation, the new and original delta grain boundaries provide nucleation sites for austenite precipitation. Figure 4.29 (b) clearly shows the nucleation of austenite on the newly recrystallized delta-ferrite grains. Comparison of Figures 4.20(a) and 4.26 (a), clearly shows that deformation prior to the onset of the delta-ferrite to austenite transformation can significantly refine the delta-grain size. The effectiveness of this method is due to the fact that the newly recrystallized grains and are quickly pinned by the precipitation of the austenite phase as shown in Figure 4.29 (b). It is critical that the deformation be carried out immediately before the onset of phase transformation in order to avoid rapid grain growth of the newly recrystallized grains.

5.5 Application to the Design of Improved TSCDR Processes

In this section, the grain growth model developed in section 5.1 and 5.2 will be used to predict the delta grain growth and austenite grain evolution in the TSCDR process prior to thermomechanical processing. The possibility of designing new alloys or new processes to produce improved more uniform fine microstructures will be discussed. This includes the use of duplex microstructures, increasing the cooling rate and increasing austenite nucleation sites during delta to austenite phase transformation

5.5.1 Apply Grain Growth Model to TSCDR Process

During typical TSCDR practice, large TiN particles are formed in the liquid during the late stages of solidification. These particles coarsen during subsequent solid state process at high temperature(Köthe et al. 1998; Nagata et al. 2002). These large precipitates exert a small Zener pinning effect(Smith 1948). Strong Zener pinning conditions are not encountered until fine Nb(C,N) precipitates are formed during thermomechanical processing(Kwon and DeArdo 1991; Palmiere et al. 1994; Poths et al. 2005). For this reason, our results on the precipitate-free model alloys can be used to model the grain-size evolution during TSCDR up to the point where the slabs exit the homogenization furnace and thermomechanical processing begins.

Table 5-12 Phase transformation temperature of APIX 60

Temperature (°C)	>1524.5	1524.5~ 1496.8	1496~ 1477.5	1477.5.~ 1448	1448~ 852
Phase	Liquid	Liquid + Delta	Delta	Delta +Gamma	Gamma

A key point that needs to be considered is that cooling rate varies from the slab surface to the slab center leading to variations in the microstructure evolution and grain-size. The grain growth model developed for delta grain growth and austenite grain growth can be used to calculate delta and austenite grain size evolution at different positions in the slab. Table 5.12 lists the relevant transformation temperatures for APIX60, as calculated from the TCFE2 database of ThermoCalc.

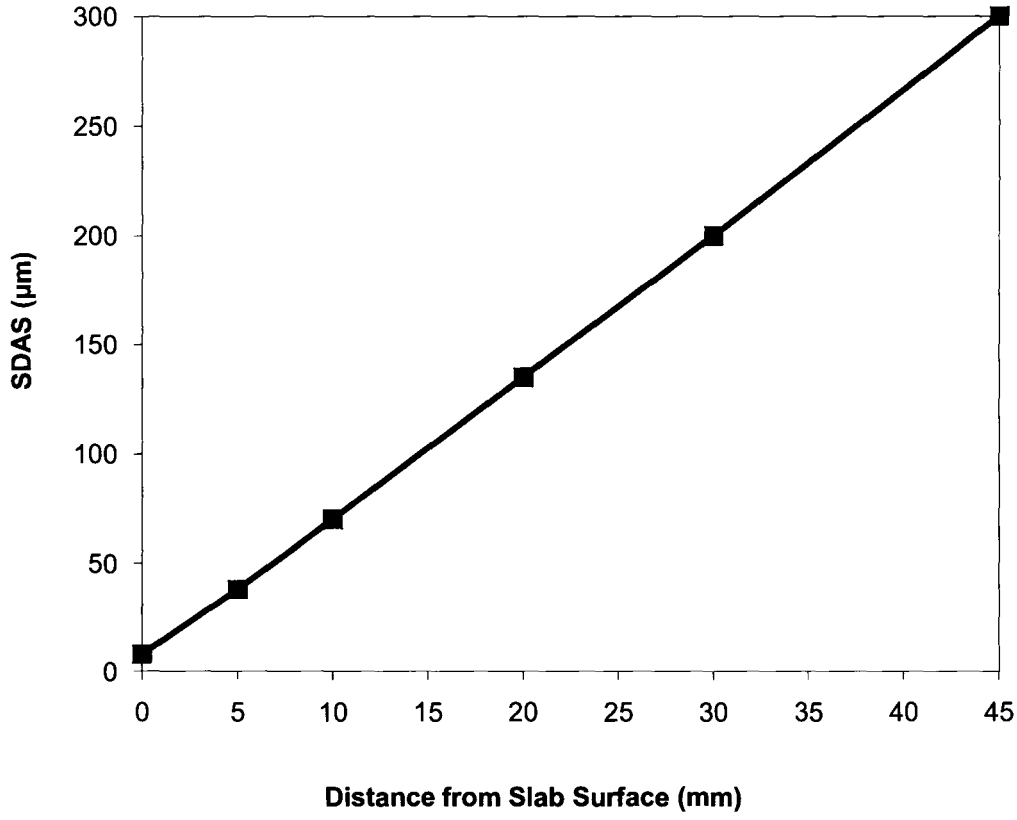

Figure 5-20 Secondary dendrite arms spacing as a function of position within the APIX60 slab. The solid line is based on the interpolation of two measurements made in this investigation

We have not attempted to model the delta to gamma transformation. Instead we simply assumed that the delta grain growth occurs down to 1470°C and austenite grain growth occurs at lower temperatures. The initial delta-ferrite grain size is taken to be the secondary dendrite arm spacing (SDAS). This was experimentally measured near the surface and at the centre of the thin slab provided by Nucor. Linear variation of the dendrite arms spacing with slab

thickness was assumed as shown in Figure 5.20. The initial austenite grain size was assumed to be smaller than the final delta grain size by a factor of 3(Yin et al. 1999; Kim et al. 2006) which allowed us to capture the effect of grain refinement due to the delta to gamma transformation. Finally, CON1D V7.0 Slab Casting Heat Transfer Model (Meng and Thomas 2003) from Nucor was used predict the cooling rate at each point of the slab. For example the cooling rates at the surface, 5mm, 10mm, 20mm, and 30mm below the surface and at the centre of the slab are shown in Figure 5.21.

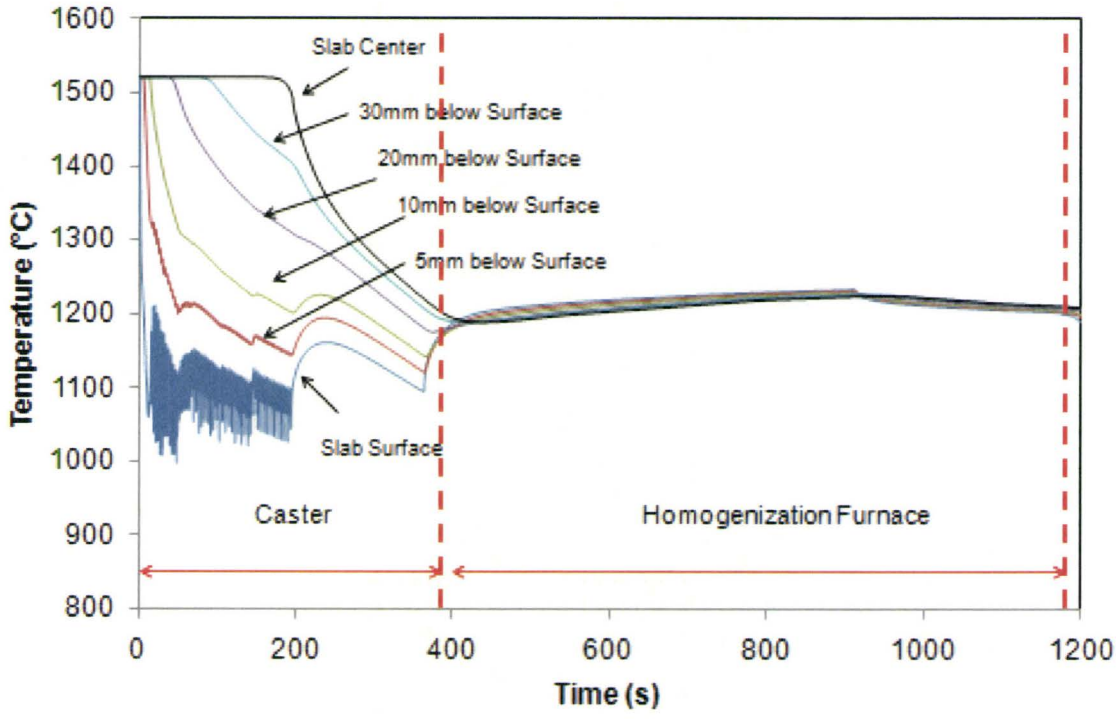

Figure 5-21 CON1D V7.0 Slab Casting Heat Transfer model predicted cooling curves at the surface, 5m, 10mm, 20mm, 30mm below the surface and the centre of the slab

An example of delta grain size evolution with time 5mm below the slab surface is shown in Figure 5.22. The austenite grain size evolution at the same position (5mm below the surface) with time just before leaving the holding furnace is shown in Figure 5.23. The solid line represents the model predicted grain diameter and the dish line represents the temperature profile in the TSCDR process at the corresponding slab position.

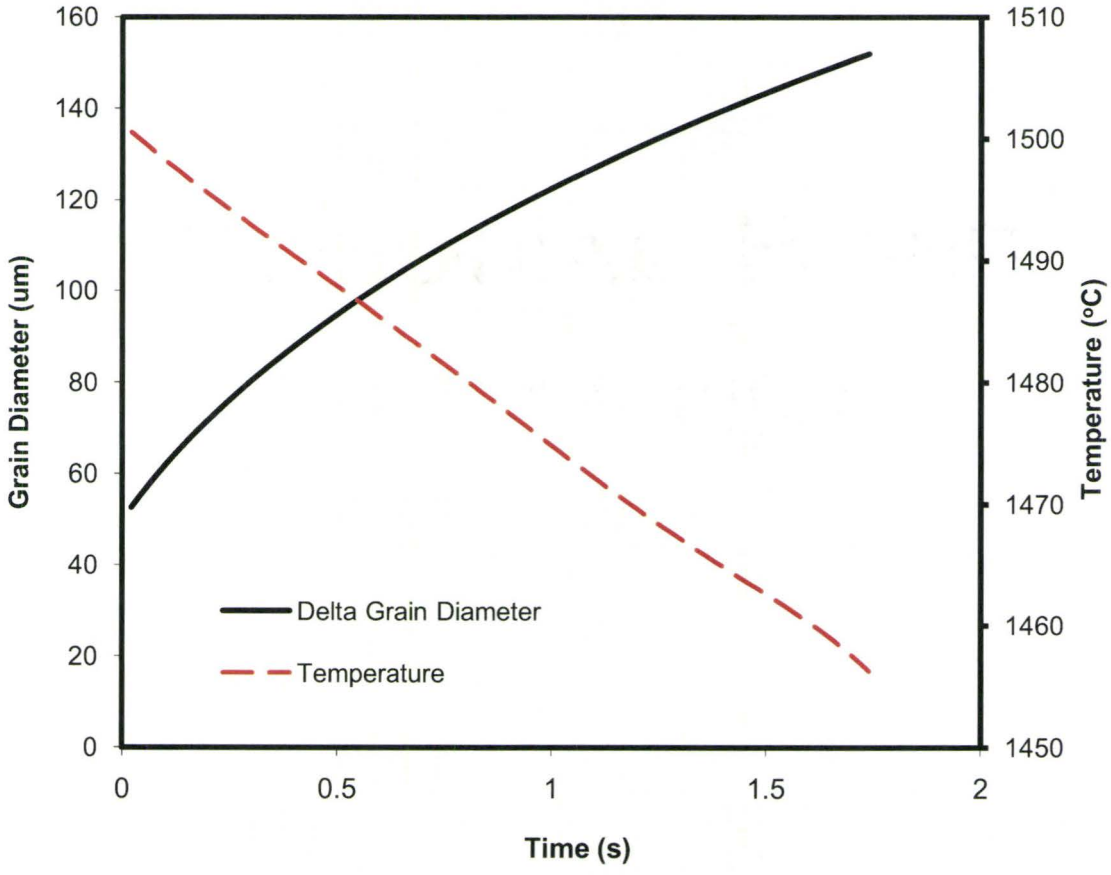

Figure 5-22 The predicted delta grain size evolution with time 5mm below the slab surface

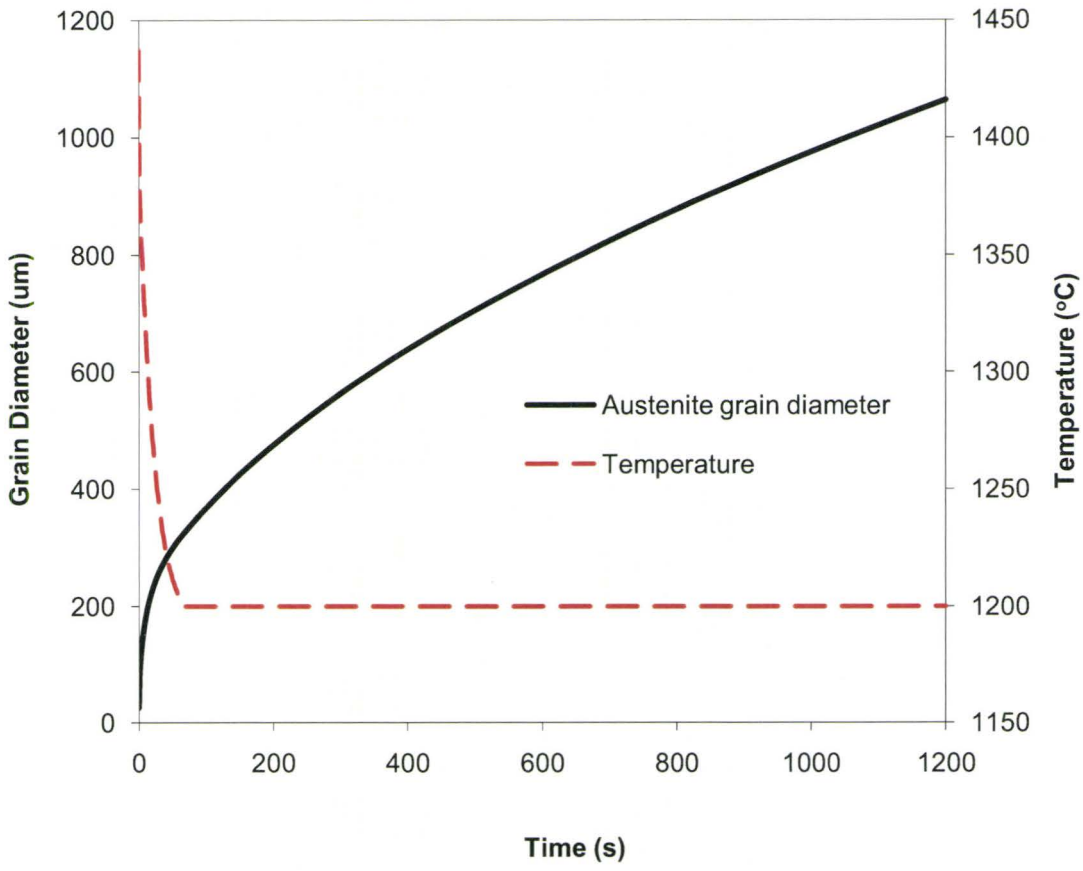

Figure 5-23 The predicted austenite grain size evolution 5mm below slab surface before leaving the HF

Similar calculations were performed as a function of the slab thickness. Figure 5.24 shows the predicted delta grain size as a function of position, just before the onset of the delta to gamma transformation. The solid diamonds are the calculated delta grain sizes at the slab surface; the solid line is used to highlight the trends of grain size change with distance from the surface of the slab. In addition, one can calculate the austenite grain size that would be expected when the slab is about to enter the homogenization furnace as shown in Figure 5.25. The grain size upon leaving the homogenization furnace is shown Figure 5.26. The solid

symbols and solid lines have the same meaning as before. The predicted gamma grain size as a function of slab thickness as the slab leaves the homogenization furnace can be compared to industrial samples obtained from the slab after leaving the homogenization furnace; an example of such data is also shown in Figure 5.25 for comparison. Very good agreement is obtained between the predicted and measured austenite grain size as a function of position. This lends further support to the simple grain-growth treatment used here.

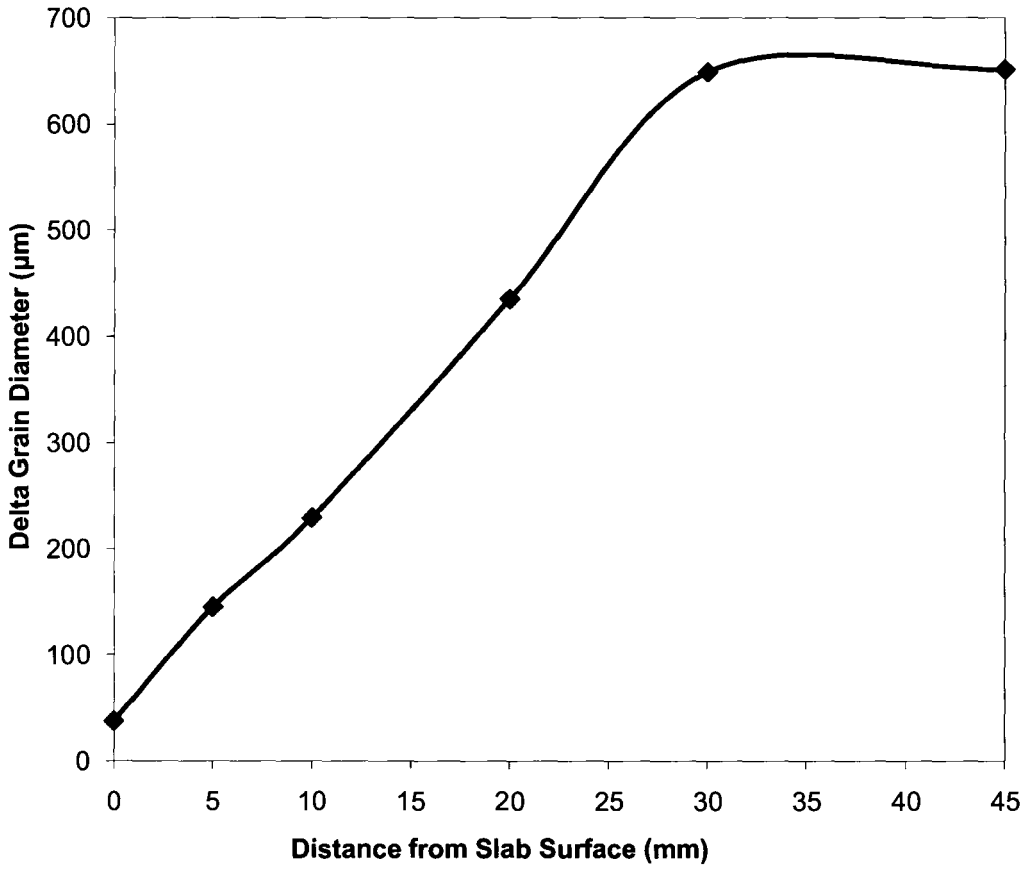

Figure 5-24 The predicted delta grain size as a function of slab position just before the onset of the delta to gamma transformation

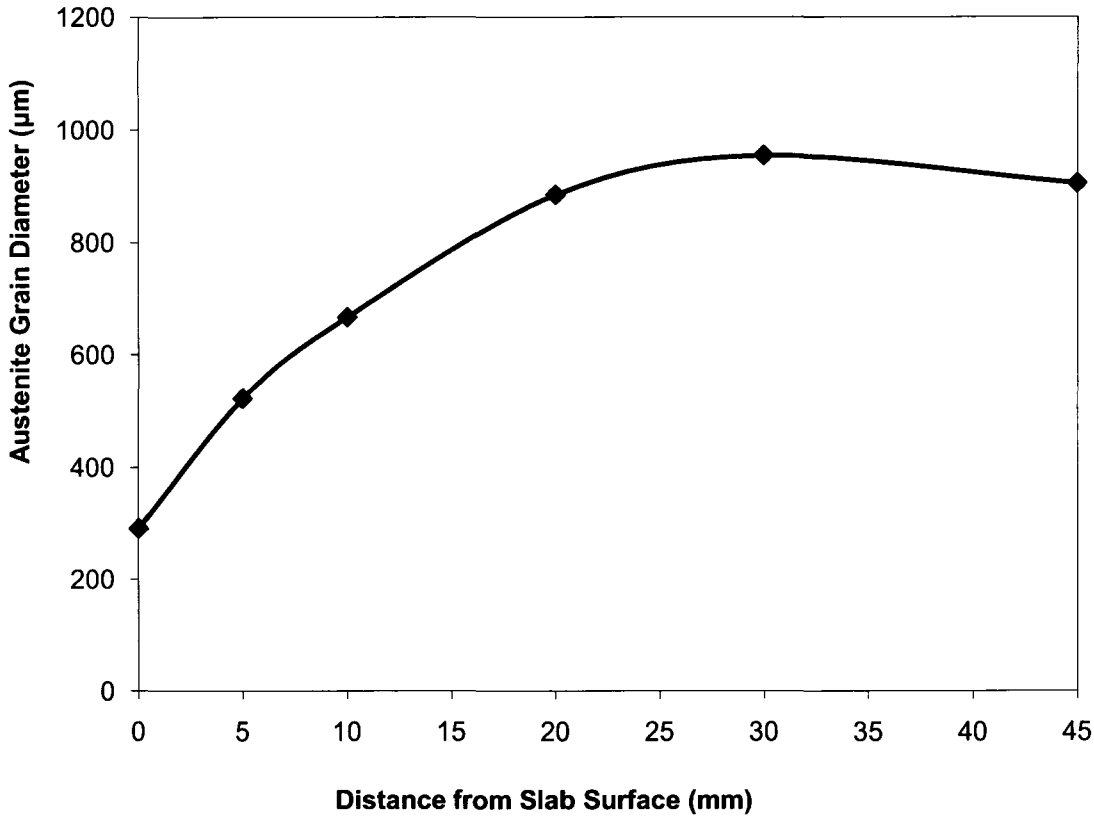

Figure 5-25 Predicted austenite grain size when the slab is about to enter the homogenization furnace

The results of Figure 5.24, 5.25 and 5.26 show that the austenite grain size before entering the homogenization furnace are non-uniform with finer grains being present near the surface. After homogenization at 1200°C, which is above the precipitate pinning temperature for the present steel (APIX60), the grains at the surface grow significantly and become comparable in size to those at the centre of the slab. If a lower homogenization temperature or higher microalloying content is used, it is possible to pin grain growth in the homogenization

furnace. This, however, would lead to a non-uniform grain size distribution, with large grains, in excess of 800 μm, being present at the centre. This seems to be the case in higher grade API steels (e.g. X80) where it is often reported that the grain size at the centre is significantly larger than that at the surface of the slab.

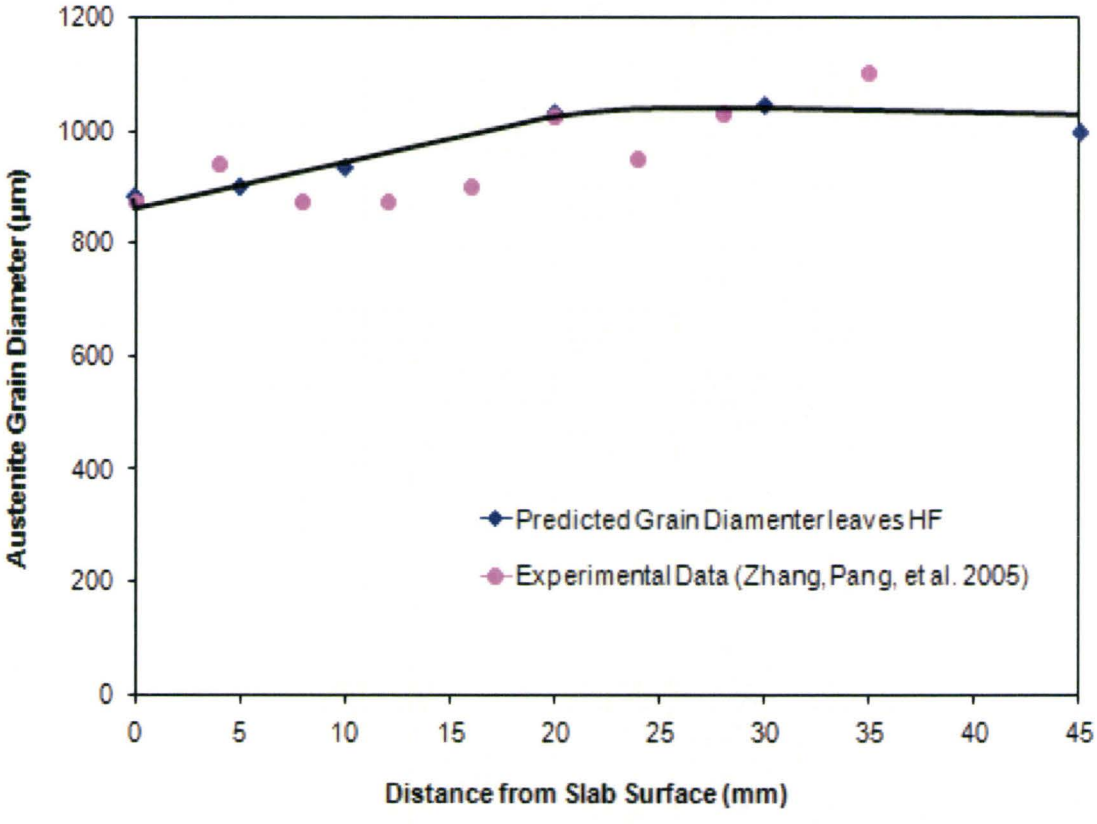

Figure 5-26 Predicted gamma grain size as the slab leaves the homogenization furnace

Another important consequence of the results shown in Figure 5.24, 5.25 and 5.26 is that grain-size control in both the delta and austenite is necessary in order to avoid the presence

of excessively large grains at the centre of the slab in the TSCDR process. Some variation in grain-size between the surface and the centre of the slab will still be present, as this is inherited from the as-cast structure (Figure 5.20)

It seems that future research efforts should focus on developing effective pinning methods for preventing grain growth in delta-ferrite and austenite prior to thermomechanical processing. This is a challenging task because rapid precipitate coarsening would be expected at high temperatures. However, austenite/delta duplex microstructure could provide a novel method to overcome this problem. The possibility is explored further in section 5.5.2.

5.5.2 Reducing Grain Growth Rate by Using Delta-Ferrite/Austenite Duplex Microstructure

As discussed in section 5.3, the delta grain growth rate is very slow when grain growth is controlled by the rate of second phase particles. For instance, when reheating to a temperature above 1200°C, the austenite particles coarsen is under bulk diffusion control. Differentiation of equation (5.8), leads to the following particle coarsening rate:

$$\frac{dr_\gamma}{dt} = \frac{1}{3r_\gamma(t)^2} \times \frac{8f(F_v)D\sigma_{\alpha\gamma}N_\alpha(1-N_\alpha)V_m}{9RT(N_\gamma - N_\alpha)^2\left[1+\partial \ln r / \partial \ln N_\alpha\right]} \quad \text{--- (5.36)}$$

Assuming particle-limited grain growth, delta grain growth rate is then:

$$\frac{dR_\delta}{dt} = \frac{\beta}{2F_v^{1/3}} \times \frac{1}{3r_\gamma(t)^2} \times \frac{8f(F_v)D\sigma_{\alpha\gamma}N_\alpha(1-N_\alpha)V_m}{9RT(N_\gamma - N_\alpha)^2\left[1+\partial \ln r / \partial \ln N_\alpha\right]} \quad \text{--- (5.37)}$$

where β is a constant. This equation cannot accurately be evaluated because of the uncertainty in the value of $f(F_v)$. Instead, the experimental grain growth kinetics in the duplex-alloy is compared with the model predictions in the absence of second phase particles. The comparison is shown Figure 5.27 (a) 1200°C, (b) 1280°C and (c) 1295°C. The solid line is the prediction of grain growth in pure materials without particle pinning. The initial grain diameter is 90μm; the delta grain boundary mobility is from equation (5.5) and the heating rate is that obtained experimentally from the data recorded by the thermocouple attached to the duplex-microstructure specimen. The solid points are the delta grain diameter in austenite/delta-ferrite duplex microstructure; the dashed line is used to guide the eyes.

When these two materials are heated to 1280°C for holding for 5 minutes, the materials without particle pinning is predicted to have a grain size of 1030μm, while, the grain in austenite/ delta duplex microstructure grows only to 117μm. In this Fe-1.5%Al model alloy, the delta-austenite two phase regions cover the temperature range 1305°C down to 780°C. Effective pinning is observed even at 1302°C. From these comparisons, it can be concluded that duplex microstructure is effective method for pinning grain growth at high temperature, at least from scientific point of view.

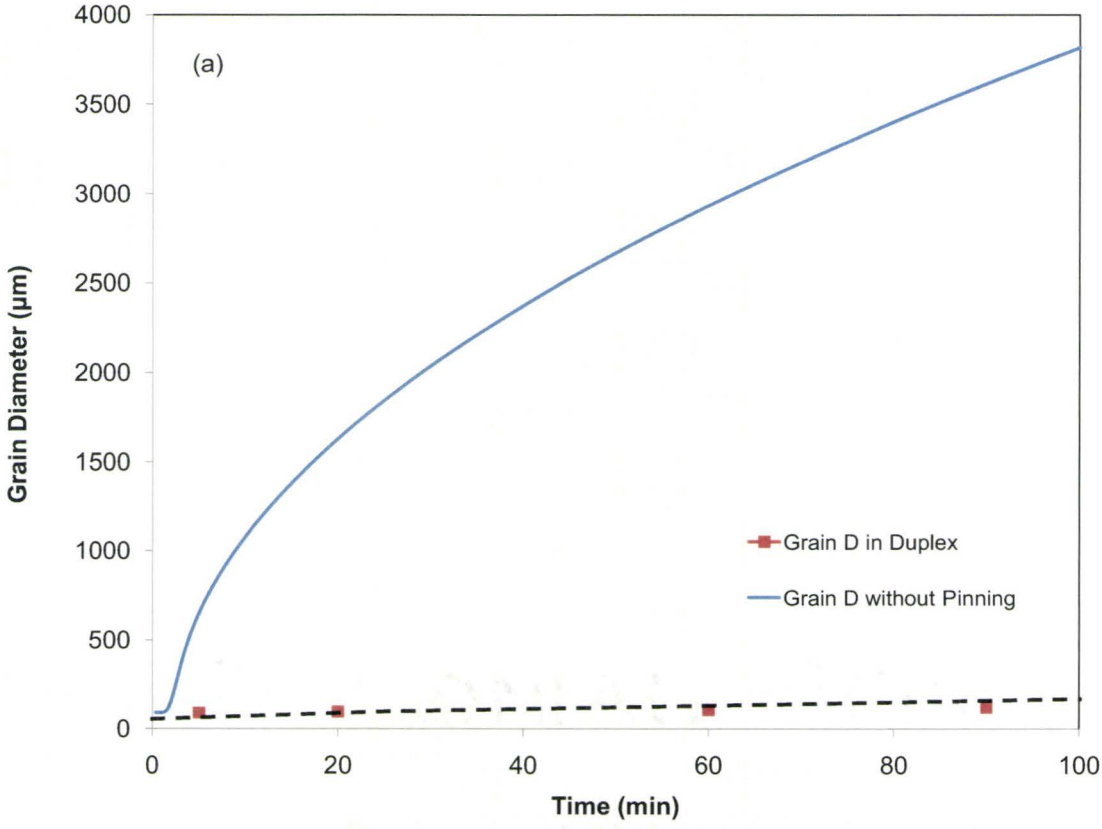
(a)
Grain Diameter (µm)
4000
3500
3000
2500
2000
1500
1000
500
0
0
20
40
60
80
100
Time (min)
Grain D in Duplex
Grain D without Pinning

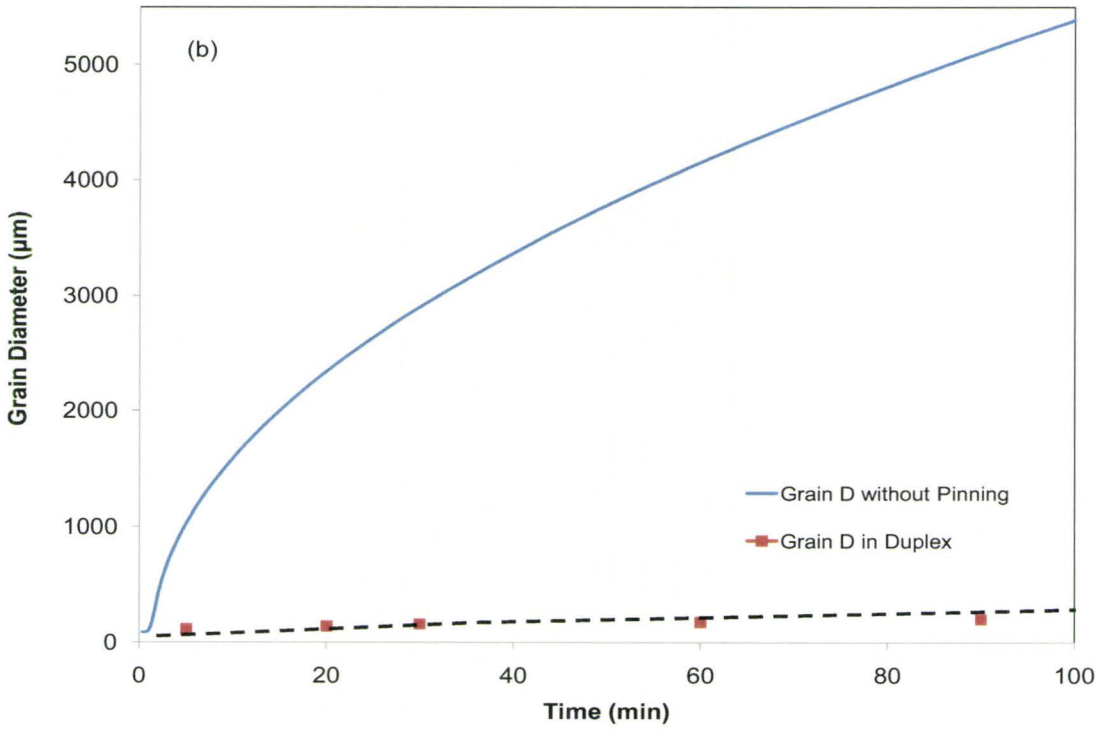
(b)
Grain Diameter (µm)
5000
4000
3000
2000
1000
0
0
20
40
60
80
100
Time (min)
Grain D without Pinning
Grain D in Duplex

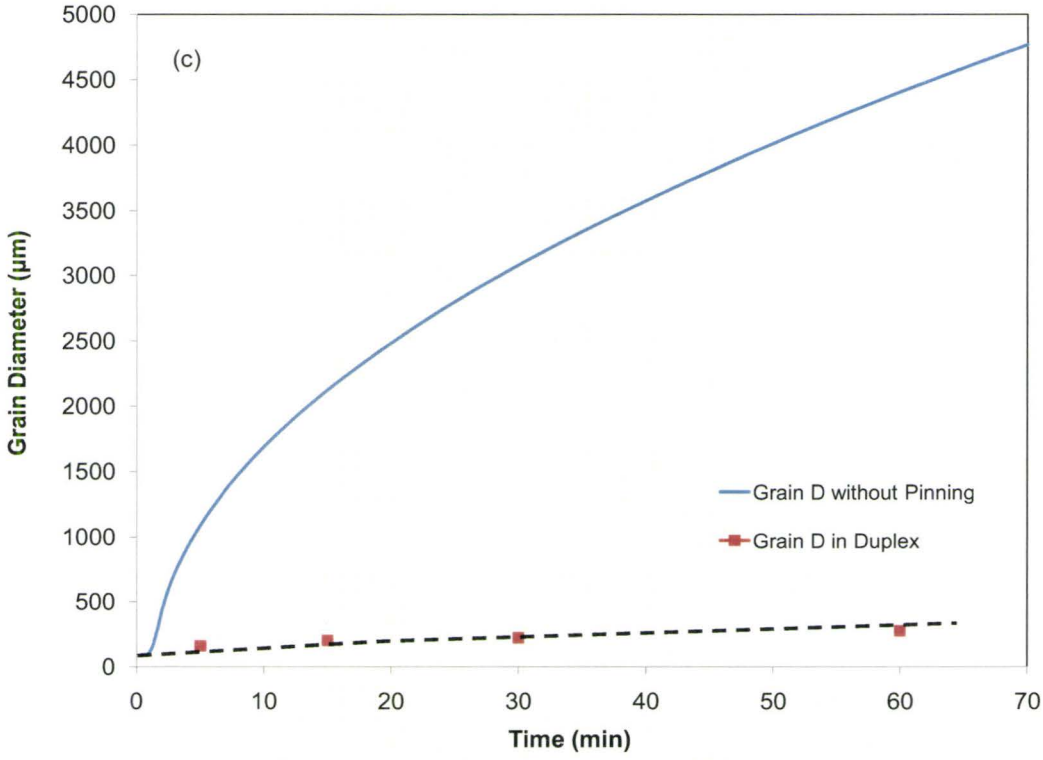

Figure 5-27 Comparison of delta grain growth without particle pinning and in delta-austenite duplex microstructure (a) 1200, (b)1280, and (c) at 1295°C

5.5.3 Increasing Cooling Rate to Refine As Cast Microstructure

Reducing the slab thickness can increase the cooling rate at the slab center and this can reduce the non-uniformity of the as cast microstructure by refining the grain at the center of the slab. In what follows, the consequences of reducing the slab thickness from 90mm to 50 mm and 30 mm are examined assuming that the only change is the enhanced cooling rate of the slab (Holzhauser et al. 1999; Gonzalez et al. 2003; Diószegi and Svensson 2005; Louhenkilpi et al. 2005). In order to determine the cooling rate and the initial secondary dendrite arm spacing, the CON1D V7.0 Slab Casting Heat Transfer

Model (Meng and Thomas 2003) from Nucor was used for slabs of 90mm, 50mm and 30mm slab thickness as shown in Figure 5.28.

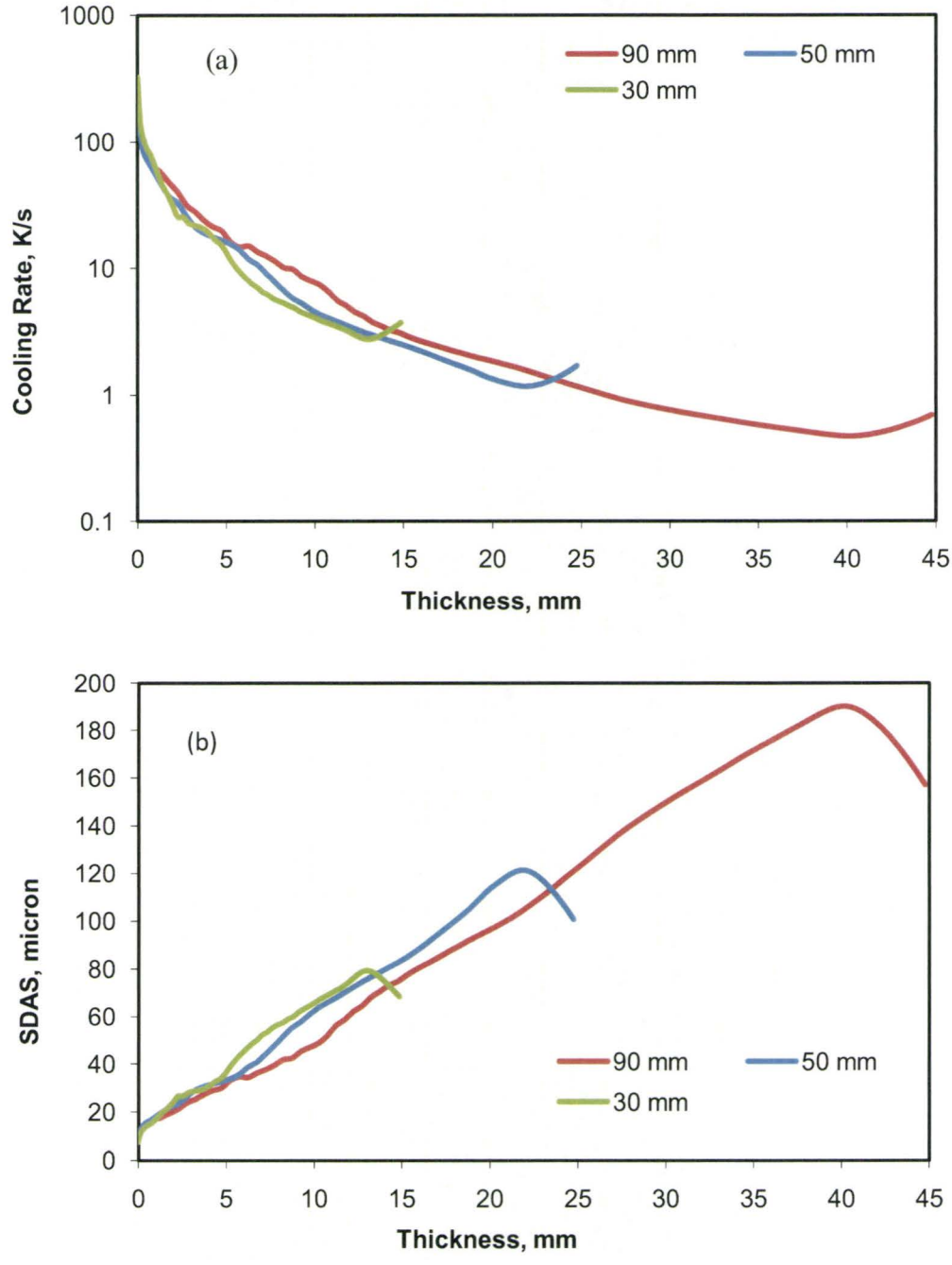

Figure 5-28 CON1D V7.0 Slab Casting Heat Transfer model predicted (a) Cooling curves and (b) SDAS at different position of 30, 50 and 90mm slab

The initial delta-ferrite grain size was, once again, taken to be the secondary dendrite arm spacing (SDAS). The model predictions of delta grain size as a function of position for the 30mm, 50mm thin slab just before the onset of the delta to gamma transformation are shown in Figure 5.29, which also includes, for comparison, the results shown earlier for the 90 mm slab. The calculated austenite grain size before entering the homogenization furnace is shown in Figure 5.30. The symbols in these Figures have the same meaning as before.

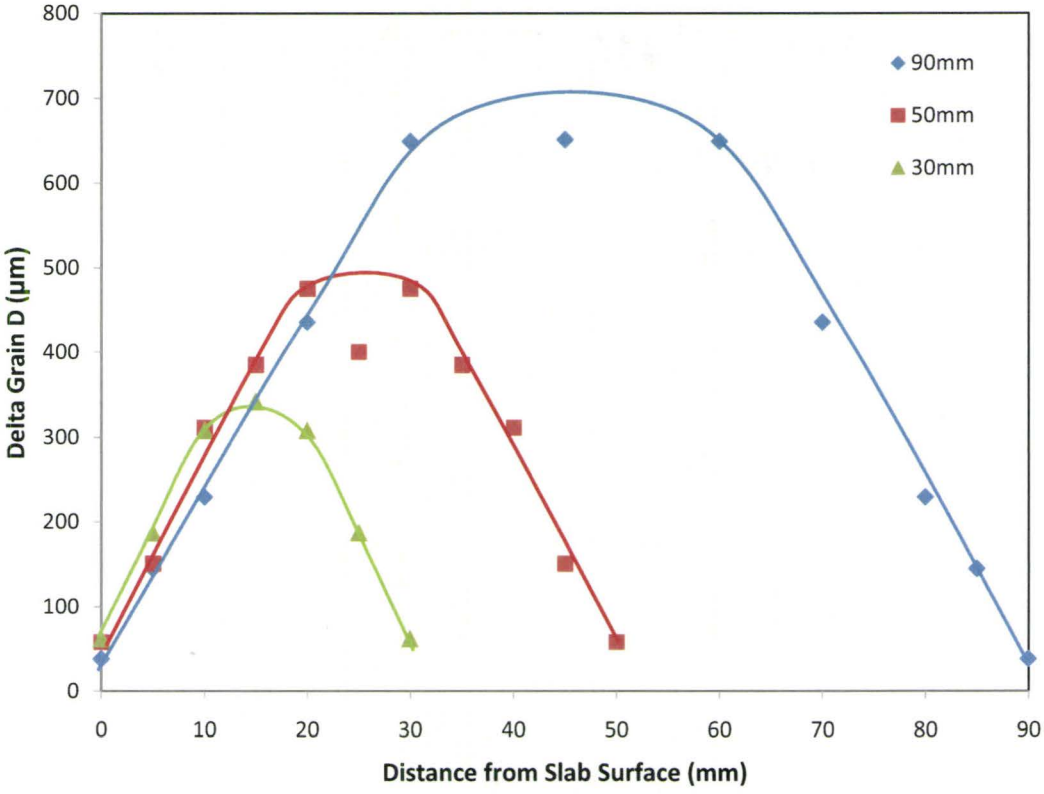

Figure 5-29 The predicted delta grain size of 30, 50, and 90mm slab as a function of slab position just before the onset of the delta to gamma transformation

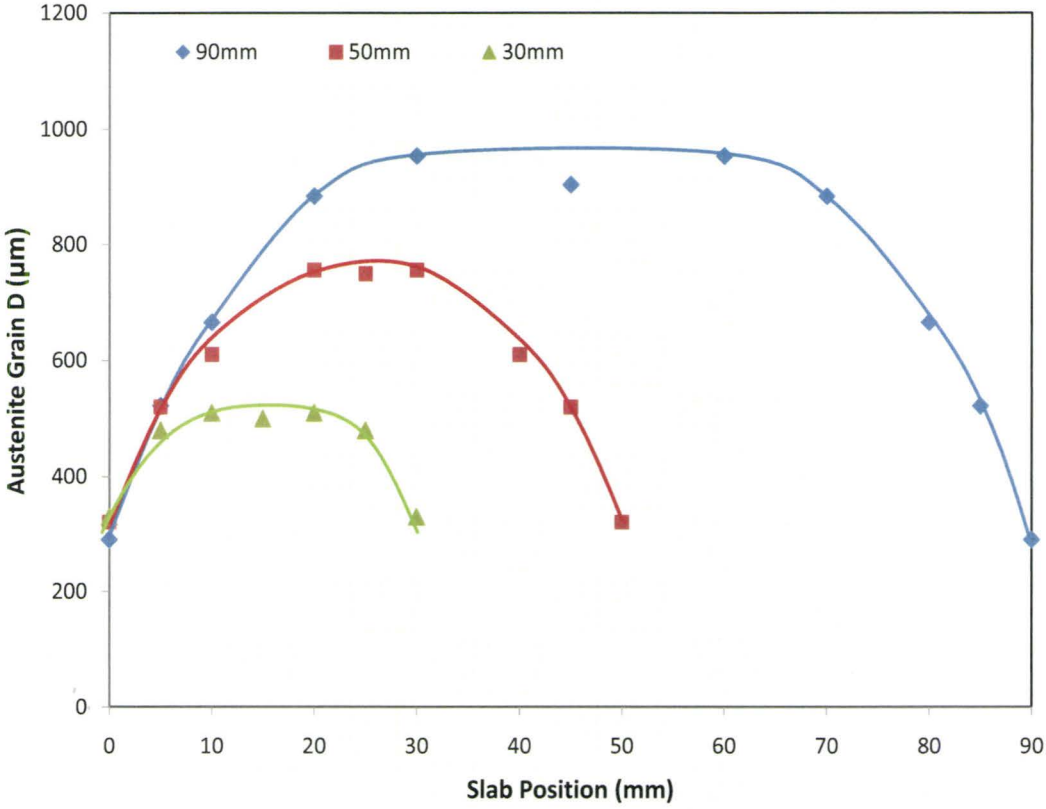

Figure 5-30 Predicted austenite grain size of 40mm slab when the slab is about to enter the homogenization furnace

It is clear from these calculations that the homogeneity of the microstructure has improved by the enhanced cooling rate at the centres of the thinner slabs. When the slabs are about to enter the homogenization furnace, the ratio of largest grain size to smallest grain size is 3.3 in 90mm slab, 2.4 in the 50mm slab and 1.5 in 30mm slab. One can conclude that reducing the slab thickness can refine and homogenize the as cast microstructure due to the enhanced cooling rate at the centre of the slab. The main

difficulty in applying this method is that it requires changing the layout of TSCDR process. In addition, the smaller slab thickness will further reduce the amount of thermomechanical processing that can be performed downstream and this may end up leading to larger average grain size and possibly more non-uniformity despite the improved initial microstructure. It would appear that an optimum thickness could be determined by considering both the solidification and grain growth (as described above) as well as the subsequent thermomechanical processing.

5.5.4 Increasing the Number of Austenite Nucleation Sites during Delta-ferrite to Austenite Phase Transformation

Another solution for achieving a better microstructure using TSCDR process is to increase the austenite nucleation sites available during delta-ferrite to austenite phase transformation. As reviewed in the literature, there are three methods that can be applied for this purpose: (a) Deformation during delta-ferrite to austenite phase transformation(Zarandi and Yue 2005; Rezaeian et al. 2008); (b) Using oxide particles to increase the nucleation sites for austenite during delta to austenite phase transformation(Karasev and Suito 2006; Suito et al. 2006); and (c) Thermal cycling near the transformation temperature (delta to austenite) to achieve repeated refinement due to the phase transformation.

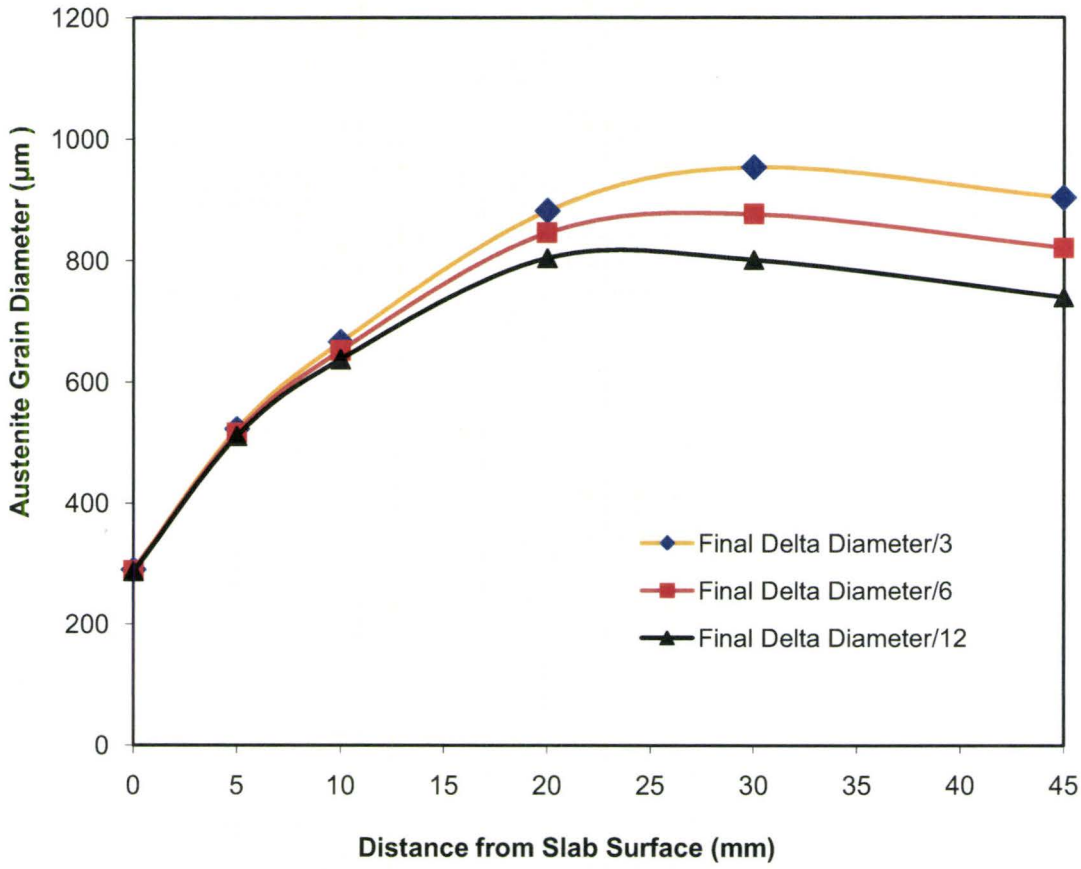

Figure 5-31 Predicted austenite grain size when the slab is about to enter the homogenization furnace with different austenite nucleation sites

As shown in Figure 4.28, deformation at just onset of the delta to austenite phase transformation will increase the austenite nucleation sites. The austenite phase particles on the recrystalized delta grain will future inhabit the delta grain growth in the downstream operation. Figure 5.31 summarized the predicted austenite grain size when the slab is about to enter the homogenization furnace for a different density of austenite

nucleation sites. The various lines represent the grain size achieved when 12, 6, and 3 austenite grains nucleate within each delta grain. The calculation reveals that these extra nucleation sites have little effect on the final grain size at the surface of the slab, the austenite grain do decrease with increasing the austenite nucleation sites.

5.5.5 Experimental Validation of the Benefits of the Model Alloy

All of the experiments performed in this contribution involved reheating samples with a very homogenous microstructure that was obtained by rolled and homogenization. Under industrial TSCDR conditions, delta-ferrite and austenite grain growth both occur in the heterogeneous (segregated) microstructure produced by solidification. In order to verify the effectiveness of the model alloy in inhibiting high temperature grain-growth under realistic starting conditions, some work on solidification was performed to reproduce the as-cast microstructures (Appendix I). These microstructures are then used as starting microstructures for studying grain growth during cooling.

As described in Appendix I, different dipping materials were dipped into the melt for different times. Once the bars were removed from the dipping bath, the solidified shells were cooled down to room temperature at different rates using air, forced air and water quenching. The reproduced cooling rates are shown in Figure 5.32, which also includes the calculated (CON1D) predicted cooling rates on the surface, 5 and 10mm below the 90mm slab surface.

The simulation cooling rate using water, forced-air and air quenching are similar to the cooling rates on the slab surface, 5mm and 10mm below the slab surface during the TSCDR process.

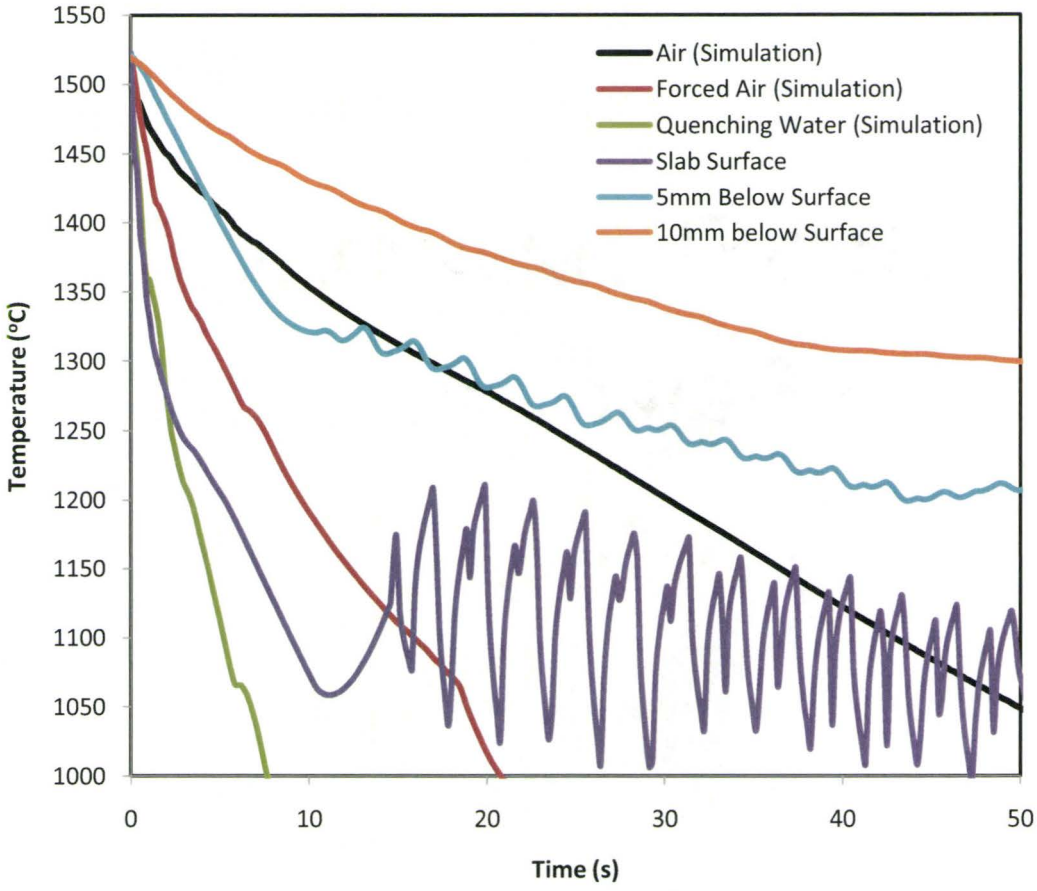

Figure 5-32 Temperature profile when the solidified shell cooling down in air, with fan and quenched into icy water.

The microstructures of Fe-1.5%Al model alloy using different cooling rates are shown in Figure 5.33 for (a) air, (b) forced air, and (c) water quenching. The microstructure of APIX60 after air quenching is shown in (d). It can be conclude that the delta grain sizes in the model alloy are much finer than the austenite grain size in the APIX60 microalloyed steel. For the model alloy, the delta grain will enter delta-ferrite/austenite two phase region and then be

stabilized to room temperature during cooling; however, the APIX60 microstructure evolution will follow the process as shown in Figure 2.1, and the austenite grains grow rapidly due to absence of pinning at high temperature.

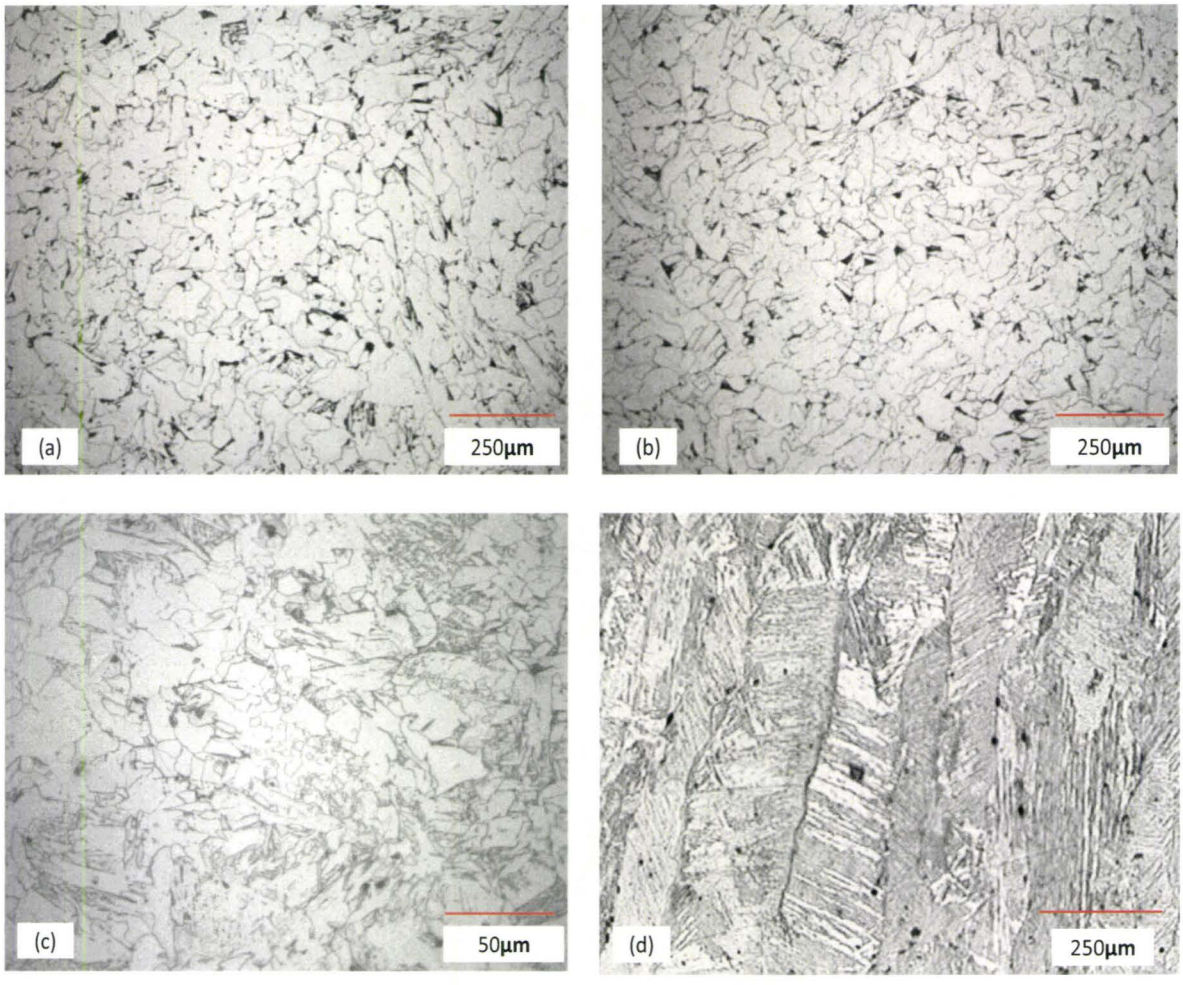

Figure 5-33 Microstructures of Fe-1.5% model alloy closed to the outside the steel dipping pipe cooling down in (a)air, (b)fan, (c) icy water. (d) microstructure of APIX60 cooling down in air

When the steel dipping pipe was emerged into the melt, solidification started inside the steel pipe and along the outside pipe as shown in Figure AI-4. Under

equilibrium cooling conditions, material solidifies as delta-ferrite and austenite precipitation occurs in the solid states. However, industrial cooling conditions, will lead to non-equilibrium solidification and some austenite will form during solidification. Figure 5.34(a) shows austenite precipitates along the delta grain boundaries: the dark phase is austenite which transformed to pearlite and the tiny grains along the big grain boundaries is also austenite phase which transformed to alpha ferrite during the cooling. The grain size bi-model distribution clearly shows transformed alpha ferrite distribution and original delta grain size distribution (Figure 5.34(b)). As discussed in Section 5.3, these austenite precipitates will pin the delta grain growth in the subsequent cooling.

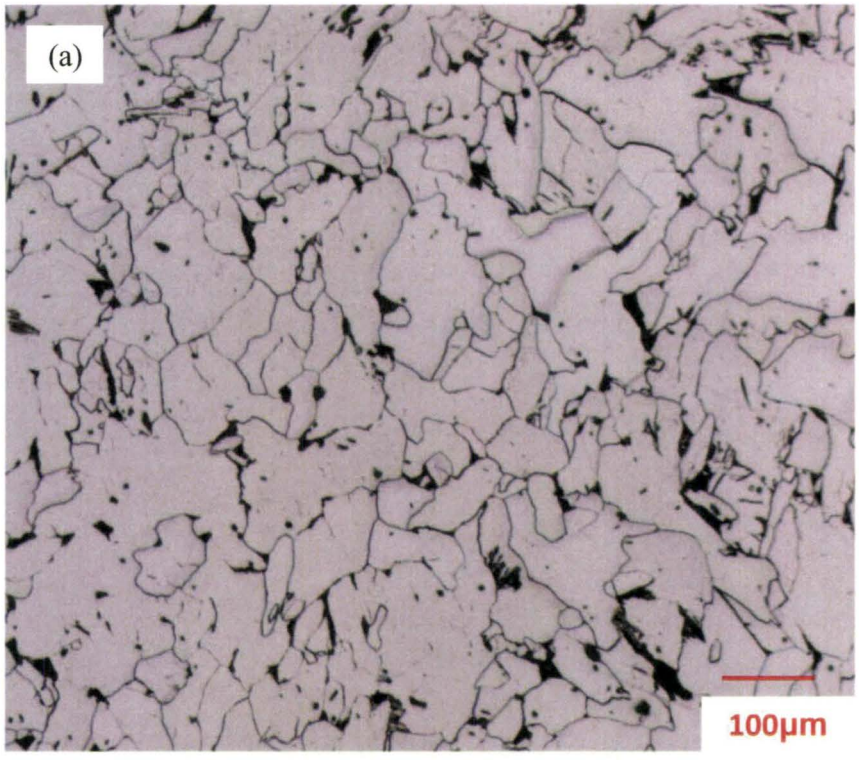

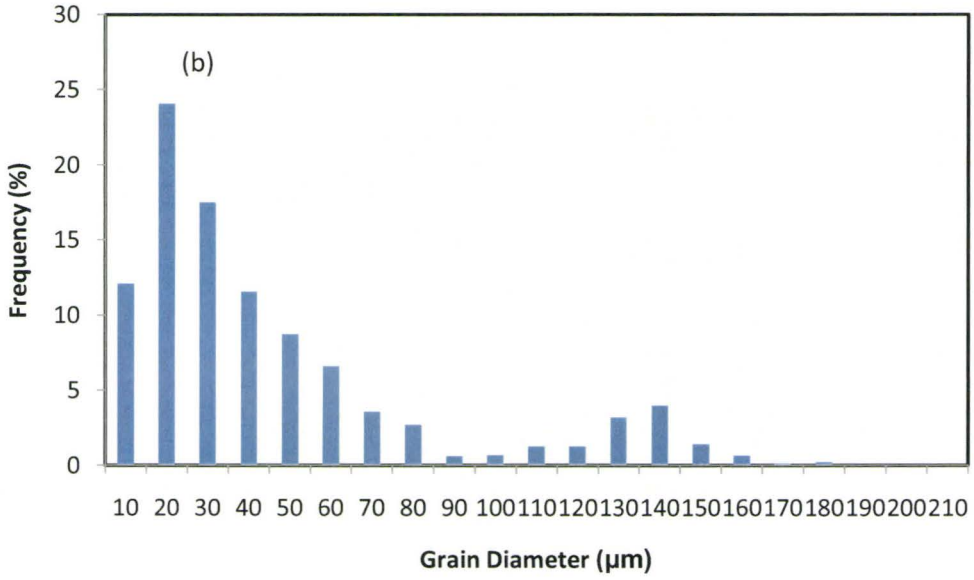

Figure 5-34 (a) Microstructures of Fe-1.5% model alloy closed to outside the steel dipping pipe cooling down in air, (b) Grain size distribution of the same sample

Using the assumption of no diffusion of the substitutional elements in the solid, the SCHEIL module of ThermoCalc can be used to evaluate the phase formed during non-equilibrium cooling of the model alloy. In this calculation, carbon back-diffusion in the solid is allowed to take place. As shown in Figure 5.35 (a), the liquid will start to solidify as the delta-ferrite at 1528°C; the substitutional solute concentration will increase due to the extremely slow diffusion in the solid. Once the temperature drops to 1455°C, the austenite phase will come out, and the liquid phase and austenite phase will exist until 1290°C. The predicted austenite mole fraction with temperature is shown is Figure 5.35(b). When the temperature reaches 1445°C, there is about 0.5% of austenite along the

delta grain boundaries, these austenite particles can pin the delta grain growth in the subsequently cooling as shown in Figure 5.34(a).

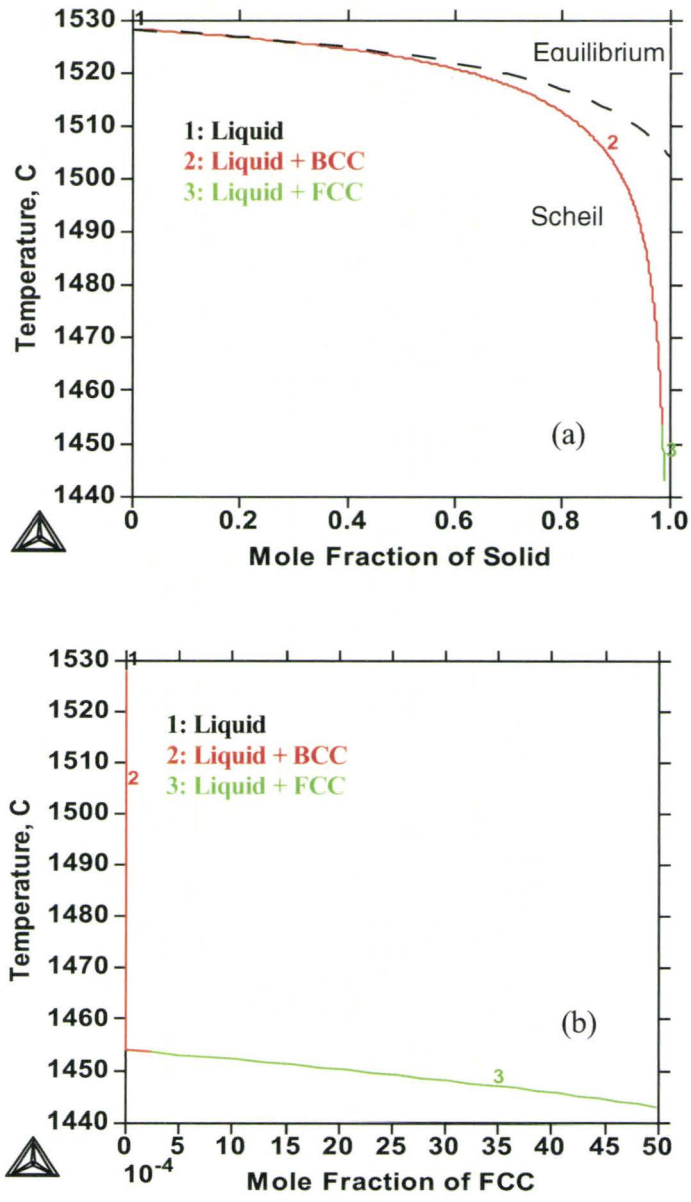

Figure 5-35 ThermoCalc using SCHEIL model predicted non-equilibrium solidification (a) mole fraction of solid and (b) mole fraction of austenite

The delta grain size evolution of the Fe-1.5%Al model alloy during the solidification process under different cooling rates can be predicted using the grain growth model described in Section 5.1. It will be assumed that the initial grain size is 7.5μm according to Figure 5.33 (c), and the delta grain boundary mobility is following equation (5.5). The results of the predicted delta grain size are compared to the experimental data with different cooling rates as shown in Figure 5.36 for (a) air, (b) forced-air, and (c) water quenching. The red dashed line is the temperature profile during the solidification process (secondary axis), the solid line is the predicted delta grain diameter without pinning, and the light orange line is the predicted austenite phase fraction formed during the solidification process using the SCHEIL model. The solid points present experimentally determined the delta-ferrite grain size. This was obtained from the mean of the second peak of the bimodal distribution shown in Figure 5.30(b) as this is believed to present the original delta-ferrite grains present at high temperature. Assuming the delta grains are completely pinned by the austenite particles as soon as the austenite phase appears, then the dashed black line in these graphs would represent the predicted the delta grain size in the model alloy taking in account the effects of pinning due to the non-equilibrium precipitation of austenite during solidification. The very good agreement between the model prediction and the experimental points confirmed the effectiveness of model alloy in inhibiting high temperature grain-growth under TSDCR process conditions.

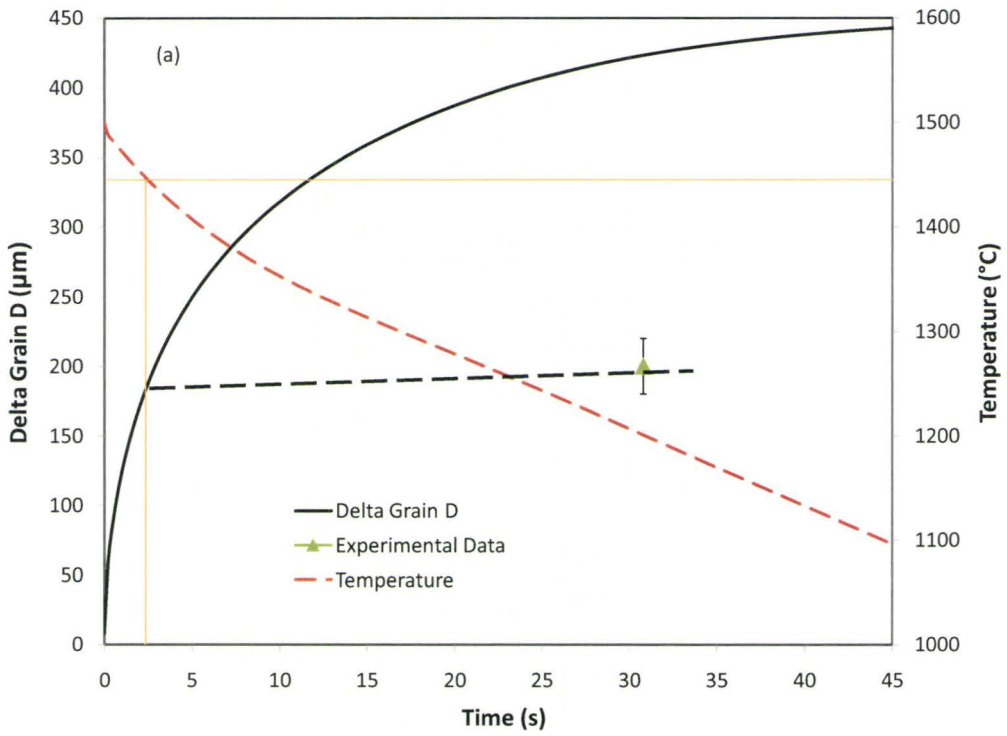
(a)
Delta Grain D (µm)
Temperature (°C)
Time (s)
Delta Grain D
Experimental Data
Temperature
0
50
100
150
200
250
300
350
400
450
1000
1100
1200
1300
1400
1500
1600
0
5
10
15
20
25
30
35
40
45

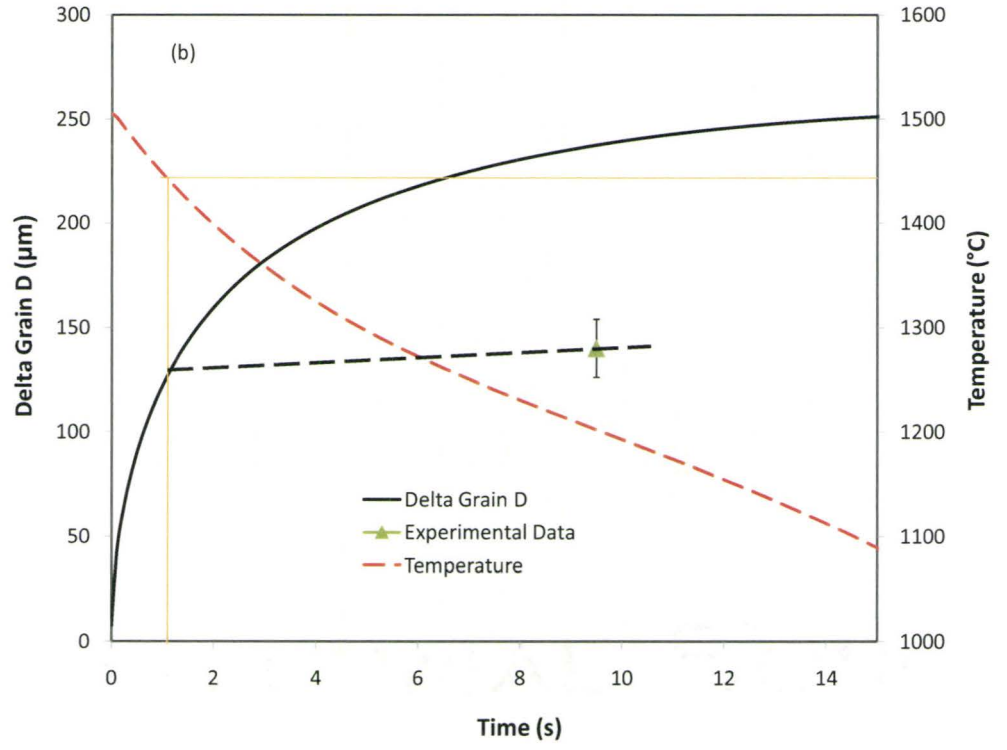
(b)
Delta Grain D (µm)
Temperature (°C)
Time (s)
Delta Grain D
Experimental Data
Temperature
0
50
100
150
200
250
300
1000
1100
1200
1300
1400
1500
1600
0
2
4
6
8
10
12
14

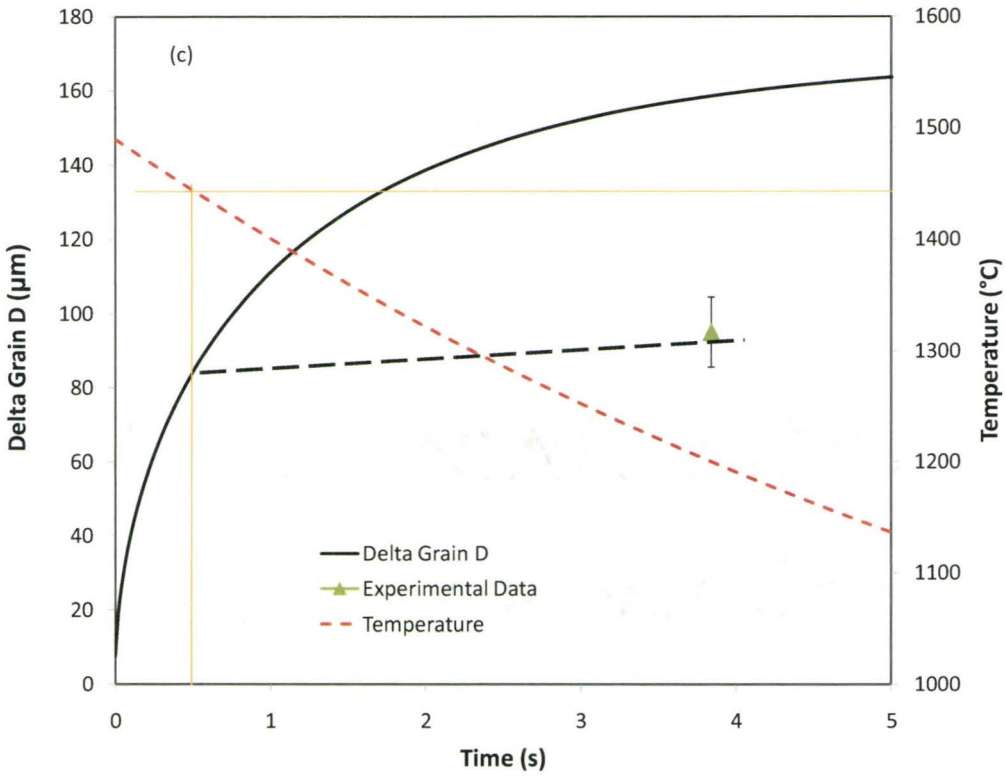

Figure 5-36 The model predicted delta grain size compared to the experimental data with different cooling rate (a) using air, (b) using forced air, and (c) using quenching water

As shown in Figure 5.32, the cooling rates obtained under water quenching, forced air and air cooling of the dipping bar are similar to the cooling rates encountered in a 90mm slab at the surface and to 5 and 10mm below the surface. One can thus estimate the grain size that would be obtained at various positions of the 90mm slab of the proposed model alloy. These grain sizes are compared to those obtained in traditional APIX60 steel just before entering the holding furnace (Figure 5.37). In order to compare under identical conditions, the experimental cooling rates recorded for the dipping experiments were used

to calculate the grain size of the APIX60 steel using the model described in section 5.1. It should be noted that the APIX60 steel transforms to austenite during cooling while the model alloy does not. As result the comparison shown in Figure 5.37 is between the austenite grain size and the delta grain size in the model alloy. The results clearly show the advantage of the proposed alloy.

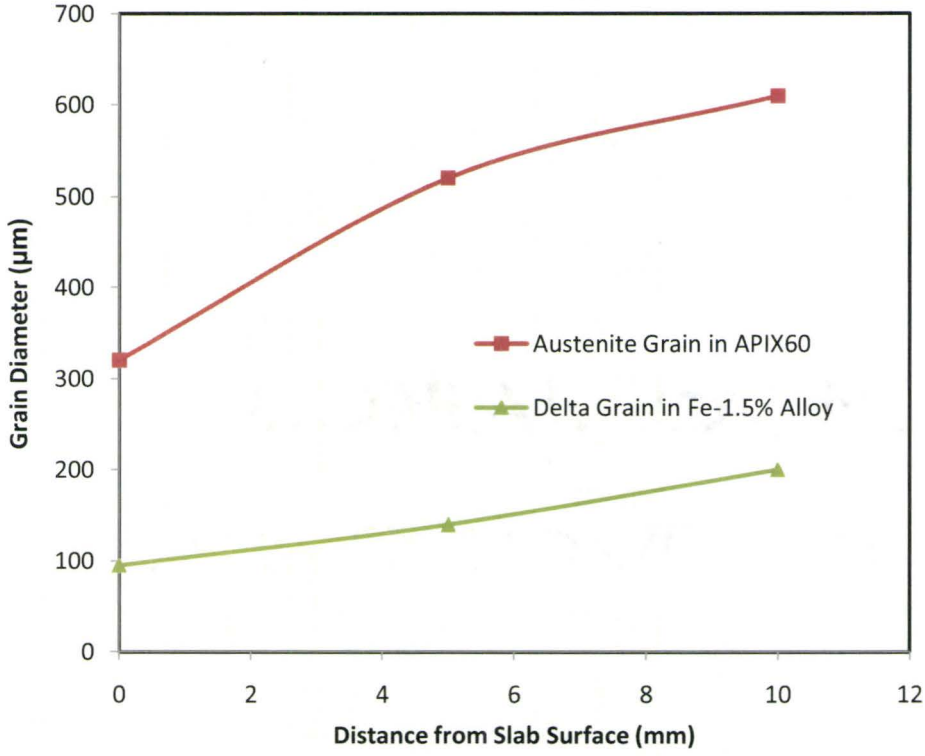

Figure 5-37 The comparison of grain size evolution with slab distance using TSCDR process to produce APIX60 and Fe-Al% model alloy

Chapter 6 Summary and Conclusions

Extensive experiments were performed to investigate the microstructure evolution of the TSCDR microalloyed steels prior to thermomechanical processing. The emphasis of this work was placed on solid state microstructure evolution including kinetics of the delta grain growth, the delta-ferrite to austenite phase transformation and the austenite grain growth. Some novel methods are applied for refining and homogenizing the as-cast microstructure of microalloyed steels so as to meet higher API standards. The main findings of this work are:

1. For the first time, the kinetics of delta-ferrite grain growth was studied using a model alloy in which delta-ferrite is stable down to room temperature. The results were modeled using a non-isothermal grain growth model. These results are applicable to the development of microalloyed steels in which particle pinning and solute drag effects are negligible at high temperatures.

2. Austenite grain growth was investigated at temperatures between 1100 and 1400°C using Nb/Ti-free alloy to bypass the complications of particle pinning and abnormal grain growth. Grain growth kinetics at 1300 and 1400°C was successfully described using a model similar to that used to model grain-growth in delta-ferrite.

3. In order to pin the delta grain growth at high temperature, a novel delta-ferrite/austenite duplex microstructure was developed, in which, a small volume fraction of austenite is used to pin delta grain growth. When the reheating temperature is higher than 1200°C, the coarsening of the austenite particles was bulk diffusion controlled. The austenite particle coarsening rate constant was predicted from modified LSW theory by coupling the equilibrium composition, diffusivity, and particle volume fraction. When the temperature is lower than 1200°C, the coarsening of austenite particles is controlled by grain boundary diffusion. When the austenite particle pinning pressure is much larger than the driving force for delta grain growth, the delta grain growth is completely arrested. When the pinning pressure is equal to the driving force for grain growth, grain growth proceeds at a rate controlled by the coarsening kinetics of the austenite particles. Finally, when the pinning pressure is smaller than the driving force, grain growth occurs with a net driving force of $P - P_z$. The model-predicted limiting grain-size is in good agreement with experimental results and a transition from a particle-boundary correlated limiting grain size to a non-correlated limiting grain size occurs at a volume fraction of about 5% in agreement with literature.

4. The kinetics of the delta-ferrite to austenite phase transformation was investigated using quenching dilatometer; the results showed that the austenite phase formed along the original delta grain boundaries, and the delta-ferrite grain growth was totally pinned by the precipitation of austenite phase. The austenite morphology changed from cellar precipitation to Widmansatten pattern when the holding temperature decreased from 1125°C to 850°C; and the austenite size coarsened with decreased

cooling rate. The growth of delta-ferrite required the partitioning of the substitutional alloying elements.

5. The developed grain growth model successfully reproduced grain growth as a function of position within the APIX60 slab in the TSCDR process. The results suggest that it is essential to control grain growth in both delta-ferrite and austenite in order to maintain a grain size of less than 400μm prior to the onset of thermomechanical processing.

6. The possibility of designing new alloys or new processes to produce improved; more uniform and fine as-cast microstructures for TSCDR process are summarized in the following:

   6.1 The use of a delta-ferrite/austenite duplex microstructure is an effective method for pinning grain growth at high temperature. In the delta-ferrite/austenite duplex microstructure, the delta grain growth rate is very slow and controlled by the rate of coarsening of second phase particles. The developed grain growth model predicts that the delta grain size is 10 times smaller in duplex microstructure than that in materials without pinning. Laboratory validation shows that the delta grains are pinned throughout the TSCDR process, starting from the final stages of solidification. The new the delta-ferrite/austenite duplex microstructure has great potential for producing more uniform as-cast microstructure for the TSCDR process as well as possible heat-resistant alloys for various engineering applications.

6.2 Reducing the slab thickness can increase the cooling rate at the slab center during the TSCDR process. Predictions of the grain growth model suggest that this would lead to less non-uniformity in the as-cast microstructure by refining the grains at the center of the slab. Once the slab thickness is reduced to 30mm, the ratio of the largest austenite grain to the smallest austenite is only 1.5.

6.3 Increasing the number of austenite nucleation sites during the delta-ferrite to austenite phase transformation is an effective method of refining and homogenizing the as-cast microstructure of TSCDR microalloyed steels. When the Fe-1.5%Al alloy was deformed prior to the onset of the delta to gamma transformation austenite nucleated prolifically along the original delta grain boundaries and the newly recrystallized delta grain boundaries. The application of 20% deformation generated more than 30 recrystallized grains in each original delta grain. In addition, the growth of these new grains was inhabited by the immediate precipitation of austenite along their grain boundaries.

BIBLIOGRAPHY

Ågren, J., Y. Brechet, C. Hutchinson, J. Philibert and G. Purdy, Eds. (2006). Thermodynamics and Phase Transformations - The Selected Works of Mats Hillert. Les Ulis Cedex A, France, EDP Science.

Andersson, M., J. Appelb, A. Tilliander, K. Nakajima, H. Shibata, S.-y. Kitamura, L. Jonsson and P. JÖnsson (2006). "Some Aspects on Grain Refining Additions with Focus on Clogging during Casting." ISIJ International **46**(6): 814-823.

Ardell, A. J. (1972). "The Effects of Volume Fraction on Particle Coarsening: Theoretical Considerations." Acta Metallurgica **20**: 61-71.

Ashby, M. F. and R. M. Centamore (1968). "The Dragging of Small Oxide Particles by Migrating Grain Boundaries in Copper." Acta Metallurgica **16**: 1081-1092.

Asimow, R. (1963). "Clustering Kinetics in Binary Alloy." Acta Metallurgica **II**: 72-73.

Bacroix, B. (2004). Recrystallization and grain growth : SF2M : proceedings of the second Joint International Conference on Recrystallization and Grain Growth. Annecy, France, Zurich ; Great Britain : Trans Tech.

Bakkaloğlu, A. (2002). "Effect of Processing Parameters on the Microstructure and Properties of an Nb Microalloyed Steel." Materials Letters **56**: 200-209.

Banks, K. M. (2005). "Microstructural Control and DWTT Toughness in Thick-Walled Nb-Ti-V Microalloyed Linepipe Steels." Materials Science Forum **500-501**: 303-310.

Bouchard, D. and J. S. Kirkaldy (1997). "Prediction of Dendrite Arm Spacings in Unsteady- and Steady-state Heat Flow of Unidirectionally Solidified Binary Alloys." Metallurgical and Materials Transactions B **28B**(4): 651-663.

Brailsford, A. D. and P. Wynblatt (1979). "The dependence of ostwald ripening kinetics on particle volume fraction." Acta Metallurgica **27**: 489-497.

Burke, J. E. and D. Turnbull (1952). "Recrystallization and Grain Growth." Progress in Metal Physics **3**: 220-292.

Cahn, J. W. (1962). "The Impurity-Drag Effect in Grain Boundary Motion." Acta Metallurgica **10**(September): 789-798.

Cahn, R. W. and P. Haasen (1983). Physical Metallurgy, North-Holland Physics Publishing.

Campanella, T., C. Charbon and M. Rappaz (2004). "Grain Refinement Induced by Electromagnetic Stirring: A Dendrite Fragmentation Criterion." Metallurgical and Materials Transactions A **35A**(10): 3201-3210.

Campbell, P., W. Blejde, R. Mahapatra and R. Wechsler (2004). "Recent Progress on Commercialization of CASTRIP® Direct Strip Casting Technology at Nucor Crawfordsville." Metallurgist **48**(9-10): 507-514.

Camporredondo-S., J. E., A. H. Castillejos-E., F. A. Acosta-G., E. P. Guttérrz-M. and M. A. Herrera-G (2004). "Analysis of Thin-Slab Casting by the Compact-Strip Process: Part I. Heat Extraction and Solidification." Metallurgical and Materials Transactions B **35B**(6): 541-560.

Castillejos-E., A. H., M. A. Herrera-G., A. Acosta-G., R. Santos-P., E. P. Gutiere-M and R. G. d. la-P. (2005). Studies for the Improvement of the Secondary Cooling System of CSP Thin Slab Casters. 33rd McMaster Symposium on Iron & Steelmaking: Thinner Slab Casting, McMaster University, Hamilton, On, Canada.

Chakrabartia, D., C. L. Davisb and M. Strangwoodc (2005). "Characterisation of Bimodal Grain Structures and Their Dependence Inhomogeneous Precipitate Distribution during Casting." Materials Science Forum **500-501**: 613-620.

Chalmers, B. (1964). Principles of Solidification, John Wiley & Sons, Inc.

Cobo, S. J. and C. M. Sellars (2001). " Microstructural evolution of austenite under conditions simulating thin slab casting and hot direct rolling." Ironmaking and Steelmaking **28**(3): 230-236.

Cramb, A. W. (2007). "From Solid to Liquid: Key Issues in the Future of Steel Casting, ." Iron & Steel Technology **July**: 59-75.

Dahle, A. K. and L. Arnberg (1997). "Development of Strength in Solidifying Aluminum Alloys." Acta Materialia **45**(2): 547-559.

Davies, C. K. L., P. Nash and R. N. Stevens (1980). "The Effect of Volume Fraction of Precipitate on Ostwald Ripening." Acta Metallurgica **28**: 179-189.

Diószegi, A. and I. L. Svensson (2005). "On the Problems of Thermal Analysis of Solidification." Materials Science and Engineering A **413-414**: 474-479.

Dunn, C. G. and J. L. Walter (1966). Secondary Recrystallization. Recrystallization, Grain Growth and Textures, Ohio, ASM.

Elwazri, A. M., D. Bai, F. Siciliano and S. Yuel (2005). "Influence of Deformation and Coiling Temperature on Mechanical Properties of a High Strength Pipeline Steel." Materials Science Forum **500-501**: 597-604.

Elwazri, A. M., D. Bai, F. Siciliano and S. Yue (2005). "Influence of Deformation and Coiling Temperature on Mechanical Properties of a High Strength Pipeline Steel." Materials Science Forum **500-501**: 597-604.

Emi, T. and H. Fredriksson (2005). "High-Speed Continuous Casting of Peritectic Carbon Steels." Materials Science and Engineering A **413-414**: 2-9.

Evans, T. and L. Strezov (2000). "Interfacial Heat Transfer and Nucleation of Steel on Metallic Substrates." Metallurgical and Materials Transactions B **31B**(October): 1081-1089.

Fischmeister, H. and G. Grimvall (1973). Ostwald Ripening - A Survey. The Third International Conference on Sintering and Related Phenomena, The University of Notre Dame, Plenum Press.

Flemings, M. C. (1974). Solidification Processing, McGraw-Hill Inc.

Flores, O. and L. Martinez (1997). "Abnormal Grain Growth of Austenite in a V–Nb Microalloyed Steel." JOURNAL OF MATERIALS SCIENCE **32**: 5985-5991.

Gilmour, J. B., G. R. Purdy and J. S. Kirkaldy (1972). "Partition of Manganese during the Proeutectoid Ferrite Transformation in Steel." Metallurgical Transactions **3**(December): 3213-3222.

Gladman, T. (1966). "On the Theory of the Effect of Precipitate Particles on Grain Growth in Metals." Proc. R. Soc. London **A294**: 298-309.

Gladman, T. (1997). The Physical Metallurgy of Microalloyed Steel. London, Institute of Materials.

Gonzalez, M., M. B. Goldschmit, A. P. Assanelli, E. F. Berdaguer and E. Dvorkin (2003). "Modeling of the Solidification Process in a Continuous Casting Installation for Steel Slabs." Metallurgical and Materials Transactions B **34B**(8): 455-473.

Greenwood, G. W. (1956). "The Growth of Dispersed Precipitates in Solutions." Acta Metallurgica **4**: 243-248.

Grong, Ø., L. Kolbeinsen, C. v. d. Eijk and G. Tranell (2006). "Microstructure Control of Steels through Dispersoid Metallurgy Using Novel Grain Refining Alloys." ISIJ International **46**(6): 824-831.

Hellman, P. and M. Hillert (1975). "On the Effect of Second-phase Particles on Grain Growth." Scand. J. Metall **4**: 211-219.

Hillert, M. (1965). "On the Theory of Normal and Abnormal Grain Growth." Acta Metallurgica **13**: 227-238.

Hillert, M. (1988). "Inhibition of Grain Growth by Second-Phase Particles." Acta Metallurgica **36**: 3177-3181.

Hillert, M. and B. Sundman (1976). "A Treatment of the Solute Drag on Moving Grain Boundaries and Phase Interfaces in Binary Alloys." Acta Metallurgica **24**: 731-743.

Holzhauser, J. F., K. H. Spitzer and K. Schweredtfeger (1999). "Study of Heat Transfer Though Layers of Casting Flux: Experiments with a Laboratory Set-up Simulating the Conditions in Continuous Casting." Steel Research **70**(7): .252-257.

Holzhauser, J. F., K. H. Spitzer and K. Schweredtfeger (1999). "Study of Heat Transfer Though Layers of Casting Flux: Experiments with a Laboratory Set-up Simulating the Conditions in Continuous Casting." Steel Research **70**(7): 252-257.

Hoo, C., I. Teleszky, A. Roosz and Z. Csepeli (2006). "Estimation of the Cooling Rate on the Basis of Secondary Dendrite Arm Spacing in Case of Continuous Cast Steel Slab." Materials Science Forum **508**: 245-250.

Hu, B. and H. Li (1998). "Grain refinement of DIN226S alloy at lower titanium and boron addition levels." Journal of Materials Processing Technology **74**(1-3): 56-60.

Humphreys, F. J. (1997b). "A Unified Theory of Recovery, Recrystallization and Grain Growth, Based on the Stability and Growth of Cellular Microstructures – II the Effects of Second-Phase Particles." Acta Materialia **45**(12): 5031-5039.

Humphreys, F. J. and M. Hatherly (2004). Recrystallization and Related Annealing Phenomena, Elsevier Ltd.

Hunderi, O. and N. Ryum (1992). "The Interaction between Spherical Particles and Triple Lines and Quadruple Points." Acta Metallurgica **40**(3): 543-549.

Hunt, J. D. and S. Z. Lu (1996). "Numerical Modeling of Cellular/Dendrite Array Growth: Spacing and Structure Predictions." Metallurgical and Materials Transactions A **27A**(3): 611-623.

Hutchinson, C. R., H. S. Zurob, C. W. Sinclair and Y. J. M. Brechet (2007). "The Comparative Effectiveness of Nb Solute and NbC Precipitates at Impeding Grain Boundary Motion in Nb-Steels." Materials Science Forum **561-565**: 53-56.

Hutchinson, W. B. and B. J. Duggan (1978). "Influence of Precipitation on Recrystallization and Texture Development in An Iron-1.2% Copper Alloy." Metal Science **12**: 372-380.

Imagumbai, M. and H. Takechi (2003). "New Process for High-Toughness Line Pipe Material of Thin Slab and Direct Rolling " Materials Science Forum **426-432**: 1157-1162.

Jayanth, C. S. and P. Nash (1989). "Review - Factors Affecting Particle-Coarsening Kinetics and Size Distribution." Journal of Materials Science **24**: 3041-3052.

Kang, S.-J. L. (2007). Recrystallization and grain growth III: proceedings of the third International Conference on Recrystallization and Grain Growth,, Jeju Island, Korea, Stafa-Zurich, Switzerland: Trans Tech Publications.

Karasev, A. V. and H. Suito (2006). "Effect of Particle Size Distribution on Austenite Grain Growth inFe-0.05mass%C Alloy Deoxidized with Mn-Si, Ti, Mg, Zr and Ce." ISIJ International **46**(5): 718-727.

Kikuchi, M., M. Kajihara and S. K. Choi (1991). "Cellular Precipitation Involving Both Substitutional and Interstitial Solutes: Cellular Precipitation of Cr_2N in Cr-Ni Austenitic Steels." Materials Science and Engineering A **146**: 131-150.

Kikuchi, M., T. Urabe, G. Cliff and G. W. Lorimer (1990). "The Loss of Driving Force due to Volume Diffusion Ahead of A Migrating Boundary in A Cellular Precipitation Reaction." Acta Metallurgica Et Materialia **38**(6): 1115-1120.

Kim, H. S., Y. Kobayashi and K. Nagai (2006). "Prediction of Prior Austenite Grain Size of High-phosphorous Steels through Phase Transformation Simulation." ISIJ International **46**(6): 854-858.

Kirchner, H. O. K. (1971). "Coarsening of Grain-boundary Precipitates." Metallurgical Transactions **2**: 2861-2864.

Klinkenberg, C. and K.-E. Hensger (2005). "Processing of Niobium Microalloyed API Grade Steel on a Thin Slab Plant." Materials Science Forum **500-501**: 253-260.

Korchynsky, M. (2005). Optimization of High Strength (HS) Products Made by Thin Slab Technology. 33rd McMaster Symposium on Iron & Steelmaking: Thinner Slab Casting, McMaster University, Hamilton , Ontario, Canada, L8S 4L7, McMaster University Steel Research Centre.

Köthe, A., J. Kunze, G. Backmann and C. Mickel (1998). "Precipitation of TiN and (Ti,Nb)(C,N) during Solidification, Cooling and Hot Direct Deformation." Materials Science Forum **284-286**: 493-500.

Kreye, H. (1970). "Einfluss von Versetzungen auf dir Umlösung von Teilchen." Z. Metallkunde **61**: 108 - 112.

Kurz, W. and D. J. Fisher (1981). "Dendritic Growth and Limit of Stability Tip Radius and Spacing." Acta Metallurgica **29**(11-20).

Kurz, W. and D. J. Fisher (1998). Fundamentals of Solidification. Switzerland, Trans Tech Publication Ltd.

Kwon, O. and A. J. DeArdo (1991). "Interactions between Recrystallization and Precipitation in Hot-deformed Microalloyed steels " Acta Metallurgica **39**(4): 529-538.

Lee, H. M. (1990). "Design of High-temperature High-strength Al Ti V Zr Alloys." Scripta Metallurgica et Materiala **24** (12): 2443-2446.

Lee, H. M., S. M. Allen and M. Grujicic (1991a). "Coarsening Resistance of M_2C Carbides in Secondary Hardening Steels: Part I. Theoretical Model for Multicomponent Coarsening Kinetics." Metallurgical and Materials Transactions A **22A**(12): 2863-2868.

Li, T., X. Lin and W. Huang (2007). "Morphological evolution during solidification under stirring." Acta Materialia **54**(18): 4815-4824.

Li, W.-B. and K. E. Easterling (1990). "The Influence of Particle Shape on Zener Drag." Acta Metallurgica **38**(6): 1045-1052.

Li, X., Y. Fautrelle and Z. Ren (2007). "Influence of a high magnetic field on columnar dendrite growth during directional solidification." Acta Materialia **55**(16): 5333-5347.

Li, X., Y. Fautrelle and Z. Ren (2007a). "Influence of an axial high magnetic field on the liquid-solid transformation in Al-Cu hypoeutectic alloys and on the microstructure of the solid." Acta Materialia **55**(4): 1377-1386.

Lifshitz, I. M. and V. V. Slyozov (1961). "The Kinetics of Precipitation from Supersaturated Solid Solutions." J. Phys. Chem. Solids **19**: 35-50.

Liu, D., X. Huo, Y. Wang and X. Sun (2003). "Aspects of Microstructure in Low Carbon Steels Produced by the CSP Process." Journal of University of Science and Technology Beijing **10**(4): 1-6.

Liu, Z., Y. Kobayshi, J. Yang, K. Nagai and M. Kuwabara (2006). "'In-sit" Observation of the δ/γ Phase Transformation on the Surface of the Low Carbon Steel Containing Phosphorus at Various Cooling Rates." ISIJ International **46**(6): 847-853.

Louat, N. (1982). "The Resistance to Normal Grain Growth from A Dispersion of Spherical Particles." Acta Metallurgica **30**: 1291-1294.

Louhenkilpi, S., M. Makinen, S. Vapalahti, T. Raisanen and J. Laine (2005). "3D Steady State and Transient Simulation Tools for Heat Transfer and Solidification in Continuous Casting." Materials Science and Engineering A **413-414**: 135-138.

Lücke, K. and K. Detert (1957). "An Quantitative Theory of Grain-Boundary Motion and Recrystallization in Metals in the Presence of Impurities." Acta Metallurgica **5**(November): 628-837.

Lücke, K. and H. P. Stüwe (1963). On the Theory of Grain Boundary Motion Recovery and Recrystallization of Metals, New York, N.Y., USA, Gordon and Breach Science Publishers, Ltd.

Lücke, K. and H. P. Stüwe (1971). "On the Theory of Impurity Controlled Grain Boundary Motions." Acta Metallurgica **19**(October): 1087-1099.

Manohar, P. A., M. Ferry and T. Chandra (1998). "Five Decades of the Zener Equation." ISIJ International **38**(9): 913-924.

Marqusee, J. A. and J. Ross (1984). "Theory of Ostwald Ripening: Competitive Growth and Its Dependence on Volume Fraction." Journal of Chemical Physics **80**(1): 536-543.

Martin, J. W., R. D. Doherty and B. Cantor (1997). Stability of Microstructure in Metallic System. Cambridge, Cambridge University Press.

Mason, J. T., J. D. Verhoeven and R. Trivedi (1982). "Primary Dendrite Spacing. I. Experimental Studies." Journal of Crystal Growth **49**(3): 516-524.

Matlock, D. K., G. Krauss and J. G. Speer (2005). "New Microalloyed Steel Applications for the Automotive Sector." Materials Science Forum **500-501**: 87-96.

McCarmey, D. G. and J. D. Hunt. (1981). "Measurements of Cell and Primary Dendrite Arm Spacing in Directionally Solidified Aluminum Alloys." Acta Metallurgica **29**(11): 1851-1863.

Megahed, G. M., S. K. Paul, T. A. El-Bitar and F. Ibrahim (2005). "Development of X60/X70 Line Pipe Steels through EAF-Thin Slab Casting Technology at Ezz Flat Steel, Ain Sukhna, Egypt." Materials Science Forum **500-501**: 261-268.

Meng, Y. and B. G. Thomas (2003). "Heat-Transfer and Solidification Model of Continuous Slab Casting: CON1D." Metallurgical and Materials Transactions B **34B**(October): 685-705.

Meng, Y. and B. G. Thomas (2006). "Simulation of Microstructure and Behavior of Interfacial Mold Slag Layers in Continuous Casting of Steel." ISIJ International **46**(5): 660-669.

Morral, J. E. and G. R. Purdy (1994). "Particle Coarsening in Binary and Multicomponent Alloys." Scripta Metallurgica et Materiala **30**(7): 905-908.

Muller, J., W. Henning and C. Bilgen (2005). Advanced CSP Casting Technology for High-Quality Steels Grades. 33rd McMaster Symposium on Iron & Steelmaking: Thinner Slab Casting, McMaster University, Hamilton, Ontario, Canada, L8S 4L7, McMaster University Steel Research Centre.

Nagata, M. T., J. G. Speer and D. K. Matlock (2002). "Titanium Nitride Precipitation Behavior in Thin-Slab Cast High-Strength Low-Alloy Steels." Metallurgical and Materials Transactions A **33A**: 3099-3109.

Nes, E., N. Ryum and O. Hunderi (1985). "On the Zener Drag." Acta Metallurgica **33**(1): 11-22.

Nishizawa, T., I. Ohnuma and K. Ishida (1997). "Examination of the Zener Relationship between Grain Size and Particle Dispersion." Materials Transactions, JIM **38**: 950-956.

Palmiere, E. J., C. I. Garcia and A. J. DeArdo (1994). "Compositional and Microstructural Changes Which Attend Reheating and Grain Coarsening in Steels Containing Niobium." Metallurgical and Materials Transactions A **25A**: 277-286.

Phelan, D. and R. Dippenaar (2004). "Instability of the Delta-ferrite/austenite Interface in Low Carbon Steels: The Influence of Delta-ferrite Recovery Sub-structure." ISIJ International **44**(2): 414-421.

Porter, D. A. and K. E. Easterling (1992). Phase Transformation in Metals and Alloys. New York, Chapman & Hall.

Poths, R. M., W. M. Rainforth and E. J. Palmiere (2005). "Strain Induced Precipitation in Model and Conventional Microalloyed Steels during Thermomechanical Processing." Materials Science Forum **500-501**: 139-145.

Pottore, N. S., C. I. Garcia and A. J. DeArdo (1991). "Interrupted and Isothermal Solidification Studies of Low and Medium Carbon Steels." Metallurgical and Materials Transactions A **22A**: 1871-1880.

Priestner, R. (1998). "Microstructural Change during the Hot Working of As-Cast Austenite." Materials Science Forum **284-286**: 95-104.

Purdy, G. R., D. H. Weichert and J. S. Kirkaldy (1964). "The Growth of Proeutectoid Ferrite in Ternary Iron-Carbon-Manganese Austenite." Transactions of the Metallurgical Society of A. I. M. E. **230**(August): 1025-1034.

Randle, V. and B. Ralph (1986). "Interactions of Grain Boundaries with Coherent Precipitates during Grain Growth." Acta Metallurgica **34**(5): 891-898.

Reip, C.-P., W. Hennig, J. Kempken and R. Hagmann (2005). "Development of CSP Processed High Strength Pipe Steels." Materials Science Forum **500-501**: 287-294.

Rezaeian, A., F. Zarandi and S. Yue (2008). "Mechanism of Hot Ductility Improvement of a Peritectic Steel Containing Vanadium Using Very-High-Temperature Compression." Metallurgical and Materials Transactions A **39**(11): 2635-2644.

Ringer, S. P., W.-B. Li and K. E. Easterling (1989). "On the Interaction and Pinning of Grain Boundaries by Cubic Shaped Precipitate Particles." Acta Metallurgica **37**(3): 831-841.

Rios, P. R. (1987). "A Theory for Grain Boundary Pinning by Particles." Acta Metallurgica **35**: 2805-2814.

Rios, P. R. (1997). "Abnormal Grain Growth Development from Uniform Grain Size Distributions." Acta Materialia **45**(4): 1785-1789.

Rios, P. R. (1998). "Abnormal Grain Growth Development from Uniform Grain Size Distributions due to A Mobility Advantage." Scripta Materialia **38**(9): 1359-1364.

Rodriguez-Ibabe, J. M. (2005). "Thin Slab Direct Rolling of Microalloyed Steels." Materials Science Forum **550-501**: 49-63.

Sellars, C. M. and E. J. Palmiere (2005). "Modelling Strain Induced Precipitation of Niobium Carbonitride during Multipass Deformation of Austenite." Materials Science Forum **500-501**: 3-14.

Sim, H. S., K. B. Lee, H. R. Yang and H. Kwon (2005). "Influence of Severe Accumulative Rolling in a Low Carbon Microalloyed Steel." Materials Science Forum **500-501**: 581-587.

Smith, C. S. (1948). "Grains, Phases, and Interfaces: An Interpretation of Microstructure " Trans. Metall. Soc. A. I. M. E. **175**: 15-51.

Sobral, M. D. C., P. R. Mei, R. G. Santos, F. C. Gentile and J. C. Bellon (2003). "Laboratory simulation of thin slab casting." Ironmaking and Steelmaking **30**(5): 412-416.

Somboonsuk, K. and R. Trivedi (1984). "Interdendritic Spacing. I. Experimental Studies." Metallurgical and Materials Transactions A **15A**(6): 967-975.

Speer, J. G. and S. S. Hansen (1989). "Austenite Recrystallization and Carbonnitride Precipitaiton in Niobium Steels." Metallurgical and Materials Transactions A **20A**: 25-38.

Speight, M. V. (1968). "Growth Kinetics of Grain-boundary Precipitates." Acta Metallurgica **16**: 133-135.

Stefanscu, D. M. (2006). "Microstructure Evolution during Solidification of Steel." ISIJ International **46**(6): 786-794.

Strezov, L., J. Herbertson and G. R. Belton (2000). "Mechanisms of Initial Melt/Substrate Heat Transfer Pertinent to Strip Casting." Metallurgical and Materials Transactions B **31B**(October): 1023-1030.

Suito, H., H. Ohta and S. Morioka (2006). "Refinement of Solidification Microstructure and Austenite Grain by Fine Inclusion Particles." ISIJ International **46**(6): 840-846.

Taha, M. A. (1986). " Influence of Solidification Parameters on Dendrite Arm Spacings in Low Carbon Steels." Journal of Materials Science Letters **5**: 307-310.

Tokuyama, M. and M. Kawaski (1984). Physica **123A**: 386.

Tokuyama, M. and M. Kawaski (1984). "Statistical-mechanical theory of coarsening of spherical droplets." Physica **123A**(2-3): 386-411.

Turnbull, D. (1951). "Theory of Grain Boundary Motion." Transactions of the American Institute of Mining Engineers **191**: 661-665.

Tweed, C. J., B. Ralph and N. Hanseen (1984). "The Pinning by the Particles of Low and High Angle Grain Boundaries During Grain Growth." Acta Metallurgica **32**: 1407-1414.

Uranga, P., A. I. Fernández, B. López and J. M. Rodriguez-Ibabe (2005). " Optimization of Rolling Conditions in Nb Microalloyed Steel Processed by Thin Slab Casting and Direct Rolling Route: Processing Maps." Materials Science Forum **500-501**: 245-252.

Vives, C. (1989). "Electromagnetic refining of aluminum alloys by the CREM process: Part I. Working principle and metallurgical results." Metallurgical and Materials Transactions B **20B**(5): 623-629.

Voorhees, P. W. and M. E. Glicksman (1984a). "Solution to the multi-particle diffusion problem with applications to Ostwald ripening—I. Theory." Acta Metallurgica **32**: 2001-2011.

Voorhees, P. W. and M. E. Glicksman (1984b). " Solution to the multi-particle diffusion problem with applications to ostwald ripening—II. Computer simulations " Acta Metallurgica **32**: 2013-2030.

Wagner, C. (1961). "Theorie der Alterung von Niederschlaegen durch Umloesen (Ostwald reifung)." Z. Eleclraehem **65**: 581-591.

Wang, R., C. I. Garcia, M. Hua, H. Zhang and A. J. DeArdo (2005). "The Microstructure Evolution of Nb,Ti Complex Microalloyed Steel During the CSP Process." Materials Science Forum **500-501**: 229-236.

Watzinger, J., K. Moerwald and A. Wagner (2005). Medium Slab Technology - The Bridge between Conventional and Thin Slabs - Principles and Operational Results. 33rd McMaster Symposium on Iron and Steelmaking: Thin Slab Casting, McMaster University, Hamilton , Ontario, Canada, L8S 4L7, McMaster University Steel Research Centre.

Wilkinson, D. S. (2000). Mass Transport in Solids and Fluids, Cambridge University Press.

Winegard, W. C. (1964). An introduction to the solidification of metals. London, Institute of Metals.

Woodhead, J. H. and W. B. Morrison (1963). "The Influence of Small Niobium Additions on the Mechanical Properties of Commercial Mild Steels." Journal of The Iron and Steel Institute **201**: 43-46.

Wycliffe, P., G. R. Purdy and J. D. Embury (1981). Austenite Growth in the Intercritical Annealing of Ternary and Quaternary Dual-Phase Steels. Fundamentals of Dual-Phase Steels, Chicago, IIIinois, The Metallurgical Society of AIME.

Yin, H., T. Emi and H. Shibara (1999). "Morphological Instability of δ-Ferrite/γ-Austenite Interphase Boundary in Low Carbon Steel." Acta Materialia **47**(5): 1523-1535.

Yoshinaga, H., T. Watanabe and N. Takhashi (1995). Grain growth in polycrystalline materials II : proceedings of the 2nd International Conference on Grain Growth in Polycrystalline Materials, Kitakyushu, Japan, Zürich, Switzerland ; Lebanon, NH, USA : Transtec Publications.

Yuan, Q., B. G. Thomas and S. P. Vanka (2004). "Study of Transient Flow and Particle Transport in Continuous Steel Caster Molds: Part II. Particle Transport." Metallurgical and Materials Transactions B **35B**(August): 703-714.

Zarandi, F. and S. Yue (2005). "Effect of High Temperature Deformation on the Hot Ductility of Nb-Microalloyed Steel." Materials Science Forum **500-501**: 115-122.

Zhang, H., G. Pang, R. Wang and C. Liu (2005). " Austenite Grain Size of Thin Slab and its Influence on Direct Hot Strip Rolling of Nb Microalloyed Steel." Materials Science Forum **500-501**: 295-300.

Zhou, L., K. Cai and J. Zhang (2001). "Principles in Cast Rolling with Liquid Core of Thin Slab Continuous Casting." Metallurgical and Materials Transactions B **32B**(6): 459-464.

Zhu, G. and S. V. Subramanian (2006). "Ultra-fine Grain Size Control and Mixed Grains Elimination in Industrial Multi-pass Rolling Processing." Materials Science and Engineering A **426** 235-239.

Zurob, H. S., C. R. Hutchinson, Y. Brechet and G. Purdy (2002). "Modeling recrystallization of microalloyed austenite: effect of coupling recovery, precipitation and recrystallization." Acta Materialia **50**: 3075-3092.

Appendix I: Laboratory Solidification Simulation

When the carbon content is lower than 0.08%, it is very difficult to reveal the as-cast microstructure of microalloyed steels. In order to study the relationship between microstructure parameters and process parameters, the first task is to develop an etching method for revealing the as-cast microstructure. This is described in detail in section 1. The effect of experimental parameters such as dipping time, bar material and bar diameter are described in sections 2-4. Validation of the initial solidification simulation is present in section 5.

1. Method to Observe As Cast Dendrite Structure of Microalloyed Steel

Solidification starts when the dipping bar is dipped into the melt. In the present simulation, the melt was prepared from an APIX60 provided by Nucor steel. The carbon content of the steel is 0.053% and such that it solidifies as delta-ferrite. Upon subsequent cooling the delta-ferrite transforms to austenite and austenite transforms to alpha ferrite. It is, therefore, very difficult to observe the delta-ferrite dendrite morphology at room temperature with such low carbon content.

Several methods have been proposed in the literature in order to reveal the as-cast dendritic microstructures. Wang et al(Wang et al. 2005) used the etching solution of 200ml of a saturated aqueous solution of picric acid, 2-4g of sodium dodecylbenzene sulfonate and 2-

4ml HCl to reveal the solidification structure and austenite grain boundaries. Hoo et al (Hoo et al. 2006) stated that the microstructure can be observed by using a special type of Oberhoffer etching solution ($CuCl_2$: 1.0g, $SnCl_2$: 0.5g, $FeCl_3$: 30g, HCl: 300cc, H_2O: 500cc, Alcohol: 500cc). Pottore et a(Pottore et al. 1991) suggested that the best etching solution to observe the as cast microstructure is 200ml of a saturated aqueous solution of picric acid, 2 to 3 g of cupric chloride, 1 to 2 g of sodium tri-decyl benzene sulfonate, and on occasions, 2 to 4 ml of hydrochloric acid. According to the New Dofasco Tool Kit, ink highlighting copper etching and sulphur printing can be used to print the primary structures in all grades of steel.

All of the above etching methods have been used in an effort to reveal the dendritic microstructure in both the as received materials and the solidified shells on the dipping bars. Unfortunately the results were not very satisfactory and did not permit for the quantification of the microstructure parameters. As result, a modified method was developed as part of this work. This method consisted preheating the sample to 970°C for 45 minutes and furnace cooling down to room temperature as first step. The sample was then etched using an aqueous solution of supersaturated picric acid with sodium dodecylbenzene sulfonate and HCl. Figure AI-1 clearly shows the dendritic microstructure of APIX60 thin slab after this treatment. Figure AI-1 (a) is closed to the slab surface and (b) is close to the slab centre. All the solidification simulation samples will use this method to reveal the dendritic microstructure.

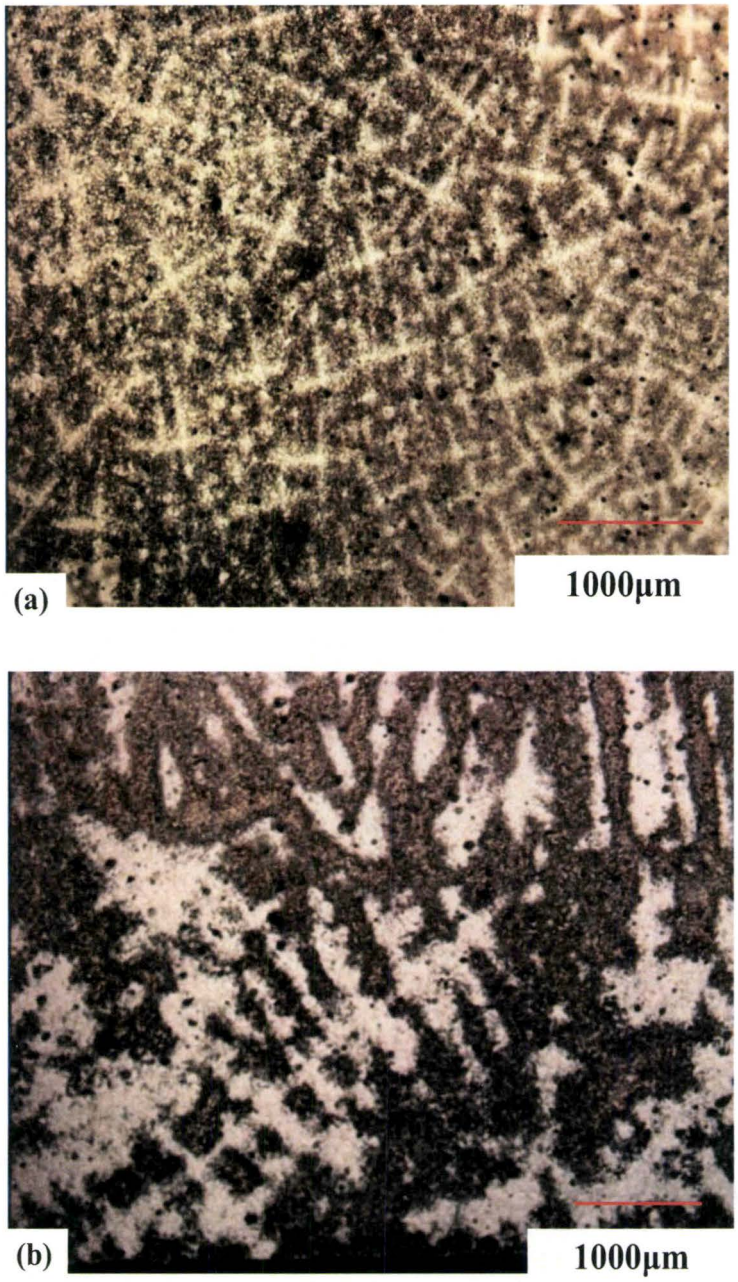

Figure AI-1. APIX60 dendritic microstructure (a) close to slab surface, (b) close to the slab centre

2. Effect of Dipping Time

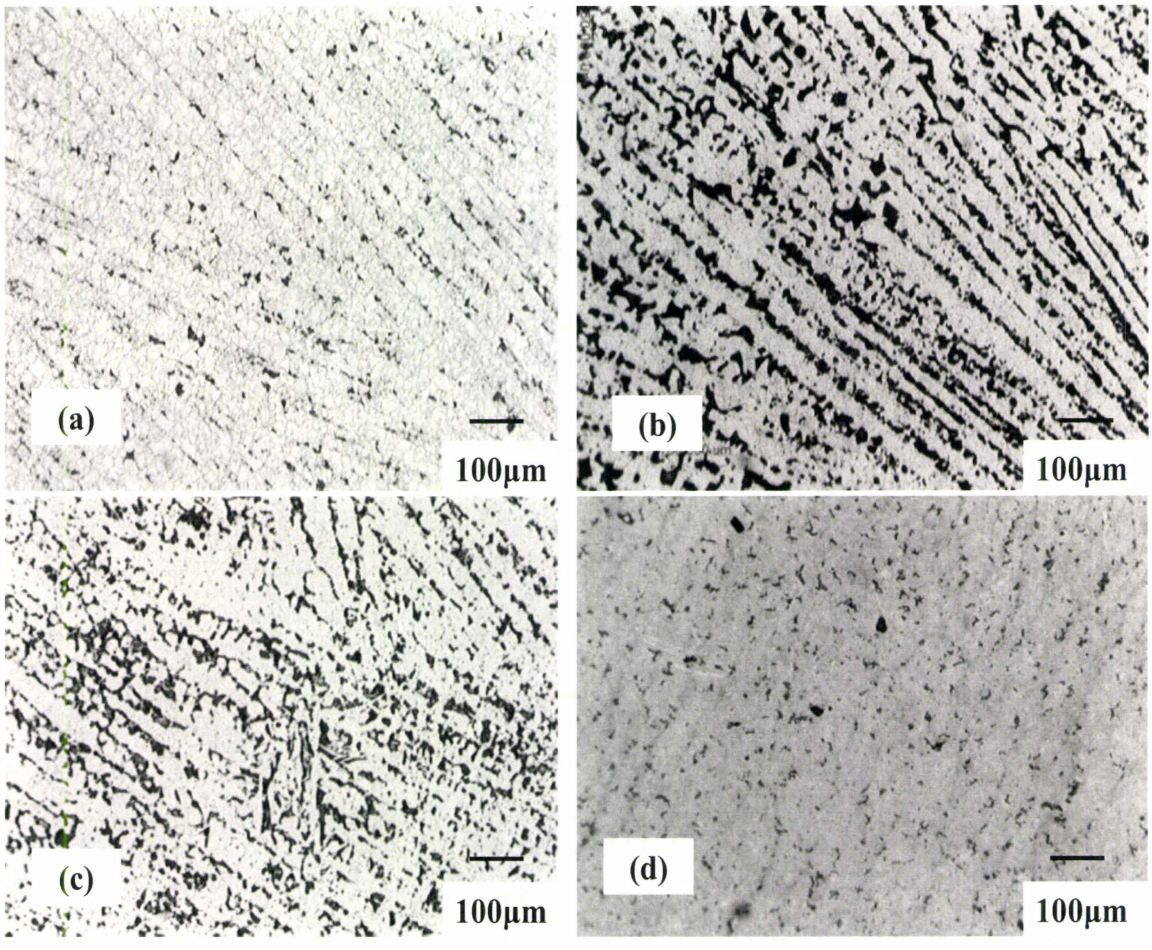

Figure AI-2. Microstructure of Ø 19mm copper dipping bar, dipping time: 4s, 7s, 10s and 15s

The solidified shell microstructures obtained when a 19mm diameter copper bar was dipped into the melt for different time are shown in Figure AI-2. All of the samples were cut in transverse direction as shown in Figure 3-3. Figure AI-2 (a) is the solidified shell on the dipping bar that was dipped into the liquid for 4 seconds. In this figure, the primary arms are close packed and secondary arms are not observed. The direction of the primary arms is parallel to that of heat extraction. Figure AI-2(b) shows the microstructure of the solidified

shell after 7 seconds in the liquid. The development of secondary arms is clearly seen in this case. Dipping into the melt for 10 seconds leads to the coarsening of the primary and secondary dendrite arms as seen in Figure AI-2(c). If the dipping bar is maintained in the liquid for 15 seconds as shown in Figure AI-2 (d), the dendritic microstructure is not observed suggesting that 15 seconds is long enough for the microstructure to homogenize.

3. Effect of Dipping Diameter

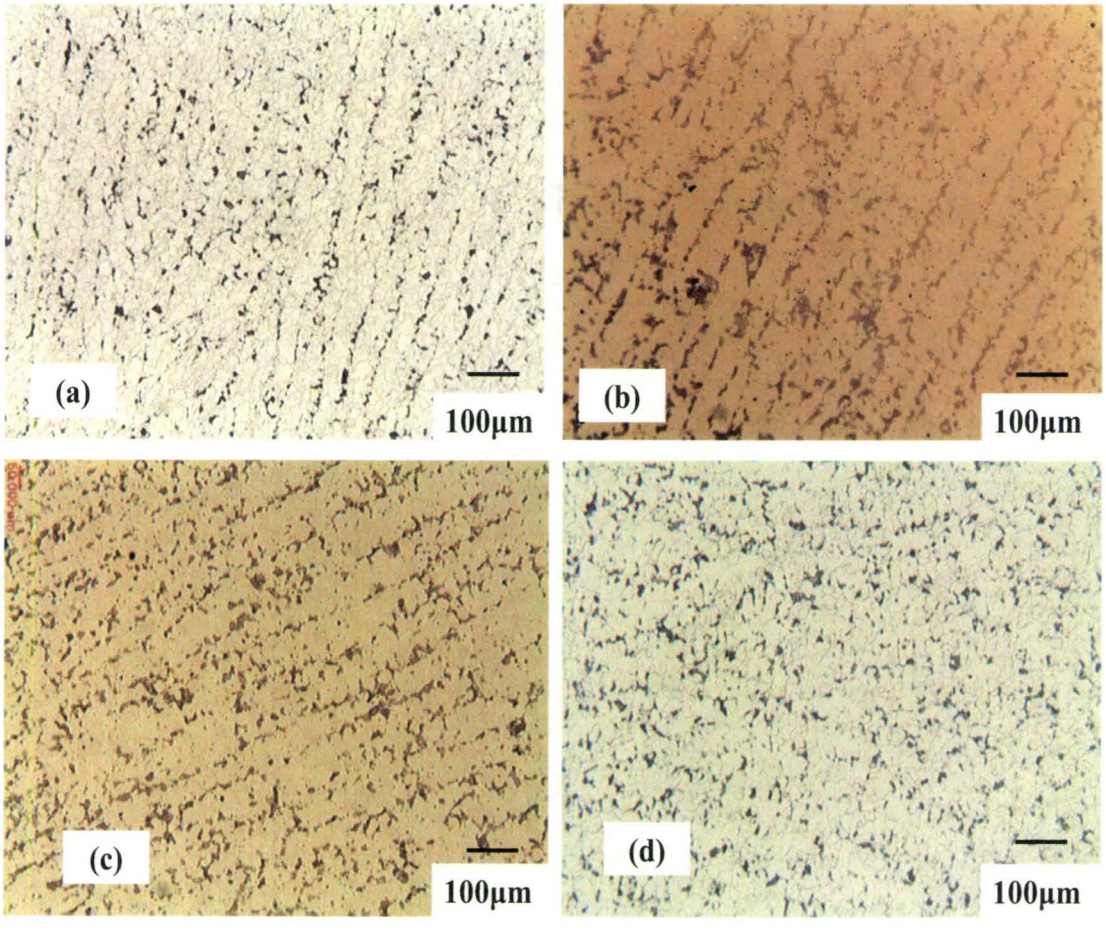

Figure AI-3. Microstructure of Ø 13mm copper dipping bar, dipping time: 4s, 7s, 10sand 15s

Changing the diameters of the dipping bar will change the cooling rates in the experiment. The microstructure of the solidified shells around a bar of 13mm diameter at different times is shown in Figure AI-3. These should be compared with the microstructure obtain in Figure AI-2 for 19mm diameter bar. The cooling rate of 13mm dipping bar should be smaller than that of 19mm. Figure AI-3 (a) is the microstructure for dipping time of 4 seconds. The primary arm spacing is coarser than that observed in Figure AI-2 (a). The same trend is observed when Figure AI-3 (b) is compared to Figure AI- 2 (b), Figure AI-2(c) is compared to Figure AI-3(c).

4. Effect of Dipping Geometry and Materials

Changing the material and geometry of the dipping bar provides another method of controlling the cooling rate during the present solidification simulations. Figure AI-4 shows the sketch of solidified shell on a steel pipe into the liquid for 7 seconds and Figure 4.5 shows the as cast microstructure at different positions of the dipping pipe. The inner and outer diameters of the pipe were 25mm and 13mm. Figure AI-5(a) is microstructure closed to the outside of the steel pipe; and Figure AI-5(b) is at the middle of the outside shell. Primary arms and secondary arms are clearly seen in these two figures. Figure AI-5 (c) is the microstructure of the material solidified inside the pipe. This microstructure consists of coarsened equiaxed dendrites because of the slow cooling rate inside the dipping pipe. At the outside corner of the pipe, the cooling rate is much higher than outside and inside; the primary arms are closed packed as shown in

Figure AI-5 (d). Microstructure inside the pipe is similar to the core of the industrial thin slab and the outside is similar to the slab surface.

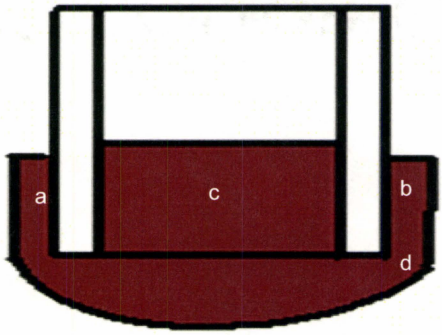

Figure AI-4. The sketch of solidified shell on a steel pipe

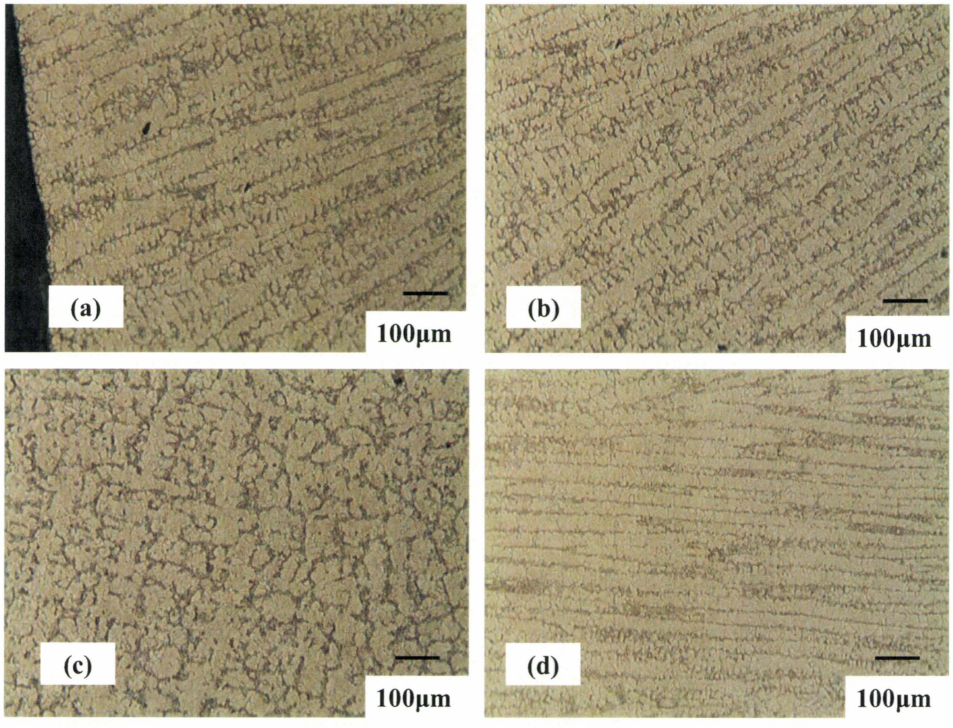

Figure AI-5. Microstructure of steel dipping pipe (a)outside, (b)centre of outside, (c) inside and (d)outside corner

5. Validation of the Solidification

As expected, the dendrite growth direction is parallel to the heat extraction (Figure 3.3). A comparison of the dendritic microstructure obtained in this simulation and that obtained in industrial thin slab is shown in Figure AI-6. Figure AI-6(a) is the microstructure obtained with an Ø20mm copper dipping bar after 7 seconds of immersion, (b) is as-cast microstructure closed to the surface of the thin slab provided by Nucor Steel (1mm from the slab surface). From the comparison it can be seen that the dendrite morphology of the simulation is similar to the industrial thin slab.

The primary arms spacing of the simulation has the same scale as industrial sample: in all the simulation samples (Figure AI-2 - AI-5), the primary arm spacing is about 100~150μm. The second arm spacing is between 30-50μm. According to Klinkenberg and Hensger (Klinkenberg and Hensger 2005; Uranga et al. 2005; Wang et al. 2005)), Uranga et al(Uranga et al. 2005) and Wang et al(Wang et al. 2005), the primary arm spacing of TSCDR slab is between 100μm and 180μm and second arm spacing is about 30-70μm.

The solidification rate is approximately 1mm/second in the simulation process; Camporredondo et al(Camporredondo-S. et al. 2004) and Castillejos et al(Castillejos-E. et al. 2005) state that the solidification rate in thin slab casting is about 1mm/s.

From above compassion, one can conclude that the set-up in the laboratory can simulate initial solidification stage of TSCDR Process.

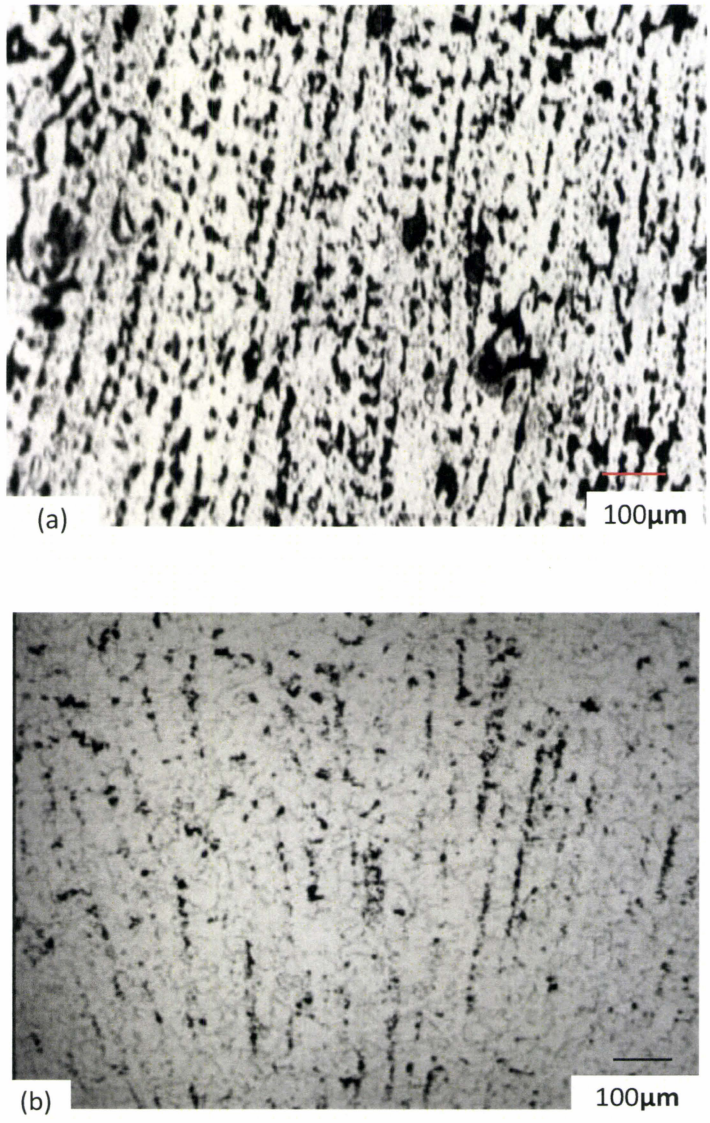

Figure AI- 6. Comparison of experimental simulation and industrial thin slab dendritic microstructure

Appendix II: Abnormal Austenite Grain Growth during Reheating of TSCDR Microalloyed Steels

As discussed in section 4.3, the APIX60 steel used in this investigation contained Nb and Ti additions which lead to the formation of complex Nb, Ti carbonitrides. During the reheating experiment, the dissolution of some of the precipitates Nb(C,N) results in the unpinning of some grains which then consume other grains by an abnormal grain growth process. The kinetics of abnormal grain growth in the present APIX60 steel are summarized and discussed below.

1. Results

The austenite grain boundaries of the as-received APIX60 steel were initially pinned by Nb and Ti carbonitrides. At 1100°C, sufficient pinning is available to prevent austenite grain growth even after extended holding. The microstructure at 1100°C after 15 and 60 minutes of holding is shown in Figure AII-1. It is clear from this figure that abnormal grain growth does not take place. When the samples are reheated to 1200°C, abnormal grain growth takes place as shown by the sequence of images in Figure AII-2. Similarly abnormal grain growth is observed when the samples are reheated to 1300°C (Figure AII-3) and 1400°C (Figure AII-4).

FigureAII-5 summarizes the austenite grain growth kinetics in APIX60. Once again, in these graphs, the times given represent the total time, including heating time, As such, the measured grain growth kinetics is not strictly isothermal and the complete thermal profile needs to be analyzed in order to quantitatively interpret the grain-growth data.

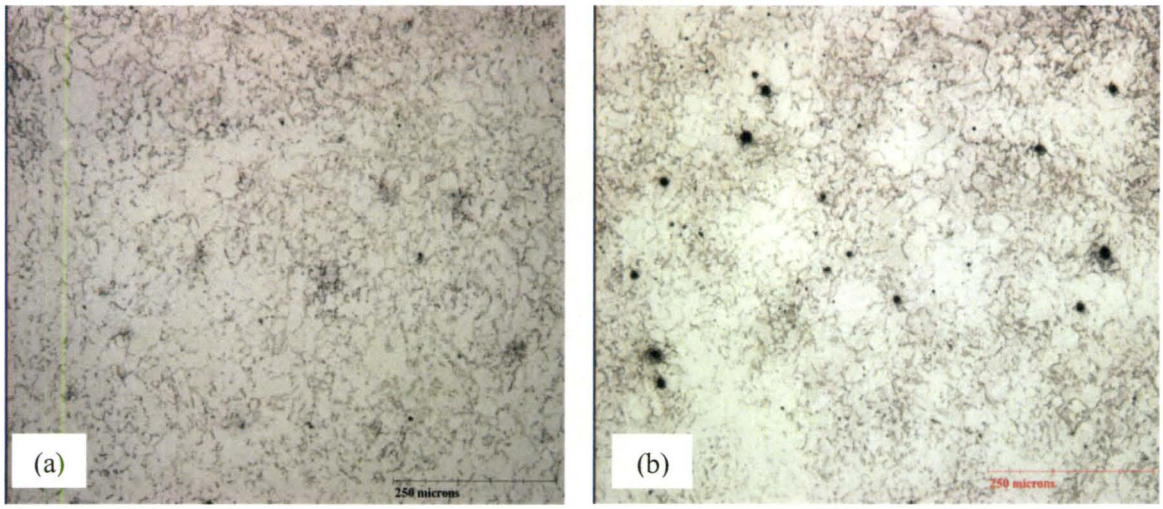

Figure AII-1 Microstructure APIX60 after heating to 1100°C for (a)15mis and (b) 60mins

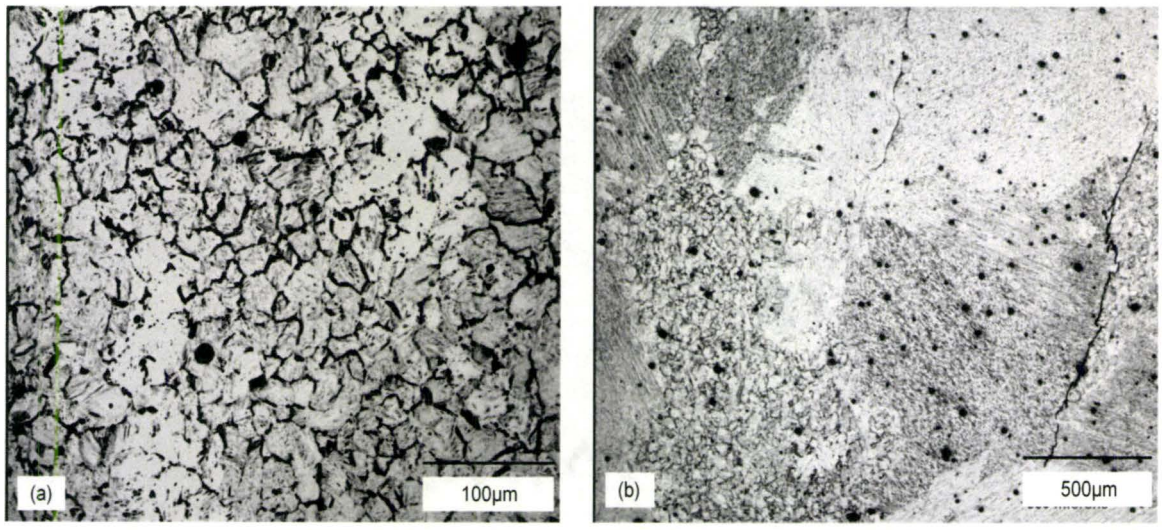

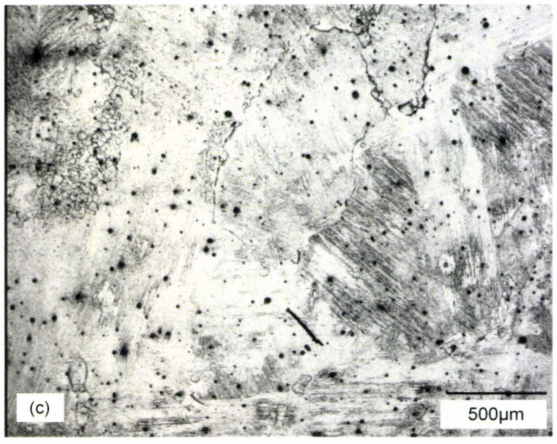

Figure AII-2 Microstructure APIX60 after heating to 1200ºC for (a)15mis, (b) 45mins, and (c) 60mins

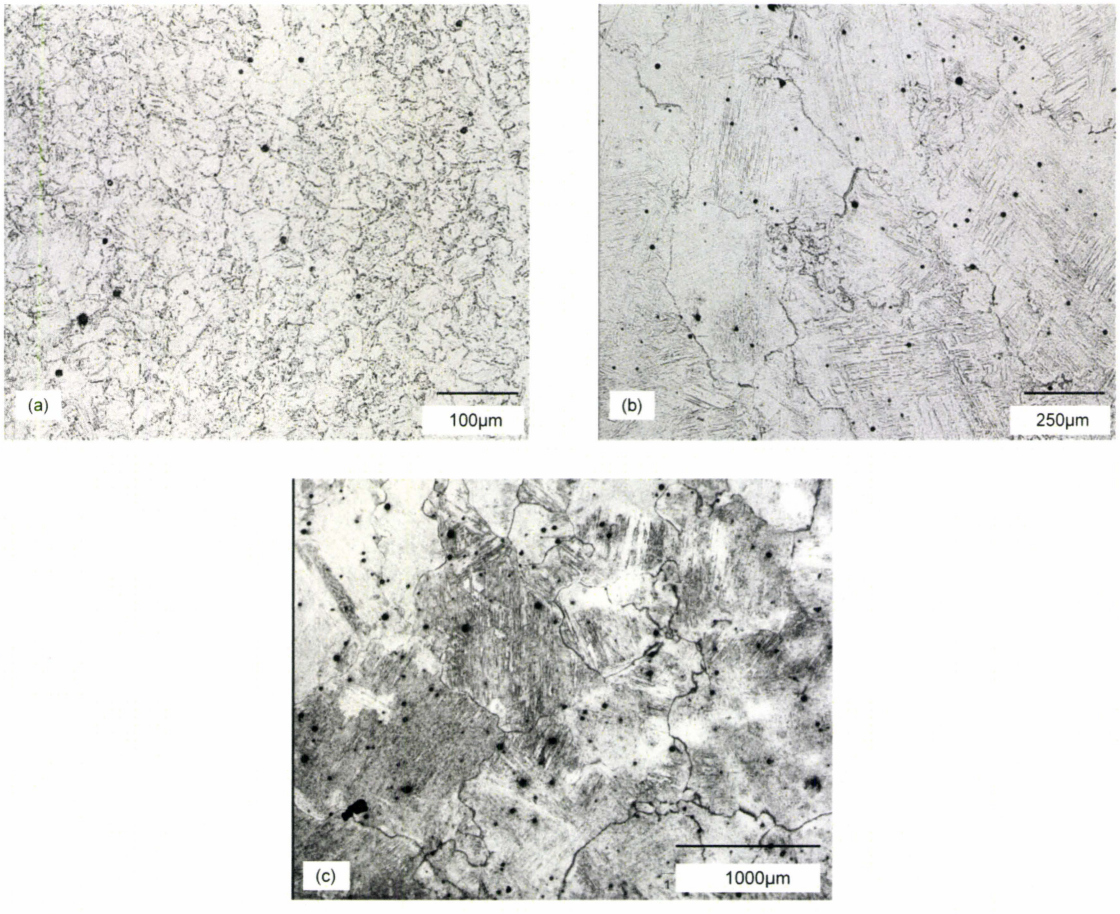

Figure AII-3 Microstructure APIX60 after heating to 1300ºC for (a)2mis, (b) 3mins, and (c) 15mins

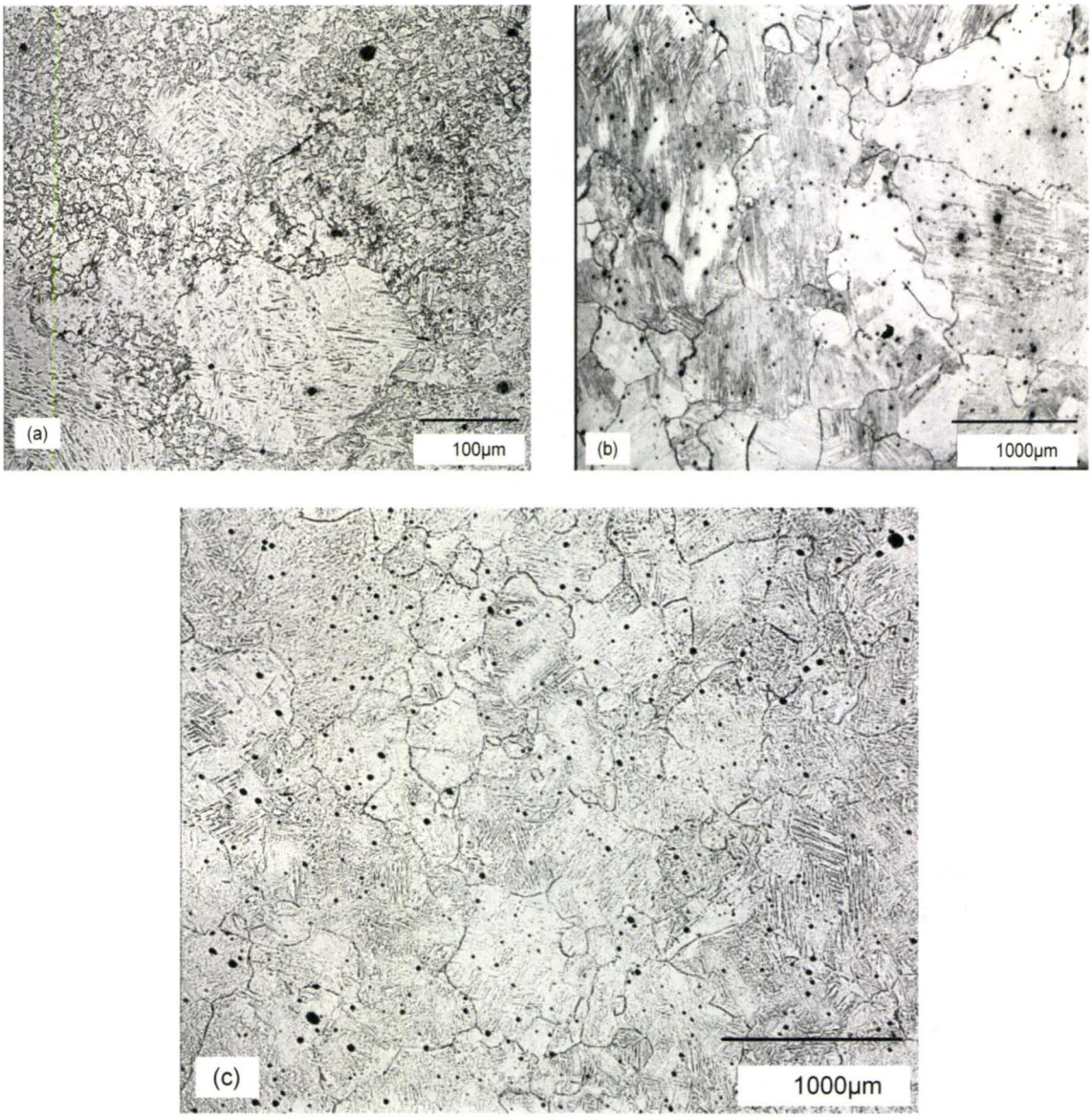

Figure AII-4 Microstructure APIX60 after heating to 1400°C for (a)1mis, (b) 5mins, and (c) 6mins

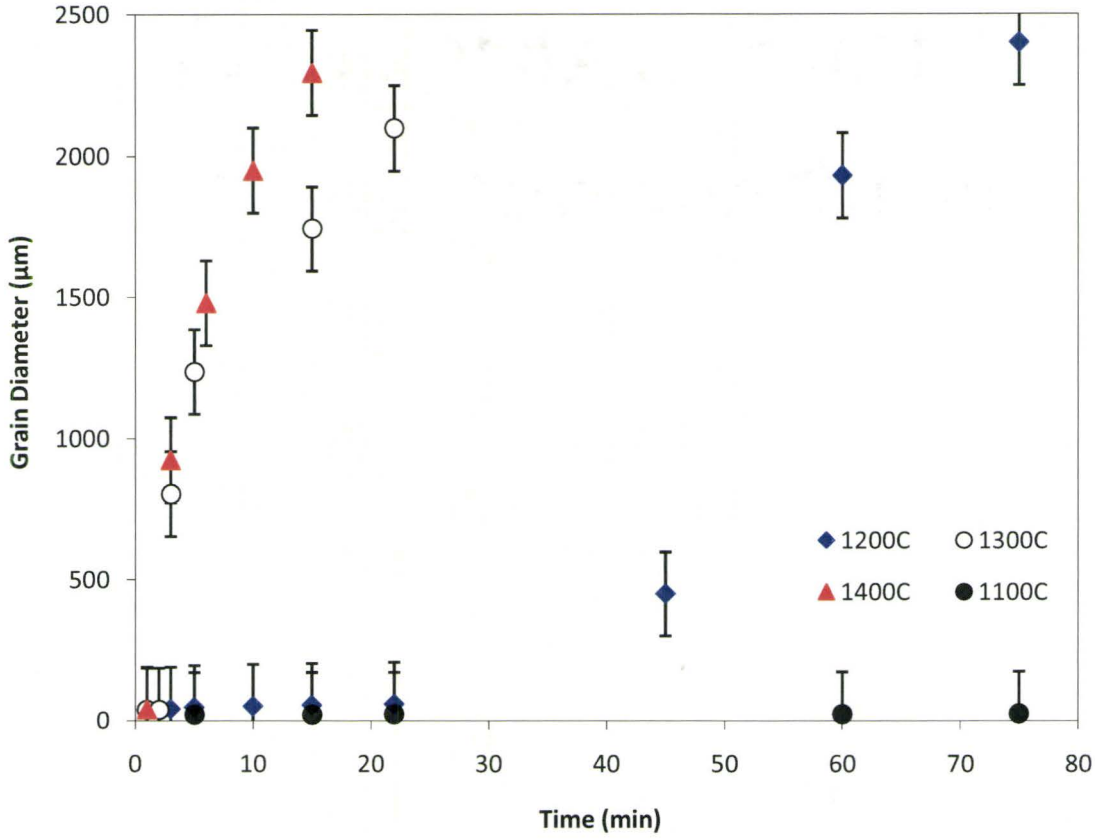

FigureAII-5 Austenite grain growth kinetics of APIX 60 steel

2. Discussion

During reheating, grain growth may be divided into two types: normal grain growth and abnormal grain growth(Hillert 1965). During normal grain growth, the microstructure changes in a rather uniform way and it is easy to predict and control. The grain size distribution is relatively narrow and independent of time. However, during abnormal grain growth a small number of large grains grow at the expense of a relatively fine matrix which is often pinned by particles and a bimodal grain size distribution develops. Eventually these large

grains impinge and normal grain growth (post abnormal grain growth) may then resume(Humphreys and Hatherly 2004). Abnormal grain growth has received a considerable theoretical attention over the half-century (Gladman 1966; Rios 1987; Flores and Martinez 1997; Rios 1997; Rios 1998), but very little information on grain-growth is available in the post abnormal grain growth stage because of the difficulties associated with determining the progress of abnormal grain growth at high temperature. In what follows, post abnormal grain growth in austenite is modeled and particular attention is given to the grain boundary mobility during post abnormal grain growth.

2.1 Abnormal Grain Growth in Austenite of APIX60:

From Figures AII-2 to AII-5, it can be seen that austenite undergoes abnormal grain growth. In an ideal grain assembly, the large grain will always grow more slowly than the average grain and eventually rejoin the normal grain size distribution. The main factor leading to abnormal grain growth in the present experiments is the dissolution of second phase particles. API standard microalloy steels contained Nb and Ti additions leading to the formation of complex Nb, Ti carbonitrides. Figure AII-6 shows the predicted mole fraction of the Ti(C,N) and Nb(C,N) precipitates of APIX60 as per the TCFE2 database of ThermoCalc. At 1100°C, the fine Nb(C,N) precipitates formed at low temperature would dissolve and the predominant precipitates present would be large Ti(C,N) precipitates that formed at high temperature(Kwon and DeArdo 1991; Pottore et al. 1991). These large precipitates are unable to pin the austenite grain growth when the temperature is higher than 1200°C. Between 1100

to 1200°C, the dissolution of the precipitates Nb(C,N) formed at low temperatures will result in the unpinning of some grains which then consume other grains by a process of an abnormal grain growth (Palmiere et al. 1994).

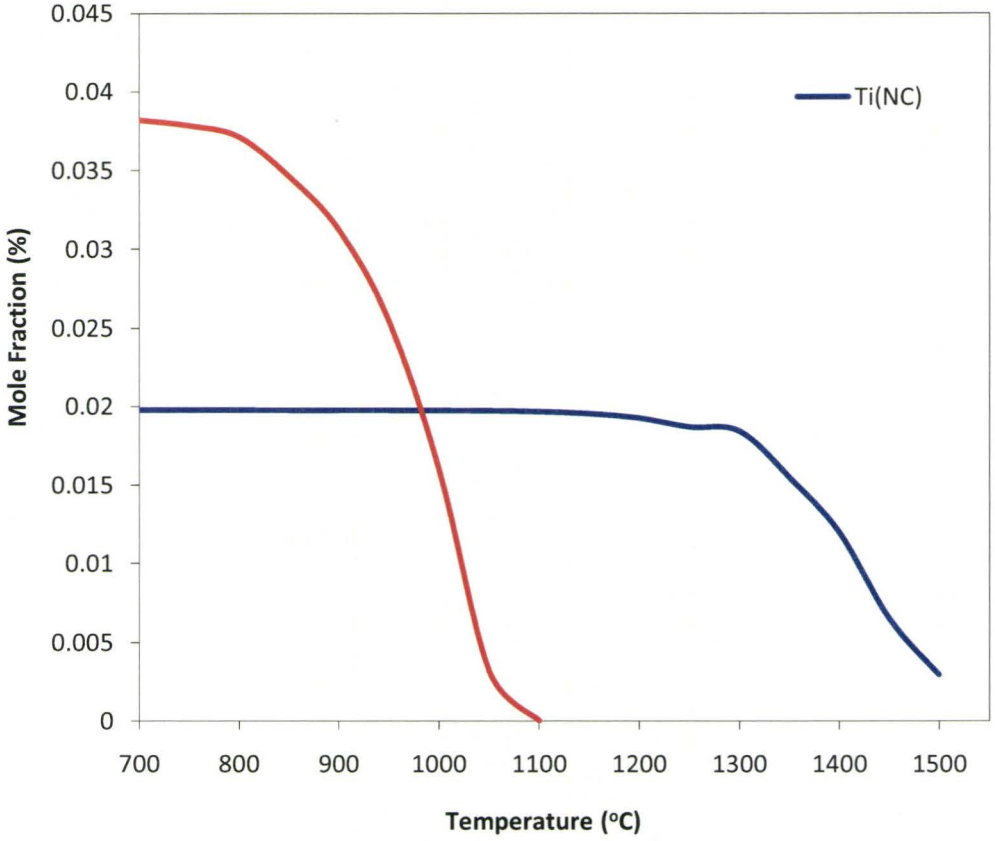

Figure AII-6 ThermoCalc predicted Nb(NC) and Ti(NC) mole fraction with temperature

When temperature is lower than 1100°C, only normal grain growth can take place because the fine Nb(C,N) particles provide effective pinning of the grain structure. According to Hillert's work(Hillert 1965), the maximum grain growth rate can be described as

$$\frac{dR_{\max}}{dt} = \alpha\gamma_{gb}M(t)\left(\frac{1}{R_{Cr}} - \frac{1}{R} - \frac{Z}{\alpha}\right) \leq 0 \qquad \text{--- (1)}$$

where *M(t)* is the grain boundary mobility, γ_{gb} is the grain boundary energy per unit of area, α is the geometric factor, Z is the pinning force which is related to the size and volume fraction of the Nb(C,N) particles, R_{cr} is the critical grain radius of grain size distribution. Grain growth requires the driving force due to curvature to be larger than the precipitate pinning force leading to a positive value of dR_{max}/dt. For reheating temperatures below 1100°C, it can be seen from Figure AII-6, that the Nb(N,C) particles are stable (Palmiere et al. 1994), and therefore grain growth is strongly pinned and there is no obvious change in grain size. This is clearly seen in Figure AII-5 when the temperature is 1100°C.

In the temperature range from 1100°C to 1200°C, the Nb(C,N) precipitates formed at low temperature dissolve(Palmiere et al. 1994; Humphreys and Hatherly 2004) leading to the pinning force to decrease. If a certain grain grows into a region in which the pinning force, Z – ΔZ, is lower than the average pinning force Z, then this grain will become unstable and abnormal grain growth may happen if the following conditions is satisfied(Rios 1997):

$$\frac{\Delta Z}{Z} > R_{cr}^3 \frac{n^3}{(n-1)^2}\left(-\frac{d(Z/\alpha)}{dt}\right)\frac{1}{M\gamma_g\alpha} \qquad \text{--- (2)}$$

In this equation, n is the ratio of maximum grain radius to the critical grain radius of the distribution. From Figure AII-2, when the reheating temperature is 1200°C, it can be seen that abnormal grain growth stared at about 30 minutes and finished at 70 minutes.

When the reheating temperature is above 1300°C, the particle pinning force will drop suddenly, dZ/dt<<0. Rios(Rios 1998) solved Eq. (1) by using Burke's law and gave the conditions for abnormal grain growth. A higher mobility combined with a pinning force can lead to abnormal grain growth development from an initially uniform grain size distribution. However, once the fine Nb(V,N) totally dissolved, the favourable local environment for abnormal grain growth may be changed and its grain boundary mobility advantage may be lost. The maximum size of the abnormal grain is limited and the abnormal grain starts to decrease its relative size to a value equal to that of the matrix, then "normal grain growth" may be resumed. From Figure AII-3(c), and AII-4(c), one can see that the grain size distribution is more uniform.

2.2 Determination of Post Abnormal Grain Growth

The progress of abnormal grain growth in APIX60 is shown in Figure AII-7. Isothermal abnormal grain growth is like isothermal primary recrystallization with respect to a plot of the fraction of sample transformed versus time (Dunn and Walter 1966). As discussed above, the abnormal grain growth depends on the dissolution of second phase particles Nb(N,C). At a reheating temperature of 1200°C, abnormal grain growth occurred after a holding time of 30 minutes. After 60 minutes, the abnormal grains impinged and a process of post abnormal grain growth began. When reheating to 1300°C, the post abnormal grain growth occurred after about 7 minutes and at 1400°C post abnormal grain growth occurred after 3 minutes.

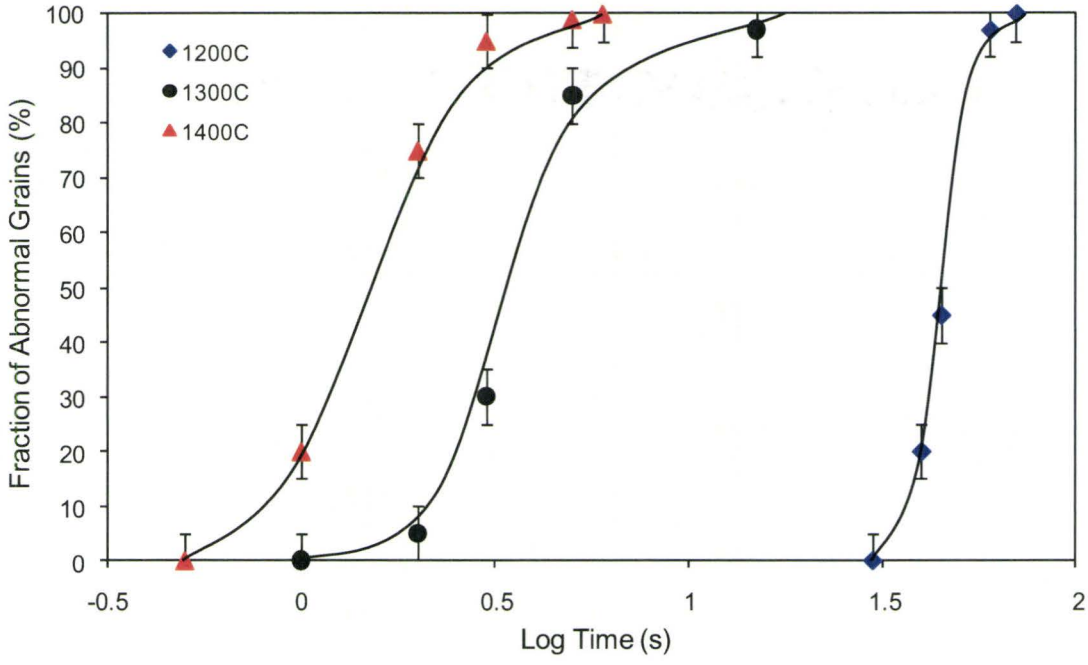

Figure AII-7 Progress of abnormal grain growth of APIX60

2.3 Comparison of Post Abnormal Grain Growth and Normal Grain Growth

Once the time for the onset of post abnormal grain growth was determined, the initial austenite grain size could be identified and the post abnormal grain growth could be modeled by equation (5.7). From the discussion in section 2.1 and 2.2, the newly formed austenite grains will be pinned at least up to 1100°C and abnormal grain growth will occur around 1200°C. In order to capture this equation (5.7), is integrated from t_1, should is the time at which the temperature reached 1200°C. The initial radius, r_o, should now be the radius when the post abnormal grain growth started. When the grain boundary mobility of equation (5.10)

is used, the predication of post abnormal grain growth is much slower than the experimental data. The best fit of the post abnormal grain growth experimental data for APIX60 was obtained by using a value which is 3 times that of equation (5.10). The results are shown in Figure AII-8. The dashed line is the temperature profile during the heating process (secondary axis), the dotted line is the model prediction of the grain diameter using equation (5.10) and the solid line is model prediction of the austenite grain diameter using three times of normal grain growth boundary mobility. As before, the solid points represent the experimental data.

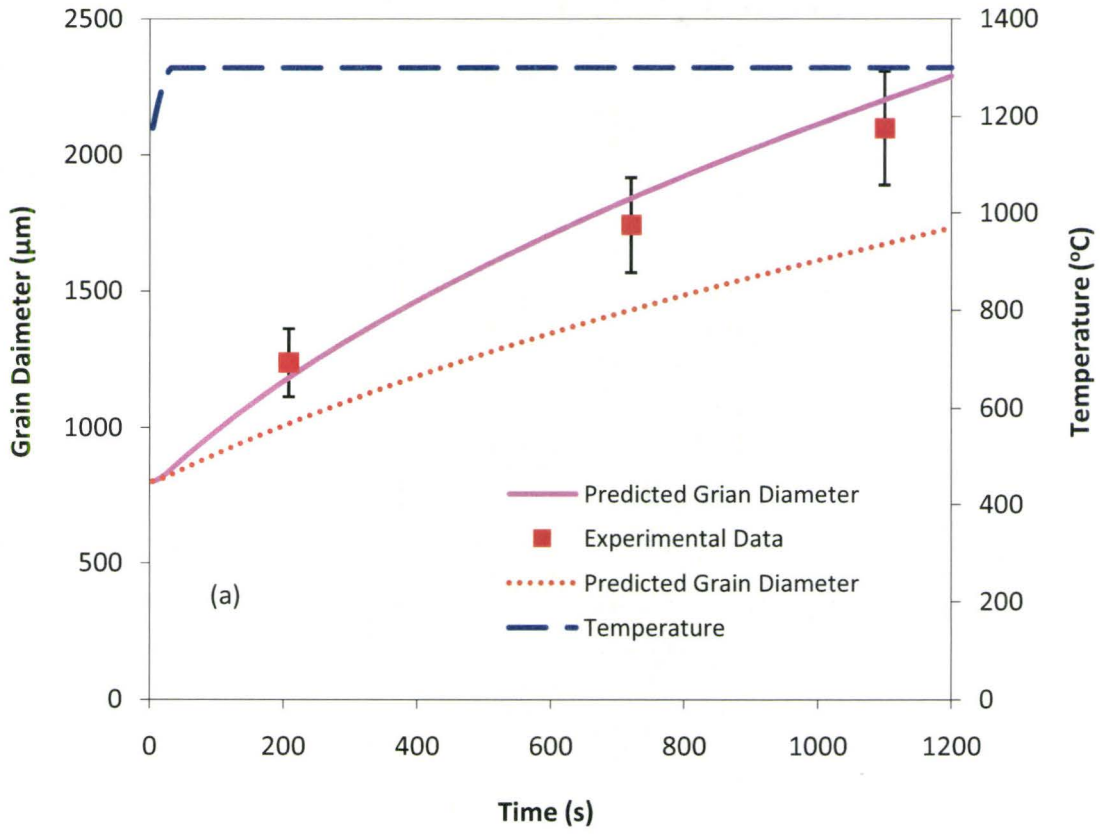

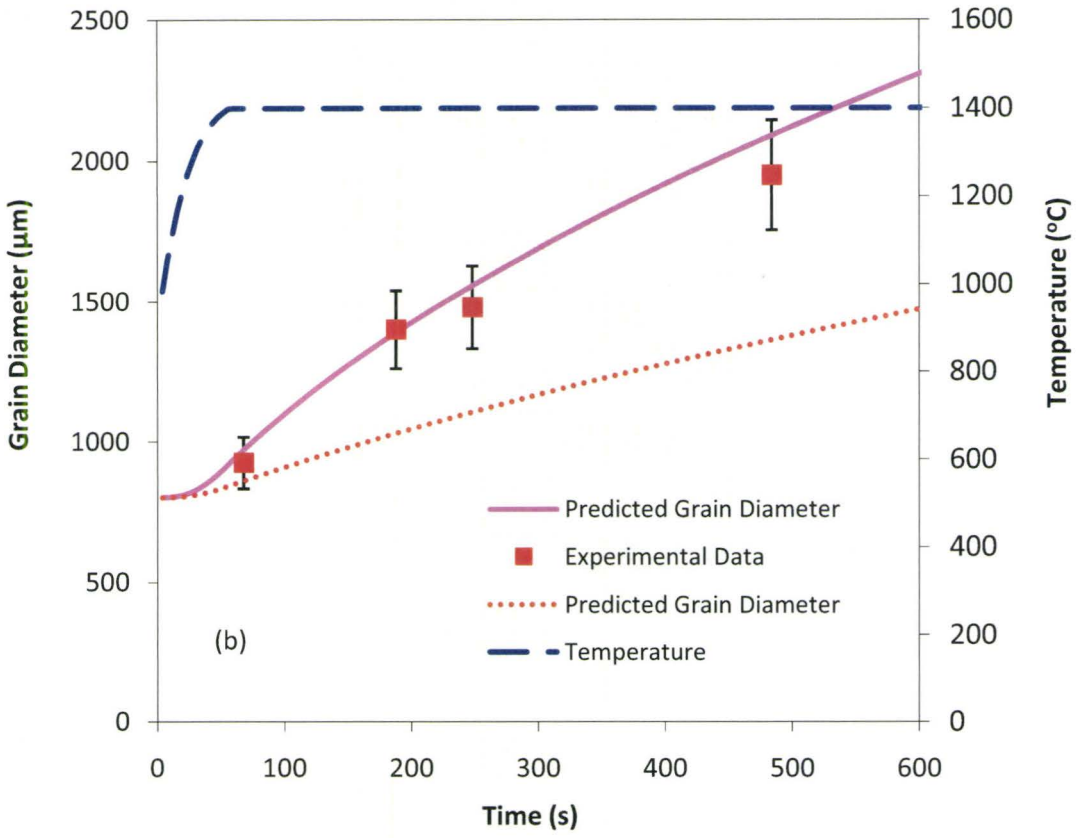

Figure AII-8Modeling prediction and experimental date of APIX60 austenite grain growth at (a)1300°C and (b)1400°C

These results suggest that the mobility of the grains present after abnormal grain growth is higher that the mobility of those present before abnormal grain growth. This is a novel observation which is still in need of an explanation

3. Conclusions

Austenite grain growth was investigated at temperatures between 1100°C and 1400°C using APIX60 and Nb-Ti free model alloy. Abnormal grain growth was observed when APIX60 specimens were heated up to 1200°C; this was attributed to the dissolution of microalloyed carbonitrides and the subsequent unpinning of some grains in the microstructure. Without Nb and Ti precipitates, the Nb-Ti free model alloy showed normal grain growth behavior within the experimental temperature range. In the post abnormal grain growth stage, the APIX60 steel showed normal grain growth behavior when the reheating temperature is above 1200°C. The post abnormal grain growth was determined at different reheating temperature. Increasing the reheating temperature, it took shorter time to enter the post abnormal grain stage. Austenite normal grain growth and post abnormal grain growth were modeled using a simple non-isothermal grain growth model. However, the grain boundary mobility of post abnormal grain growth was three times bigger than that of normal grain growth.